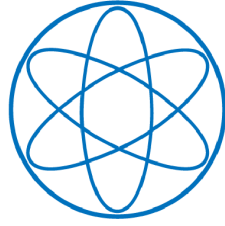# Optical Purification Study of the LAB-based Liquid Scintillator for the JUNO Experiment

DISSERTATION

von

SABRINA MELANIE FRANKE

TECHNISCHE UNIVERSITÄT MÜNCHEN

Technische Universität München

Physik-Department

Lehrstuhl für Experimentalphysik und Astroteilchenphysik

Prof. Dr. Lothar Oberauer

Optical Purification Study of the LAB-based Liquid Scintillator for the JUNO Experiment

Sabrina Melanie Franke

Vollständiger Abdruck der von der Fakultät für Physik der Technischen Universität München zur Erlangung des akademischen Grades eines

Doktors der Naturwissenschaften (Dr. rer. nat.)

genehmigten Dissertation.

Vorsitzender:		apl. Prof. Dr. Norbert Kaiser
Prüfer der Dissertation:	1.	Prof. Dr. Lothar Oberauer
	2.	apl. Prof. Dr. Andreas Ulrich

Die Dissertation wurde am 23.10.2018 bei der Technischen Universität München eingereicht und durch die Fakultät für Physik am 30.04.2019 angenommen.

Zusammenfassung

Das primäre Ziel des JUNO Experiments ist die Bestimmung der Neutrinomassenhierarchie mit Hilfe eines 20 kt umfassenden Neutrinodetektors, basierend auf der Flüssigszintillator-Technologie.

Zur Bestimmung des Typs der Neutrinomassenhierarchie wird eine Energieauflösung von mindestens 3 % bei einer Energie von 1 MeV benötigt. Um das zu erreichen, muss die Abschwächlänge mehr als 20 m bei einer Wellenlänge von 430 nm haben.

Der JUNO Szintillator wird aus drei Komponenten bestehen: dem eigentlichen Szintillator LAB und zwei Fluoren in den Konzentrationen 3 g/l PPO und 15 mg/l BisMSB. Die optischen Eigenschaften von LAB wurden bisher mit handelsüblichen UV/Vis Spektrometern und Küvettenlängen von maximal 10 cm gemessen. Dies führt zu absoluten Unsicherheiten in der selben Größenordnung wie die Abschwächlängen selbst. Im Rahmen dieser Doktorarbeit wurde ein Experiment entwickelt, welches die Abschwächung von Licht in flüssigen Medien bis zu einer Länge von 2.0 m misst, genannt das Precision Attenuation Length Measurement (PALM) Experiment. Messungen zeigten zeitliche Intensitätenschwankungen von 0.25 %. Die größte systematische Unsicherheit ist gegeben durch vorhandene Vibrationen, welche von der Laborumgebung in das Experiment gelangen. Optimierungen zur Vibrationsdämpfung wurden vorgenommen und ermöglichten die Vermessung verschiedener LAB Proben im Experiment, welche als mögliche Ausgangsmaterialen für den JUNO Szintillator in Erwägung gezogen werden. Zum ersten Mal ist es möglich, absolute Werte für die positive Wirkung einer Reinigungsmethode mit Aluminiumoxiden auf die Abschwächlänge von LAB anzugeben. Des Weiteren wird zum ersten Mal nachgewiesen, dass das in mehreren Schritten aufwendig gereinigte LAB von einer anfänglichen Abschwächlänge von 14.92 ± 0.74 m auf 28.07 ± 2.94 m aufbereitet werden konnte.

Im zweiten Teil der Arbeit wurde ein neuartiges Experiment zur Bestimmung der Lebensdauer von Positronium im Dreikomponentenszintillator von JUNO entwickelt. Da der inverse β-Zerfall die dominante Nachweisreaktion in JUNO ist, verzerren entstehende, langlebigere Positronium-Zustände die zeitliche Koinzidenz zwischen der Energieabgabe des Positrons an die Szintillatormoleküle und dem Entstehen der beiden 511 keV-γ bei dessen Annihilation. Um diesen Einfluss genau zu vermessen, wurde das Positronium Lifetime Determination (PoLiDe) Experiment im Rahmen dieser Arbeit entwickelt und ist in der Lage, die Lebensdauer der Positronium-Zustände im JUNO Flüssigszintillator zu bestimmen. Dafür nutzt es eine Koinzidenz zwischen drei Signalen, was einen großer Unterschied zu den typischen Positron Annihilation Lifetime Spectra (PALS) Experimenten darstellt. Ein erstes Ergebnis für die Lebensdauer von Ortho-Positronium (o-Ps) im JUNO-Szintillator ist 2.97 ± 0.04 ns, wobei eine statistische Unsicherheit angegeben ist.

Abstract

The primary goal of the JUNO experiment is the determination of the type of the neutrino mass hierarchy with a 20 kt liquid scintillator based neutrino detector. To determine the mass hierarchy, an energy resolution of at least 3% at 1 MeV is required. To achieve this resolution an attenuation length of more than 20 m at 430 nm has to be achieved. The favored three component scintillator is based on LAB, with 3 g/l PPO and 15 mg/l Bis-MSB as wavelength shifters. Measurements of the optical properties of LAB have been performed with UV/Vis spectrometers and cuvette lengths of 10 cm so far, which result in total uncertainties in the same order of magnitude as the attenuation length. To obtain precise measurements, the Precision Attenuation Length Measurement (PALM) experiment with light path lengths up to 2.0 m is built in the framework of this work. Furthermore, characterization measurements reveal a time stability of 0.25 % of the setup. The main source of systematic uncertainty is the presence of vibrations, which are coupled into the sample tube from the surroundings. The setup is optimized for vibration suppression and several favored LAB samples are measured in PALM. For the first time, absolute attenuation length values for the positive effect of a two step aluminum oxide purification technique, applied to LAB, are determined. Furthermore, it is found, that the attenuation length of the favored LAB can be improved from 14.92 ± 0.74 m to 28.07 ± 2.94 m at a wavelength of 430 nm after applying several purification steps. A second part of this work is the development of a new experiment for the determination of the positronium lifetime in the JUNO scintillator. Due to the fact, that the inverse β-decay is the dominant detection channel in JUNO, the production of positronium states distorts the time coincidence between the energy deposition of the positron and the 511 keV γ of its annihilation and therefore, the Positronium Lifetime Determination (PoLiDe) experiment is developed and built. Its purpose is the determination of the positronium lifetimes in the JUNO scintillator mixture and it uses a triple coincidence for a sufficient background rejection, which is, amongst others, a major difference to common Positron Annihilation Lifetime Spectra (PALS) experiments. A first result for the lifetime of ortho-positronium (o-Ps) in the final JUNO scintillator with its statistical uncertainty is determined to be 2.97 ± 0.04 ns.

Contents

Chapter 1

Introduction into neutrino physics

During the 1930's, W. Pauli was studying the energy spectrum of the radioactive β-decay [Paul30]. Although this reaction was explained as a two body decay that time, the detected energy was not discrete as expected, but continuous. To conserve energy and momentum, he postulated a third particle called "neutron", carrying the missing energy and momentum [Paul30]. This hypothetic particle also had to be electrically neutral with a mass in the same order as electrons and less than 0.01 times the mass of a proton as well as with spin 1/2. Furthermore, it had to have a finite but small magnetic moment of 10^{-13} ecm [Paul30][Fuk08]. Pauli, at this time, was not sure if such a particle could ever be detected. After the discovery of a new electrically neutral particle also named neutron by Chadwick, the postulated particle from Pauli got a new name by Enrico Fermi in 1932: the neutrino. In 1956, 25 years after its postulation, Reines and Cowan detected the first neutrino particle, the electron antineutrino $\nu_{\bar{e}}$ with a reactor neutrino experiment using the inverse β decay [Rei56]. They calculated the resulting cross section for the interaction of a neutrino with their detector to be $\sigma = (1.1 \pm 0.3) \cdot 10^{-43}$ cm^2 [Sch97]. Reines was awarded with the nobel price for this discovery in 1995. A second neutrino particle was found with the accelerator based Brookhaven neutrino experiment in 1963, called the muon neutrino ν_μ [Dan62]. In 2000, the DONUT experiment discovered the third neutrino type ν_τ[Don01].

The neutrinos are embedded in the standard model theory as massless, uncharged fermions with spin 1/2. They are classified as leptons with negative helicity and are only interacting via weak interaction [Bil12b]. The theory classifies three groups of leptons, ordered by their masses. The different neutrino flavors are ordered into the lepton group with increasing masses as:

$$\begin{pmatrix} e \\ \nu_e \end{pmatrix} \begin{pmatrix} \mu \\ \nu_\mu \end{pmatrix} \begin{pmatrix} \tau \\ \nu_\tau \end{pmatrix} \tag{1.1}$$

In 1956, first hints for an incomplete description of the standard model arised. R. Davis found discrepancies between the predicted and the measured solar neutrino flux with his radiochemical Homestake experiment, as did other experiments after him, too [Gno05] [SuK98] [Sag02]. This discrepancy could be solved by giving the neutrinos a mass, contradicting to the standard model, which would lead to a phenomenon called neutrino oscillations. Due to a nonzero mass, there is the possibility for a flavor change between the three neutrino flavors. This fact was confirmed by the Superkamiokande[SuK98] and SNO[Sno02] experiments and was awarded with the Nobel price in 2015 [Nob15].

1.1 Neutrino oscillations in vacuum

Assuming that neutrinos are weakly interacting particles, it implies a theoretical description with flavor and mass eigenstates. Based on the assumption of three different neutrino types called flavors, the different flavor eigenstates $|\nu_\alpha\rangle$, with $\alpha \in (e, \mu, \tau)$ and $\langle\nu_\beta|\nu_\alpha\rangle = \delta_{\alpha\beta}$, and also mass eigenstates $|\nu_i\rangle$, with i $\in$(1, 2, 3) and $\langle\nu_j|\nu_i\rangle = \delta_{ji}$, the flavor eigenstates are a coherent superposition of the orthonormal mass eigenstates. This can be described as [Bil12a]:

$$|\nu_\alpha\rangle = \sum_{i=1}^{n} U_{\alpha i} |\nu_i\rangle \tag{1.2}$$

with U the mixing matrix. This is due to the fact, that mass and flavor eigenstates are not equal. The approach was investigated by Pontecorvo, Maki, Nakagawa and Sakata (PMNS), similar to the mixing matrix in the quark sector [Mak62]. The mixing matrix has n^2 parameters and 2n-1 relative phases [Sch97]. For the case of three different neutrino flavor eigenstates[1], three mixing angles, one CP-violating phase δ and two Majorana phases α_1, α_2 as parameters. The mixing matrix U can be written in the form:

$$U = \begin{pmatrix} U_{e1} & U_{e2} & U_{e3} \\ U_{\mu 1} & U_{\mu 2} & U_{\mu 3} \\ U_{\tau 1} & U_{\tau 2} & U_{\tau 3} \end{pmatrix} \tag{1.3}$$

For the antiparticles, the matrix is complex conjugated. The PMNS matrix can be written as a multiplication of three rotation matrices and reduces to a form

$$U = \begin{pmatrix} c_{12}c_{13} & s_{12}c_{13} & s_{13}e^{-i\delta} \\ -s_{12}c_{23} - c_{12}s_{23}s_{13}e^{i\delta} & c_{12}c_{23} - s_{12}s_{23}s_{13}e^{i\delta} & s_{23}c_{13} \\ s_{12}s_{23} - c_{12}c_{23}s_{13}e^{i\delta} & -c_{12}s_{23} - s_{12}c_{23}s_{13}e^{i\delta} & c_{23}c_{13} \end{pmatrix} \tag{1.4}$$

---

[1]The number of flavors is determined experimentally by the measurement of the Z-boson width from studies of their production during e^+e^- collisions. For further detail see [Oli15].

with s_{ij} and c_{ij}, standing for $\sin(\Theta_{ij})$ and $\cos(\Theta_{ij})$, after neglecting the Majorana phases. This can be done because the neutrino oscillation probability is the same for both Dirac and Majorana neutrinos [Akh00].

For a neutrino with flavor ν_α, produced in a weak interaction at t=0 s, the time propagation of the flavor eigenstate can be written as[2]

$$|\nu_\alpha(t)\rangle = e^{-iE_i t} |\nu_\alpha(0)\rangle . \tag{1.5}$$

In the ultrarelativistic case, the energy of a neutrino with momentum $\vec{p}$, mass m_i and energy

$$E_i = \sqrt{p^2 + m_i^2}, \tag{1.6}$$

can be approximated to ($m_i \ll p$, $p \sim E_i$)

$$E_i \approx p + \frac{m_i^2}{2p}. \tag{1.7}$$

With the mass eigenstate system, the time propagation of the neutrino flavor ν_α is

$$|\nu_\alpha(t)\rangle = \sum_{i=1}^{3} U_{\alpha i} e^{-iE_i t} |\nu_i(0)\rangle . \tag{1.8}$$

The transition probability is given by the absolute squared transition amplitude A:

$$P_{\nu_\alpha \to \nu_\beta} = |A_{\alpha \to \beta}|^2 . \tag{1.9}$$

The transition amplitude is a projection of the time propagated neutrino state $|\nu_\alpha\rangle$ to the state $\langle\nu_\beta|$ [Sch97]

$$A_{\alpha \to \beta} = \langle\nu_\beta|\nu_\alpha\rangle . \tag{1.10}$$

This leads to a transition amplitude for the transition from the flavor state ν_α into ν_β:

$$A_{\alpha \to \beta}(t) = \sum_{i=1}^{3} U_{\alpha i} U_{\beta i}^* e^{-i\frac{m_i^2 L}{2E}} \tag{1.11}$$

where the approximation L $\sim$ t is used. The baseline L is the distance between the neutrino source and the detector. By comparing the transition amplitudes of neutrino and antineutrino states, it is found that

$$A_{\bar{\alpha} \to \bar{\beta}} = A_{\beta \to \alpha} \neq A_{\alpha \to \beta}. \tag{1.12}$$

due to the CPT theorem[3]. The left handed neutrino is mathematically transformed in a right handed antineutrino. Looking at the PMNS matrix, it can be seen that for the phase δ being zero, all transition amplitudes in equation 1.12 are the same.

---

[2]In the following natural units are used.

[3]C-charge conjugation, P-parity, T-time inversion. The neutrino state is changed into an antineutrino state by C, the parity flips the helicity of the particle and the time inversion changes the direction of the transition in theory [Sch97].

This would mean that the CP violation is non existent. As a consequence, CP violation can be checked by comparing the oscillations between a flavor α and β and their inversed transitions [Sch97]. The transition probability can be expressed by the amplitudes as described in formula 1.9

$$P_{\nu_\alpha \to \nu_\beta} = \left| \delta_{\beta\alpha} + \sum_{i=1}^{3} U_{\beta i}^* U_{\alpha i} (e^{-i\delta m_{ij}^2 \frac{L}{2E}} - 1) \right|^2 \tag{1.13}$$

for $\delta m_{ij}^2 = m_i^2 - m_j^2$ and E the neutrino energy. For three neutrino flavors, there are three squared mass differences, where two are independent:

$$\delta m_{31}^2 = m_3^2 - m_1^2 \tag{1.14}$$

$$\delta m_{21}^2 = m_2^2 - m_1^2. \tag{1.15}$$

The third squared mass difference is given by the others

$$\delta m_{32}^2 = \delta m_{31}^2 - \delta m_{21}^2. \tag{1.16}$$

Finally, the probability for a flavor change can be determined:

$$P_{\nu_\alpha \to \nu_\beta} = \delta_{\alpha\beta} - 2Re \sum_{j>i} U_{\alpha i} U_{\alpha j}^* U_{\beta i}^* U_{\beta j} [1 - e^{-i\frac{(m_i^2 - m_j^2)L}{2E}}] \tag{1.17}$$

The factor $\frac{L}{E}$ is important for neutrino experiments. It can be seen, that for zero squared mass differences, no neutrino flavor oscillations are taking place. Due to the fact, that neutrino oscillations have been confirmed[4], it is clear that at least one of the squared mass differences is nonzero, leading to the fact that also at least one neutrino mass eigenstate is nonzero, too.

The survival probability for a neutrino produced and staying in flavor α after propagating with time can be calculated to be

$$P_{\alpha \to \alpha} = 1 - \sum_{i \in \{\beta, \gamma\}} P_{\alpha \to i}. \tag{1.18}$$

Table 1.1 shows the current values for the neutrino oscillation parameters [Oli15].

1.2 Two flavor case

With respect to current experimental data, the reduction to a two neutrino oscillation framework is a good approximation of the neutrino mixing for some experimental approaches [Oli15]. For two different neutrino flavors, the PMNS matrix is reduced to a 2 x 2 matrix of the form of a rotation matrix with the mixing angle θ:

$$U = \begin{pmatrix} cos(\theta) & sin(\theta) \\ -sin(\theta) & cos(\theta) \end{pmatrix} \tag{1.19}$$

---

[4]The first hint for neutrino oscillations was found by R. Davis in 1956 and was confirmed by the SNO and SuperKamiokande experiment. Both collaboration spokesmen A. McDonald and T. Kajita were awarded with the Nobel price of physics in 2015 for this achievement [Nob15].

parameter	value
$\sin^2(\Theta_{12})$	$0.307^{+0.013}_{-0.012}$
$\sin^2(\Theta_{23})$	0.51 (NH) / 0.50 (IH) $\pm$ 0.04
$\sin^2(\Theta_{13})$	$(2.10 \pm 0.11) \cdot 10^{-2}$ (averaged)
$\delta\mathrm{m}^2_{12}$	$(7.53 \pm 0.18) \cdot 10^{-5}$ eV^2
$\delta\mathrm{m}^2_{32}$	$(2.52$ (NH) $/ 2.45$ (IH) $\pm 0.05) \cdot 10^{-3}$ eV^2

Table 1.1: Current neutrino oscillation parameter values, taken from [Oli15]. Note that for $\sin^2(\Theta_{23})$ and $\delta\mathrm{m}^2_{32}$ values for normal (NH) and inverted hierarchy (IH) are given, due to the unknown sign of the squared mass difference, see section 1.3. Also note that for $\sin^2(\Theta_{13})$ an averaged value is given. For further details see [Oli15].

With respect to the approximation (1.7) and the ultrarelativistic case, the transition probability of a neutrino, changing its flavor into another is given by [Akh00]

$$P(\nu_\alpha \to \nu_\beta) = sin^2(2\theta) \cdot sin^2\left(\frac{\Delta m^2 L}{4E}\right) \tag{1.20}$$

and the survival probability of a given flavor is $1 - P(\nu_\alpha \to \nu_\beta)$. This case is often used to describe the transition between $\bar{\nu}_e$ into ν_μ neutrinos, which is the case for reactor neutrino experiments with short distances L (< 5 km) [Oli15].

1.3 Neutrino mass hierarchy

The absolute values of the neutrino mass eigenstates are not known, but the determination of the squared mass differences has been investigated over the last years. From solar and reactor neutrino experiments, the squared mass difference $\delta\mathrm{m}^2_{12}$ is determined to be $\delta\mathrm{m}^2_{12} = +(7.53 \pm 0.18) \cdot 10^{-5}$ eV^2 , using the MSW[5] effect. With definition of the squared mass difference, it is clear that the mass eigenstate ν_2 has more mass than ν_1 [Oli14]. Combining measurements of atmospheric neutrino and long baseline accelerator experiments, a value[6] $\delta\mathrm{m}^2_{32} = (2.44 \pm 0.06) \cdot 10^{-3}$ eV^2 [Oli15]. Due to the fact, that the sign of $\delta\mathrm{m}^2_{32}$ is not known, there are two possibilities for arranging the mass eigenstates. For a positive sign, the mass eigenstate ν_3 has more mass than ν_2. This configuration is called the normal hierarchy. The inverted hierarchy configuration is defined for a negative sign of $\delta\mathrm{m}^2_{32}$, where ν_3 has less mass than the other two neutrino mass eigenstates. Fig. 1.1 shows both the normal and the inverted hierarchy of the neutrinos. Each mass eigenstate (ν_1, ν_2, ν_3) is a linear superposition of the three neutrino flavor eigenstates (ν_e, ν_μ, ν_τ), which is indicated by the three different colors of each mass eigenstate.

---

[5]The Mikheyev-Smirnov-Wolfenstein-effect is the resonance enhancement of the neutrino oscillation probability due to matter effects for neutrinos traveling through matter. Refer to [Akh00].

[6]The experimental data used for this values are from SuperK, T2K and MINOS and summarized in [Oli14].

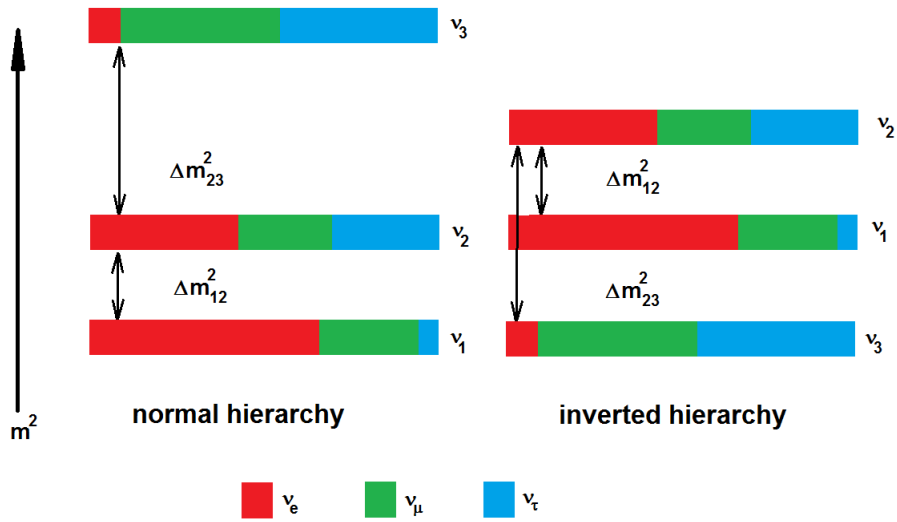Figure 1.1: Sketch of the normal and inverted mass hierarchy for the neutrino mass eigenstates. The mass eigenstates are different mixtures of the flavor eigenstates ν_μ, ν_τ, ν_e. For the neutrino mass eigenstates it is known that $\nu_1 < \nu_2$. Also the absolute value between mass eigenstate ν_2 and ν_3 is known, but not the sign. Therefore two different mass orderings are possible.

Comparing the values of both determined squared mass differences δm_{32}^2 and δm_{12}^2, the squared mass difference δm_{13}^2 can be calculated and it can be seen, that

$$\delta m_{31}^2 \approx \delta m_{32}^2 =: \delta m_{atmos}^2. \tag{1.21}$$

Because of the fact that the oscillation length is given by the squared mass differences and the oscillation amplitude by the mixing angles, the comparison reveals two different scales of oscillation lengths. δm_{atmos}^2 describes an oscillation in the order of 10^3 m per MeV, whereas δm_{12}^2 determines an oscillation length in the order of 10^5 m per MeV [7]. This fact leads to an oscillation dominated by δm_{12}^2 with a second oscillation from δm_{atmos}^2.

In principle there are different ways to determine the neutrino mass hierarchy experimentally [Zha08a]. Precision measurements of the squared mass differences $|\delta m_{32}^2|$ and $|\delta m_{31}^2|$ would determine the mass hierarchy, but this is very difficult since the δm_{21}^2 is very small compared to the others, which makes a measurement precision of more than 3 % necessary. The MSW effect, a resonance enhancement of the oscillation probability in matter, may amplify the effects of the mass hierarchy for experiments with baselines in the order of several hundreds of kilometers. Such experiments can only be performed with huge detectors and accelerator based neutrino beams. Accelerator based long baseline experiments like T2K [Men06], T2KK [Hag07] and NOvA [Men05] use muon neutrino (antineutrino) beams to detect the ν_e or $\bar{\nu}_e$ appearance [Zha08a]. This approach of the neutrino mass hierarchy determination is challenging, because the CP-violating phase is mixed into the hierarchy information for this measurement method. These can be suppressed by using a special baseline of around 7,000 km, but would need a very intensive neutrino source, which is not available in the near future [Zha08a].

Atmospheric neutrinos as neutrino source with energies of E ~ 1 GeV have distances in the region of 10^4 km between detector and their point of production [8] and can be used to determine the neutrino mass hierarchy also due to resonance enhancement of the neutrino oscillation probability in matter. For this approach, a measurement precision of better than 2 % for $|\delta m_{32}^2|$ is needed [Yan15]. PINGU [Ge13] is one of the experiments, which will investigate the determination of the neutrino mass hierarchy with this approach, using the same matter effect differences as accelerator based long baseline experiments [Yan15].

A rather promising third method is the usage of reactor neutrinos as neutrino source and intermediate baselines L (40 to 65 km) as detector distances. With a Fourier transformation of the L/E-reactor neutrino spectrum, and E as the mean neutrino energy, the neutrino mass hierarchy can be determined [Zha08a]. Such a detector would need an energy resolution better than $3 \% / \sqrt{E_{vis}}$ [Zha08a]. The approach with an intermediate baseline reactor antineutrino experiment will use, due to the

---

[7]Due to their first experimental detections, the different squared mass differences are also called the atmospheric and the solar squared mass difference.

[8]This is true for very small values of Θ_{13}, or even zero [Zha08a].

smaller baseline, the mechanism of neutrino oscillations in vacuum. Experiments like JUNO in China, RENO50 [Kim15] in South Korea and WATCHMAN [Alo14] [Ask15] in the U.S. are proposed intermediate baseline neutrino experiments. The JUNO experiment is currently under construction and will be described in the following chapter.

2 Chapter 2
The JUNO Project

The Jiangmen Underground Neutrino Observatory (JUNO) is an intermediate baseline neutrino experiment based on the liquid scintillator technology, which enables the detector to achieve energy thresholds of less than 1 MeV. Its primary goal is the determination of the neutrino mass hierarchy by optimizing the distance between detector and the neutrino source. Therefore, the JUNO detector is built next to two power plants, Yangjiang and Taishan, which provide a thermal power of 18 GW each. It will be built 700 m underground in a laboratory near Jiangmen, Guandong, China, which corresponds to a water equivalent of 1,900 m [Sal18]. The experimental site can be seen in fig. 2.1. The detector is placed in a distance of 53 km to optimize the disappearance of the reactor $\bar{\nu}_e$. Fig. 2.2 shows the $\bar{\nu}_e$ survival probability for both normal and inverted hierarchy and in dependence on the parameter L/E. Shown are the cases of normal neutrino mass hierarchy (blue) and inverted hierarchy (red) as well as the pattern for no neutrino oscillations at all (dashed black line). For a parameter value of ~ 10 to 11 km/MeV, the normal and inverted hierarchy pattern show their maximal differences [Ran17]. The mean energy of the reactor $\bar{\nu}_e$ is approximately 5 MeV [Sal18]. To resolve the differences of both neutrino mass hierarchies, an energy resolution of at least $3\,\%/\sqrt{\mathrm{E_{vis}(MeV)}}$ has to be achieved [Zha08a]. The energy resolution E_R is determined mainly by electron-photon statistics

$$\mathrm{E}_R = \frac{1}{\sqrt{\mathrm{n_{pe}}}} \tag{2.1}$$

with $\mathrm{n_{pe}}$ the total number of photo-electrons. These are proportional to

$$\mathrm{n_{pe}} = \epsilon_{\mathrm{coverage}} \cdot \epsilon_{\mathrm{quantum-efficiency}} \cdot n_\gamma \cdot e^{\frac{-\mathrm{x}}{\Lambda}}, \tag{2.2}$$

where $\epsilon_{\mathrm{coverage}}$ is the photocathode coverage and $\epsilon_{\mathrm{quantum-efficiency}}$ the quantum efficiency of the photomuliplier tubes, n_γ the light yield of the scintillator material, x the path length of light traveling through a medium and Λ the so called attenuation
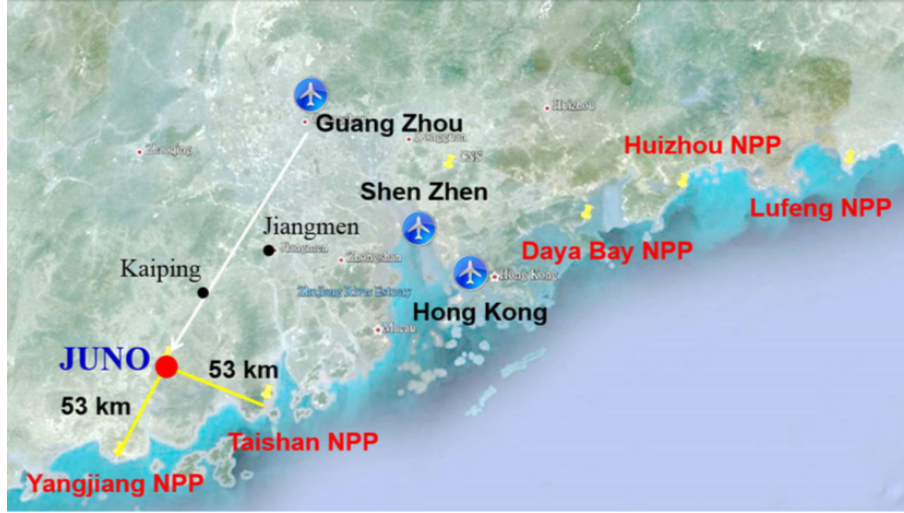
Figure 2.1: Experimental site of the planned JUNO detector in reference to the nuclear power plants Yangjiang and Taishan, which will provide reactor $\bar{\nu}_e$ for the experiment [JUN15].
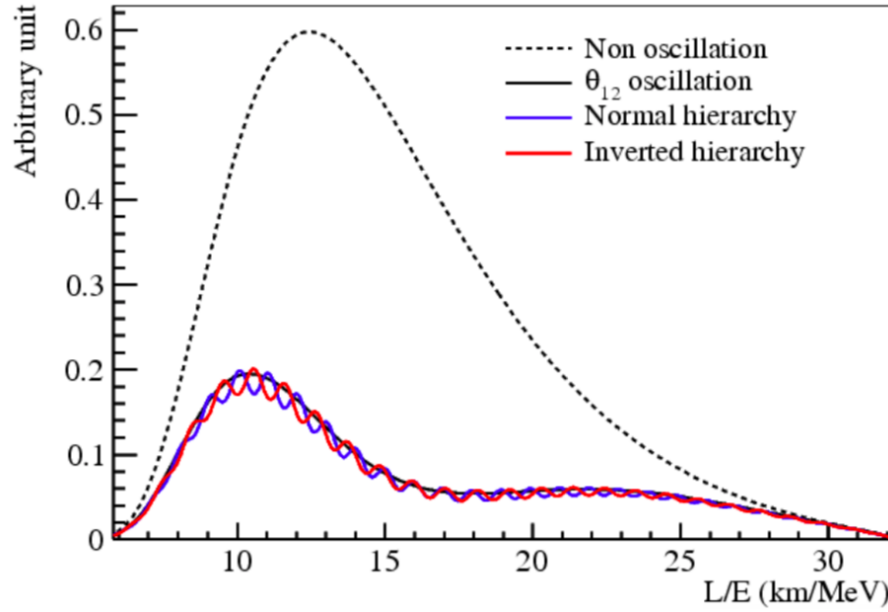
Figure 2.2: $\bar{\nu}_e$ survival probability in reference to the parameter L/E with L the distance between neutrino source and detector and E the mean energy of the reactor neutrinos. Plotted are the survival probability pattern for normal neutrino mass ordering in blue and the inverted neutrino mass hierarchy in red. The dashed black line correspond to the case without neutrino oscillations at all. Picture taken from [Ran17].
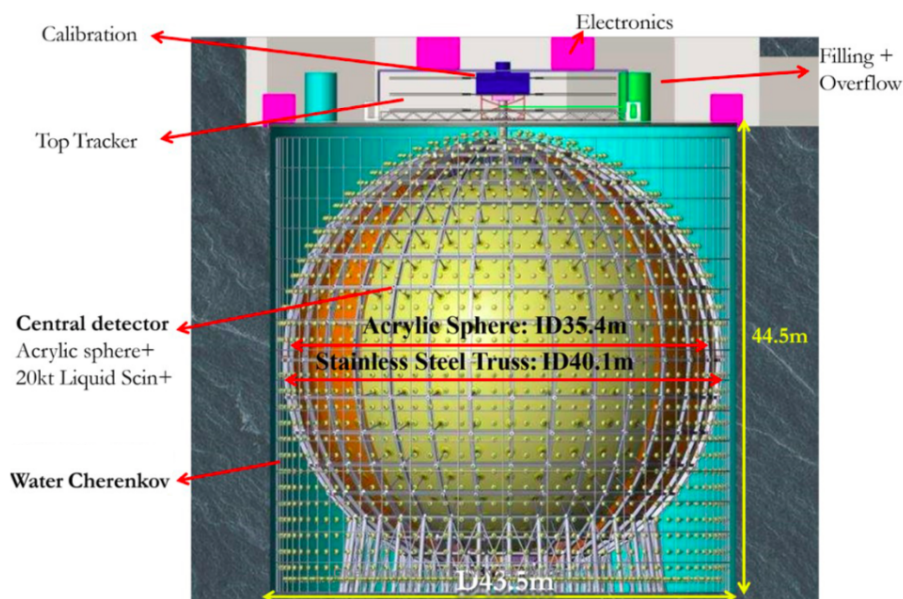
Figure 2.3: Scheme of the JUNO detector. The inner acrylic target vessel has a diameter of approximately 35 m and is filled with 20,000 tons of a three component liquid scintillator. 18,000 20 inch and 25,000 3 inch photomultiplier tubes monitor particle interactions in the target volume. Both outer support structure and acrylic sphere are dived in a purified water pool acting as a water Cherenkov detector, which is monitored by additional 2,000 20 inch PMTs. On top of the detector, also top trackers are mounted to identify particles crossing the medium. Figure adapted from [Ran17].

length[1]. An energy resolution of 3 % at 1 MeV can be achieved by improving the photomultiplier tube (PMT) photocathode coverage to 75 %, as well as achieving a quantum efficiency of at least 35 % and a minimal attenuation length of 20 m at 430 nm for the liquid scintillator[2] [An12] [An13] [An14]. Note that many other factors like PMT dark noise and electronics noise will also alter the energy resolution. The JUNO detector is designed under these conditions. It is built spherically and contains a fiducial volume of 20,000 tons of liquid scintillator. A scheme of the detector in progress is shown in fig. 2.3. For the neutrino target, 20 kilotons of liquid scintillator are filled into an acrylic vessel with a diameter of approximately 35 m, which is supported by a stainless steel structure. The target material will be monitored by 25,000 3 inch and 18,000 20 inch PMTs, which are mounted to the steel structure. The detector target will be dived into a purified water pool and scintillator panels are placed on its top. The water pool is acting as a Cherenkov

---

[1]The attenuation length is a crucial optical parameter and is explained in section 3.1.

[2]This improvements are based on a Monte Carlo simulation and are in good agreement with real Daya Bay data [An12] [An13] [An14].
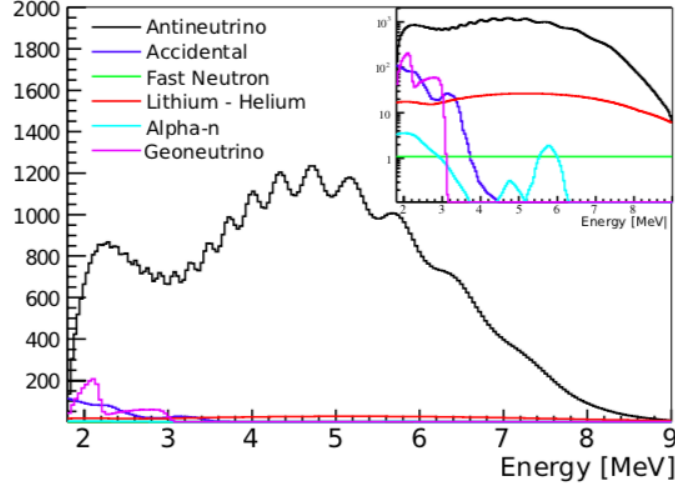
Figure 2.4: Energy spectrum of reactor $\bar{\nu}_e$ (black) and its five dominant background
          contributions expected in JUNO [JUN15]. Shown are accidental events
          (blue), fast neutron events (green) and long lived isotopes (red), geoneu-
          trinos (magenta) and events from α radioactivity (cyan). For a better
          comparison, the plot can be found in the upper right corner with a log-
          arithmic scale.

detector and is monitored by additional 2,000 PMTs. Both water Cherenkov detec-
tor and scintillator panels are part of the veto system to screen off incoming photons
or muons [JUN15] [Zha08b] [Sal18].
Besides the determination of the neutrino mass hierarchy, the JUNO experiment is
able to answer several fundamental particle and astrophysical questions due to its
high statistics and unprecedented energy resolution. It is able to detect neutrinos of
different sources, which are shown in the following. For a more detailed description
of the physics goals and JUNO's potentials, please refer to [An15b].

Reactor neutrinos

In JUNO, the dominant detection channel for incoming reactor electron antineutri-
nos $\bar{\nu}_e$ is the inverse beta decay on protons of the scintillator material:

$$\bar{\nu}_e + p \rightarrow n + e^+. \tag{2.3}$$

The produced positron will interact with the target material and deposit its kinetic
energy, before it will annihilate eventually with an electron. Two characteristic
$511\,\text{keV}$ annihilation γs are produced. $200\,\mu\text{s}$ after the release of the annihilation γs,
the neutron is captured on hydrogen of the scintillation material, emitting another
characteristic $2.2\,\text{MeV}$ γ-ray. Combined, both signals give a clear signature, which
can be used for background rejection [Fra11]. The five main background contribu-
tions to the IBD signal can be found in fig. 2.4. Shown are the energy spectra of

the reactor $\bar{\nu}_e$ in black. The largest background contribution originates from natural radioactivity, creating accidental coincidences. This background component is irreducible and multiple sources like the PMT glasses and the outer detector walls have to be taken into account. The α-radioactivity is counted separately and is referred to as (α, n). Such events result in neutrons being ejected from stable nuclei and are shown in cyan. Neutrinos originating from the Earth, called geoneutrinos, are considered as background for the reactor $\bar{\nu}_e$ spectrum (magenta) and have to be subtracted statistically. Spallation and cosmogenic muons on the liquid scintillator molecules result in fast neutrons (green) and in long lived ^{8}He and ^{9}Li isotopes (red), decaying via β-n [Gra16].

JUNO is designed to detect a high $\bar{\nu}_e$ flux with an excellent energy resolution and an accurate energy response. It will be able to determine the oscillation mixing parameters Θ_{12}, δm_{21}^2 and the effective mass splitting[3] Δm_{ee}^2 in the sub-percent level [Gra16]. Furthermore, it will be the first liquid scintillator experiment, which is able to simultaneously observe the neutrino oscillations of both solar and atmospheric neutrinos and multiple cycles of atmospheric squared mass difference oscillations [Gra16] [JUN15].

Supernovae burst neutrinos

The observation of supernovae neutrinos (SN) in JUNO may answer fundamental questions in particle and astrophysics [JUN15]. The data can help to understand the trigger mechanism of a supernova and may also give a hint to the conditions inside massive stars during their evolutions as well. JUNO can provide answers for several other related questions to the core collapse supernovae understanding. Furthermore, the new proposed scintillator detector is able to detect neutrino burst events from supernovae in a comparable rate as SuperKamiokande. This is not only due to the detection of IBD events, but also complementary channels like neutral current interactions on protons or elastic scattering or ^{12}C of neutrinos on electrons or protons can be detected [An15b] [Gra16] [JUN15].

Diffuse supernova neutrino background

The Diffuse Supernova Neutrino Background (DSNB) may be an integrated neutrino flux over all past core collapse supernovae in the visible universe and would give information amongst others about the rate of cosmic star-formation as well as failed supernovae [An15b]. The DSNB could be detected in JUNO, if backgrounds, especially those caused by atmospheric neutrinos, can be handled. Reactor and atmospheric neutrino background determine an energy window from 11 to $\sim 30\,\text{MeV}$ for the observation of DSNB neutrinos. Simulations show, that after 10 years of data taking, a signal within the 3σ level can be achieved. A non-detection would improve current limits significantly [JUN15].

---

[3]Defined parameter is a superposition of other mass-squared differences, but is independent of the unknown neutrino mass ordering. Detailed information can be found in [An15a].

Solar neutrinos

Neutrinos from the sun can be monitored by JUNO. Their detection can solve current discrepancies within the standard solar model and the helioseismologic measurement results, called solar metallicity problem. It can be solved by the more accurate measurement of the ^{8}B and ^{7}Be fluxes combined with neutrinos originating from the CNO cycle. The combined data can point down the appropriate version of the standard solar model, as they differ in their prediction of the ^{8}B and ^{7}Be fluxes [Gra16] [JUN15].

Atmospheric neutrinos

Atmospheric neutrinos are created in the atmosphere of our planet and have broad ranges in their energies ($10\,\mathrm{MeV} \sim 10\,\mathrm{TeV}$) and baseline lengths ($15\,\mathrm{km} \sim 13{,}000\,\mathrm{km}$) [JUN15]. They are able to penetrate the Earth, where their oscillation behavior will be affected by matter effects, which differ for normal and inverted mass hierarchy. JUNO will be able to measure these events and would be capable to use this information, too, to point down the neutrino mass hierarchy. After 10 years of data taking, the neutrino mass hierarchy can be determined at the 1σ to 2σ level. Furthermore, JUNO is able to measure the atmospheric mixing angle Θ_{23} and can search for CP-violating effects, too [JUN15].

Geoneutrinos

A neutrino flux from the inside of the Earth has been detected, called geoneutrino flux, which are created by radioactive β-decays of heavy elements and can be detected in JUNO as an $\bar{\nu}_e$ flux via IBD. By detecting geoneutrinos, it is possible to get a deeper understanding of the mechanisms within the Earth as well as its composition. The question, if the Earth's surface heat flow is a fraction of radioactive or primordial sources (or both) can be answered as well as the chemical layering or the energy needed for plate tectonic movements. [Gra16].

3 The JUNO liquid scintillator

When charged particles cross matter, they loose parts of their kinetic energy by excitation or ionization processes with molecules of the medium. In the case of scintillators, the molecules of the material can de-excite by luminescence, which can be detected by light detectors [Bir64]. For the ability of luminescence, optically active molecules have to be present. Such molecules typically contain benzene structures in the case of organic scintillators [Bir70]. A scheme of a benzene molecule can be seen in fig. 3.1. Benzene rings contain six carbon atoms, with one bound hydrogen atom each. The carbon atoms are sp^2 hybridized, which means that the built s- and p-orbitals can mix, resulting in sp^2 hybrid orbitals. In the case of benzene, three equivalent hybrid orbitals are built and one p-orbital per carbon atom remains unmixed. As the hybrid orbitals are arranged in a plane with equal angles, the resulting geometric structure of benzene is a flat, hexagonal ring. The hybrid orbitals have the ability to interact with each other, forming strong, so called σ-bonds. The unmixed p-orbitals of the carbon atoms can also interact with the sp^2-orbitals, producing so called π-bonds. This leads to delocalized electrons in the benzene molecule, which are responsible for the ability of luminescence [Bir64] [Bir70].

When charged particles deposit a part of their energy in the material, different excitation states of the molecules can be excited. Fig. 3.2 shows a Jablonski diagram, which summarizes the possible excitation and de-excitation processes. For a typical organic molecule, electronic singlet states S_i can be populated, where the spin of the involved electrons couple to zero. Also sub levels s_{ij} of the singlet states S_i, so called vibrational (sub-) levels, may occur. It is also possible to populate states with total spin one, which are called triplet states T_i with their own vibrational sub levels t_{ij}. These excitations can only be produced by the deposition of energy from crossing charged particles, whereas singlet states S_i can also be excited by a photon absorption process [Bir70]. After excitation of an optically active molecule, there are several de-excitation processes possible. Radiative de-excitations occur, if an electron can transfer from higher into lower electron states by emitting a photon. This is only possible for the first excited singlet S_i and triplet state T_i of
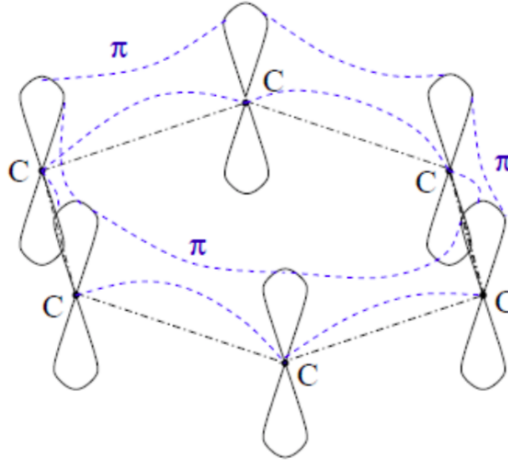
Figure 3.1: Scheme of a typical benzene molecule, according to [Bir64]. It contains
           six carbon atoms, which are arranged in a ring structure. The carbon
           atoms are sp^2 hybridized and the unmixed p-orbitals can interact with
           each other, forming π-bonds, which are responsible for the ability of
           luminescence.

an optically active molecule. The de-excitation per photon emission can differ in
its multiplicity[1]. For the same multiplicity, the transition between states is called
fluorescence, which is the case for the de-excitation via photon emission of the
first singlet state S_1. The transition between states with different multiplicities
is called phosphorescence and is present for the de-excitation of the first triplet
state T_1 [Bir70]. Also a radiationless transition is possible, which is often the case
for higher excited singlet and triplet states or between vibrational levels of different
electron states. Here, radiationless cascades can occur for states with the same
multiplicity, known as internal conversion, and for states with different multiplicity,
called intersystem crossing. Transitions between vibrational levels are in most cases
created by radiationless thermal activation from the initial state or followed by
thermal deactivation of final electron states [Bir70].

The absorption spectrum of typical optically active molecules contains absorption
bands in the UV as well as visible region. These bands are attributed to transi-
tions into excited singlet states of the π-electrons [Bir64]. In summary this means
that excited molecules in any π-singlet state S_i can de-excite radiationless via in-
ternal conversion. Thermal degradation lifts the current state into a vibrational
adjacent state of the first exited singlet state S_1, where fluorescence is possible for
de-excitation into the ground state S_0. For triplet states T_i, intersystem crossing
from triplet into singlet states is possible, resulting in delayed fluorescence light due

---

[1]For a total spin S, the multiplicity is defined to be 2S + 1, giving the amount of linear independent
   states with different spin orientations. In the given context, singlet (S=0) with multiplicity 1
   and triplet (S=1) states with multiplicity 3 are present.
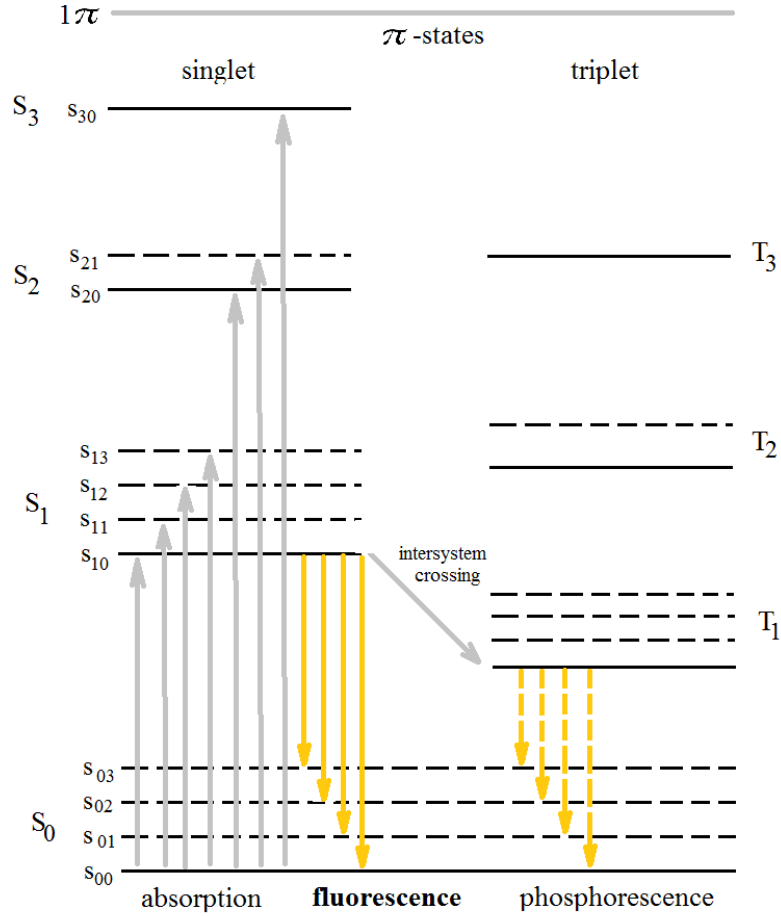
Figure 3.2: Jablonski diagram of possible electron states and vibrational sublevels for a typical organic molecule. Shown are electron singlet states from the ground state S_0 to the excited states S_1, S_2, ... as well as electron triplet states T_1, T_2, ... with its corresponding vibrational sublevels s_{ij} and t_{ij}. The grey arrows correspond to transitions from the ground state to energetic higher states, whereas the yellow arrows mark the de-excitation via luminescence. Figure adapted from [Bir70].

to spin forbidden transitions between first excited triplet state T_1 and the ground state S_0 [Bir64] [Bir70].

For organic scintillator molecules, the photon absorption and emission spectrum typically overlap, which is also the case for Linear-Alkyl-Benzene (LAB), used as scintillator solvent for JUNO. This leads to the possibility of a reabsorption of emitted scintillation photons and decreases the amount of photons which can be detected by photomultiplier tubes (PMTs). To suppress the reabsorption probability, substances can be added to the scintillator solvent LAB, which separate the emission spectrum from the absorption spectrum for less overlap. Such substances are called wavelength shifters. In the case of the JUNO scintillator, two wavelength shifters are used in small concentrations: 2,5-Diphenyloxazole (PPO) and 1,4-Bis(2-methylstyryl)benzene, shortened as BisMSB. In this combination, the emission maximum of LAB is shifted from 290 nm to 430 nm with both present wavelength shifters. The excitations are transferred non-radiative from LAB to PPO and mainly non-radiative from PPO to Bis-MSB[JUN15]. For the JUNO scintillator, LAB is chosen as scintillator solvent and the Fluor PPO is added in a concentration of 3 g/l, and the second Fluor Bis-MSB is used, in a concentration of 15 mg/l, decreasing the overlap of emission and absorption spectra of the three component scintillator from the near UV region to a wavelength of approximately 430 nm. This enables a much higher detectable photon rate due to the fact, that most photons are no longer self-absorbed and are able to reach the PMTs, mounted outside the acrylic vessel[JUN15]. The proposed energy resolution of 3 % at 1 MeV corresponds to $\sim 1,200$ photoelectrons (pe) per MeV deposited energy in the scintillator material, which have to be achieved at minimum. This introduces strong conditions to the transparency and the light yield of the liquid scintillator material used. Due to the fact that LAB is a petroleum derivative, its composition and impurities can differ for different petroleum sources and production methods.

3.1 Optical transparency

A high optical transparency of the LAB used for the JUNO scintillator is crucial. It has to be guaranteed, that the light produced in an interaction in the center of the fiducial volume can reach the photomultiplier tubes on the outer structure. Furthermore, the stated energy resolution has to be achieved to determine the neutrino mass hierarchy with JUNO[JUN15]. If electromagnetic waves traverse through a medium, they are attenuated by scattering and absorption processes. This is called extinction. For homogeneous media, the dominant attenuation process is absorption. For the case that multiple scattering is negligible, the intensity $I(x)$ of a light beam traveling a distance x through a medium is attenuated exponentially [Boh83]:

$$I(x) = I_0 \cdot e^{-\alpha_{\text{extinction}} \cdot x}, \tag{3.1}$$

with I_0 the incident intensity and $\alpha_{\text{extinction}}$ the extinction parameter, which is a result of both scattering and absorption processes:

$$\alpha_{\text{extinction}} = k \cdot C_{\text{absorption}} + C_{\text{scattering}}, \tag{3.2}$$

with k the number of particles per unit volume and C_i the absorption and scattering cross sections [Boh83]. Instead of using extinction, one can define the attenuation length parameter Λ. It is the path length light beam has to travel through a medium, after which its incident intensity I_0 decreases to $1/e \cdot I_0$ and is known as the Beer-Lambert-Bouguer-Law [Vog95]

$$I(x) = I_0 \cdot e^{-\frac{x}{\Lambda}}. \tag{3.3}$$

Analog to the extinction, the attenuation length is also correlated to scattering and absorption lengths:

$$\frac{1}{\Lambda} = \frac{1}{\Lambda_{\text{absorption}}} + \frac{1}{\Lambda_{\text{scattering}}}. \tag{3.4}$$

The attenuation length Λ is a composition of different light attenuation processes within a medium and consists of absorption processes with and without reemission as well as Rayleigh- and Mie-scattering [Zho15]. For a liquid scintillator medium, absorption processes convert the scintillation light into heat or reabsorbed photons, whereas scattering changes the direction of the produced photons within the medium. This leads to the fact that absorption processes have to be suppressed [Zho15].

For the favored JUNO liquid scintillator, several purification methods have been applied to improve the optical transparency of the scintillator solvent LAB, which will be described in the following [JUN15].

3.2 Purification techniques for liquid scintillator solvent LAB

Due to the fact that commercially available LAB may not reach the requirements for the optical transparency, an aluminum oxide column purification as well as a distillation, water extraction and nitrogen stripping purification technique are investigated for JUNO [JUN15].

The aluminum oxide column purification uses aluminum oxides as solid material, which have valence-unsaturated surfaces, where substances can be attached to. This fact can be used to remove impurities from LAB. As several aluminum oxides are available in different modifications, crystalline structures and concentrations of chemical bound water, the usage of different aluminum oxides may have different influences on LAB and its impurities. The aluminum oxide is typically filled in a column and the sample LAB is inserted on top. With pressure differences, the filtration process can be accelerated. Fig. 3.3 shows a scheme of an aluminum oxide column setup. The LAB is filtrated into a sample container after passing the

Chromatography column

Raw
Scintillator

Aluminum
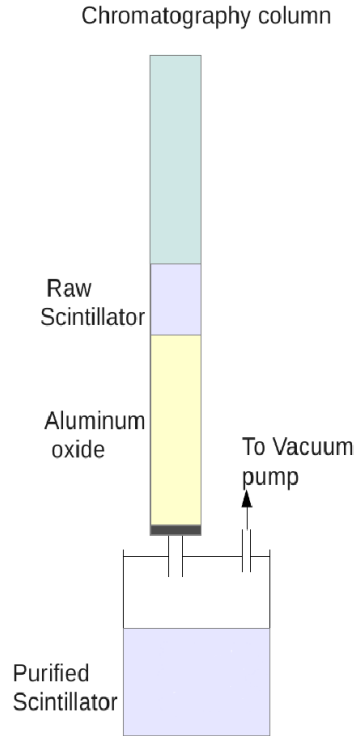oxide

To Vacuum
pump

Purified
Scintillator

Figure 3.3: Scheme of an aluminum oxide column purification. The solid material is filled in a chromatography column and the LAB is inserted on top. With the help of a vacuum pump, the LAB is filtrated through the aluminum oxide. Impurities can attach to the surface and remain in the solid material. Figure adapted from [Pru15].

aluminum oxide powder. During contact, impurities are bound to the surface of the aluminum oxide and remain in the solid material. The usage of different aluminum oxides (alkaline, neutral or acid) make it possible to bind different polar and non-polar organic impurities [Gri87] [Kra96] [Hol07]. Investigations by [Pru15] and [JUN15] reveal an improvement of the attenuation length after purifying the LAB sample with aluminum oxides. Furthermore, results from [Pru15] show that the combination of alkaline and acid aluminum oxides can improve the attenuation length of the LAB sample over a wider range of wavelengths.

Another purification technique is the fractional distillation, where the LAB is partly evaporated, and a scheme of the distillation can be found in fig. 3.4. The technique is based on a mass and heat transfer between a liquid and a gas stream. LAB is vaporized in a boiler, creating an upward gas stream. As the vapor rises, it cools and parts of the vapor condensate inside the distillation column. The concentration of volatile components of the LAB is increasing in the vapor phase and less volatile substances enrich the liquid condensate. Using a multiple stage column of certain
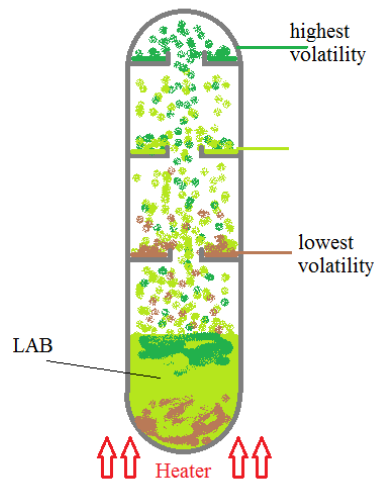
Figure 3.4: LAB is inserted in a column with several stages and is heated. Due to
different boiling points, the vaporized components condensate at different stages. The distillation is used to separate substances with different volatility.

length, several equilibrium stages between vapor and condensate are present. In the case of the petroleum derivate LAB, components with differing volatility can be (partly) oxidized organic molecules, or shorter alkyl-benzene chains, because the liquid is a superposition of several alkyl benzenes and possible impurities. Its constitutes have different boiling points, which makes fractional distillation a favored purification method. Also a separation from solid components is possible, e.g. for radioactive metals. In most cases, the technique is used to remove impurities like uranium, thorium and potassium. Investigations show that the distillation purification of LAB can increase the attenuation length at 430 nm and its radiopurity, also [JUN15] [For15].

A third purification technique, which is investigated for LAB in JUNO, is water extraction. It uses the polarity of water molecules to separate polarized impurities from LAB. In a (heated) multistage column water and LAB are inserted. As the density of LAB is smaller than the density of water, the LAB is inserted on the bottom of the column and water on top. Because of the density differences, the LAB liquid will start to flow upward and the water downward. Both liquids are stirred and brought in close contact to each other and charged, ionized or polarized impurities can attach to the water molecules more easily and concentrate in the heavy phase at the bottom of the column. A scheme of the water extraction method can be found in fig. 3.5. The water extraction method can remove charged as well as polarized particles very efficiently, as well as heavy metal species like uranium or thorium. Unfortunately, optical impurities are not removed efficiently, as these are often unpolarized, oxidized organic molecules [For15].
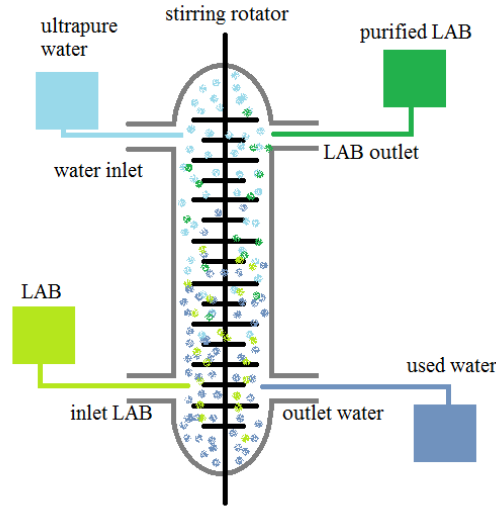
Figure 3.5: LAB as raw material is filled in a column from the bottom, whereas the pure water is inserted on the top. Due to density differences, the water is streaming downward, whereas LAB begins to flow upward. A rotator construction stirs both substances, bringing them in close contact. Possible polarized or charged impurities can attach to the water and are removed.

A fourth technique studied for the LAB purification in JUNO, is the method of gas stripping and a scheme can be seen in fig. 3.6. It is based on the difference in vapor-liquid partitioning. In a stripping column, the preheated sample liquid is inserted from the top of the column and falls down by gravity in unstructured packings. A gas stream is inserted from the bottom of the column. As both streams come in close contact, dissolved gases and volatile components of the liquid can be removed efficiently. Ultra pure nitrogen, which itself can be purified with active carbon, is used as stripping gas to reduce radioactive impurities in JUNO. This method is used to purge the LAB from radioactive gases as well as oxygen and also possible water molecules, which can remain after a water extraction process [JUN15] [For15].

All four methods are considered to purify the LAB used for JUNO. Therefore, several studies and first purification plant prototypes are constructed and are currently tested at the Daya Bay underground laboratory in China.

The attenuation length is one of the crucial parameters for achieving the energy resolution, which is necessary to determine the neutrino mass hierarchy in JUNO. Attenuation length measurements have been performed with commercial UV-Vis spectrometers with a wavelength range between 190 and 900 nm [JUN15]. These spectrometers measure the attenuation of light in a 10 cm cuvette, which represents the maximal path through a medium. Because the attenuation lengths of the liquids are in the order of 20 m at 430 nm the determined values from attenuation measurements in 10 cm cuvettes contain huge uncertainties. This makes it difficult
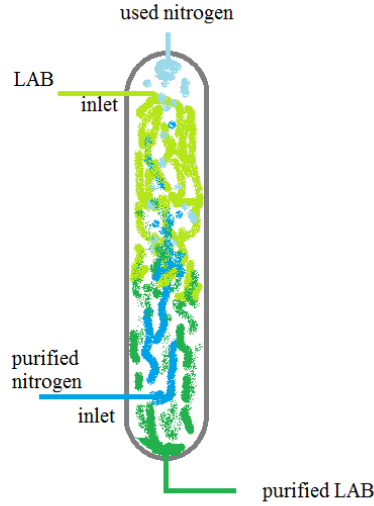
Figure 3.6: LAB is inserted on top and falls down due to gravity in unstructured
packings. Purified nitrogen gas is inserted on the bottom and flows
upward, removing dissolved gases from LAB during close contact.

to obtain precise values for the needed parameter and it is not possible to evaluate
the efficiency of the purification techniques in reference to the goal of the JUNO
collaboration. To determine the attenuation length precisely, a new experiment is
designed and built in the framework if this work and is described in chapter 4.

Precision Attenuation Length Measurement (PALM) Setup

For several years, the attenuation length spectra of liquid scintillator samples have been performed with commercial UV/Vis spectrometers. With these instruments sample containers up to a maximal length of 10 cm can be used to measure the attenuation of the medium. A special calculation method, first introduced in [Abe08], is used to determine the attenuation length from the measured spectra. Due to the required energy resolution of 3 % at 1 MeV for JUNO, the attenuation lengths of the scintillator samples have to reach values of at least 20 m at 430 nm and the extrapolation from 10 cm to such sizes produces huge uncertainties and it has been difficult to give precise absolute attenuation length values for the measured samples and the effect of the purification methods, described in section 3.2, could not be determined precisely [Pru15] [JUN15]. Fig. 4.1 shows a calculation of attenuation lengths for measurements of different treated LAB samples with a commercial UV-Vis spectrometer and a container size of 10 cm. It can be seen, that the resulting uncertainties are huge, making a decision whether the attenuation length of the sample probe is achieving the goal of at least 20 m at 430 nm or not difficult.

To make sure that the absolute attenuation length of the scintillator is at least 20 m at 430 nm and to show that it can be improved by several purification methods, new experimental approaches have been developed over the last years to improve the attenuation length measurement precision.

One of the first approaches featured an experiment with a light path of 5 m and attenuation length results are published by [Hel15a]. A similar experimental approach to [Hel15a] with a smaller sample tube is currently investigated by [Yu15], measuring different treated and manufactured LAB samples from the Chinese manufacturer. First results are presented in [Yu15] and [Cao18], showing evidence for attenuation lengths in the region of 20 m at 430 nm. H. Enzmann also uses a similar experimen-
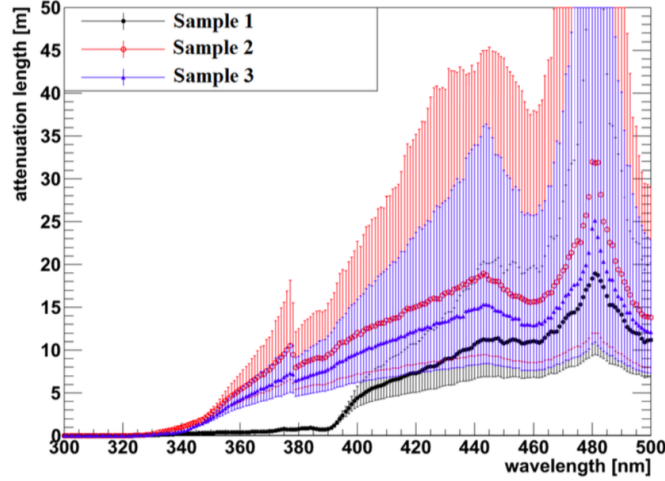
Figure 4.1: Exemplary calculation of the attenuation length spectra from measurements of different treated and untreated LAB samples, performed with a commercial UV-Vis spectrometer. The method used for calculation is described in [Abe08]. As can be seen, the resulting propagated total uncertainties make it impossible to determine a precise absolute value for the optical parameter especially at 430 nm as well as to compare different samples. Figure plotted with data from [Pru15].

tal approach to develop a live monitoring attenuation length measurement, which will be used during the filling of the JUNO detector [Enz16]. A rather different approach is proposed by [Hei18], where an optical cavity is used to extend the effective medium light path to improve the measurement precision of the attenuation length. In this work a new experiment is developed, which is based on the experience of the work done by [Hel15a] and is designed to overcome the stated shortcomings. Furthermore, this work focuses on the precise determination of the attenuation length of LAB.

4.1 Former long tube setup

Over several years, an attenuation length measurement setup with light paths up to 5 m has been built and tested by [Hel15a]. The author describes two different experiments, which are able to determine the attenuation length precisely. The first approach uses a LED and a PMT, whereas a second generation setup uses a halogen light bulb and a CCD camera instead. Focusing on the second generation experiment in this work, a sketch of the improved setup is shown in fig. 4.2. The experiment uses five special coated stainless steel tubes with lengths of 1 m each, which are mounted together horizontally, generating light paths from 1 to 5 m in 1 m steps. A halogen lamp is used as a continuous light source. With a condenser lens the light is collected before it passes a band-pass wavelength filter with a wavelength range from
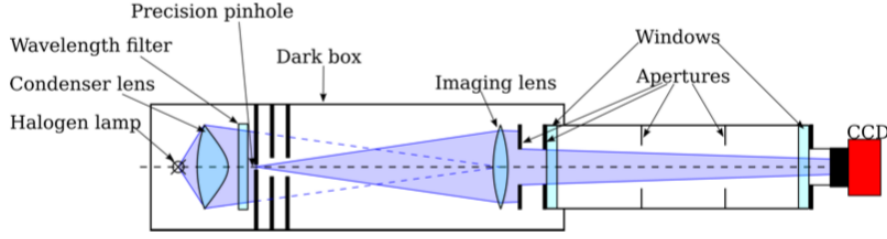
Figure 4.2: Sketch of the second generation setup for determining precise attenuation length values. A halogen light bulb produces continuous light, which is collected by a condenser lens and passes a band-pass wavelength filter. The filter cuts away wavelengths, which are not in the region between 420 nm and 445 nm. After passing a precision pinhole, the light is imaged to the light detector by an imaging lens and is collimated by an aperture, crossing the sample tube with its glass windows, sample liquid and stray light suppressing apertures [Hel15a]. Picture taken from [Hel15a].

420 nm to 445 nm. After passing the filter, the light crosses a precision pinhole and apertures before it is imaged to the light detector by an imaging lens and another aperture. Both components are used to collimate the light, before it crosses the glass windows and sample tube. Within the sample tube stray light suppressing apertures are installed. The light detector is a 8.4 MPx CCD camera to measure light intensity and beam position information simultaneously [Hel15a]. The author measures untreated LAB from Egypt in this setup and gives a first result for the attenuation length at a wavelength of around 430 nm to be $(9.60 \pm 0.05\,(\text{stat}) \pm 0.10\,(\text{syst}))\,\text{m}$[1]. Systematic uncertainties, which are taken into account, are time instabilities of the setup as well as tube length variations, influences of the window cleaning process, CCD camera pixel by pixel gain calibration uncertainties, CCD camera linearity and broken pixels [Hel15a]. The author describes disadvantages and problems with the improved setup[Hel15a]:

- The fixed module tube lengths of 1 m restrict the light path to limited points,

- the manufactured tube diameter and lengths require a sample volume of 24 l for each sample measurement,

- the light path can only be varied by remounting the tube modules. This requires the opening of the system and maximizes the hazard of polluting the system during this period,

- due to remounting and cleaning the tube, the measurement time for one transition measurement takes three days,

---

[1]The first generation experiment determined an attenuation length of the same untreated LAB sample to be $(8.89 \pm 0.05\,(\text{stat})\,^{0.59}_{-0.53}\,(\text{syst}))\,\text{m}$, which is in agreement to the result of the second generation experiment.

- the usage of a wavelength filter limits the experiment to one wavelength only. To change the wavelength, the optic has to be changed as well,

- due to the used materials, the UV region is not accessible. This makes comparisons with former results measured with commercial UV-Vis spectrometers difficult.

Based on this experiences, a new experiment is developed in this work to overcome the stated shortcomings and to enable measurements of several LAB samples provided by the JUNO collaboration.

4.2 Setup of the PALM experiment

A scheme of the proposed experiment can be found in fig. 4.3. This next generation experiment plans to use a stainless steel tube of 5 m in total, but vertically mounted[2]. The sample is filled into the tube by lifting the sample storage tank. This makes it possible to create each light path between zero and maximal filling level without changing the system or opening the tube and minimizes a possible pollution of the sample during fill height changes. The sample tube and tank system are isolated from shock by dampers and can be connected to a nitrogen supply for sample flushing. The sample tube is special coated like in the previous experiment, but has a much smaller diameter, reducing the needed sample volume from 24 l to 2 l per sample. No apertures are mounted inside the sample tube any more, but within a baffle tube, which is installed on top of the sample tube for stray light suppression. This is motivated by the result of a Monte Carlo simulation, which shows that apertures mounted after the sample tube are more effective [Hel15b]. Two glass windows seal the ends of the sample tube. They are made of quartz glass to enable measurements in the UV region. A CCD camera is installed on top of the baffle tube to detect light intensity, beam shape and beam position simultaneously.

4.2.1 Realization of the proposed design

A picture of the new optical system can be found in fig. 4.4. Similar to the former setup, a continuous light source is used to create a light beam and a quartz glass condenser lens to collect the intensity. The halogen lamp itself is driven by a precision power supply unit to guarantee very small fluctuations. Instead of a band-pass wavelength filter, a double prism monochromator is used to create a monochromatic light beam and to choose a wavelength. Without changing the optical system, a wavelength between 180 and 3,500 nm can be selected. A customized mirror system is built to focus the light to a spot in a distance of more than 5 m and the focused light beam is coupled into the sample tube by a deflection mirror. Due to the nature of the focusing mirror optic, an aperture is used to limit the beam size to a

---

[2]Due to laboratory restrictions, the length of the stainless steel tube had to be changed to 3 m. For further detail, see section 4.2.2.
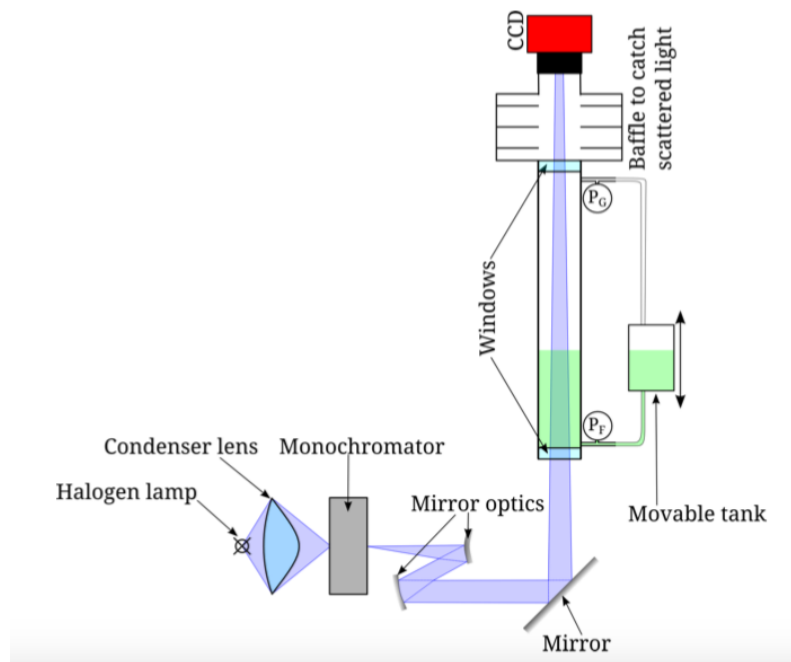
Figure 4.3: Sketch of the improved experiment for precise attenuation length measurements. The sample tube is mounted vertically and has a length of 5 (3) m in total. The liquid filling level can be varied continuously by lifting a movable tank without opening the system. On top of the sample tube, a baffle tube is mounted, which contains stray light suppressing apertures instead of placing them within the sample tube. On top of this baffle tube, the CCD camera is installed as light detector. A halogen light bulb is used as a continuous light source and a monochromator select the wavelength without a change of the optical components. The monochromatic light is focused to the CCD sensor by a mirror optic and is coupled into the sample tube by a deflection mirror. Picture taken from [Hel15a].
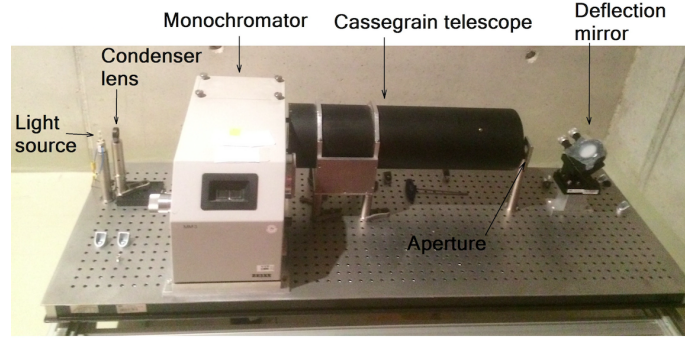
Figure 4.4: Picture of the optical system used for the PALM experiment [Pru15].
Continuous light is produced by a halogen lamp and is collected by a
condenser lens. The beam passes a double prism monochromator, where
a wavelength can be selected and the monochromatic light is focused
by a customized mirror system to a point in more than $5\,\text{m}$ distance.
It is deflected into the vertically mounted sample tube by a deflection
mirror. After the light crosses the glass windows, sample liquid and stray
light baffle, the attenuated monochromatic light is detected by the CCD
camera.

size comparable to the deflection mirror. After deflection, the light beam passes the
glass windows, the sample probe and the stray light baffle, before being detected by
the light detector. The optic is built in a special coated dark box.

Optic and sample tube system are not coupled mechanically. The sample tube is
mounted vertically to the walls of the experimental site with four straight holders
and damper inlets, which mount the tube perpendicular to the optical table. A
picture of the whole system can be seen in fig. 4.5.

In order to adjust the beam spot on the centimeter sized CCD sensor in a distance
of several meters, special opto-mechanical systems are needed. Due to the fact, that
optical table and sample tube are not connected, the two decoupled systems have
to be adjusted in reference to each other. Therefore, not only the deflection mirror
can be moved, but also the whole optical table is a constructed translation stage.

4.2.2 Laboratory restrictions

Unfortunately, the proposed length of $5\,\text{m}$ of the sample tube could not be achieved,
as the experimental site at the accelerator hall of the Maier-Leibniz laboratory in
Garching is restricted and closed. Other available laboratory sites did not have the
proper height of more than $5\,\text{m}$ for a vertically mounted sample tube. Therefore, a
new, shorter sample tube of $3\,\text{m}$ in total is manufactured and the setup is rebuilt
at the underground laboratory at Garching, providing a laboratory hall height of
$4.3\,\text{m}$.

The location of the PALM setup is chosen carefully due to the needed requirements.
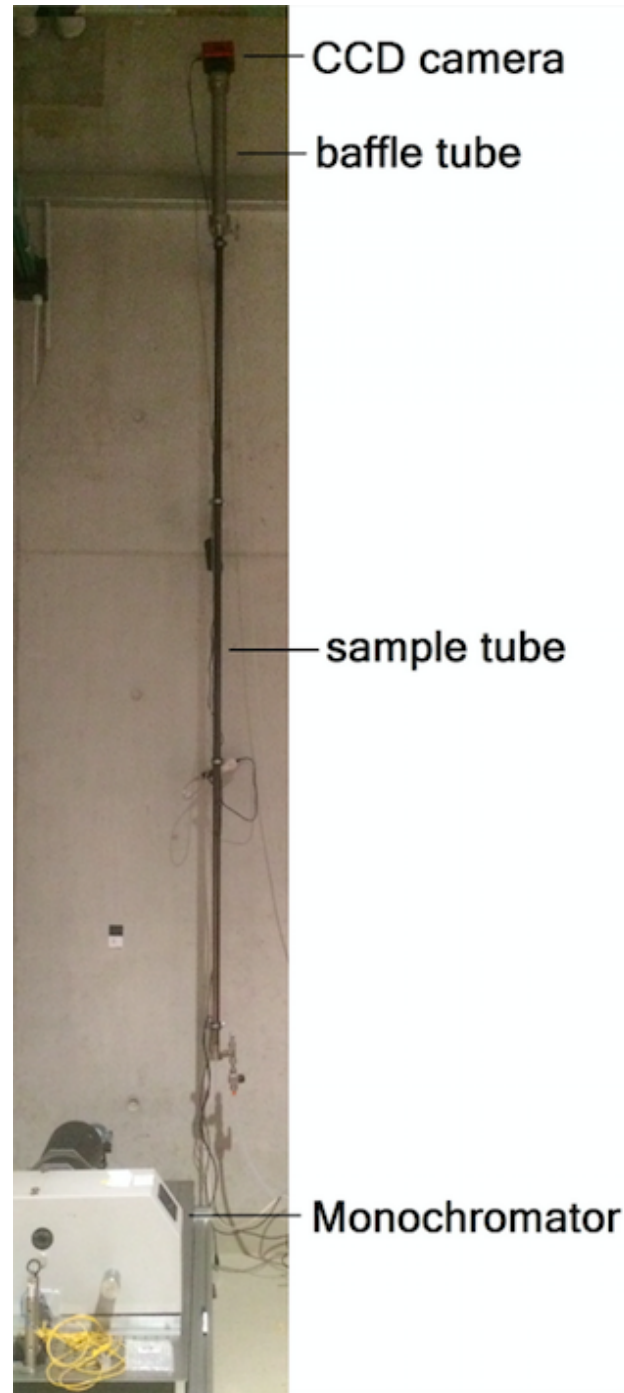
Figure 4.5: Picture of the full PALM setup without dark boxes [Pru15]. The sample tube is mounted vertically to the wall with four clamps and the optical system is mounted on a horizontal optical table, which itself is a translation stage to enable the adjustment of the light beam to the small CCD sensor in several meters distance. The light is deflected by a deflection mirror into the sample tube, passing glass windows, sample liquid and stray light baffle, before it reaches the light detector.

Considering the handling of scintillator liquids, only an experimental site with a chemically resistant floor is appropriate and because of a crane, which is used stationary for different cryogenic experiments, the PALM setup is located outside its driveway near the walls of the laboratory. This conditions restrict the vertically mounted sample tube to a spot on the walls next to the hall doors and climate system inlet and outlet tubes. The new location within the underground laboratory is shown in fig. 4.6. The sample tube is mounted to the walls of the underground laboratory with four rigid mounts. Next to it, the filling system is located with two guide rails and the inlet and outlet tubes of the climate system of the underground laboratory are adjacent, providing fresh air. The optical system and the sample tube are placed within special black curtains, which work as a flexible dark box.

During the whole measurement process with PALM, the surrounding conditions changed significantly. Constructional work inside, like the installation of a clean tent and clean room, and outside the laboratory, like the beginning of the construction of the new physics department, lead to perturbations, which affected the measurements sufficiently. The influence of the changing surrounding conditions is considered in the following.

4.3 Measurement principle

For a measurement, the sample liquid has to be filled into the sample storage tank without polluting it and therefore, has to be handled with care. After the filling, the storage tank is placed in its lifting construction and connected to the sample tube via two PTFE tubes. With a valve, both systems are connected and the sample tube is filled by hydrostatic pressure, showing the same (decreased) liquid level as the storage tank. The filling level within the sample tube is determined with two pressure sensors. The CCD sensor is cooled with its internal cooling system to -15 °C for dark noise suppression and the halogen lamp is warmed up for a few minutes, before the current of the lamp is increased to its working point. After a thermalization time of several hours, which is determined in section 4.5.5, the setup is ready for measurements. A fixed wavelength and a fill height are selected. For each liquid level, the beam spot has to be centered on the camera sensor for optimal measurement conditions and an exemplary picture can be seen in fig. 4.7. For beam adjustments on the sensor both deflection mirror and optical table translation stage are used. For optimizing the signal to background ratio of the detector and by taking into account the linearity range of the sensor, the measured light intensity can be varied by changing the monochromator slit width and the exposure time of the sensor. After optimizing beam position and intensity, sample measurements can be performed. To determine the attenuation length of the sample at the selected wavelength, a measurement series for several fill height levels has to be done. For each filling level, at least eight pictures are taken for statistics. Afterwards another filling level has to be adjusted by using the lever next to the storage tank construction. Before redoing the data taking, the setup needs a stabilization time of several
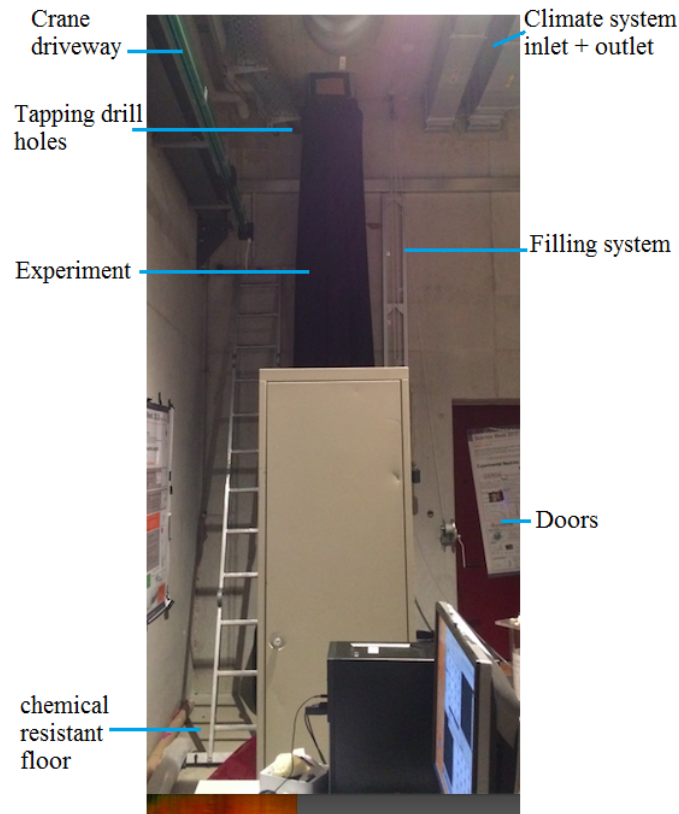
Figure 4.6: New experimental site of the PALM setup in the underground laboratory (UGL). The experiment is built on a chemically resistant floor, due to the handling with scintillator liquids. The sample tube is installed on the laboratory walls, out of the driveway of the crane, next to the doors to hall 2. The black curtain is used as a second dark box. The filling system contains guide rails, which are mounted next to the experiment. Furthermore, the inlet and outlet tubes of the climate system of the laboratory are neighbored to the setup.

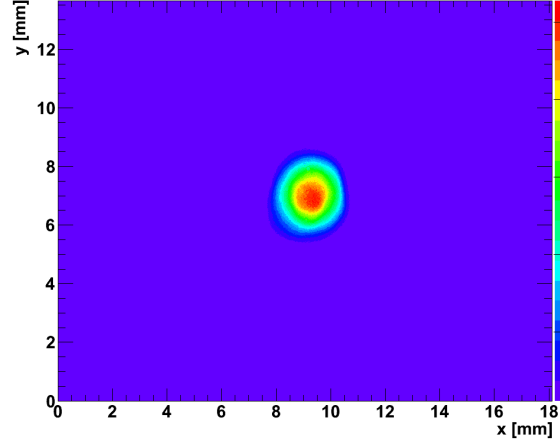Figure 4.7: Colorized, raw sensor picture of a beam spot, adjusted on the sensor after traversing the emptied experiment. The x and y axis show the size of the sensor in mm and the colors correspond to the measured intensity. It is crucial, that the beam is centered on the sensor to guarantee the detection of the full intensity information.

minutes and the attenuated light beam has to be centered on the sensor again. For a full measurement series, the intensity at least eight to ten fill height level is measured. Dark pictures are taken after each measurement series by using the internal CCD shutter or after switching off the halogen lamp. The mean intensity integral of each filling level is calculated and plotted against the corresponding fill height. To access the attenuation length, the Beer-Lambert law is used.

The Beer-Lambert Law

Multiple CCD pictures are taken, measuring the intensity integral for the given exposure time over two dimensions for a sample measurement at a given wavelength and fill height. For each fill height level, the mean intensities I_{ij} of each pixel ij of all measured pictures are calculated, excluding broken pixels.
After subtracting the mean dark noise measurement from the intensity means, a calibration for each CCD sensor pixel is performed:

$$I_{ij} = c_{ij} \cdot \left[< I >_{ij} - < I >_{ij}^{\text{dark}} \right] \tag{4.1}$$

with c_{ij} the calibration factor for each pixel, $< I >_{ij}^{\text{dark}}$ the mean intensity of the dark measurements and $< I >_{ij}$ the calculated integral means of each pixel. To obtain the intensity integral $I_{\text{fillheight}}$ attributed to the measured fill height, the integral over all mean pixel intensities I_{ij} is determined:

$$I_{\text{fillheight}} = \sum_{i=1}^{N} \sum_{j=1}^{M} I_{ij} \tag{4.2}$$

with N, M the amount of all sensor pixels in x and y direction. After this calculation, the intensity integrals are plotted against the corresponding fill heights, showing a decreasing trend of the intensity for increasing fill height levels. The final attenuation length can be obtained by fitting the Beer-Lambert-Law

$$I(x) = I_0 \cdot e^{-\frac{x}{\Lambda}} \tag{4.3}$$

to the data, where I_0 is the incident intensity, which is a free fit parameter, $I(x)$ is the measured attenuated intensity after the light traveled a distance x through a medium and the attenuation length Λ.

4.4 Expected attenuation effect

To determine an attenuation length of at least $20\,\mathrm{m}$ at $430\,\mathrm{nm}$ in the PALM setup, it has to be guaranteed that the experiment is able to resolve the attenuation effect of the light accurately. The maximal effect of the intensity attenuation with respect to equation 4.3 can be calculated via

$$\Delta I = I_0 - I_0 \cdot e^{-\frac{x}{\Lambda}}, \tag{4.4}$$

with I_0 the incident intensity, $\Delta I = I_{x=x_{max}}$ - I_0 , x the light path length through a medium and Λ the attenuation length.
Taking into account a light path length of at least $2.0\,\mathrm{m}$ and an expected attenuation length of around 20.0 m at $430\,\mathrm{nm}$, the effect in % is determined to be

$$\frac{\Delta I}{I_0} = 1 - e^{-\frac{x}{\Lambda}} \sim 9.5\%. \tag{4.5}$$

Compared to former measurements performed with UV/Vis spectrometers and maximal path length of $0.1\,\mathrm{m}$, the effect is ~ 0.5 %, which makes it rather difficult to determine the attenuation length precisely in such devices. Fig. 4.8 shows the expected relative intensity attenuation effect $\frac{\Delta I}{I_0}$ in dependence of the attenuation length. Therefore, the uncertainties of the PALM experiment have to be $\sim 1\%$ to be able to measure the attenuated intensities accurately and the expected effect of sample liquids with attenuation lengths of more than $20\,\mathrm{m}$ at $430\,\mathrm{nm}$.

4.5 Characterization of the experiment

To test the performance of the experiment, several components and their characteristics are investigated. The spectrum of halogen lamp and monochromator used in PALM as well as the performance of the CCD sensor is tested, fill height sensors are calibrated and also the time stability of the system is checked.
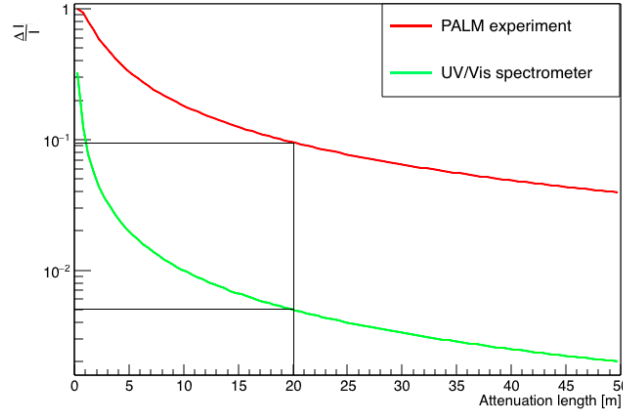
Figure 4.8: Expected maximal light attenuation in dependence of the attenuation length of the liquid. Plotted is the relative intensity difference against the attenuation length in m for both PALM experiment (red) and the common UV/Vis spectrometer devices (green).

4.5.1 Accessible wavelength region

The accessible wavelength range of the PALM experiment is limited by its optical components: the monochromator as well as the CCD sensor, quartz glass condenser lens and window glasses and the provided light spectrum of the halogen lamp. The monochromator can provide monochromatic light between 180 and 3,500 nm [ZeiXX] and quartz glass is used as material for windows and lens to access the UV region [Pru15]. The CCD sensor is able to measure in this region, too [Eas10] and the accessible wavelength region is limited by the halogen light spectrum in the first place. Measurements with a spectrometer show a continuous wavelength spectrum of the lamp from 370 nm to approximately 1,200 nm, which can be seen in fig. 4.9. Commercial UV/Vis spectrometers operate in a range between 250 and 800 nm [Pru15] and 190 to 900 nm [JUN15], which makes it able to compare obtained results of both setups in a wavelength range of 370 nm to 800 (900) nm.

4.5.2 CCD sensor and calibration

The 8.4 MPx CCD sensor is used as light detector and measures the intensity integral over a selected exposure time per pixel, given in a two dimensional intensity histogram. It provides intensity and also spatial information of the light beam shape and position on the sensor. The CCD sensor used in PALM is the same device already characterized and operated by [Hel15a]. To determine the performance and reliability of the sensor, several issues have been investigated by [Hel15a], identifying broken pixels, studying the linearity of the device and providing a pixel-by-pixel gain calibration. Due to the fact that some of the pixels may be broken, measurements have been performed by [Hel15a] to identify such pixels by their extremely increased
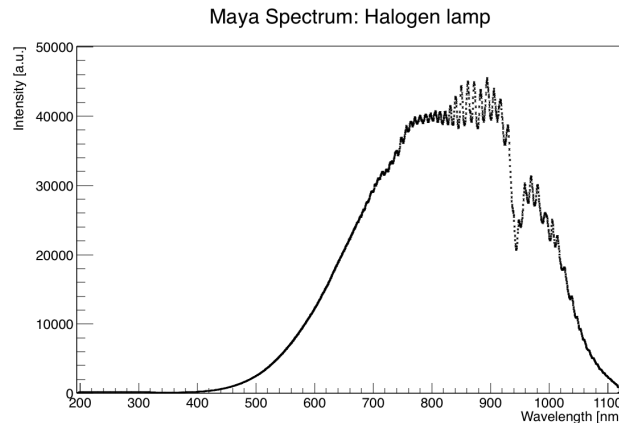
Figure 4.9: Spectrum of the halogen lamp used in the setup, measured with a spectrometer. The lamp produces a continuous light spectrum between 370 nm to 1,200 nm approximately.

dark noise rate during measurements in a dark environment. This so called hot pixels are determined by 100 measurements. From this data, the intensity distribution from each pixel is fitted with a Gaussian distribution using χ^2[Hel15a]. A pixel is declared as hot, if the intensity condition $I > \mu + 5\sigma$ is fulfilled. Pixels, which are tagged as hot at least three times in 100 measurements, are excluded from the data analysis[Hel15a].

During the measurements with the new developed PALM setup, new hot pixels have been identified and are excluded as well. Fig. 4.10 shows the amount and location of all identified broken pixels with such dark noise excesses. In (a) the full sensor pixel range is shown with rescaled red dots indicating the broken pixels. The pixels in this picture are scaled for better contrast. In (b) a zoom at a broken pixel row is shown, which is detected after the delivery of the camera device from the manufacturer. The pixels in this picture have their original sizes.

Linearity measurements are performed for three different ways to guarantee reliable information on the linearity range of the sensor [Hel15a]. It is found, that for all three different approaches no deviation from the linearity character can be detected and therefore, the performance of the sensor is very good [Hel15a]. Due to the fact, that single pixels have different collection efficiencies, they show different gain factors for light collection. This gain differences have an impact on the sensor resolution and can be corrected by a pixel-by-pixel gain correction factor c_{ij}, which is determined by a linear fit to the data for each pixel [Hel15a]. This determined gain correction factors are also applied for the calibration of the same sensor used in the PALM setup. For detailed information see [Hel15a]. To further improve the performance of the light detector, the sensor is cooled to -15 °C. This reduces the dark noise level of the single pixels.

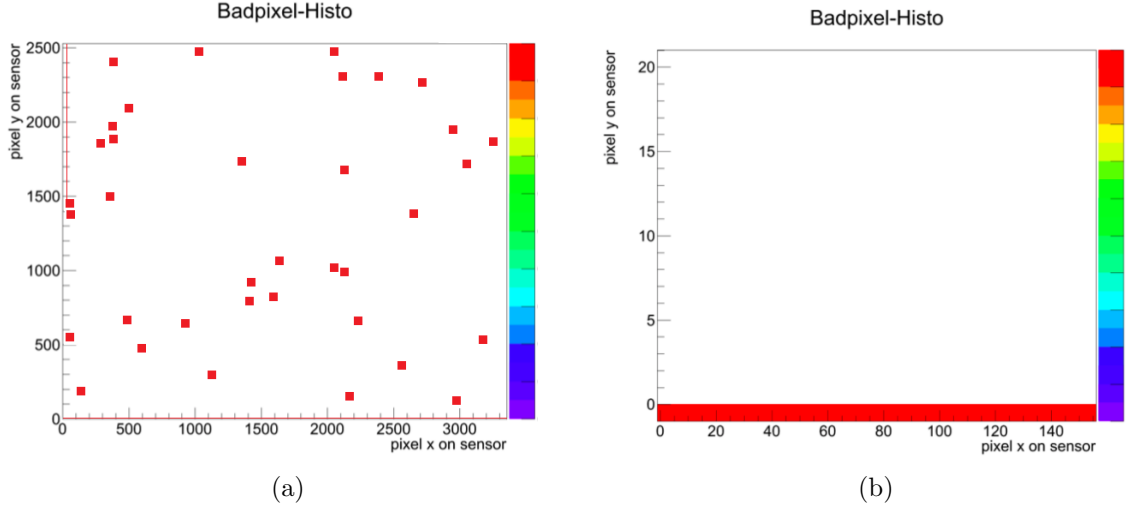(a)   (b)

Figure 4.10: Two dimensional sensor pixel histogram with colorized broken pixels.
The pixels in a) are rescaled for better identification, those of the
zoomed region, shown in b), are in their original size. As can be seen,
there are single pixels which seem to detect a lot of intensity, however
no real intensity exposure is taking place. These falsify the intensity
integrals of the measurements and have to be identified and excluded.

4.5.3 Fill height sensor calibration

Due to the windowless stainless steel tube, two pressure sensors are mounted on top
(gas pressure sensor) and on the bottom (liquid pressure sensor) of the sample tube
to determine the pressure difference after filling the tube with a certain amount of
liquid. To calibrate the sensor data, the sample tube is filled with different liquid
volumes and the liquid level of the outer tank is measured in reference to the inlet
window of the sample tube. Because of the filling principle via hydrostatic pressure,
storage tank and sample tube have the same liquid level after filling. Fig. 4.11 shows
the resulting calibration data for different fill height levels in m and in dependence
on the pressure sensor difference given in channels. An uncertainty for the liquid
level measurements of $\sim 2\,\text{mm}$ and $\pm\,1\,\text{digit}$ [Wik13] [Key17] for the pressure sensors
are considered for the fit. The obtained calibration function is

$$y(p) = (0.00143 \cdot p + 0.03007)\,\text{m}, \tag{4.6}$$

with $y(p)$ the corresponding fill height in m and p the pressure difference in channels.
This calibration is used for all following liquid sample measurements.

4.5.4 Slit width and wavelength selection

The double prism monochromator enables to select a wavelength between 180 and
3,500 nm as well as exit slit widths up to 2 mm [ZeiXX]. To check if the device is
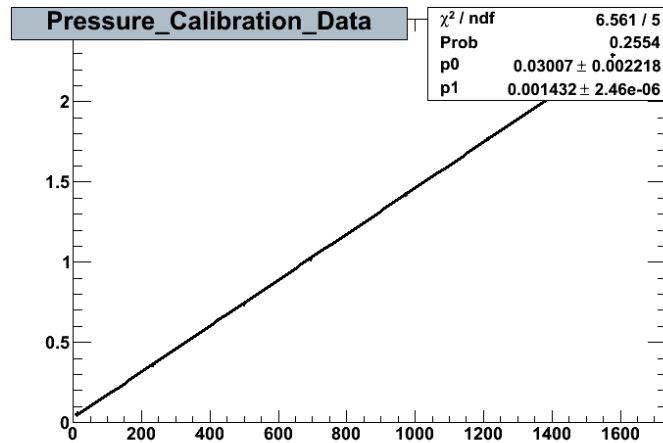
Figure 4.11: Calibration data of the pressure sensors for determining the liquid level within the stainless steel sample tube. Plotted are the measured fill heights of the tube in m against the sensor pressure difference in channels. The fit is obtained with the consideration of an uncertainty of 2 mm for the filling level measurements and an uncertainty of 1 digit for each pressure sensor. The data set is obtained by measuring the pressure difference of the sensors for different filling levels and the liquid level height of the storage tank in reference to the inlet window of the sample tube.

working properly as well as to determine the monochromatic light (spectrum) after passing the monochromator, several measurements are performed with an optical fiber spectrometer. Fig. 4.12 shows an exemplary picture of the light after passing the monochromator exit slit of 2 mm. It can be seen, that the exiting light shows a rectangular shape, which is expected for the exit slit and no other distortions can be identified.

The spectrum of the light beam passing the double prism monochromator is investigated for different wavelengths. Fig. 4.13 shows an exemplary measurement of the spectrum of the light beam after passing the exit slit of 2 mm in width for a selected wavelength of 430 nm. It can be seen that the continuous light beam is limited to a wavelength range between $\sim$ 410 nm to 450 nm. It is found, that for a maximal opened monochromator exit slit, the device provides a light spectrum with a full width at half maximum (FWHM) of 9 nm, which will be used in the following as a wavelength uncertainty. Furthermore, the peak position of the selected wavelength of 430 nm shows a small offset of 0.7 nm. No second order monochromator effects can be identified for all measurements and the monochromator is performing well. Further investigations show, that FWHM and offset position are changing with changing slit widths for a fixed wavelength of 430 nm. As both information are needed for an appropriate systematic uncertainty determination, the measured FWHM and offset data are plotted as a function of the slit width and are interpolated with a linear

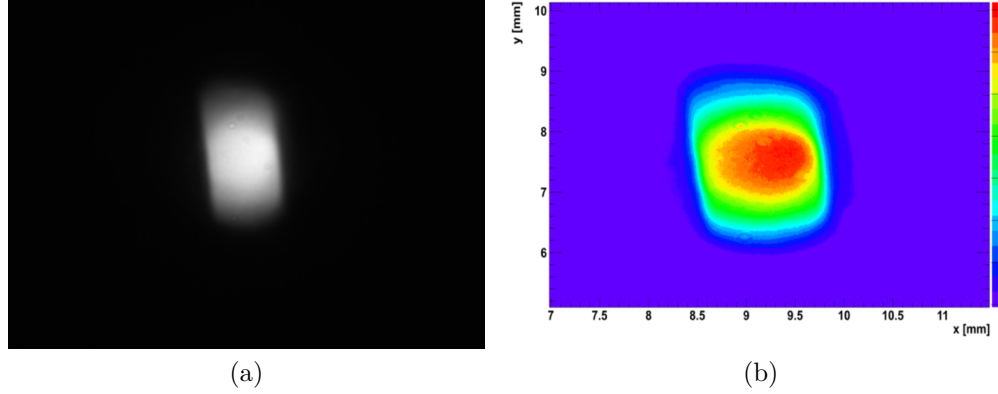(a)   (b)

Figure 4.12: Raw sensor picture for an emptied setup to investigate the performance
of the monochromator. In a) an unprocessed, raw sensor picture is
shown, whereas in b) a zoomed beam can be seen, which is colorized
for better contrast. The colors correspond to the measured intensity.
The rectangular shape of the exit slit of the monochromator can be
seen very clearly and no distortions can be identified.
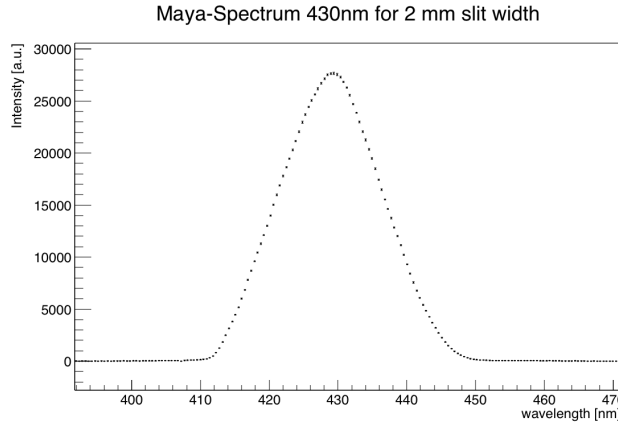
Figure 4.13: Wavelength spectrum of the continuous light beam after passing the
monochromator for a selected wavelength of 430 nm and a slit width
of 2 mm. Plotted is the intensity in arbitrary units as a function of
the wavelength in nm. It can be seen that for a completely opened
monochromator slit width, a wavelength offset of less than 1 nm is per-
formed. Furthermore, the full width at half maximum (FWHM) is
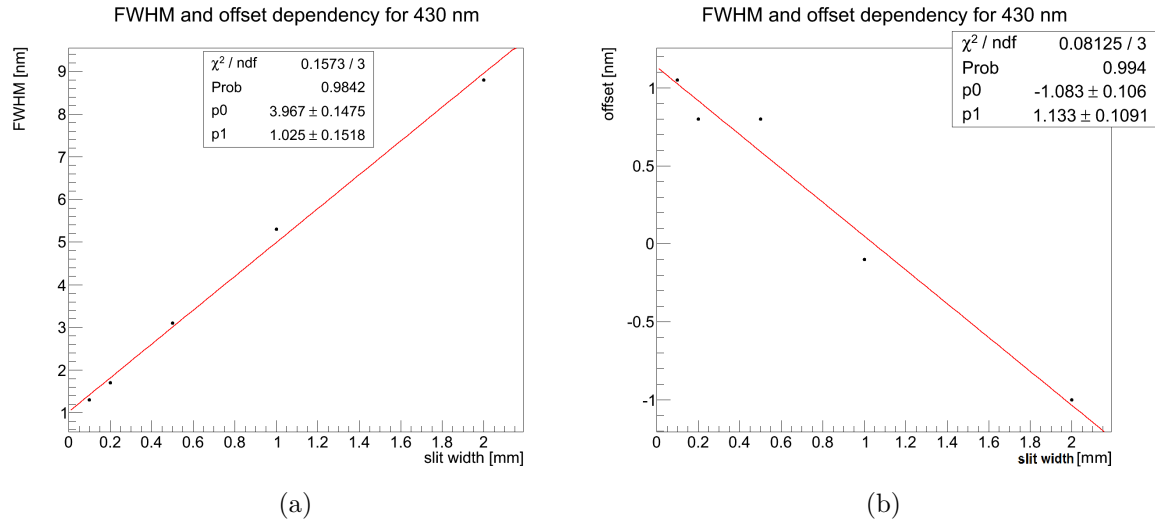determined to be 9 nm.

Figure 4.14: Linear interpolation of the determined FWHM (a) and wavelength off-set (b) of the monochromator with respect to changing slit widths at 430 nm. It can be seen, that the FWHM is increasing with increasing slit widths, whereas the offset of the selected wavelength shifts from higher values (positive sign) to lower ones (negative values). These plots are used as a reference to determine the wavelength uncertainty for 430 nm and different setup adjustments.

function. The results can be seen in fig. 4.14. It is found, that the FWHM at 430 nm is increasing with increasing exit slit widths. Furthermore, the offset of the peak position compared to the selected wavelength is showing a decreasing behavior. The offset is chosen to be positive if the peak position is located at smaller wavelengths than the selected one and is negative, if the peak position is shifted to a higher wavelength than the chosen 430 nm. Both fit results can be used as a reference to determine the wavelength uncertainty for different setup adjustments. These are needed for different samples and other wavelengths, too. Further measurements are investigating the dependence of the offset and FWHM on different wavelengths and monochromator exit slit width configurations. To give a full picture, the results are shown in table 4.1 for the FWHM and in table 4.2 for the offset dependence on wavelength and monochromator exit slit width variations.

Additionally, it has to be investigated, wether the monochromator exit slit or the wavelength can be varied within a measurement series and their influence on the result has to be considered. Due to the fact, that both parameters are selected by a mechanical wheel, the reproducibility of the chosen selection has to be taken into account. As the change of the monochromator exit slit width is changing the intensity significantly, a first approximation of the change in intensity for reproducing the same slit position shows an uncertainty of more than 4 %. Reproducing the selected wavelength also has an impact on the measured intensity. This can be explained by

slit width		0.1 mm	0.2 mm	0.5 mm	1 mm	2 mm
wavelength	390 nm	1.3	1.5	2.3	4.2	6.9
	430 nm	1.3	1.7	3.1	5.3	8.8
	500 nm	1.7	2.3	4.5	8.5	14.0
	550 nm	1.8	2.8	5.7	11.0	18.0

Table 4.1: Determined wavelength FWHM in nm for different wavelengths, given in nm and monochromator exit slit widths in mm. This information is needed to interpolate the corresponding wavelength uncertainties for different setup adjustments.

slit width		0.1 mm	0.2 mm	0.5 mm	1.0 mm	2.0 mm
wavelength	390 nm	+1.2	+1.0	+0.9	+0.5	0
	430 nm	+1.1	+0.8	+0.8	-0.1	-1.0
	500 nm	+0.1	0	0	-1.0	-2.0
	550 nm	-0.2	-0.4	-0.6	-2.0	-3.0

Table 4.2: Determined wavelength offset in nm between selected and real wavelength in dependence on different wavelength and monochromator exit slit width configurations. A negative sign indicate an offset to smaller wavelengths than the selected one, whereas a positive sign a shift to higher wavelengths. This information is meant to be used to interpolate the systematic wavelength uncertainties for different setup adjustments.
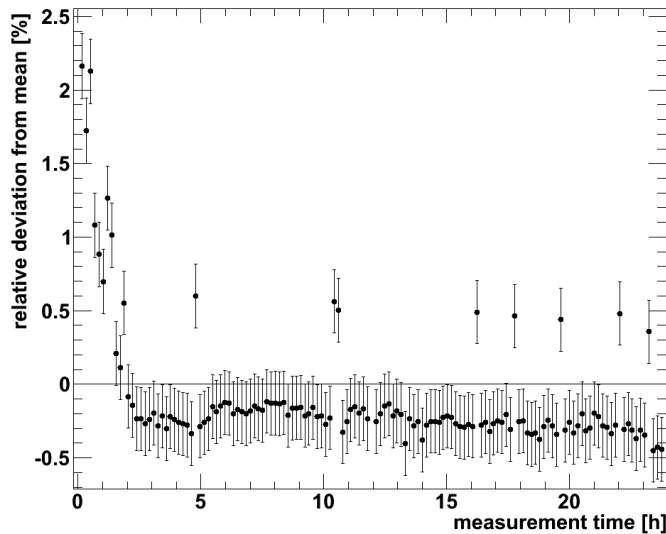
Figure 4.15: Longterm stability measurement of the intensity integral over a time period of 24 hours after switching on the power supply with an emptied tube, taking data each ten minutes. Plotted are the deviations from the intensity mean divided by the mean. It can be seen, that the whole setup has an thermalization time of ∼ 5 hours. High outliers can be identified and explained by fluctuations in the exposure time, which is due to the mechanical shutter of the CCD sensor. These can be identified easily in the offline data acquisition and are excluded.

the spectrum of the halogen lamp, where a change in the wavelength would change the incident intensity significantly. In the region of interest, a small change of 1 nm would lead to a non-negligible change in the intensity due to the big slope in the spectrum of the halogen lamp. These uncertainties are not negligible and should be avoided in any case. Therefore, no change of these parameters within a measurement series is done to eliminate these effects.

4.5.5 Stability of optical and electronic components

Due to the fact that a small fluctuation of the optical components has a huge influence on the beam shape and its position on the CCD sensor at several meters distance, longterm measurements are performed to identify systematic uncertainties and instabilities of the electronic and optical components. Therefore, empty tube measurements are performed over a time period of several days, starting after switching on the lamp and power supply. Therefore, the power supply unit is started and the light beam is adjusted and centered on the CCD sensor. With a cooled sensor at -15 °C, a measurement picture is taken each 10 minutes over a time period of 24 hours at a wavelength of 430 nm. Fig. 4.15 shows the intensity integrals measured after switching on the power supply. The plot shows the deviation from
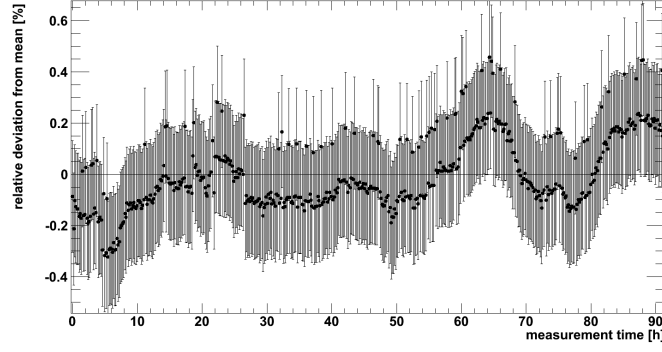
Figure 4.16: Longterm stability measurement series over a time period of 90 hours, starting after 24 hours of measurement. Each 10 minutes a picture is taken.   Plotted are the deviations from the mean intensity integral divided by the mean integral of the measurement. Increased outliers can be identified and can be explained by exposure time fluctuations, which is due to a problem with the internal mechanical shutter of the CCD sensor. Excluding these outliers, the measurement series shows fluctuations within 0.25 %.

the intensity mean, divided by the mean itself, giving the deviation from mean in percentage over time. After a thermalization time of the setup of around 5 hours, the intensity integrals reach a stable plateau. A few increased intensity outliers can be identified over the whole measurement time. These can be explained by exposure time fluctuations caused by the internal mechanical shutter of the CCD device. The outliers can be identified in the offline data analysis and are excluded. To guarantee that the stability plateau is no coincidence, the measurement time is increased to 114 hours, which can be seen in fig. 4.16. This longterm measurement shows a time period of 90 hours, starting directly after 24 hours of measurement, which is shown in fig.4.15. It can be seen, that after neglecting the exposure time induced outliers, the fluctuations over time are limited to ~ 0.25 %, showing promising measurement conditions. To ensure that no mechanical shift or change is taking place, the beam position of single measurement pictures from the beginning and the end of the whole series are compared to each other. Taken are two representatives after the thermalization time of 5 hours and after 24 hours of measurement respectively in fig. 4.17. Comparing the position of both beams on the sensor, it can be seen, that a small shift can be identified, which may result from further thermalization. Note, that the shift is negligible for measurements and the mechanical components show a good time stability.

4.6 First sample measurements and problem handling

After performing empty tube stability measurements to guarantee optimal measurement conditions, measurements with an untreated LAB sample from the same batch
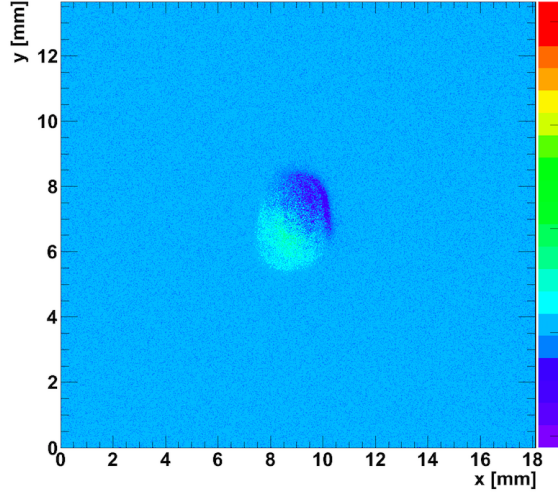
Figure 4.17: Comparison of two single pictures after 5 and 24 hours of measurement to identify mechanical instabilities. Shown are the colorized raw data pictures of the sensor. The colors correspond to the intensity differences between both light beams. As can be seen, a small deviation indicating a shift can be detected.

used by [Hel15a] are performed for comparison. The empty sample tube is filled by lifting the storage tank and the beam position has to be re-adjusted because of the effect of the liquid. A fill height of 2.3 m is chosen for first test measurements. Fig. 4.18 shows the colorized, adjusted beam spot before centering it on the sensor. The colors correspond to the measured intensity, showing a well defined point like beam shape, however with small distortions.

To investigate systematic uncertainties which are coupled to the sample liquid, another longterm stability measurement series is performed under same conditions as for the longterm empty tube measurements. The results of an exemplary measurement at a wavelength of 530 nm can be found in fig. 4.19. Plotted are the intensity integrals over a time period of approximately 22 hours. It is found, that the fluctuations of the intensity integrals are huge. To identify the reason for such fluctuations, single picture series are taken into account and are shown in fig. 4.20. Plotted are the raw data pictures without any processing, which are taken 60 to 70 seconds apart. The first picture is taken directly after filling the sample tube, showing an almost undistorted, focused beam spot. After a time period of about 60 to 70 seconds, the same beam spot started to distort and to broaden in its size. This increase in size can be observed for several minutes, before the new shape stops to broaden, showing a steady, unchanging picture for time periods of more than several hours. It is found that mechanical vibrations couple into the system. The external perturbation forces the sample tube to vibrate, transferring its oscillations to the sample liquid. The fact, that the distorted picture is stable for long time periods is a hint, that the external perturbation seems to be constant, too, and convection
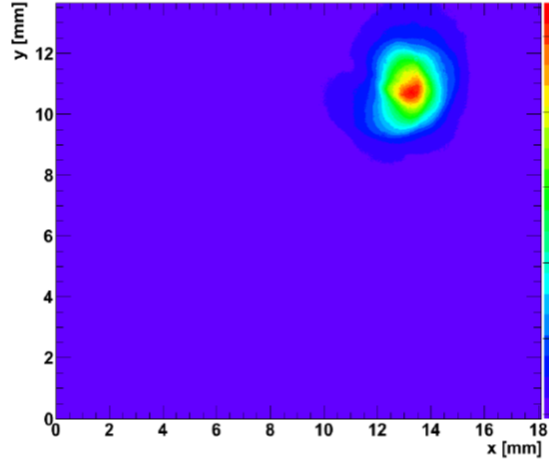
Figure 4.18: Colorized sensor picture after filling the tube and re-adjusting the beam
on the sensor. The photo is taken directly after the filling ended. The
adjustments from the emptied tube measurements have to be optimized.
It can be seen that the beam spot is focused nicely on the sensor, and
small beam shape distortions are present because of the influence of the
sample liquid. Furthermore, it is possible to adjust the beam properly
after the light passed $2.3\,\mathrm{m}$ through the sample medium.
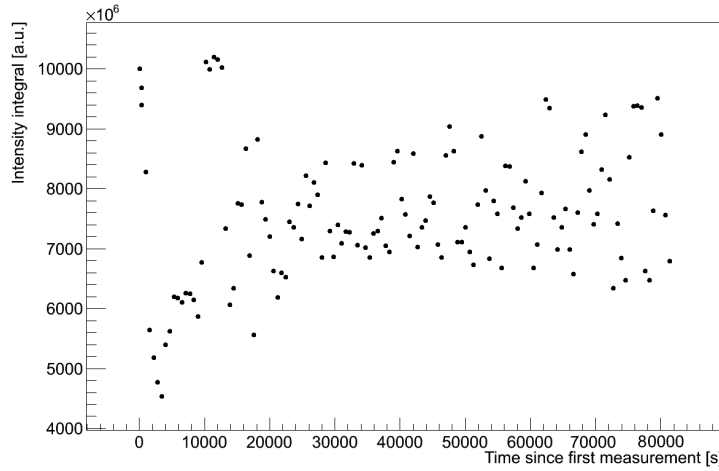
Figure 4.19: Longterm stability measurement with a filled sample at a fill height of
$\sim 2.3\,\mathrm{m}$. The intensity integral is plotted over a time period of approx-
imately $22\,\mathrm{hours}$. The plot shows the absolute intensity integrals over
the time in seconds. It can be seen, that for the same unchanged light
beam, huge fluctuations are visible. This can be explained by changes
in the beam shape and position, caused by perturbing vibrations. Note
that no uncertainties are given.

Figure 4.20: Raw data pictures taken during a test measurement with a filled sample tube at a fill height of about 2.3 m and a wavelength of 530 nm. The pictures show the same light beam for different times. The first beam spot is taken directly after the filling procedure and the adjustment on the sensor. After several seconds, the beam started to distort and broadened for several minutes. After a time period of 5 minutes, an unchanging, broadened, distorted beam shape is observed. This phenomenon can be explained by vibrations coupling into the sample tube and its liquid.
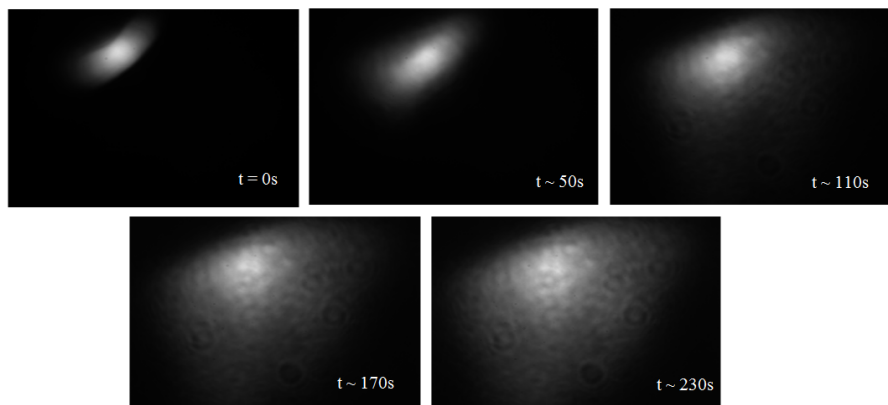
may be neglected. As the liquid starts to vibrate, also standing waves may occur within the sample tube, showing a steady, unmoving perturbed picture. Due to the limited size of the light sensor and the broadening of the beam shape to a size in the order of the diameter of the sample tube, intensity information is lost on the sensor edges, making a precise attenuation measurement impossible. The fact, that for lower filling levels, the beam size is bigger due to a focus in several meters distance, this vibration induced broadening maximizes the loss of intensity at the edges and explains the huge fluctuations. Furthermore, the mechanical changes not only lead to distortions, but also shift the beam position, destroying the incident adjustments. As a consequence, the beam wanders off and parts of the intensity are lost for detection, visible as a huge fluctuation of the determined intensity integral. Another problem arising is the fact, that the distorted beam size is in the same size as the tube diameter. Parts of the beam are reflected at the tube walls, distorting the intensity information, which is parasitic for attenuation measurements and an exemplary picture can be found in fig. 4.21.

Although the optical table and the sample tube are isolated with dampers, vibrations are coupled into the sample tube. This can not be seen for the emptied tube, as sample tube and light beam are not connected indirectly by a sample liquid. Precise attenuation measurements are not possible in this case, making it crucial to suppress the in-coupled vibrations.
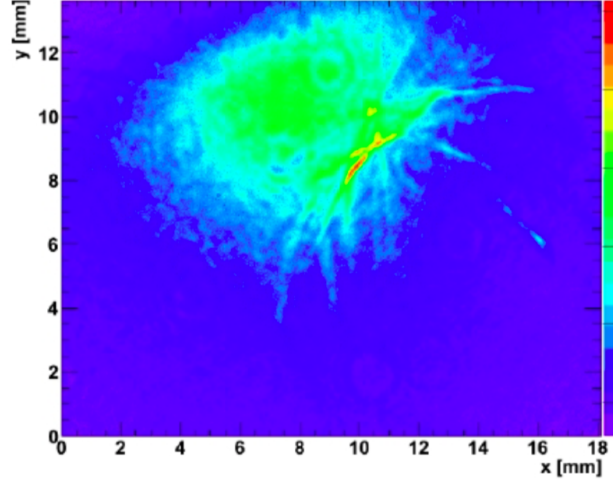
Figure 4.21: Colorized sensor picture taken during a test measurement at a fill height of $2.3\,\mathrm{m}$ and a wavelength of $530\,\mathrm{nm}$. Due to the beam broadening, parts of the beam are reflected at the tube walls because of the limited diameter of the sample tube. Furthermore, the beam is broadening to a size bigger than the light sensor itself, leading to a loss of intensity on the sensor edges.

4.6.1 Forced mechanical oscillations

A forced oscillation is the oscillation of a system caused by an external perturbation. For a permanent, periodic perturbation the system is forced to oscillate permanently, too, with the frequency of the external perturbation and with a time-independent amplitude. Due to the system's own resonance frequency f_{res}, the oscillation amplitude of the driven oscillation is increasing if the external frequency is moved towards f_{res}. The amplitude can be amplified to huge values, which may destroy the system in case the damping constant of the system is too low [Dem04]. For a forced, damped harmonic oscillator, the oscillation process can be described with the equation of motion [Dem04]

$$m \cdot \frac{d^2\vec{r}(t)}{dt^2} = -k \cdot \vec{r}(t) - c \cdot \frac{d\vec{r}(t)}{dt} + \vec{F}_{\mathrm{external}}(t), \qquad (4.7)$$

with m being the mass of the system, $\vec{r}$ the time dependent spatial vector for three dimensions x, y, z, the external force $\vec{F}_{\mathrm{external}}(t)$, the restoring force constant k and the damping constant c. Assuming a one-dimensional damped, forced, decoupled oscillation, the solution of the equation of motion for a periodic external force $F(x) = F_0 cos(\omega t)$ is [Dem04]:

$$x(t) = A_1 e^{-\gamma t} \cdot cos(\omega_1 t + \phi_1) + A_2 cos(\omega t + \phi), \qquad (4.8)$$

which contains the solution of the free damped harmonic oscillation

$$x_1(t) = A_1 e^{-\gamma t} \cdot cos(\omega_1 t + \phi_1). \qquad (4.9)$$

Hereby, A_1 is the amplitude, γ the damping constant, ω_1 the frequency and ϕ_1 the phase of the oscillation. Equation 4.8 further includes the solution, where the oscillation of the free damped oscillator faded and a stationary state of the forced oscillation is reached [Dem04]:

$$x_2(t) = A_2 cos(\omega t + \phi), \tag{4.10}$$

with the driving frequency ω, the phase ϕ and the amplitude of the forced oscillation:

$$A_2(\omega) = \frac{F_0/m}{\sqrt{(\omega_0^2 - \omega^2)^2 + (2\gamma\omega)^2}}. \tag{4.11}$$

The resonance frequency of the system in this case is given by [Dem04]

$$\omega_{\text{res}} = \sqrt{\omega_0^2 - 2\left(\frac{c}{2m}\right)^2}, \tag{4.12}$$

with $\omega_0 = \sqrt{\frac{k}{m}}$ and $\gamma = \frac{c}{2m}$, whereas for the free damped oscillation, the resonance frequency is [Dem04]:

$$\omega_{1-\text{res}} = \sqrt{\omega_0^2 - \left(\frac{c}{2m}\right)^2}. \tag{4.13}$$

The oscillation amplitude of the system depends on the external force as well as on the damping characteristic of the system and also on the forcing perturbation frequency [Dem04]. In most cases, the occurring oscillations are not decoupled, leading to complex oscillations in more dimensions. To determine complex systems and their oscillatory behavior, a modal analysis can be used to determine the oscillation characteristics. In most cases, these are computer based, numerical modelings, which model the dynamical characteristics of the systems [Str11]. Due to the fact that PALM is a complex oscillatory system and a modal analysis is a time consuming effort, which typically takes several years [Str11], it is focused to a more experimental approach to determine the vibrational behavior in the case of this experiment.

The oscillations of the setup are mostly limited to the sample tube, which is the receiver of a time dependent external force. The liquid of the sample tube starts to oscillate, too, excited by the vibrating steel tube, and waves may traverse through the sample. After a superposition of forced and reflected waves takes place, a stationary vibrational picture is obtained, which is in good agreement to the observations, as the distorted beam spot is no longer changing after a couple of minutes.

The external force, driving the oscillations, has to be seen as a superposition of several different external perturbing forces with different frequencies. In the case of the experiment, these external forces have different origins. This means, that some are periodic and fluctuating with time and some only appear an instant, being an external in-coupled shock from the ongoing constructional work inside and outside the laboratory[3]. Although the resulting oscillations $f(t)$ may not be harmonic, it can

---

[3]As mentioned in section 4.2.2, the surrounding conditions of the experiment change significantly during the whole measurement process due to the constructional work inside (clean tent, clean room) and outside the laboratory.

be described as a superposition of harmonic oscillations with different frequencies ω_n, amplitudes a_n and phases ϕ_n [Dem04]:

$$f(t) = a_0 + \sum_{n=1}^{\infty} a_n \cdot cos(\omega_n t + \phi_n). \tag{4.14}$$

This is called a Fourier transformation and can be used to determine the frequency spectrum of the perturbing vibrations influencing the setup.

The external forces can have different origins and possibilities to be coupled into the system. Because of the mounting of the tube with four rigid, damped wall mounts, these have to be considered as possible points of excitation. This rigid mounting also has an influence to the nodal points and antinodes of the oscillation, forcing the sample tube into its vibrational modes.

4.6.2 Identification of the origin of occurring vibrations

It is known so far, that the vibrational perturbations distort and broaden the detected beam spot as well as shift it towards the sensor edges. Because of the focused beam, the size of the beam spot increases for decreasing fill height levels and the perturbation induced broadening is no longer negligible. This is the reason for intensity losses at the sensor edges and the occurrence of reflections at the stainless steel tubes. Intensity integral measurements over time periods of several tenths of hours reveal also time dependent, changing beam distortions, which give evidence that the perturbing external force is a superposition of different contributions. After the occurrence of a new perturbation contribution, it is found that the beam shape starts to distort and broaden for a couple of minutes, before showing an unmoving, stable distorted beam shape picture again, if no other external force occurs in this time period. This external force contributions differ with time, as for different measurement days the resulting distorted beam shape is not possible to be reproduced reliably. As a consequence, identifying and eliminating sources of vibrational perturbation forces is crucial.

Identification of perturbation sources

To eliminate the perturbations, their origin has to be identified. Due to the fact, that neither beam distortions nor fast beam position shifts are found for the empty tube measurements, the sample tube is identified as the vibration receiving device. Therefore, different sources of vibrations are considered:

- shutting doors and people next to the experiment,

- fill height sensors,

- usage of crane,

- undamped pumps from nearby experiments,

- constructional work inside and outside the laboratory,

- CCD camera device and the

- climate system of the laboratory.

Longterm intensity measurements and single sensor pictures are used as tools to identify possible effects. Investigating the influence of doors and people, it is found that due to the rigid PTFE material used for the filling tubes, perturbations can be coupled into the sample tube with wiggling filling tubes. This is the case for people entering the experimental site next to PALM and the shutting and opening of the doors neighbored to the experiment. No hint for an influence originating from the fill height sensors is found. Also tests with a working crane show no effect on the measurements in PALM. Because of the results from the filled tube measurements, a dominant, omnipresent perturbation is identified to be coupled into the sample tube. This omnipresent vibration can not originate from the pumps in the laboratory used by several experiments, because of their limited run times and present vibrations for offline pumps. There are contradicting results for the influence of the running pumps on the experiment. The results for a negative effect could not be confirmed clearly, because the omnipresent vibrations are dominant and mask their effect. To be sure, all pumps within the laboratory have been damped or decoupled from the floor.

Due to constructional work inside the laboratory for a long time period and the start of the construction of a new building on the outside, external shocks are identified, which are coupled into the laboratory halls. There is a promising coincidence between the occurrence of external shocks in the experiment and the labor and lunch time of the workers on the building sites, identifying the constructional work as a source of such shocks. These have an un-negligible impact on the measurements, however, they can not explain the omnipresent perturbations.

The CCD camera device is taken into account as a possible source of excitation, as the device has an integrated cooling system, which is used during all measurements. As the device is in direct contact to the baffle tube and is mounted rigidly to the sample tube, vibrations from the cooling system can be coupled into the setup. This would be an omnipresent source of vibrations.

Another tool, which can be used to identify present perturbations, are so called amplitude-frequency profiles. The perturbing force is a superposition of different contributions, which force the sample tube and its liquid to oscillate. The complex oscillation can be described by a superposition of harmonic oscillations, as is shown in equation 4.14 in section 4.6.1, called a Fourier transformation. The acceleration amplitude of a movement can be measured as a function of time with acceleration sensors. The amplitude-time spectrum contains information about the periodicity of the perturbation. By using a Fourier transformation, the spectra can be transformed into frequency spectra, revealing all contributing frequencies of the complex oscillations. In most cases, the Fast Fourier Transformation (FFT) is used to transform the acceleration amplitude-time profile into the amplitude-frequency profile.

The FFT is an algorithm, which uses symmetry arguments to reduce the computing time significantly [Che18]. The detectable contributing frequencies are limited by the sampling rate of the acceleration sensor. The sampling theorem can be used to approximate the frequency range, which can be determined via [Che18]

$$f_{\text{sampling}} \geq 2 \cdot f_{\text{measurable}}. \tag{4.15}$$

Hereby, f_{sampling} is the sampling frequency and $f_{\text{measurable}}$ the maximum frequency, whose modulation can be resolved reliably.

In a first check, the acceleration sensors of a mobile phone and a freeware app[4] are used to investigate the oscillation characteristics of the PALM experiment. The freeware app uses the three axis acceleration sensors of a smart phone to measure the acceleration amplitudes in units of $g = 9.81 \frac{m}{s^2}$ over a fixed time period of $10.2\,s$. Furthermore, it provides also the contributing frequencies in a range between zero to $50\,Hz$. With this freeware app, first checks are performed to identify possible excitation sources and to understand the in-coupling mechanisms. Different locations at the PALM experiment are investigated to reveal different points of excitation as well as differing amplitudes of the perturbation frequencies and to optimize the damping materials. At each location, several measurements are performed with the freeware app and are processed with ROOT. Due to the fact, that the external perturbations are time dependent, it is difficult to reproduce the measurements for statistical uncertainties. This is also the case for baseline measurements. Therefore, the spectra shown in the following do not include statistical uncertainties and baseline corrections. The results are only meant as a first check to identify possible perturbation frequencies. For a more sophisticated frequency determination, an acceleration measurement device is developed and described in section 4.6.8.

Due to the direct contact of CCD camera and sample tube, an acceleration measurement series is investigated at the position of the camera device to identify possible perturbing frequencies caused by the detector itself. Fig. 4.22 shows an exemplary measurement at the top of the CCD housing with an online cooling system. The plot shows the acceleration amplitude for all three dimensions in units of g over a time period of $10.2\,s$ with the x dimension in black, y in cyan and z in magenta in reference to the acceleration sensor. The exemplary measurement shows an oscillation, which is slightly enhanced in y direction (cyan), which could not be reproduced. The data are used to calculate the amplitude-frequency profile after a Fourier transformation to access the contributing frequencies. Fig. 4.23 shows the corresponding amplitude-frequency spectrum and an increased frequency contribution in the range of around $40\,Hz$ to $50\,Hz$ for all measurements. Due to the lack of a baseline correction and possible uncertainties, a frequency peak, which has an amplitude of at least twice the size of most other appearing peaks is defined as a significant peak. There also seems to be a small contribution in the region of $10\,Hz$, visible for the x dimension (black) in the exemplary measurement. Other measurements show similar perturbation frequencies but with less dominant amplitudes, as can be seen in

---

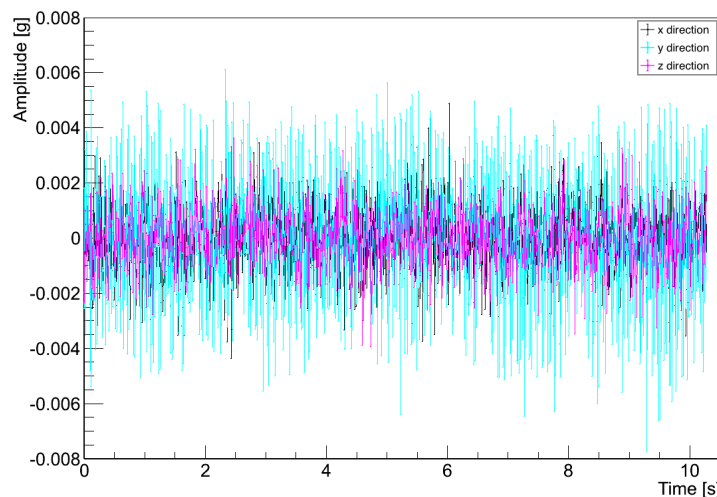[4]Vibro Checker ACE, see www.ace-ace.de.

Figure 4.22: Exemplary acceleration amplitude measurement over a time period of
10.2 s. Measurement point is on top of the CCD housing with a run-
ning cooling system to identify perturbing frequencies originating from
the device. These data are used to generate the amplitude-frequency
profiles.
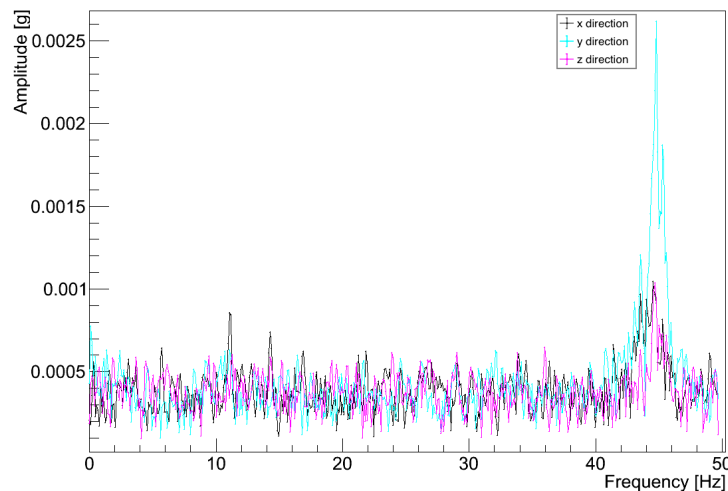
Figure 4.23: Calculated amplitude-frequency profile of the time profile shown in fig.
4.22 to identify contributing perturbation frequencies. Measurement
point is on top of the CCD housing with a running cooling system.
Note, that these results are single measurements without uncertainties,
which are only used as a first check. At a frequency of ~ 44 Hz, an
increased amplitude is observed for all three dimensions. Also hints for
a perturbation frequency with a smaller amplitude is found at 10 Hz for
the x dimension (black).

Figure 4.24: Reproducibility measurement of the amplitude-frequency profile at the CCD housing of fig. 4.23 to reproduce the found perturbation frequencies. The identified frequencies between 40 and 50 Hz can also be seen, but with less dominant amplitudes.
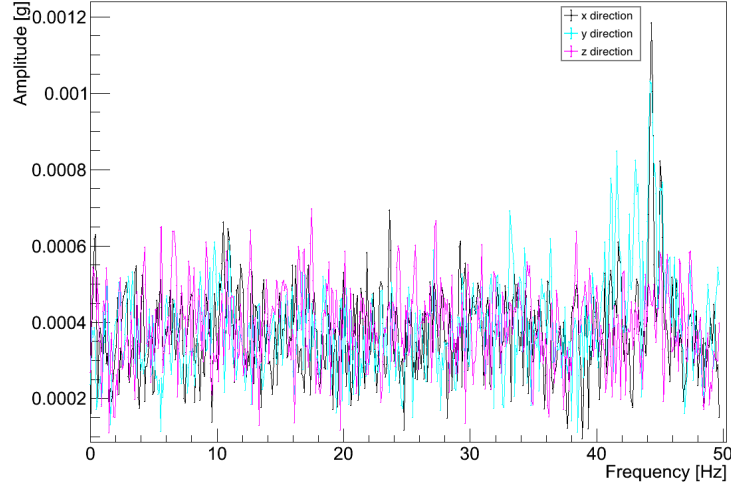
fig. 4.24. This is a hint, that the found frequency may not be the omnipresent perturbing source. To cross-check, if the found frequencies are related to the CCD device, the cooling system is stopped and another acceleration measurement series is performed with the CCD sensor working at room temperature of 22 °C. Fig. 4.25 shows an exemplary measurement of the series for the uncooled CCD sensor on top of the housing. Shown are the Fourier coefficients over the contributing frequency for three dimensions. Several measurements reveal a strong contribution of a frequency between 12 Hz and 14 Hz, which can in some cases also be seen for the cooled sensor. The contribution in (40-50) Hz seem to be present, but less dominant compared to the cooled device. Other frequency contributions can not be reproduced reliably, showing that the contribution is changing with time and may be random, which is also valid for a contribution at around 40 Hz. The frequencies in (0-1) Hz appear irregularly as well. To further check, if the contribution between 40 Hz and 50 Hz is correlated to the CCD device, the camera is switched off for a third acceleration measurement series. The results can be found in fig. 4.26. Comparing the measurement with the former results with and without a running cooling system, it can be seen that both contributions in the frequency ranges of 12 Hz to 14 Hz and 40 Hz to 50 Hz are no longer detectable. Other dominant frequency contributions can not be detected at this point. This implies not only that both contributions are produced by the camera module itself but also that due to a direct mounting to the baffle and sample tube system, a transfer into the sample tube is likely. This means, that the light detector itself is a source of vibration and its direct connection to the sample tube is the point of transfer.
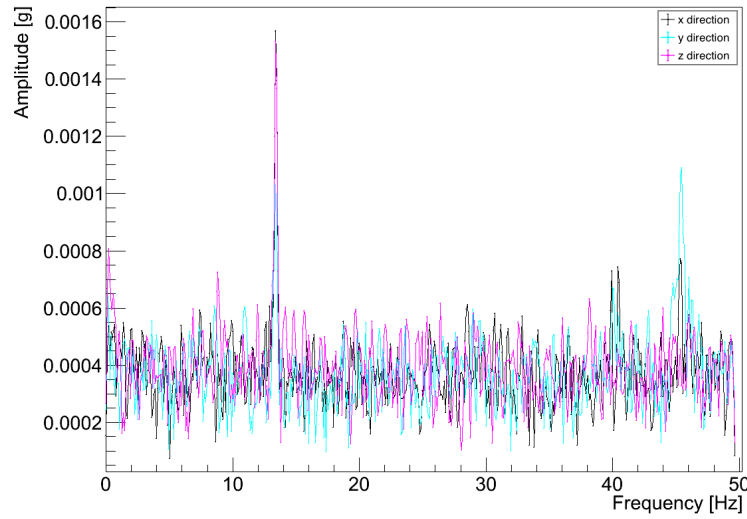
Figure 4.25: Amplitude-frequency profile of the acceleration measurements on top of the CCD housing with a stopped cooling system and a sensor working point at room temperature for all three dimensions. It can be seen, that frequencies in the range of 12 Hz to 14 Hz can be identified for all dimensions and in (40-50) Hz for the x (black) and y dimension (cyan) as possible perturbations.

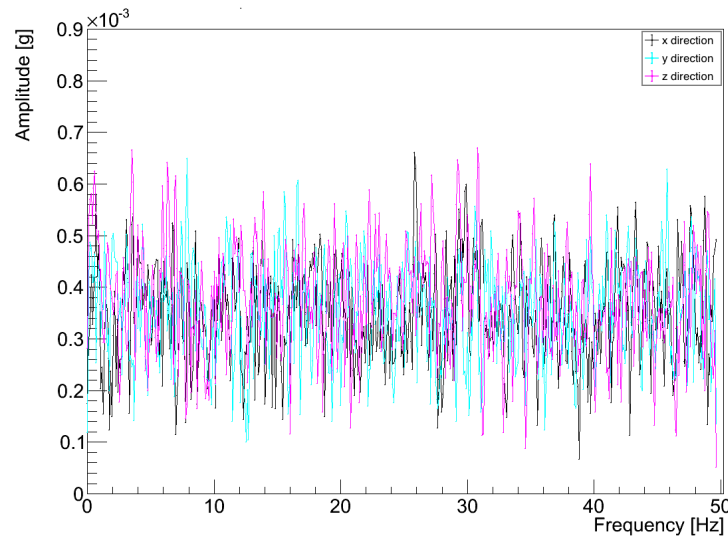
Figure 4.26: Amplitude-frequency profile of the acceleration measurements for an offline camera device on top of the housing. Shown are the measurements for all three dimensions. It can be seen, that the contributions found for cooled and uncooled CCD device, shown in 4.24 and 4.25, are no longer visible.
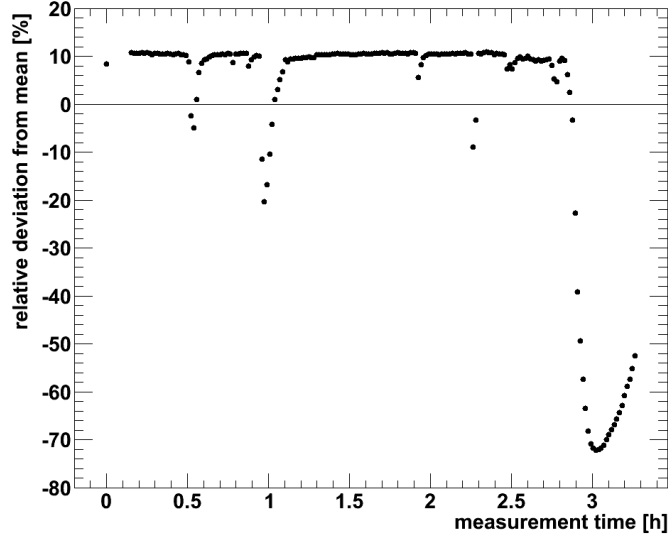
Figure 4.27: Longterm stability measurement of the measured intensity integrals
during a test, where the climate system is offline. Plotted are the
relative deviations from the mean of the intensity integral in dependence
on the measurement time. Several breakdowns can be seen in the period
without a running climate system (t< 2.8 h). These are identified as
external shocks, which are coupled into the system and change the
beam position on the sensor. Characteristic for such external shocks is
the respective relaxation afterwards. After approximately 3 hours, the
climate system is switched on. As can be seen, there is a huge external
shock coupling into the experimental setup in coincidence, forcing the
beam out of its adjustment.

In another study, the climate system is taken into account as a possible source of
perturbations. As the climate system is online for 24 hours a day, providing fresh
air for the laboratory, it is present in all measurements, too. A possible excitation
may be possible by air steam or due to vibrations originating from the inlet and
outlet tubes neighbored to the experiment[5]. To suppress an excitation by air flow,
a second, flexible dark box is installed around the whole setup. The dark box is
a special black fabric, whose manufacturing purpose is the absorption of ambient
light and acoustic noise. In the case of the PALM experiment, it is used as a
shielding against air streaming. The installation of the fabric could not suppress
the occurrence of the dominant vibration perturbations, which gives a hint that
the excitation of the sample tube via air stream is not the dominant perturbation
transfer. Longterm intensity measurements are performed to identify the influence
of the climate system on PALM and an exemplary measurement can be seen in fig
4.27.
The figure shows a longterm stability measurement for an unchanged light beam,

---

[5]See section 4.2.2 for detail.

adjusted on the center of the sensor at a fill height level of $\sim 2.3\,\mathrm{m}$ and a selected wavelength of $530\,\mathrm{nm}$. The measurement is performed without a running climate system, which is switched on after approximately three hours of measurement. Plotted are the deviations of single intensity integrals from the mean in percent[6]. It can be seen, that the intensity integrals show several breakdowns within the first 2.8 hours. These are not correlated to the climate system, but are identified as external shocks, forcing the sample tube to move in its mounting and destroying the adjustment between tube and optical table. The adjusted beam spot is shifted out of its centering on the sensor, resulting in an intensity cut off of a part of the light beam on the sensor edges. Such external shocks appear for an instant, but due to its instant occurrence the system relaxes to its incident adjustment after a short relaxation time. This can be seen for all occurring intensity breakdowns within the first 2.8 hours of the measurement. Several other measurements confirmed a coincidence between the occurrence of external shocks and constructional work inside and outside the laboratory. After starting the climate system, a shock is traversing through the laboratory halls and has the same impact on the system, but is much stronger than the shocks from the outside, and can be identified as an enormous break down at ~ 2.8 hours. To identify the climate system as dominant source of perturbation, single data pictures are used for cross-checking the occurring vibrations. Fig. 4.28 shows two single data pictures, colorized for better contrast with logarithmic intensity scales. Picture (a) shows a rather focused beam spot directly before starting the climate system. The beam looks like the a monochromator exit slit rectangle. The beam shape stays focused during the whole measurement time with an offline climate system. After starting the system, an external shock forces the beam out of its adjustment at first. The beam shape starts to distort and broadens into a characteristic vibrationally perturbed light beam, as is shown in (b). Several cross-checks reproduce the influence and identify the climate system as the origin of the dominant vibrations.

The climate system can only be switched off for small time periods, as it provides the laboratory with fresh air. A common measurement series takes several hours, but it would be possible to perform measurements without a climate system. Because of the usage of cryogenic gases in the laboratory, a steady air exchange is required for personal safety and a full measurement series is difficult.

Also temperature and pressure test measurements are performed with an installed barometer and temperature sensor chip. Neither a coincidence between the occurrence of vibrations nor a significant change in one of the parameters is found. First tests show a rather constant temperature difference between the top and the bottom of the experiment, which may lead to natural convection. No experimental hints have been found so far, that natural convection has a non-negligible effect on the data, neither with nor without running climate system. Therefore, the influence of convection is smaller than the detected vibrations and can be neglected. As the dominant vibrational source can not be eliminated, it is necessary to decouple the

---

[6]The mean is calculated from all plotted intensity integrals.

(a)   (b)
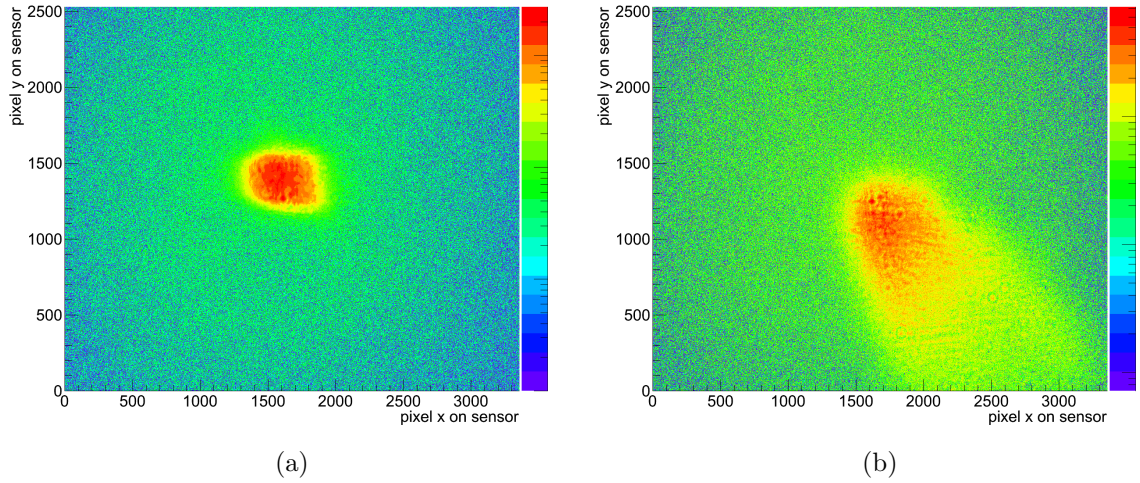
Figure 4.28: Single colorized, raw sensor pictures without (a) and with (b) a running
climate system. The colors correspond to the measured intensity, scaled
logarithmically for better contrast. It can be seen in (a), that the beam
spot is undistorted and rather focused, looking like the monochroma-
tor exit slit. In (b) the same beam is shown, but several minutes after
starting the climate system. As can be seen, the beam shape is dis-
torted, showing the characteristic dominant vibrations, which can be
identified for all test measurements. There seem to be a light halo for
both pictures, which originated from the mirror optic and is eliminated
by optimizing the dark box.

Figure 4.29: Amplitude-frequency profile based on the acceleration measurements at the position of the sample tube itself for a possible perturbation frequency identification. Shown are all three dimensions. It can be seen that no dominant perturbation frequency is found in the range up to 50 Hz.
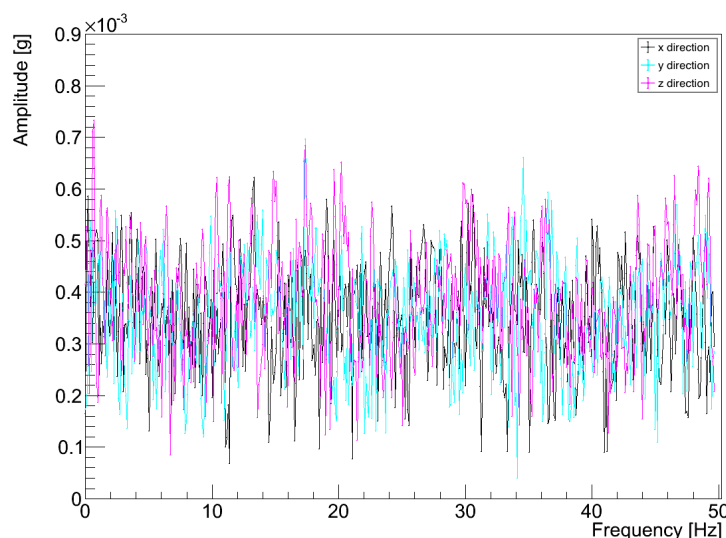
system from its surroundings and eliminate the points of in-coupling.

Due to the rigidity of the PTFE filling tubes, small wiggles may be coupled into the system, caused by a constant air stream in the laboratory or by closing doors next to the setup. Furthermore, the wall mounts of the sample tube have to be investigated as possible exciters, as the inlet and outlet tubes of the climate system are located directly next to the mounts. It may be possible that due to the opening in the concrete, the walls and the ceiling may be forced to vibrate by the air streaming through the mounted inlet and outlet tubes of the climate system. In a first check acceleration amplitude measurements are investigated at the lower entrance window of the sample tube to identify possible perturbing frequencies. Fig. 4.29 shows an exemplary measurement of the series for three dimensions to investigate the vibrations at the sample tube. As can be seen, no significant perturbation frequency can be identified up to 50 Hz. The same result is found for the investigation of the rigid wall mounts, as is shown in fig. 4.30. This implies, that the excitation frequency can not be found in the range between (0 - 50) Hz and no possible in-coupling mechanism can be excluded so far. As a consequence, the dominant external frequency is either not present at these points or, more likely, is at a frequency range above 50 Hz. This makes it difficult to optimize the dampers for proper vibration suppression.
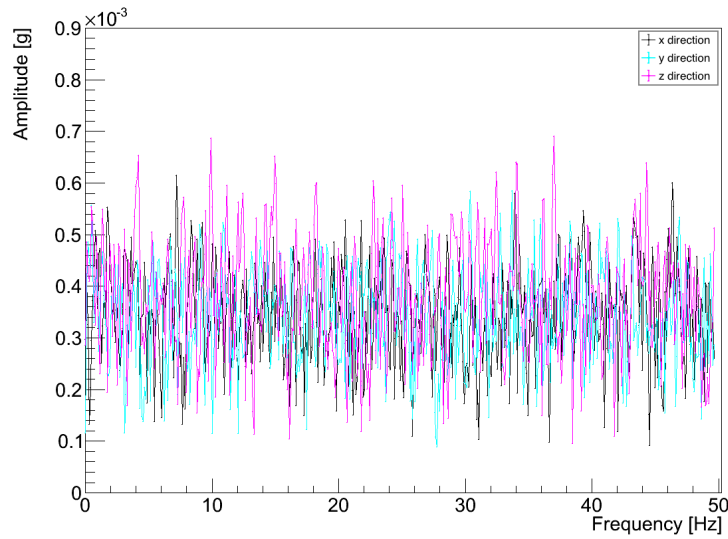
Figure 4.30: Amplitude-frequency profile calculated from the acceleration measurements at the position of the rigid wall mounts of the sample tube, shown for all three dimensions. It can be seen that no dominant perturbation frequency can be found for the sample tube vibrations in the range up to 50 Hz.

4.6.3 Elimination and suppression of in-coupled vibrations

Due to the fact that the climate system and the light detector are identified as perturbing vibrational sources, an elimination of these vibrations is not possible. Therefore, the sample tube has to be decoupled or damped instead. For an elimination, not only the frequency for the usage of a proper damping material has to be known, but also the points of in-coupling or excitation. In principle, several points of in-coupling can be possible:

- the filling tubes connecting storage tank and sample tube,

- the storage tank itself with its liquid,

- the stiff mounting of the CCD camera to the baffle tube, which itself is connected directly to the sample tube,

- the mounting of the sample tube itself,

In the case of the vibrating CCD camera, it is clear, that the in-coupling of a perturbing frequency into the sample liquid is located at the direct contact between detector and steel tube. To guarantee that the detector device is no longer coupling vibrations into the sample tube, a new CCD holder is designed and constructed and can be found in fig 4.31. Due to the fact that the whole setup is built modularly, the new CCD holder can be mounted easily via flanges on top of the stray light

(a)   (b)
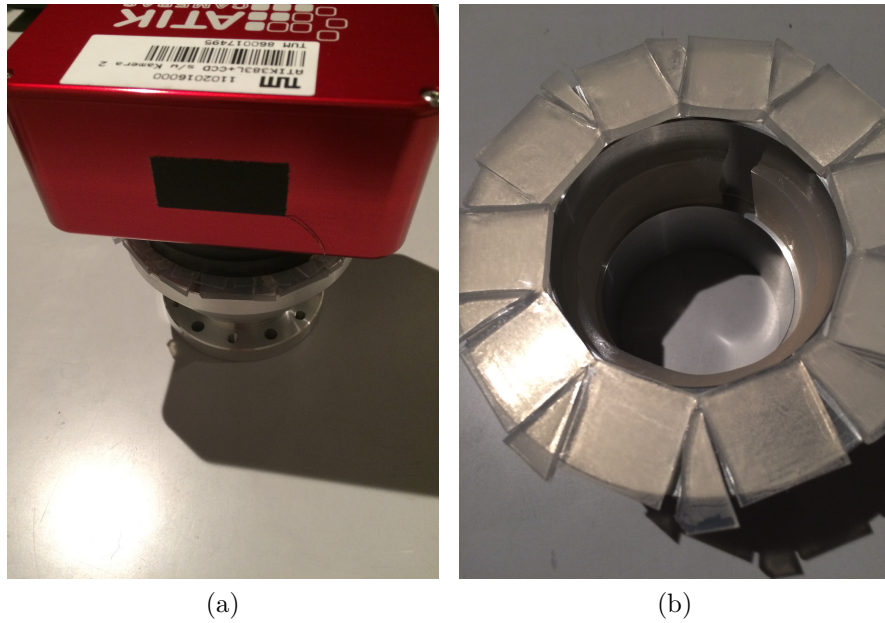
Figure 4.31: Photographs of the manufactured CCD holder. In (a) the CCD device
             is placed on the holder and is guided by the inner mount to a centered
             position. The holder can be installed easily on the flange of the stray
             light baffle. It has an inner mount for the detector, where silicone gel
             dampers are installed to eliminate direct contact, see (b). Due to the
             fact that the sensor is placed on top of the surface of the holder, the
             top surface is damped with silicon dampers as well.

baffle. The CCD holder is designed to have an inner mount for the camera for better reproducibility. The device is placed on top of the holder and centered in reference to the light beam path by the inner mount. To decouple the detector from the holder, optimized silicone gel dampers are used, which suppress the identified perturbation frequencies in the range of 40 Hz to 50 Hz sufficiently. This damping material is installed on the contact surfaces and the inner mount. The contact between CCD camera and guide rail is not firm at all, to enable the proper working of the dampers.

Damping the vibrations from the climate system is not that simple. Because of the unknown perturbation frequencies from the surroundings and the climate system, a suppression of the vibrations by changing the damping material is challenging. Furthermore, due to their construction, it is not possible to change the damping material of the wall mounts. A new mounting concept is investigated, where the tube is mounted like a free pendulum, enabling the setup on the same time to adjust itself perpendicular to the optical table by its own weight. For an appearing external shock, the pendulum is possibly forced out of its adjustment, but is able to relax and readjusts itself. Further investigations show, that the center of mass is shifted towards the upper third of the system, which may influence the relaxation of the tube at a certain angular dis-adjustment. To limit the displacement of the pendulum, two contact points are considered. At one point, the pendulum is mounted, whereas on the second, the movements of the tube are limited. This point of contact can also be used to adjust the tube to the optical table more easily. Considering this issues, a new mount is designed to eliminate the possibility of an excitation by the wall mounts, which implies, that the wall itself is transferring the external perturbation force from the rigid mounts into the sample tube. The new pendulum mount is installed at the ceiling and is constructed from stainless steel. The sample tube system is hold by two clamps, which are isolated from the tube by specialized damping materials. Both clamps are needed to stabilize the sample tube in reference to the optic at the table. Therefore, a clamp is installed at the stray light baffle and another at the sample tube next to the upper flange. These clamps are also mounted with a specialized construction, which acts as a two dimensional translation stage to adjust the sample tube properly in reference to the optic and they are also mounted to the ceiling mount. A scheme of the designed ceiling construction can be seen in fig. 4.32. It is a steel cage structure mounted to the ceiling, holding a base plate. On the steel cage, both clamps with dampers and their translation constructions are mounted, enabling the translation in two dimensions each. The sample tube is hold by both clamps similar to a free pendulum above the optical table. Fig. 4.33 shows the constructed ceiling mount with the sample tube. Both clamps are installed at the steel cage, holding the sample tube in place and they can be moved in x and y direction, making it possible to adjust the sample tube in reference to the optical table. The sample tube has no direct contact to the ceiling cage but to the damper material inlets of the clamps. These are constructed in a way, that the damping material can be inserted and changed easily. The material used for the dampers is made of α-gel [Tai18], which has its resonance frequency in a range of 15 to 22 Hz
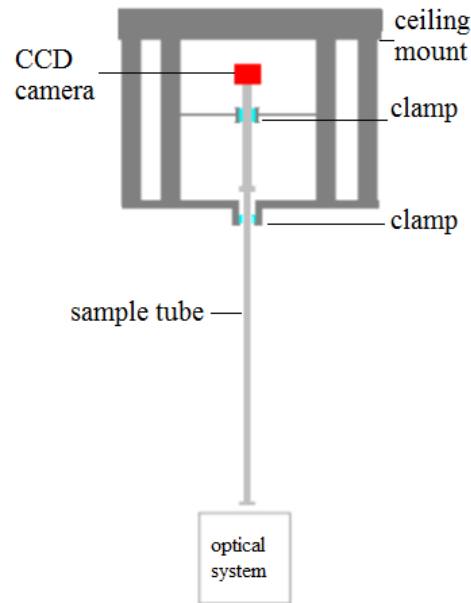
Figure 4.32: Scheme of the design for a decoupled ceiling mount. It is constructed from steel, guaranteeing a solid mount for weights of at least 300 kg. The sample tube is hold by two clamps, one at the stray light baffle near the light sensor and the second on the sample tube. Both clamps are adjustable by specialized translation constructions for x and y dimension and are decoupled with special damping materials. The sample tube is mounted like a free pendulum to readjust itself after the occurrence of external shocks. For details see text.

(a)   (b)

Figure 4.33: Pictures of the constructed ceiling cage, showing the new steel con-
struction with a base plate on the bottom. The plate can be parted
to install the sample tube, which is hold by two clamps. Two transla-
tion constructions allow to adjust the system in two dimensions each
in reference to the optical table. Both clamps are damped to suppress
vibrations.

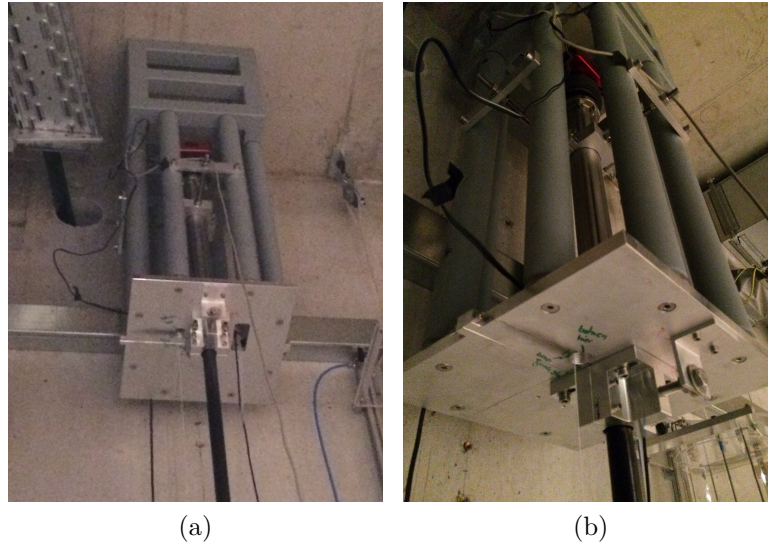and suppress frequencies above 30 Hz sufficiently [Tai18].

As is mentioned in section 4.6.2, it has been considered, if the perturbations can
excite the sample tube via air flow. Therefore, a special fabric is used as a second
dark box, covering the full experiment in at least two layers for vibration suppression.
The CCD camera and baffle tube on top of the experiment are also shielded from
air flows with plates, which are mounted to the ceiling cage[7]. Tests show, that the
additional dark box can not remove the observed perturbations, which is a hint,
that this is not the dominant in-coupling mechanism of the vibrations and favors
the possibility of present mechanical vibrations at the ceiling. Taking into account
the experimental site, the inlet and outlet tubes of the climate system are located
several cm from the setup. The constant air stream through the tubes may excite the
walls and the ceiling both and the inlet and outlet tubes itself may be the possible
exciters.

Performance of holder and ceiling mount

After applying the new holder and ceiling mount and reactivating the setup, test
measurements are performed to investigate their influences on the system. Fig. 4.34
shows a raw sensor picture at a wavelength of 530 nm and a fill height level of around
2.3 m after the installation of the ceiling cage and the new CCD holder. The raw

---

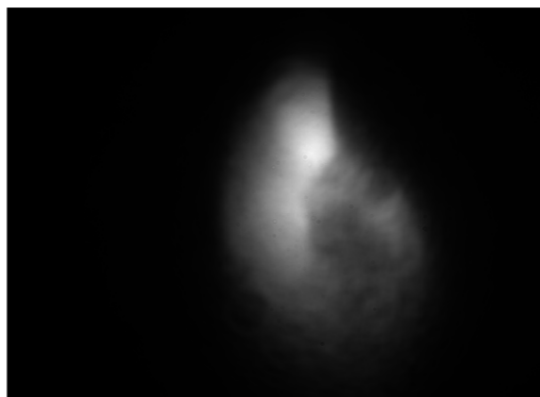[7]The installed fabric is shown in fig. 4.6 already.

Figure 4.34: Raw data picture to test the performance of the installation of a new ceiling mount with optimized damping materials and a new CCD holder. The test measurement is performed at a wavelength of 530 nm and a fill height level of approximately 2.3 m. Both pictures show the same beam shape, which is inhomogeneously illuminated but also less perturbed. The inhomogeneous illumination is a hint for a mechanical change during the exposure to the light detector. It can also be seen, that the full intensity beam can be adjusted on the small sensor at this fill height level.

sensor picture shows a light beam, which is well centered on the small sensor. This enables the detector to observe the full intensity information at a fill height level of 2.3 m. Furthermore, the beam shape is in-homogeneously illuminated, which is a hint for mechanical instabilities. During the exposure to the detector, the beam seems to shift, changing its position on the sensor. In reality, the light beam is unchanged, but the sample tube mounted as a pendulum is moving during the measurement time, affecting the detector device as well. Such movements can be caused by the rigid PTFE filling tubes. Wiggling on the filling tubes influences the position of the sample tube, mounted as a free pendulum and are created by air movements as is the case for closing and opening the doors located next to the setup. Furthermore, it is found that the PTFE tubes also affect the sample tube for changes of the liquid fill height and can also dislocate the tube permanently for small fill height levels. Because of the ongoing constructional work, the free pendulum is dislocating several times during measurement periods, which affects precise measurements, too.

Restricting mechanical movements

This facts motivate the installation of a third clamp on the bottom of the sample tube to fix its adjustment in reference to the optical table. A picture of the manufactured third clamp can be found in fig. 4.35. It is produced from aluminum and can be parted to position the sample tube. Furthermore, it has a guide to place and position the damping material properly. The material is the same as for both other clamps,
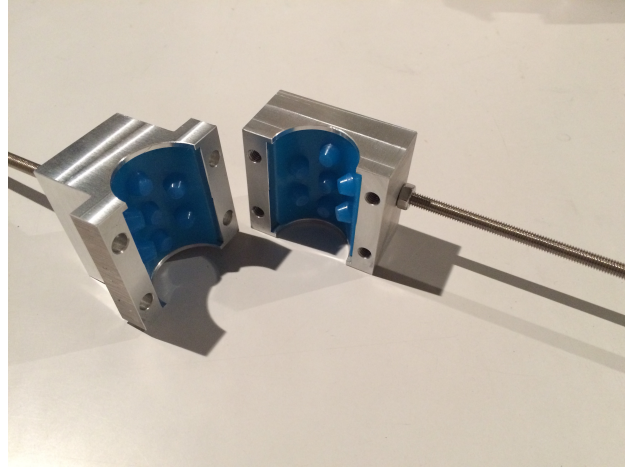
Figure 4.35: Picture of the manufactured clamp and its damping material inlet. The clamp is manufactured from aluminum, which can be parted, and has a small guidance for an easy change and positioning of the damping material inlets. The material is a silicon gel damper, which damps frequencies $\geq 30\,\mathrm{Hz}$ sufficiently and has its own resonance frequency in the region from 15 to $22\,\mathrm{Hz}$.

which is made from silicon gel. It has good damping characteristics for frequencies $\geq 30\,\mathrm{Hz}$. The clamp is installed at the bottom flange of the sample tube and on top of the dark box to eliminate possible vibrations coupled into the system from the walls. A two dimensional translation stage is constructed and used to fix the position of the sample tube in reference to the optical table. Fig. 4.36 shows a picture of the installed construction.

The setup with the third clamp, together with its damper inlet can be seen as well as the translation stage construction located at the optical table. This is due to the fact, that a mounting to the walls may increase the vibrations. Stability measurements performed with an emptied tube show no evidence for vibrations, which affect the optical table and motivates the decision. The usage of the new clamp changes the free pendulum mounting to a fixed sample tube. This affects the system in a way, that the automatic readjustments after perturbations are difficult, but mechanical motions of the sample tube are suppressed, which stabilizes the system during measurements.

Another possibility to restrict mechanical movements is the change of the filling tube material. This can be done by using materials, which are compatible to the sample liquid, like silicon tubes. Unfortunately, these materials are too porous and as a consequence, the LAB sample can diffuse from the inside to the outside of the filling tubes within a short time. Therefore, only the air exhaust tube can be changed to silicon material permanently. As other materials are currently not characterized in reference to their chemical long time compatibility to LAB, PTFE is still in use for the inlet filling tube.
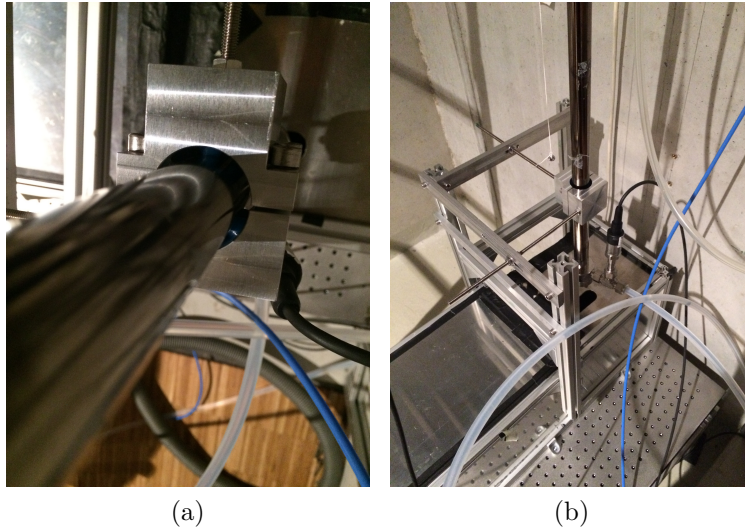
(a)   (b)

Figure 4.36: Pictures of the setup after installing a third fixing clamp and its trans-
lation stage construction on the optical table from the top (a) and in
a side view in (b). The clamp has a damper inlet holding the sample
tube without direct contact. The purpose of the clamp is to fix the
position of the sample tube perpendicular to the deflection mirror and
to suppress mechanical movements during measurements.

After installing the ceiling cage, CCD holder and clamps, the sample tube has to be
adjusted perpendicular to the optical table manually and the beam spot has to be
readjusted on the cm sized sensor again. With a small pendulum, which is installed
at the ceiling cage as well, the sample tube is positioned perpendicularly (see 4.36
(b)). After the tube is located and fixed in reference to the optical table, the beam
adjustment can be performed with the translation stage of the optical table as a
first step. In a second step, the translation stage and screws of the deflection mirror
are used for fine tuning.
Measurements of the performed optimizations show, that fill height levels between
2.1 and 2.3 m can be measured precisely, which correspond to light path lengths
of about 20 cm through a medium. This is twice the length possible for measure-
ments with commercial UV/Vis spectrometers, but is not enough for the precise
determination of the attenuation length, needed in JUNO.

4.6.4 Restricting the beam size

Parallel to the optimization of the setup and damper materials for the suppression
and elimination of vibrational sources, the idea of a modified optical system is inves-
tigated. The idea of limiting the beam size is considered as vibrations and the focus
of the light beam affects its size, especially for small fill height levels. Therefore, the
beam is restricted by a small aperture to a diameter, which is smaller than the light

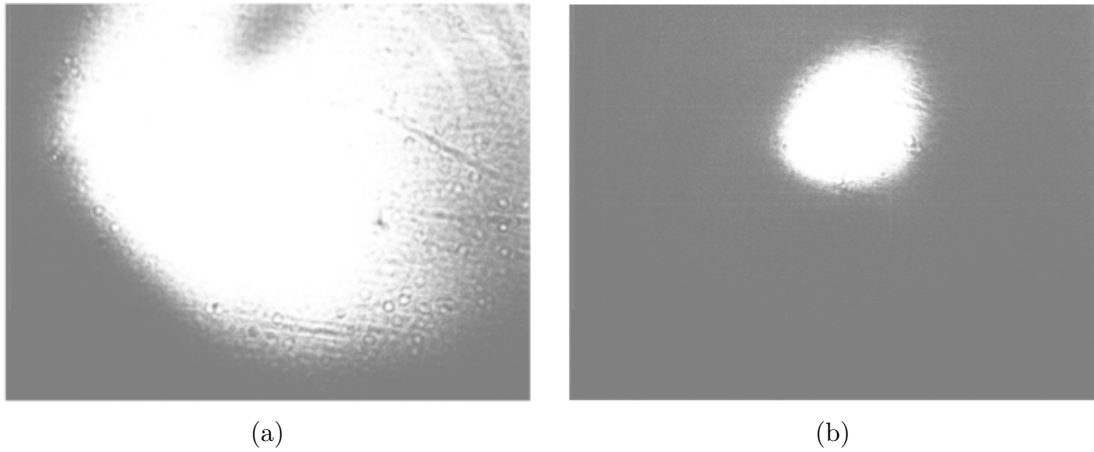(a)   (b)

Figure 4.37: Raw sensor pictures with increased contrast settings at a wavelength of 530 nm and a fill height level of approximately 2 m before (in (a)) and after (see (b)) changing the aperture to a smaller size. It can be seen, that the resulting beam shape before changing the optical component is illuminated in-homogeneously and shows reflections as well as a large part of the beam not detected by the sensor. After applying the optimization, the resulting beam (b) shows none of this distorted artifacts, but vibrational perturbations.

sensor, despite the effect of vibrations. The light beam passes the monochromator exit slit and is focused by a mirror system to a point in a distance of several meters. An aperture is installed after the mirror system to limit the beam shape to a size smaller than the deflection mirror, at which the light is coupled into the sample tube, but also leads to a decreased intensity. Fig. 4.37 shows a test series to investigate the influence of the restriction on the sample measurements at a fill height level of approximately 2 m and a wavelength of 530 nm. Plotted is a picture before (a) and directly after (b) installing the smaller aperture with increased contrast settings for better comparison. Before changing the optical component, the detected light beam has a similar size as the sample tube entrance window. This leads to unpredictable effects on the light beam, which are caused by the moving entrance window of the sample tube. A consequence is an in-homogeneously illuminated beam shape, which is further affected by the occurrence of vibrations. Reflections of parts of the increased beam shape at the tube walls are a consequence, too. After changing the aperture (b), the beam stayed small enough for adjustments on the sensor, not showing inhomogeneous parts or reflections any more. The usage of apertures with diameters of 1 to 5 mm enables the setup to measure longer light paths through the medium without sufficient intensity losses, making precise attenuation length measurements possible.

To investigate the influence on the maximal light path through a medium, where measurements are possible without sufficient intensity losses, several test measure-
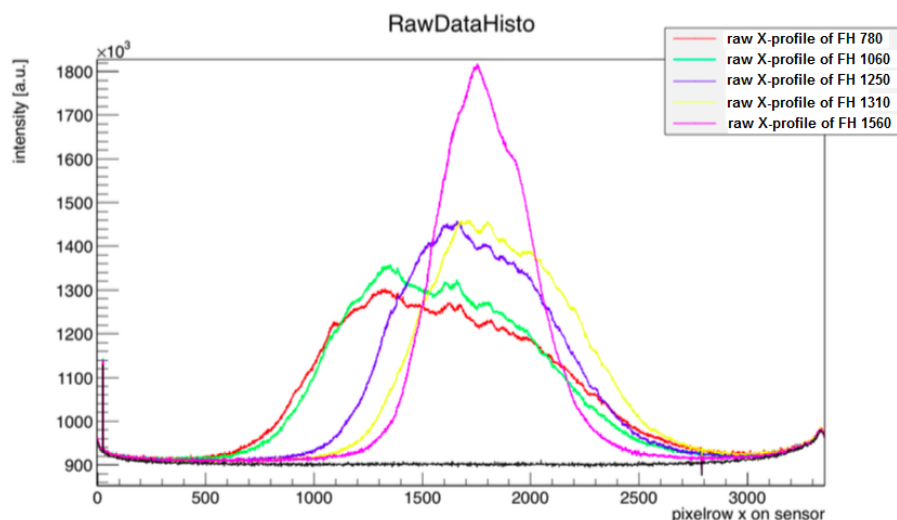
Figure 4.38: Uncalibrated and unprocessed intensity distributions without a dark noise correction, plotted for different fill height levels, which are given in channels. From the two dimensional intensity sensor histograms, one dimensional intensity distributions of the light beams are calculated, showing the intensity distribution detected over the x axis in pixel rows. The colors correspond to different fill height levels, except the black curve, which is the dark noise for comparison. The uprising dark noise at the edges is due to pixel gain factor differences and not due to ambient light. The sharp peak at around zero is due to a damaged pixel row. The distributions show the broadened beams, which can be adjusted completely on the CCD sensor.

ments are performed after the optimization.

Therefore, raw data pictures are taken for different fill height levels of the PALM setup as well as dark measurements. The two dimensional sensor pictures are used to generate one dimensional intensity histograms. For this, the intensity over one dimension is integrated to obtain the intensity distribution of the light beam. Such, so called intensity profiles[8], are shown in fig. 4.38. Several test pictures are taken for different fill heights and their corresponding intensity distribution against the pixel rows in x dimension can be found in different colors. The intensity entries are integrated over the y dimension and the corresponding intensity distribution is given in arbitrary units and depend on the pixels in x direction of the sensor. The size of the sensor in x direction is 18 mm. The figure show the uncalibrated and unprocessed summarized intensity values, which are plotted in different colors for the fill height level, given in channels. The black curve corresponds to the dark noise measurement, showing an increase on the sides of the sensor. These can be explained by the missing pixel gain calibration and is not due to parasitic ambient light. The sharp peak at around zero is due to a damaged pixel row, which is excluded in the

---

[8]A more detailed explanation on the intensity profiles can be found in section 5.1.2.

data processing. The plotted fill heights correspond to filling levels between 1.15 m (780 ch) and 2.26 m (1560 ch). It can be seen, that the intensity distribution of the beam for a fill height of 2.26 m shows a focused, almost undistorted light beam. With decreasing fill height levels, the intensity distribution is getting broader, its peak height is decreasing because of the focus and present vibrations. Furthermore, it shows that the beam shape can be centered and the tails of the distributions can also be located on the sensor. This demonstrates that precise measurements of attenuated intensities for light paths of at least 1 m through the sample medium are possible, enabling the PALM setup to proceed[9].

4.6.5 Changing the resonance frequency of the system

Taking into account a simple model of an oscillatory system (see equation 4.12 in section 4.6.1), which is excited by an external periodic force, the resonance frequency of a one dimensional oscillation depends on mass and damping characteristics as well as the restoring force constant. For an increasing mass $m_{new} = m \cdot p$ the resonance frequency of a one dimensional, forced, damped, simple oscillation model can be changed to other frequencies

$$\omega_{\text{res}}^{\text{new}} \approx \sqrt{\frac{1}{p} \cdot \omega_0^2 - 2 \cdot \frac{c^2}{(2m \cdot p)^2}} \tag{4.16}$$

It is clear, that for a complex, more dimensional oscillatory system the dependencies between frequency, mass, damping constant and restoring force constant are different. The PALM experiment is a more complex oscillatory system, and the idea of changing the resonance frequency of the setup by changing the mass is investigated to influence the occurring vibrations. Because of its construction, it is rather difficult to decrease the mass of the experiment, except for removing the sample volume. Assuming a dependency between resonance frequency and mass of the system, increasing the mass to higher values may shift the resonance frequency of the experiment to other regions, which would amplify other in-coupled frequencies. This can be used to suppress the observed dominant perturbations. Changing the fill height level also affects the mass of the system and shifts the resonance frequency, too. To stabilize the resonance frequency of the system, additional correction masses can be added to correct the mass change from the filling process. For this purposes, a damping mass tube is designed and manufactured and can be found in fig. 4.39. The tube is produced from brass and can be parted in two for an easy installation. With screws it can be mounted and is pressed firmly to the sample tube. The weight tube adds not only mass to the system, but also changes its center of mass and can be placed on each spot, investigating the influence on the vibrational mode. Due to its mass of approximately 18 kg, it doubles the mass of the tube system. To stabilize the resonance frequency of the setup for changing fill height levels, it is possible to

---

[9]A detailed determination of the maximal light path is shown in section 5.1.3 after applying several other optimization steps.

Figure 4.39: Picture of the manufactured damping mass tube. The massive tube can be separated into two parts to position it around the sample tube. With screws, both parts can be connected together, pressing firmly against the tube. The damping tube has a weight of approximately 18 kg, which can be increased by mass add ons, mountable to the damping tube with additional screws.

install additional masses to the damping tube, mountable with screws. This mass add ons can be used to further shift the resonance frequency, but also to correct the mass differences from filling by adding the exact mass difference to the system. In principle such a customized mass difference correction device could be a bottle of water or sand, its weight equal to the removed liquid.

First test measurements are performed with the installed damping mass tube, where it is placed at different positions along the whole sample tube. There is a hint, that the installation of the mass tube at the bottom of the sample tube may increase the distorted beam shape, whereas other tests showed hints for a decreased influence of vibrations by placing the device on top of the sample tube, but these could not be reproduced reliably. Also hints for a decreased influence of neighbored pumps are found. Unfortunately, the start of the constructional work at the same time changed the surroundings significantly. This makes it difficult to reproduce the measurements under same conditions and to compare the results with the former state of the experiment. Further investigations have to be made to clarify the influence of the damping mass tube.

4.6.6 Decoupling the sample tube from the storage tank system

To eliminate the filling tubes as a potential point of in-coupling, an express decoupling device is installed, separating the sample tube inlet from the storage tank.

Figure 4.40: Express decoupling device installed between sample tube and filling tubes to separate both systems during measurements. Decoupling the sample tube from the filling system, possible perturbations originating from the subsystem can be eliminated.

This separation is supposed to eliminate vibrations, which are coupled into the system by the wiggling of the filling tubes or storage tank as well as movements of the liquid, resulting in fluctuations of the filling level. Fig. 4.40 shows the installed express decoupling device. The separation should disable in-coupled perturbations originating from the wiggling of the filling tubes, the storage tank and its liquid volume for less vibrations. The device is connected to both parts of the PTFE filling tube and can be parted. First tests show, that the decoupling device has a huge setback during the (de-)coupling process, which is transferred to the sample tube because of the rigidity of the PTFE tubes. This setback forces the sample tube and its mounting clamp, together with its adjustment construction out of position, making time consuming re-adjustments of the system in reference to the optical table as well as the fine tuning of the beam spot on the CCD sensor necessary for each decoupling process.

Fig. 4.41 shows exemplary test measurements during an offline climate system, performed to determine the influence of the express decoupling device on the setup for a connection process. In (a) the adjusted intensity beam spot on the sensor can be seen for disconnected systems. The colors correspond to the measured intensity in a logarithmic scale. It can be seen, that the beam shape is focused and shows small distortions due to present vibrations, which can be neglected. In (b) the same intensity beam can be seen after connecting the sample tube to the filling system again. The setback of the decoupling device during connection is transferred to the sample tube via rigid PTFE tubes and forces the sample tube out of its position. Because of the change of the location of the sample tube in reference to the optical table, beam distortions and dislocations can occur, as can be observed in (b). As a consequence, each coupling process leads to a dislocation of the sample tube, which has to be corrected by time consuming re-adjustments and fine tuning of the
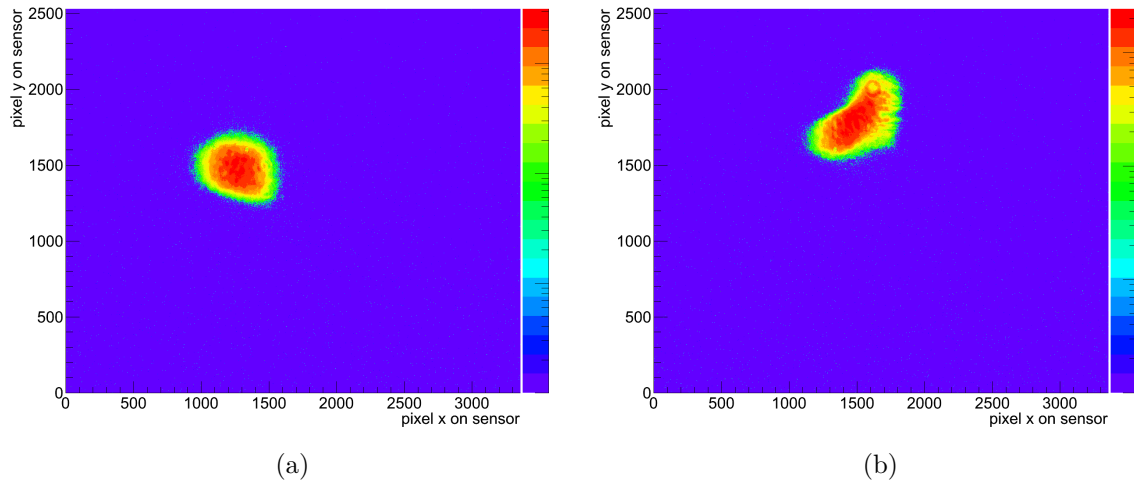
Figure 4.41: Test measurements to investigate the influence of the decoupling of the sample tube and its filling system during an offline climate system period. Both pictures show the colorized intensity in a logarithmic scale. In (a) the intensity beam of the disconnected filling system can be seen. The beam shape stays focused and almost undistorted, although small vibrations are still present. In (b) the same beam spot is shown, but after connecting both systems again. It can be seen that the beam position changes and the shape is distorted, due to the impact of the coupling process. Comparing both beam shapes, there is no hint for a reduction of vibrational distortions.

(a)   (b)
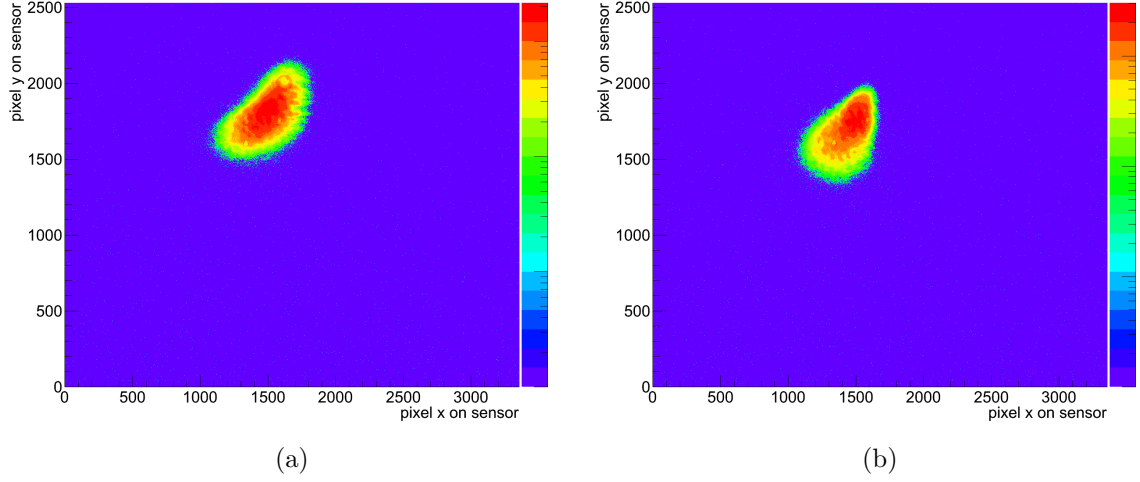
Figure 4.42: Measurements to test the influence of the disconnection on the setup.
In (a) the intensity beam for a connected sample tube to the filling
system is shown. The beam shape is distorted due to a dis-adjustment
of a former connection process. In (b) the same beam spot can be seen,
but after disconnecting both systems. It is found, that the mechanical
setback of the device dislocates the sample tube and the beam spot. A
significant reduction of occurring vibrations is not found.

position of the beam spot on the sensor afterwards. A reduction of the present
vibrations can not be observed. Fig. 4.42 shows the influence of the device on the
setup for the case of a decoupling process for an offline climate system. In (a) a
beam spot can be seen for decoupled sample tube and filling system. The visible
distorted beam shape results from a mechanical dis-adjustment of the sample tube,
which originates from a connection process several minutes before. In (b) the beam
spot can be seen, but after the disconnection of both systems. The change in the
beam position can be explained by the mechanical setback. Comparing connection
and disconnection process, it seems that the connection process affects the system
more than disconnections. It is not clear, if the beam distortions can be reduced
by the disconnection of both systems. Therefore, the effect of the express decou-
pling device and its influence on the system is investigated for present dominant
perturbations and exemplary results can be found in fig. 4.43 for an online climate
system. In (a) a characteristic beam spot with present dominant vibrations can
be seen for connected sample tube and filling system. The beam is centered on
the sensor and distorted compared to the beam shown in fig. 4.41 (a). For better
contrast, the measured intensity is colorized and plotted with a logarithmic scale.
Disconnecting both systems, it can be seen in (b), that the beam is not reducing its
distorted beam size to the expected, almost undistorted beam shape for an offline
climate system. This is a hint, that the point of in-coupling is not located at the
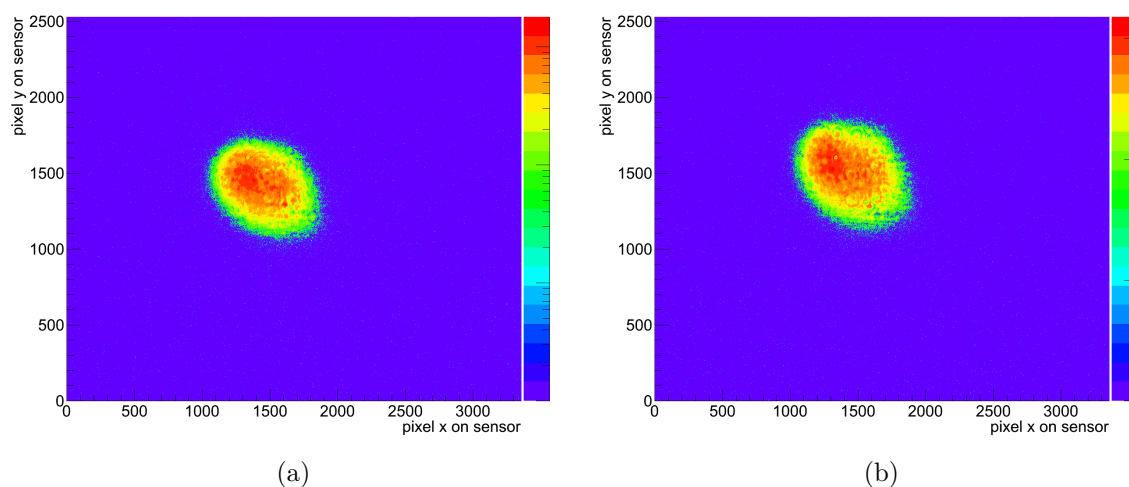
Figure 4.43: Test measurements to investigate the influence of the express decoupling device on the occurrence of the dominant vibrations. In (a) the beam spot for a connected sample tube and filling system is shown, whereas in (b) the systems are disconnected. The colors correspond to the measured intensity, which is plotted with a logarithmic scale. It can be seen, that the beam distortions look similar. Due to the mechanical setback of the device, the beam changes its position.

filling tubes, although wiggles or liquid movements in the storage tank can influence the measurements. Several tests reveal similar results and an improvement of the measurement situation has not been found. Summarized this means, that although filling tubes and the storage tank as well as its liquid can move and may couple perturbations into the sample tube, a characteristic change of the beam distortions is not found.Taking into account the setback, the necessity of time consuming re-adjustments after each use of the express decoupling device, the loss of liquid during each decoupling and the fact, that no improvement can be seen for the beam shape, the express decoupling device is not used for the sample measurements.

Instead of the usage of the device, the closing valve of the storage tank can also be used to decouple liquid movements within the storage tank from the sample tube. Due to the fact, that a direct connection between the filling tubes and their movements and the sample tube are given, this will not eliminate the possible point of in-coupling. Further investigations are needed to check the chemical long term compatibility of alternative materials to replace the remaining rigid PTFE filling tube.

4.6.7 Suppressing liquid movements

Another approach to handle the vibrational occurrence is the idea to flatten the moving surface. Due to the moving surface of the sample liquid, the traversing light beam is refracted to different directions at the boundary surface between liquid and air. This can affect position, illumination and size of the beam. The idea is to flatten the surface of the liquid to suppress its movements. The created flat boundary surface is perpendicular to the light beam and stable over time and makes time consuming re-adjustments unnecessary for changing external perturbing forces. Such a flattening can be achieved on the current setup by filling the sample tube to its upper exit window. Because of the construction of the sample tube and filling mechanism this is not possible and would reduce the possible measurable filling level to a single height. Therefore, a new device has to be installed in the tube, which can be positioned at the boundary surface of the filling level. It has to move with changing fill heights and at the same time is transparent for the traversing light beam. A possible realization is the usage of a floating gauge on top of the liquid. Due to its weight, it will immerse to a certain depth into the liquid. Because LAB is a petroleum derivative and is used as a sample, the density of the ideal gauge has to be smaller than the density of LAB to swim at the surface. Furthermore, it should be manufactured from materials, which allow to measure the wavelength range between 370 to 1,200 nm and have to be chemically compatible at the same time. To access the UV region, the floating gauge has to have a window made from materials like quartz glass, which has a rather high density compared to LAB. The positioning of the device at the surface of the sample is difficult, as well as its position stability over time. Up and down movements of the floating gauge at the surface as well as a small angular displacement would cause huge effects on the light beam position on the sensor. The designed floating gauge is manufactured from PTFE and can be seen in fig. 4.44. It is a tube with very small wall widths to reduce weight and to not affect the traversing beam spot. On one end, an acrylic glass window is glued to the PTFE tube with epoxy resin for a first check of the working principle of the gauge. The choice of an acrylic glass as boundary surface limits the accessible wavelength region of PALM, but may improve the current measurements. The gauge tube will have a length of at least 3 cm and bars at its outer surface. These bars and the length is used to guide the gauge within the tube. On the one hand this will suppress tilting within the tube and on the other hand it will help to stabilize the gauge over time. Fig. 4.45 shows a scheme of the inserted floating gauge in the sample tube. Inserting the new device, the attenuated light beam crosses the acrylic window, before being detected at the light sensor. The immersed acrylic window is in direct contact to the liquid and eliminates influences of a moving surface.

To investigate the benefit of the floating gauge, it is inserted on top of the sample tube. Unfortunately, the gauge get stuck several times at several positions within the stainless steel tube, although the dimensions are rechecked. This leads to the fact that the diameter of the stainless steel tube has much bigger manufacturing uncertainties than expected. The reduction of the dimensions of the gauge can not

Figure 4.44: Picture of the manufactured floating gauge. The gauge is made of PTFE for its density and chemical compatibility with LAB. An acrylic window is glued on one end of the tube with epoxy resin, where the light beam has to traverse the gauge. Small bars are manufactured at the outside surface of the gauge for guidance and stabilization within the sample tube.
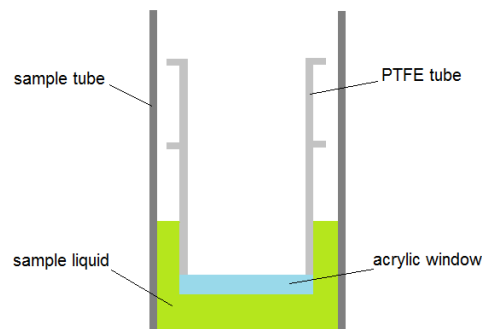

Figure 4.45: Scheme of the working principle of the floating gauge in the sample tube. The gauge is placed on top of the liquid and will immerse to a certain depth. Bars on its outside and its length guide the device along the sample tube and stabilize its position. The attenuated light beam crosses an acrylic window, which is glued on one end of the device.

solve the problem to get stuck because the tube seem to be not straight over its full length, too. A further reduction of the diameter and the length will increase the position instability within the tube and enables the gauge to tilt or rotate within the tube. Furthermore, occurring external shocks may also cause the gauge to move up and down but also to wedge within the sample tube. Another problem arising is the longterm compatibility of epoxy resin with LAB, which is not known, as well as the current limitation of the wavelength.

For further investigations, it has to be determined in which degree the gauge overcomes its shortcuts and brings advantages to the system. As PALM is a customized UV/Vis spectrometer, also the UV range should be accessible, which is possible by using fused silica materials. But due to the density differences between petroleum and fused silica, the floating gauge would immerse (almost) completely into the liquid in its current dimensions, which may be a problem with respect to occurring external shocks and may immerse it completely. The usage of a window adds several new surface boundaries to the light path of the beam, deflecting it even further due to different refractive indices.

The scaling to a longer version of the gauge will limit the maximal reachable fill height because of the construction of the flanges and sample tube system. Furthermore, without the usage of a honed steel tube, it will get stuck in the tube or will be too loose to guarantee stable measurements. As a consequence, the idea of using a floating gauge at the current sample tube is dismissed.

4.6.8 ViPi – vibration identification device

For a more sophisticated and reliable determination of the frequencies contributing to the perturbations, a portable acceleration measurement device is constructed. The portable device uses an acceleration sensor, which is able to measure the acceleration amplitude for three dimensions simultaneously. The chip has a three axis gyroscope function, too. A raspberry pi [Ras18] computer is used for the data taking and processing, reading the data from the sensor via I^2C. Fig. 4.46 shows the sensor and raspberry pi computer. The sensor is mounted to a base plate, fixing its position in reference to the plate. The base plate can be placed at locations or places to investigate the occurrence of vibrations. Due to its small size, the device can be placed also at small surfaces for measurements. The sensitivity of the acceleration sensor can be changed from $\pm 2\,g$ up to $\pm 16\,g$. First test measurements confirmed a sampling rate of $400\,Hz$, making it possible to determine frequency contributions from zero to $200\,Hz$ reliably (see equation 4.15 in section 4.6.2.), which is an improvement to the VibroChecker application. First measurements with the acceleration sensor are performed and an exemplary test is shown in fig. 4.47. The acceleration amplitude is measured over time in seconds, using the maximal sampling rate for determining frequencies up to $200\,Hz$. The measurement is taken at the power supply unit for the halogen lamp to investigate possible perturbation frequencies. With a fast Fourier transformation, the acceleration amplitude-time profile is transformed in an amplitude-frequency profile, identifying possible perma-
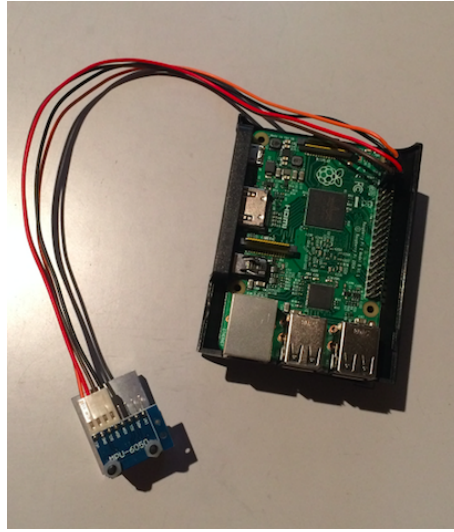
Figure 4.46: Picture of the built mobile vibration measurement device. The acceleration-gyroscope-sensor is mounted to a base plate to guarantee solid contact to the surface for measurements. For data acquisition, a raspberry pi is used, taking data from the sensor via I²C.

Figure 4.47: Acceleration amplitude measurement of the x-dimension over time with the ViPi device. The sensor has a sampling rate of $400\,\mathrm{Hz}$, which enables to resolve perturbation frequencies up to $200\,\mathrm{Hz}$ reliably. The device is placed at the power supply unit of the experiment.

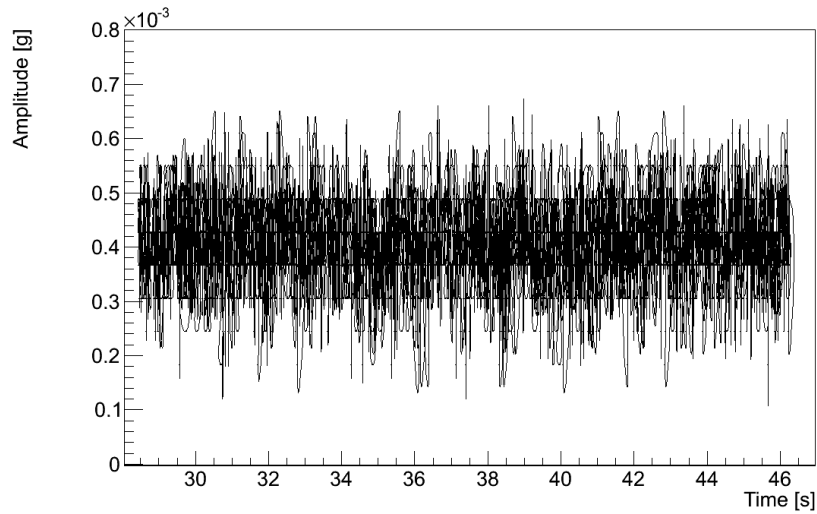nent perturbation candidates. Systematic uncertainties have to be investigated like calibration, a nonlinearity behavior, temperature dependent fluctuations or instabilities of the device. The manufacturer considers an initial calibration tolerance of $\pm 3\%$ and a nonlinearity behavior of 0.5% [Inv13]. A housing is manufactured to guarantee a solid, flat contact to the measurement surface for reproducible measurements.

Before an appropriate vibration investigation is performed with the device its reliability has to be tested. As the results found for the CCD sensor and its cooling system are measured with the VibroChecker application, measurements under similar conditions should be performed to compare the results. Furthermore, the device should be tested in a surrounding with well known or even without occurring vibrational frequencies to testify its performance. For future measurements, also the gyroscope of the sensor can be used to determine angular positions and possible changes, which would provide data for a better understanding of the present vibrations, as well as the absolute position of the sensor itself. This can help to identify possible mechanical changes, too, which may be visualized and monitored by computers.

4.6.9 Further ideas and outlook

Due to the ongoing constructional work and the change in the surrounding conditions of the laboratory, it can not be excluded, that at some point, also perturbations are observed, which influence the optical table. Therefore, the idea of decoupling the experiment from its surroundings is considered. In the case of the sample tube, such a decoupling device can be used to shield the tube from excitations and at the same time suppress its oscillation amplitudes. The sample tube can be damped over its full length to suppress the vibrational modes and to eliminate the contact to the excitation points. This can be done by placing the sample tube into a much bigger tube, which will be filled with damping material. A promising and cheap candidate is the usage of sand. For PALM the space at the experimental site is rather limited and the application of such a device has to be designed for a vertically mounted tube. Therefore, the idea of a bigger tube filled with sand and the sample tube placed in its center is considered. The sand damping tube is placed above the optical table. It is crucial to prohibit damping material to enter the optic. A suggestion how to realize a sealing can be found in fig. 4.48. The bottom of the damping tube is closed by an aluminum plate, which is mounted with screws. The plate has a hole in its center, where the sample tube can be installed. With a special elastic polymer plate, a seal is constructed and can be placed between the damping tube and its bottom plate. This polymer plate has a hole in its center, but with a much smaller size than the diameter of the sample tube (and its lower entrance flange). The elastic polymer plate is put over the sample tube during its installation, pressing tight against the walls of the sample tube and sealing mechanically the contact between tube and polymer plate. With a clamp, the seal is fixed and supported against the weight of the damping material to not open with time. Due to the fact that for this length
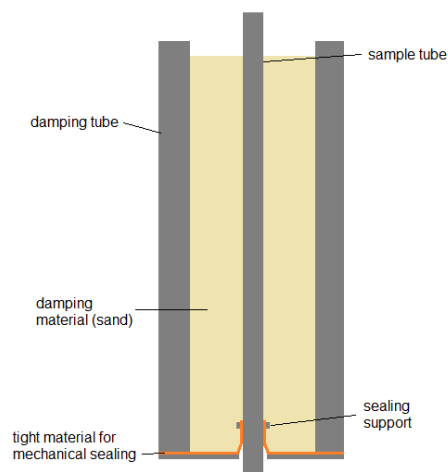
Figure 4.48: Scheme of a sealing for the damping tube. A polymer plate is used to seal the damping material from falling into the optical system underneath. The plate has a hole in its center, which is smaller than the diameter of the sample tube and is pulled over it. Due to the weight of the planned damping material, a support clamp should be used for safety.

the total weight of the chosen damping material is rather heavy, it is also discussed to part the damping tube in several smaller modules, guaranteeing that the seals withstand the weight with time.

The optical table can be placed at a decoupling device, which consists of a steel plate, placed within a steel bin. The bin is placed on dampers itself. Between steel plate and bin, several decoupling devices are installed, whose material may differ for the observed perturbations. Such devices can be springs, sand or customized decoupling devices. A scheme of the installation solution for the whole setup is shown in fig. 4.49.

Furthermore, the usage of a bigger CCD sensor is under consideration, enabling the measurement to detect beam sizes bigger than the current sensor size of 13 mm times 18 mm. An advantage is a much easier detection of the intensity of distorted beams. The new CCD sensor device has to be calibrated as well as investigated for broken pixels and replaces the older device. Due to the bigger size, the intensity loss at the edges of the sensor for distorted light beams decreases, leading to a further decreased measurable liquid fill height level. It would be possible to monitor the whole area of the sample tube, which would make adjustments much easier. But it will not solve the problem of focus and vibration induced beam broadening at all, as the beam shapes are increasing with lowering filling levels to a size, that, although centered on the sensor, parts of the beam are reflected at the walls of the stainless
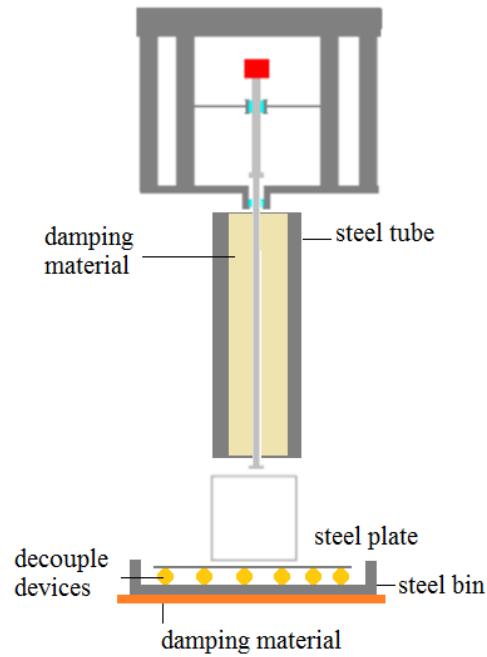
Figure 4.49: Suggestion to completely damp and decouple the experiment from its surroundings. The sample tube is placed within a much bigger steel tube and filled with sand as damping material for suppressing vibrations and shielding it from excitations. The optical table itself is placed at a decoupling device, too.

steel tube. These reflections are still present and will distort the measurements, unless a sample tube with a bigger diameter is used.

4.7 Performance of the optimized setup

Different approaches are studied to suppress the present vibrations and several optimizations are realized on the experiment. The optimized setup contains

- the ceiling mount,

- three clamps for a fixed sample tube position in reference to the optical table,

- the decoupled CCD holder,

- the installation of the damping weight tube,

- a small aperture before the deflection mirror,

- the installation of a fabric as an additional dark box.

With these optimizations, the performance of the experiment is tested with respect to influences of external perturbations. First, the effect of the climate system is investigated by several starting and stopping cycles. Therefore, measurements are taken over a time period of approximately half an hour each with and without a running climate system. Fig. 4.50 shows raw data pictures with increased contrast settings, taken during the starting cycle of the climate system. Plotted is the same adjusted light beam during the offline phase (see (a)) and after starting the climate system (in (b)). During the offline mode, the intensity beam shows a focused beam shape over the whole period, but small vibrational distortions remain. In (b) the same light beam spot is shown, but approximately five minutes after starting the climate system. It can be seen clearly, that a beam distortion is taking place, increasing the diameter of the beam drastically. Because of their constant presence, the distorted beam shape is not changing over time significantly. The influence of the climate system can also be reproduced during shut down processes, as can be seen in fig 4.51. The comparison between the beam shapes with (see (a)) and without (b) an online climate system shows, that the dominant source of perturbation could not be eliminated with the optimizations but the distorted beams can be centered almost completely on the sensor for fill height levels around 1.2 to 2.0 m
To determine a possible perturbation frequency after applying the optimizations, acceleration-amplitude measurements are performed again, using the top of the installed damping mass tube as contact point. A resulting amplitude-frequency profile can be found in fig. 4.52. The damping weight tube is mounted at a height of 2.4 m in reference to the entrance window of the sample tube. The acceleration-amplitude measurements described in 4.6.2 are used to search for differences after applying all optimizations. Note that these measurements are done with a freeware app and

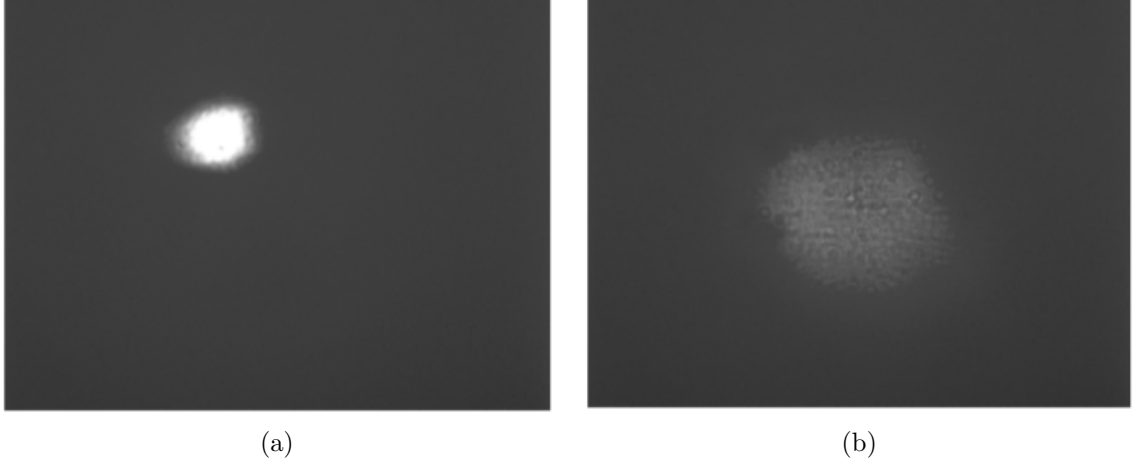(a)   (b)

Figure 4.50: Raw sensor measurements to investigate the influence of the climate system on the optimized setup at a fill height of 2.3 m and a wavelength of 530 nm. In (a) the light beam during the offline phase of the climate system is shown and in (b) the beam is plotted several minutes after the climate system is started. It is found for all tests that the beam size is distorting to the characteristic perturbed beam shape. Note that the contrast is increased for better comparison.

(a)   (b)
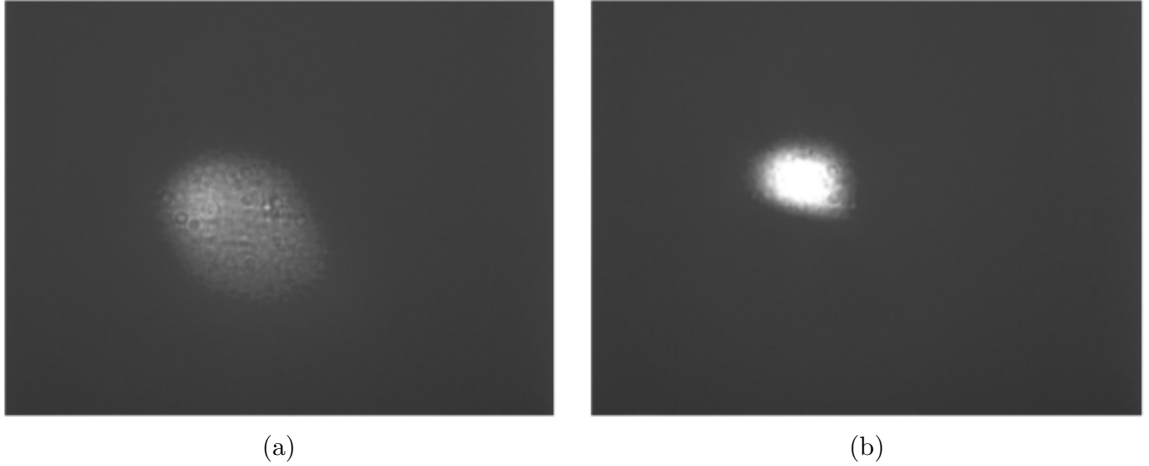
Figure 4.51: Test measurements to investigate the influence of the climate system on the optimized setup with increased contrast settings. In (a) the intensity beam at a fill height level of 2.3 m and a wavelength of 530 nm with an online climate system is shown, whereas in (b), the climate system has been switched off several minutes before. The effect found in fig. 4.50 can be reproduced.
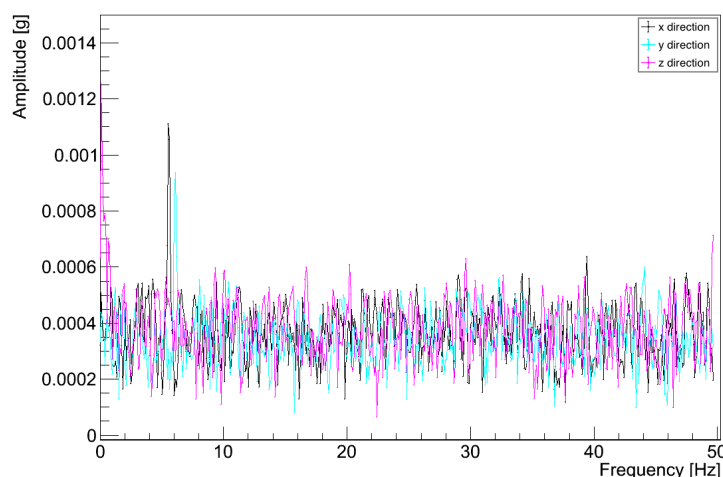
Figure 4.52: Corresponding amplitude-frequency profile from acceleration measurements over a time period of 10.2 s to identify changes for the optimized setup with a freeware app. Measurement point is on top of the installed damping weight tube, which is in direct contact to the sample tube. For all measurements, a perturbation frequency between 5 to 6 Hz is visible.

the acceleration sensors of a mobile phone. Furthermore, no statistical nor systematic uncertainty is given and no baseline correction is done. These measurements are only meant as a first check. Plotted are the calculated Fourier coefficients in arbitrary units against the frequency, which are determined from acceleration-time measurements. For all test measurements, a perturbation contribution between 5 to 6 Hz can be identified, which is not observed for measurements without the damping weight tube. Also contributions at around 1 Hz occur randomly and there are hints for contributions at 50 Hz.

Summarizing the results obtained in this chapter, the climate system is identified as the dominant perturbation source, which causes dominant vibrational perturbations on the measured beam shapes. Decoupling the sample tube from the filling system show no clear evidence for an improvement of the beam sizes and implies, that either a local excitation from the climate system at this point is not taking place or another point of in-coupling exists. Tests of vibration measurements imply, that the omnipresent perturbation frequency is above 50 Hz. After the optimizations, a perturbation frequency between 5 to 6 Hz is found and the optimized CCD holder and damping materials show a good performance compared to the perturbation frequency results found before their installation. The climate system can not be switched off for longer time periods, which would be needed for measurement series. The optimization of the optical setup limits the beam spot to a size, where it is able to perform precise intensity measurements for light paths up to 2.0 m, although there are vibrational perturbations present. With this improved setup, first sam-

ple measurements can be performed. Due to the influence of the vibrations, their contribution to the systematic uncertainties has to be investigated very precisely.

5 Optimized PALM setup

As described in chapter 4, the PALM setup is optimized to enable sample measurements. A new ceiling mount with specialized translation stage clamps and optimized damping materials is installed. Also an optimized CCD camera holder is applied for perturbation elimination. Although it is not used during the following sample measurements because of its shortcomings, an express decoupling device is installed between the sample tube inlet and the filling tubes. A PTFE filling tube is used to connect sample tube and storage tank. A damping weight tube is mounted to the sample tube to influence the resonance frequency of the whole system. To increase the measurable light path length through the sample medium, a smaller aperture is installed. With this optimizations, sample measurements are performed and the results can be found in this chapter.

5.1 Characterization of the optimized PALM setup

To investigate systematic uncertainty sources, the optimized setup with a filled sample liquid is tested for time fluctuations again. Furthermore, several test measurements are performed to identify systematic uncertainties and possible error sources. For all measurements in this section, LAB from Egypt is used to compare the results with those found by [Hel15a].

5.1.1 Longterm stability of the experiment

After changing the components of the PALM setup for sufficient vibration suppression, another longterm stability study is performed. These measurements are used to determine possible systematic effects correlated to optic, sample tube, liquid and electronics. They are also compared to former longterm stability studies with an empty tube, which is shown in section 4.5.5. Fig. 5.1 shows a stability measurement for a current of $5.0\,\mathrm{A}$, a monochromator exit slit width of $2\,\mathrm{mm}$ and a fill height level
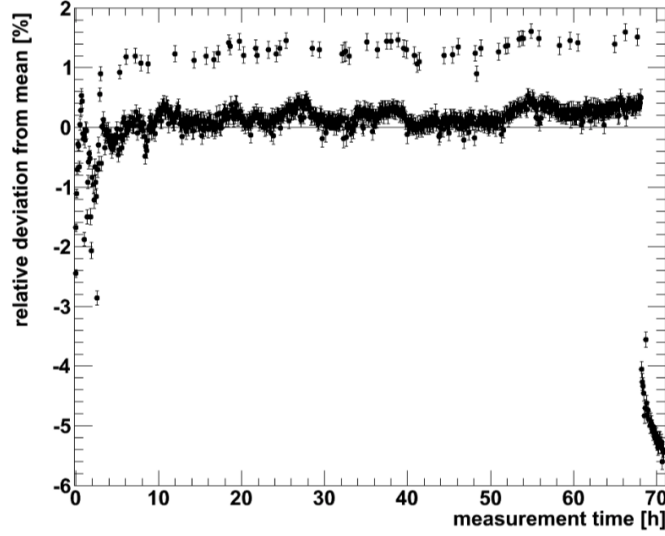
Figure 5.1: Sample stability measurement at a wavelength of 530 nm and a fill height
level of approximately 2.3 m, performed under similar conditions as the
empty tube stability measurements in section 4.5.5. Plotted are the
relative deviations from the mean intensity integral, measured over a
time period of 70 hours. After starting the halogen lamp at t=0 s, an
increase of the intensity between zero to ∼ 5 hours is visible, which marks
the thermalization time of the setup. The breakdown at 68 hours is
explained by an external mechanical shock, which forces the beam out of
its adjustment on the sensor. The increased outliers are due to exposure
time fluctuations.

of around 2.3 m at a selected wavelength of 530 nm over a time period of 70 hours.
Plotted are the relative deviations from the determined mean intensity integral. Af-
ter starting the halogen lamp at t=0 s, an increase of the intensity can be seen.
After a thermalization time of ∼ 5 hours, the relative deviations show small fluctu-
ations. Increased intensity outliers can be identified, which originate from exposure
time fluctuations caused by the internal mechanical shutter of the CCD device[1]. An
enormous breakdown of the intensity integrals can be seen after 68 hours of data
taking. This is due to an external mechanical shock coupled into the system, de-
stroying the beam adjustment on the sensor. The external shock originates from the
start of the constructional work of the physics department next to the underground
laboratory and has to be taken into account during measurement series as a crucial
systematic error source.
Fig. 5.2 shows a zoom of the stability study in fig. 5.1 for better comparison to the
measurement results with an empty tube, plotted in fig. 4.16. Within the given time
window, and neglecting the increased outliers caused by exposure time fluctuations,
the relative deviations are approximately 0.3 %. This is in good agreement to the

---

[1]These outliers are also visible for empty tube studies, as are shown in fig. 4.15
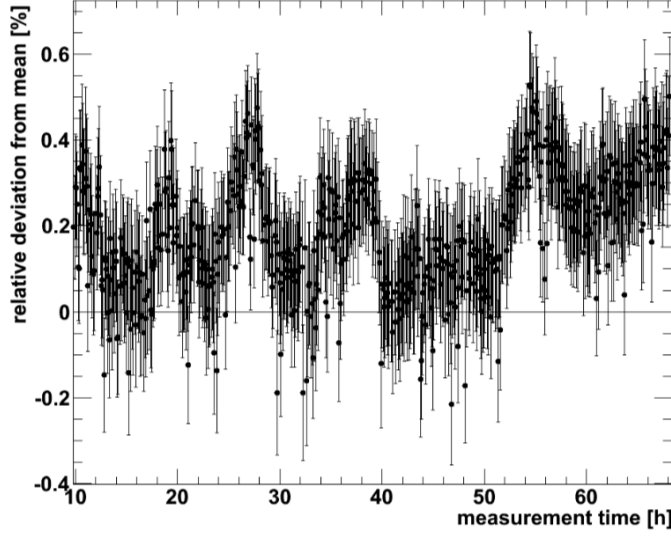
Figure 5.2: Zoom into the stability measurement of fig. 5.1. Plotted are the relative deviations from the mean of all intensity integrals within a time gate of 60 hours. After neglecting outliers correlated to exposure time fluctuations, the deviations show fluctuations of approximately 0.3 %.

results found for empty tube measurements, which are shown in section 4.5.5.

5.1.2 Identification of systematic uncertainties

During the test measurements with raw LAB incident intensity fluctuations of 0.25 % are determined. Several sources have been found during systematic uncertainty investigations and are taken into account:

Exposure time fluctuations

As could be seen in the longterm stability measurements, outliers with increased intensities are present. These can be identified to have increased exposure times in the order of 10 to 120 ms more than the selected one and are caused by the internal mechanical shutter of the CCD device. To eliminate the fluctuations of the exposure time, an exposure time correction is implemented. Assuming that the measured intensity is proportional to the exposure time, the intensity integrals I_{measured}, which show a deviation from the exposure time chosen $t_{\mathrm{exp-chosen}}$, are corrected with a correction factor:

$$I_{\mathrm{corrected}} = I_{\mathrm{measured}} \cdot \frac{t_{\mathrm{exp-chosen}}}{t_{\mathrm{exp-observed}}}. \tag{5.1}$$

Hereby, $I_{\mathrm{corrected}}$ is the processed intensity integral and $t_{\mathrm{exp-observed}}$ is the increased exposure time from the measurement.

Temperature fluctuations

Not only fluctuations in the exposure time can be observed, but sometimes also the internal cooling system of the CCD device shows deviations from the chosen temperature. The CCD sensor is cooled to -15 °C in order to suppress dark noise sufficiently. Fluctuations of ~ 2 °C change the dark noise and affect the determined intensity integrals. With a temperature cut, data sets with deviations in the sub-percent level from the chosen temperature are identified and excluded from the data.

Linearity deviations of the sensor device and pixel saturation

Although no deviations from a linear behavior of the sensor have been found by linearity tests [Hel15a], the sensor is used at its optimal working point during measurements. The highest detected raw intensity value is limited to 2/3 of the maximum detectable intensity for each single pixel. This is realized by optimizing the width of the monochromator exit slit and the exposure time. Furthermore, this eliminates the occurrence of a pixel saturation of single pixels at the same time, which would lead to a loss of intensity and would affect the attenuation length also.

Calibration uncertainty of the CCD sensor

The CCD sensor has to be calibrated due to different pixel gain factors. As single pixels have different gains, the intensity detected by a certain pixel is weighted differently and distorts the intensity integral. Therefore, a pixel-by-pixel gain calibration is applied [Hel15a], which means that for each pixel a calibration factor and corresponding uncertainty is determined and used in the offline analysis to correct the measured intensity integral. Comparing the sum of all calibration uncertainties to the sum of all measured intensity entries for a whole sensor picture, it is found that the sum of the calibration uncertainties is in the order of 10^{-4} times the measured intensity integral and is negligible.

Reproducibility of monochromator exit slit and wavelength selection

Another uncertainty which has to be taken into account is the reproducibility of the selected wavelength and monochromator slit width, which was already explained in section 4.5.4. A change of the wavelength as well as of the monochromator exit slit width within a measurement series will affect the incident intensity crucially and, thus, has to be avoided in any case. As both parameters are selected manually by a mechanical wheel, it is doubtful that re-adjustments and reproductions are very exact. To compare the measurements for different levels of the liquid, the wavelength as well as the monochromator exit slit width are not varied, eliminating these sources of uncertainties.

Systematic uncertainty of chosen wavelength

Not only the reproduction of the selected wavelength within a measurement series is taken into account, but also systematic uncertainties correlated to the chosen wavelength have to be considered (described in section 4.5.4). It is found, that the created monochromatic light shows a wavelength spectrum which depends on the exit slit width of the monochromator. Furthermore, the position of the peak of the wavelength spectrum is defined to be the selected wavelength. The FWHM of the spectrum is determined to be the uncertainty of the selected wavelength, which shows a correlation to slit width and wavelength selection. For the case of 430 nm, a combined uncertainty of 9 nm is determined.

Fill height sensor correlated systematic uncertainties and calibration

A calibration of the fill height sensors is performed and was already shown in section 4.5.3. The calibration parameters are determined to be:

$$y(p) = (0.00143 \cdot p + 0.03007) \text{ m}, \qquad (5.2)$$

with $y(p)$ the corresponding fill height level in m, and p the pressure difference in channels. A fill height uncertainty of 2 mm is used and also systematic uncertainty sources related to the sensor operation [Wik13], [Key17] are taken into account.

External mechanical shocks

As could be seen in the stability measurement in fig. 5.1, external shocks can be coupled into the system. This shocks force the sample tube out of its adjustment, moving the tube mechanically in reference to the deflection mirror. As a consequence, the intensity beam seems to change its position on the sensor and shifts to the sensor edges in most cases, where parts of the intensity are cut off. Such mechanical, external shocks can be identified clearly by the abrupt break down of the intensity integral. Another characteristic is the relaxation of the system afterwards, re-adjusting itself almost completely on the sensor in most cases. For data selection, either each single data set has to be checked manually or longterm intensity measurements can be used to identify beam shifts automatically, marking the time at which data sets have to be excluded.

Change of the superposition of vibrations

Test measurements show that the sum of perturbations, which are coupled into the sample tube are changing with time. This has an effect on the distortion of the beam shape and its resulting beam size and can be identified in fig. 4.28. The climate system changes the sum of the present perturbations into a new superposition of dominant vibrations. These broaden the beam size significantly and increase the possibility of intensity losses because of a limited sensor size. Due to the used focus, the initial beam sizes increase for decreasing fill height levels, too, making the

appearance of vibrations more problematic. After a change of the vibration mode, the beam has to be re-adjusted on the sensor and its size has to be checked for a possible loss of intensity each time. To limit the intensity cut off, a minimal filling level is determined, called critical fill height level, which is explained in section 5.1.3.

Shifts of the beam position

External shocks and vibration mode changes are effects, which change the system mechanically. A result of this are shifts of the initial beam position and changes of its shape and size. Such beam shifts can also appear by the change of filling levels, which make re-adjustments of the beam necessary for each level change. For identification, the two dimensional sensor picture can be used because it stores spatial information about the position and the intensity distribution of the light beam. From the two dimensional intensity histogram a one dimensional (1-dim) intensity distribution against each sensor axis can be calculated, showing the intensity distribution along each dimension. These are called x and y-intensity profiles in the following. Fig. 5.3 shows a typical two dimensional (2-dim) raw sensor histogram at a fill height of 0.5 m and at a wavelength of 430 nm, together with the corresponding x and y-intensity profiles. By integrating over one dimension of the 2-dim data histogram, the intensity distribution of the detected light beam over the second dimension can be calculated. On the left, the intensity profile for the y axis is shown, whereas on top, the x-intensity profile is plotted. The resulting distributions have a characteristic peak, where the center of the beam spot is located on the sensor. It can be seen, that due to distortions, the beam intensity distribution is asymmetrically distorted, and at the sensor edges intensity is lost. The intensity profiles can be used as powerful tools to identify occurring beam dislocations and shifts.

A shift of the centered beam towards the sensor edges induces an intensity loss. This loss can not be observed by eye during the data taking, but after applying the offline analysis tools. Fig. 5.5 shows two 2-dim raw sensor pictures with a present beam shift, colorized and with logarithmic scale of the detected intensity for better comparison. In (a) a measurement directly after the beam adjustments is shown, whereas in (b) the same beam spot is plotted after several minutes of data taking. A beam shift to the right corner of the sensor can be identified. The corresponding x-intensity profiles of the pictures can be found in fig. 5.5. Shown are the x-intensity profiles for the adjusted beam spot in (a) and the shifted light beam in b). It can be seen, that the adjusted beam in (a) shows a well centered intensity distribution, which is, compared to the beam shown in b), also smaller in width. In most cases, the beam is moved from the center towards the sensor borders. It can be seen, that an un-negligible part of the intensity is not detected due to the limited size of the sensor. This effect can also be found for the y-intensity profiles, which are shown in fig. 5.6 for completion. The influence of the shift can be identified for the y-profiles, making it necessary to take both dimensions into account for the intensity losses. Furthermore, the application of quality cuts can be used to identify beam shifts automatically and on the same time limit the intensity losses. These
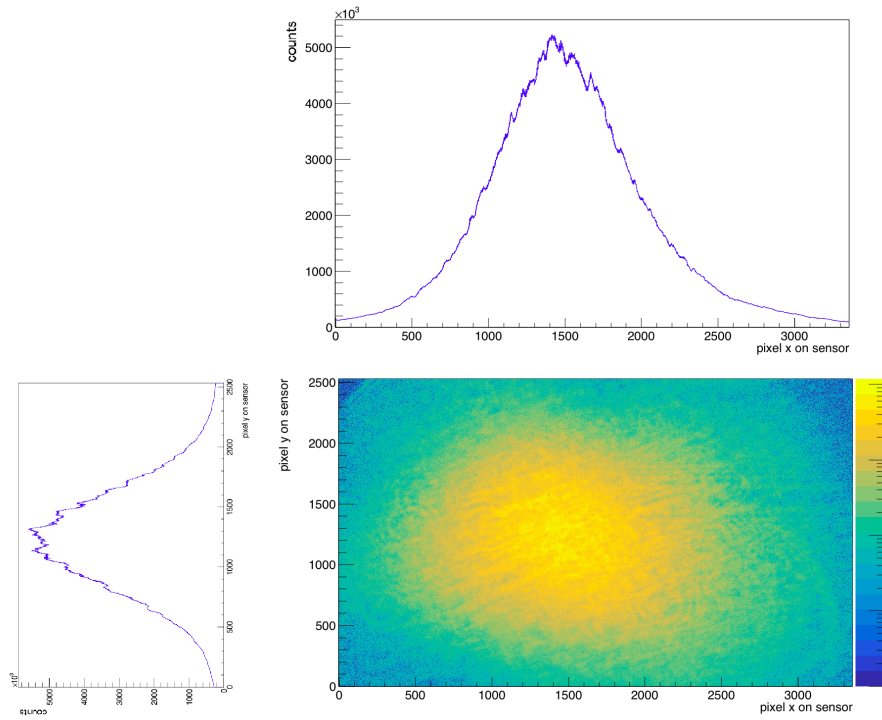
Figure 5.3: Raw 2-dim picture taken with the CCD sensor at a wavelength of 430 nm and a fill height level of around 0.5 m. The intensity profiles show the intensity distribution of the beam for each dimension and can be used for the identification of systematic uncertainties and error sources. The histogram on top shows the x- and the plot on the left the y-intensity profile.
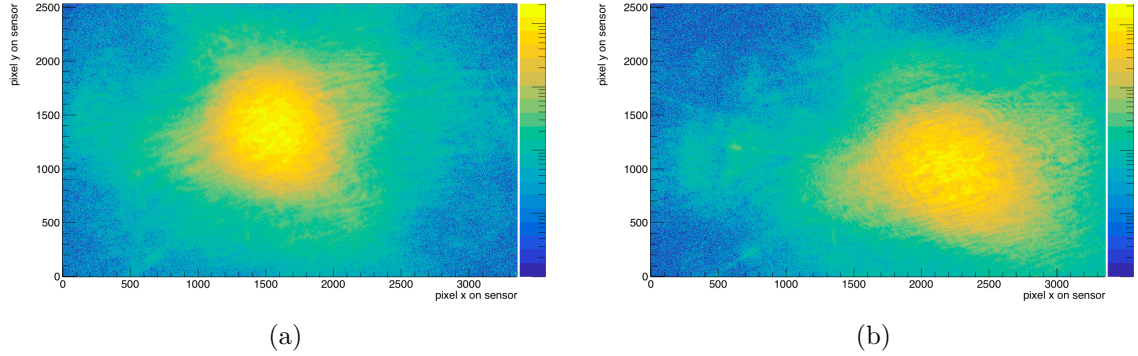
Figure 5.4: Raw sensor pictures with present beam shift and colorized logarithmic
           intensity scales for better contrast. In (a) the adjusted beam at the
           beginning of the measurement can be found. In (b) the same beam is
           shown, which started to wander off after several minutes. It can be seen,
           that intensity is lost at the edges of the sensor. In most cases, this can
           not be identified during measurements but after applying offline analysis
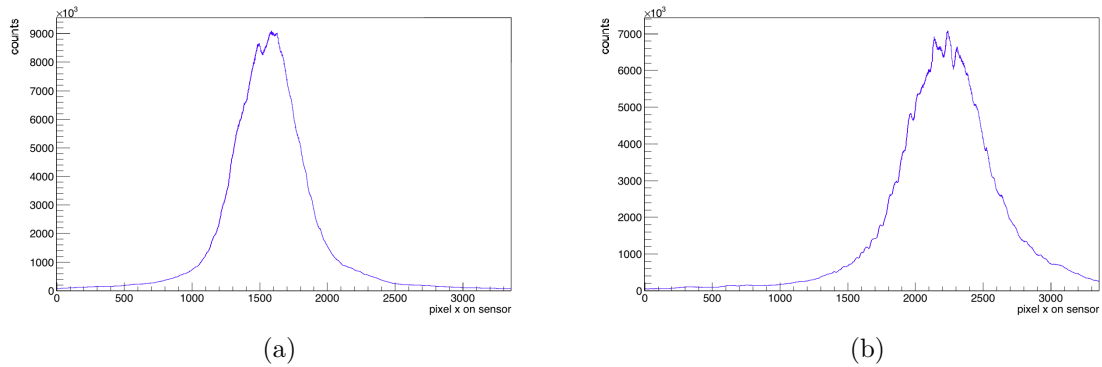   tools, like in this case.

Figure 5.5: X-intensity profiles for the measured beams shown in 5.4. It can be seen
           in a), that the adjusted beam is well centered on the sensor. In (b) the
           intensity distribution is shifted towards the right corner of the sensor and
           a part of the intensity is not detected any more, reducing the intensity
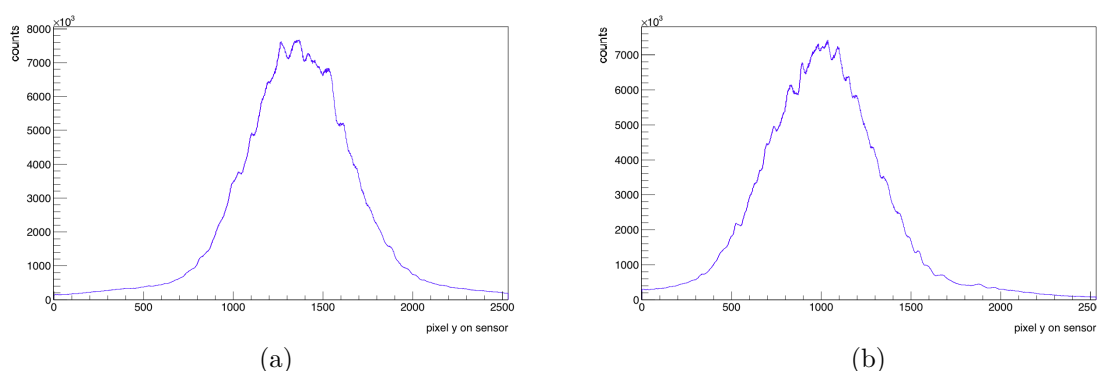   integral.

Figure 5.6: Y-intensity profiles for the measurements shown in fig. 5.4. The beam is well centered in a), whereas in (b) the distribution is plotted for the shifted beam spot. Also a dislocation of the distribution to the lower edge of the sensor can be found.

losses are systematic influences for the determination of the attenuation length and have to be considered. A possible reconstruction of the lost intensity can be used to correct the systematic effect, considering the information of the intensity profiles and is explained in section 5.1.4.

Beam broadening

There are two different origins, which cause a beam broadening: the focus induced and the vibration induced broadening of the beam size. Due to a focus of the light beam to a spot in a distance of several m, the beam diameter is becoming bigger for decreasing distances to the mirror optic. As a result, the beam size is growing with decreasing fill height levels, as can be seen in fig. 5.7.
In (a) the measurement at a filling level of 2.66 m is shown in its original contrast settings. In (b) a readjusted beam spot is shown at a fill height level of 0.87 m. It can be seen, that both beam spots show rather different shape sizes. Furthermore, vibrations are present, too, which increase the size of both beams even more. Due to the increased beam size, intensity can be lost due to a limited sensor size. Although the beams seem to be well centered and their shape smaller than the sensor size by eye, offline analysis and increased contrast settings reveal intensity losses. Fig. 5.7 shows a maximum brightness to contrast ratio of the same data pictures. To limit the losses due to beam broadening, a critical fill height is determined and is explained in section 5.1.3.

Reflections

With increasing beam sizes, possible reflections of light at the sample tube walls can occur. These reflections look either as sharp edges or points with a lot of intensity and can be identified in the intensity profiles as sharp peaks. In some cases, also

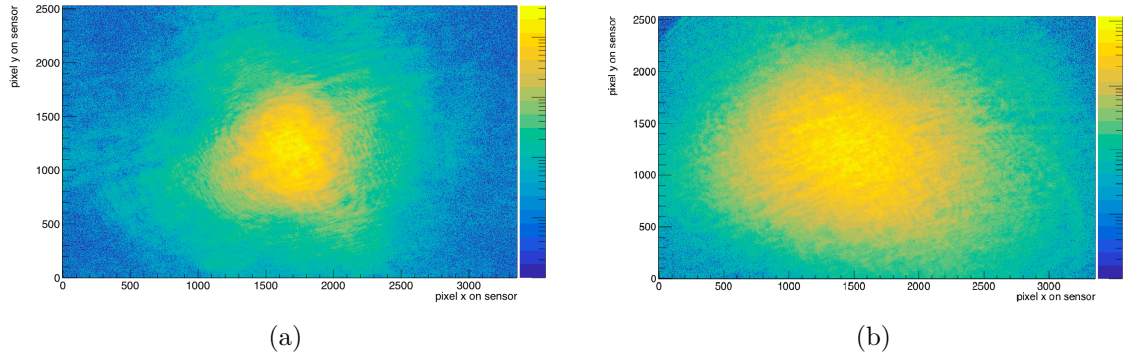(a)   (b)

Figure 5.7: Raw, colorized sensor pictures with logarithmic intensity scale for better contrast. In (a) the beam spot at a fill height level of 2.66 m can be seen. The beam shape is well centered and rather focused, except for the occurring vibrations. In (b) the beam size of the light for a fill height level of 0.87 m is shown after re-centering the beam on the sensor. It can be seen that due to focus and vibrations, the beam size is broadening with decreasing filling levels.

a saturation of single pixels occurs and distorts the sharp peak to a flat plateau. Reflections located near the center of the intensity peak of the beam can not always be extracted from the intensity measured within the intensity profiles. Therefore, the information of the 2-dim sensor picture has to be taken into account, too. A typical reflection within the sample beam can be seen in fig. 5.8. It shows a raw data picture taken at a wavelength of 650 nm and a fill height level of approximately 1.3 m. X and y-intensity profiles both are shown on top and on the left, respectively, whereas in the middle, the raw data histogram is plotted and shows a distorted beam shape. Different reflections can be identified on the right lower corner, whereas a sharp reflection dot with much higher intensity can be seen on the left of the center of the light beam.The x-profiles show no sharp peak, but a cut off peak at the location of the highly illuminated intensity spot because of pixel saturation. Reflections with smaller intensity can not be identified clearly in the profile, but the distribution is broadened due to their occurrence next to the corners.

Diffraction

The optical system is optimized by using a smaller aperture, which reduces the beam size of the light beam and acts on the same time as a single slit with width a. This can cause diffraction effects, if the following equation is found true [Tip04]:

$$\sin(\Theta) = \frac{m \cdot \lambda}{a}. \tag{5.3}$$

Hereby, λ is the wavelength of the light beam, $m = 1, 2, 3...$ and Θ the diffraction angle. The equation describes the diffraction angle, at which diffraction minima can
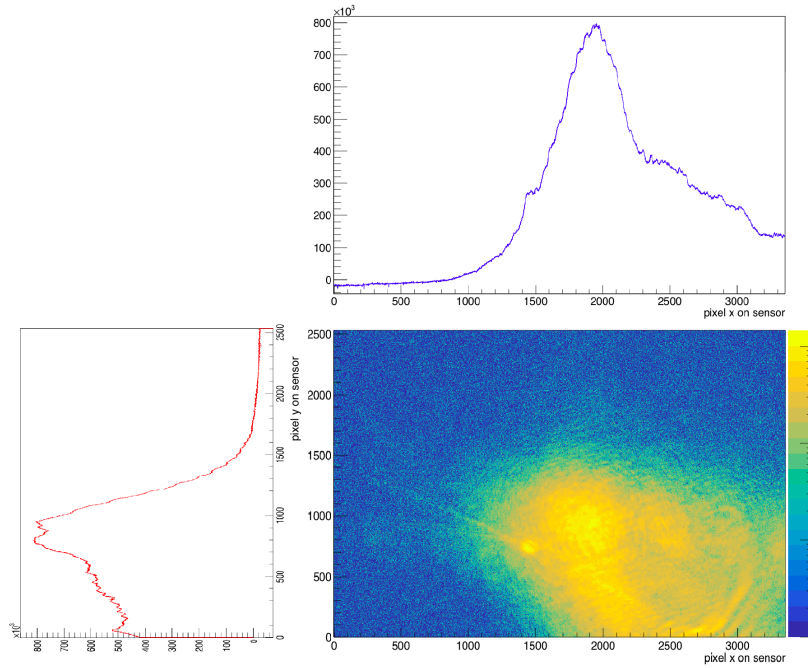
Figure 5.8: Occurrence of reflections of parts of the light beam at the sample tube walls due to a bad adjustment or too big beam sizes. In the middle, the raw data picture is shown, taken for 650 nm at a fill height level of approximately 1.3 m. A sharp reflection dot can be identified on the left, next to the beam center, but also reflections with smaller intensity can be seen on the other side of the beam. The picture on top (on the left) shows the x (y)-intensity profile. The sharp reflection dot can be identified as a sharp increase of the intensity, but with a cut off peak due to pixel saturation in the x intensity profile, presenting a small plateau. The other smaller reflections at the tube walls can not be identified clearly within the distribution, which is broadened asymmetrically. This has to be taken into account for an automatization of the data analysis.

be found. Furthermore, the distance between the central diffraction maximum and the mth diffraction minimum can be determined via

$$\tan(\Theta_m) = \frac{y_m}{l}, \tag{5.4}$$

with the mth diffraction angle Θ_m, the distance l between the single slit and the detector and y_m the distance between the central diffraction maxima and the mth diffraction minimum [Tip04]. In the case of the PALM experiment, the aperture has a diameter of 1.5 mm, and the distance between the aperture and the CCD sensor is around 3.5 m. Taking into account the crucial wavelength 430 nm, the distance between central maximum and first diffraction minimum is $y_1 \sim 1$ mm, which corresponds to less than 200 pixels and is rather negligible[2]. This can also be seen in the intensity distribution of the beam shown in fig. 5.15.

For mechanical position changes between the entrance flange and the optical table, there is the possibility, that the flange is cutting partially into the adjusted beam spot, resulting in a decreased intensity as well as a smaller, elliptical beam shape. In this case, the entrance flange is acting as an aperture, which leads to the occurrence of partial diffraction rings at the cut beam side. Such partial diffraction rings can be identified within the intensity profiles. Fig. 5.9 shows a measurement with typical diffraction patterns at a wavelength of 650 nm and a fill height of approximately 1.3 m. It can be seen, that the beam spot is centered on the CCD sensor as well as distorted by occurring vibrations. Furthermore, a sharp edge can be seen, followed by several spots of high intensity. The entrance window of the sample tube cuts into the light beam after deflection and a part of the intensity is cut. As a consequence, diffraction occurs at the cut edge, showing only parts of the created diffraction rings. Re-adjusting the optical table in reference to the sample tube eliminates this effect. Due to vibrations, the beam is distorted to an in-homogeneously illuminated light beam, masking the effects of diffraction. For the shown data picture, the x-intensity profile is plotted in fig. 5.10. A sharp, well centered intensity peak can be identified as well as a decrease of the intensity can be seen at the position, where the entrance window cuts into the light beam. As a consequence, partial diffraction rings occur. Neighbored to the sharp edge, several increased intensity spots occur, marking the position of these diffraction rings. The occurring intensity spots in the raw data picture correspond to several intensity peaks next to the light beam. The identified peaks appear periodically with the same distances between two neighbored peak maxima. This characteristic can be used to automatically check the data set for possible diffraction in the future.

Stabilized halogen lamp

One source of systematic uncertainties that can not be eliminated is the change of the incident intensity. Using a new halogen lamp, it takes approximately 200 hours of running, before the intensity stabilizes to a certain point and the lamp can be

---

[2]For a wavelength of 632.8 nm, the corresponding value is $y_1 \sim 1.5$ mm.
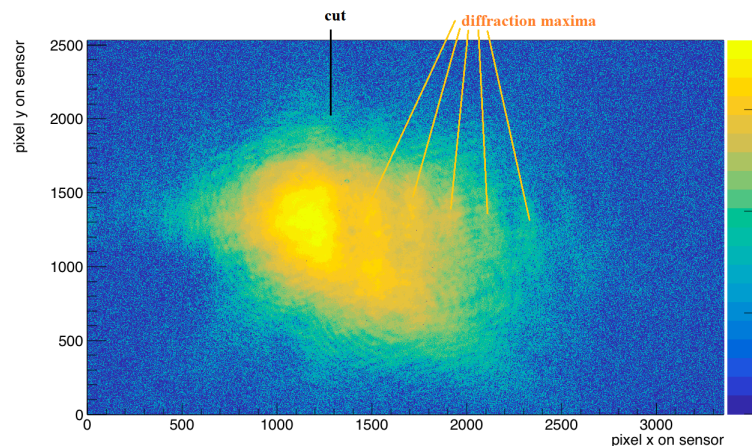
Figure 5.9: Raw data picture taken during a measurement series with a sample fill height of 1.3 m at a wavelength of 650 nm with colorized, logarithmic plotted intensity entries. The beam shows its characteristic distorted shape due to vibrations. Furthermore, a sharp cut can be identified on the right of the distribution's peak. Several increased intensity areas can be identified near the sharp cut edge, looking like an in-homogeneously illuminated light beam. This is explained by the occurrence of diffraction.
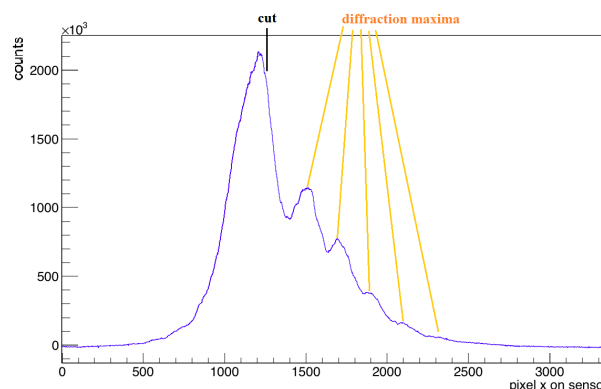

Figure 5.10: Calibrated intensity profile of the measurement shown in fig. 5.9, plotted over the x dimension. The intensity beam can be identified as a peak in the distribution, showing a sharp edge at the right side due to a cut off. The resulting diffraction maxima occur as periodically appearing peaks with same peak to peak distances.
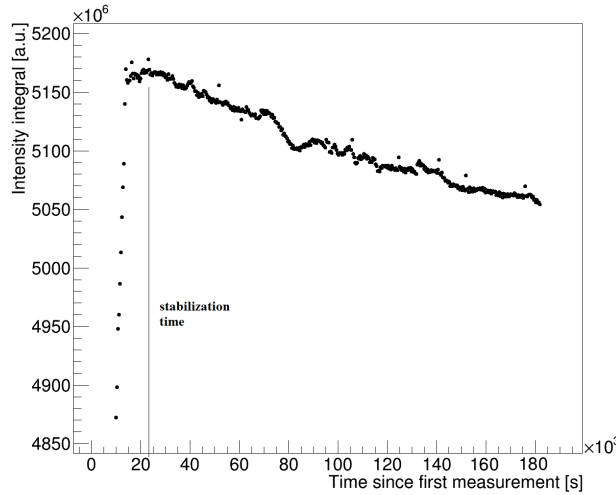
Figure 5.11: Intensity integral - time measurement over several hours to monitor
the stability of a brand new halogen lamp. For a usage of the lamp
in PALM, the lamp has to reach its stability plateau. It can be seen
that after a current change, the setup needs several hours to thermalize.
Furthermore a steady decrease of the incident intensity is visible. The
lamp has to be run for approximately 200 h to get to a stable plateau,
before it can be used as a light source in the experiment.

used as a light source for PALM. Such a process of preparing a new lamp can be seen
in fig. 5.11. Shown are the calculated intensity integrals in arbitrary units over a
measurement time of approximately 47 hours. The measurement started several days
after switching on the halogen lamp at a filling level of 2.66 m, a wavelength of 430 nm
and an initial current of 5.0 A[3]. Starting a second stability measurement, a working
point at 8.4 A is selected for the lamp. The increase of the intensity at the beginning
is due to this change of the current and a stabilization time of approximately 2.5
to 3 hours is identified. Afterwards the intensity starts to decrease continuously
except for small fluctuations. The steady decrease can not be explained by sudden
beam shifts or vibration mode changes, but due to changes of the incident intensity.
Longterm stability measurements are used to monitor the lamp intensity to prepare
new halogen lamps for the experiment. After a stabilization time of approximately
200 hours for the used type of halogen lamps, the intensity reaches a steady plateau.
Reaching the stabilized plateau, following measurements show stability fluctuations
of 0.25 %, which could be seen in section 4.5.5 for an empty and in 5.1.1 for a filled
sample tube already.

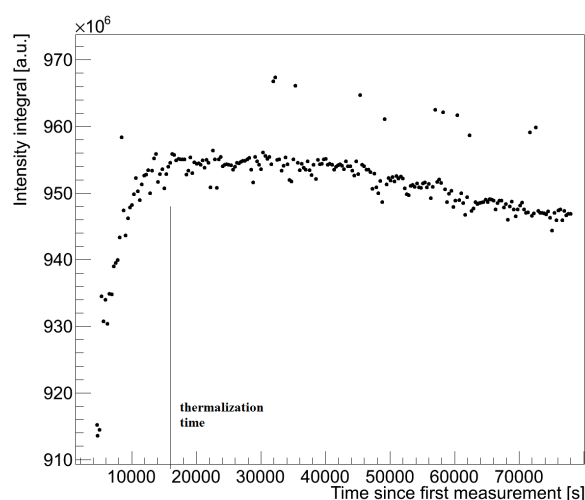[3]This is due to another investigation and is arbitrary.

Figure 5.12: Stability measurement at a filling level of around 2.3 m and a wavelength of 530 nm. Plotted are the calibrated, processed intensity integrals over time. The measurement starts after selecting a working point of 5.0 A at the power supply unit. This can be seen as a significant increase of the intensity integral within the first hours. The outliers with increased intensity spread over the whole measurement time can be explained by a fluctuation in the exposure time. After a stabilization time of several hours the expected stable intensity plateau can not be observed, but a steady decrease of the integrals.

Aging process of a halogen lamp

Halogen lamps also have a limited lifetime, and the intensity will start to decrease with time, too, when the lamp is going to die. This so called lamp aging process starts after a run time of approximately 2,000 hours for the lamp type used[4] and can be identified as a very small, steady decrease of the intensity integrals over time at first. Such a behavior can be identified in longterm intensity measurements over several hours and is shown in fig. 5.12. The picture shows a stability measurement for a filling level of around 2.3 m at 530 nm and a current of 5.0 A[5]. Plotted are the calibrated, processed intensity integrals over time. The increase of the intensity in the beginning is due to the selection of the current and a corresponding thermalization time. Outliers with increased intensity integrals can be identified and are caused by fluctuating exposure times. The halogen lamp has been operated for at least 2,000 hours, before the incident intensity starts to decrease. This sudden appearing decrease can not be explained by shifts or beam distortions or other changes within the setup and is identified as an aging process of the material in the halogen lamp. Fig. 5.13 shows a brand new halogen lamp on the left next to a halogen

---

[4]The halogen lamp type is Osram HLX 64623.
[5]The optimal working point is 8.4 A, which is used for all sample measurements.
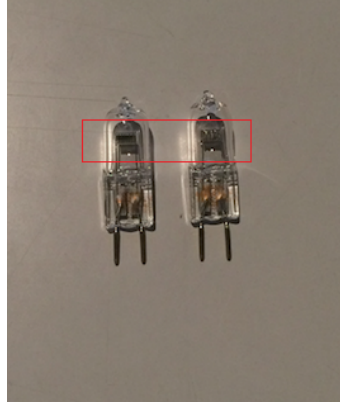
Figure 5.13: Picture of halogen lamps used as light sources for the PALM experiment. On the left, a brand new halogen lamp is shown, neighbored to a lamp, which was used for more than 1,000 hours and which has to be exchanged due to material aging. It can be seen, that the filament material of the used halogen lamp is degenerating with time.

lamp reaching the end of its lifetime on the right. Differences of the aging material of the spiral-wound filament can be identified, giving a hint to the changing ohmic resistance. As the lamp is operated at around 100 W, parts of the material of the filament start to evaporate and may condensate on the filament or quartz glass of the lamp. With time, this change in the filament is influencing the output intensity of the lamp. Furthermore, the observed change in the resistance of the lamp can be used to identify aging processes as a steady increase of the voltage for a fixed current, too. As a consequence, the aging process can be cross-checked by monitoring the voltage at the precision power supply unit. Experience shows, that voltages higher than 12.0 V, at a fixed current of 8.4 A indicate the end of the lifetime of the halogen lamp. First tests revealed that a lamp aging at this point influences the calculated intensity integrals by at least 1 %. As the incident intensity changes with time, measurement series over longer time periods can be biased by the intensity decrease. This will change the slope parameters of the exponential decay function, which is fitted to the single measurement data points for the determination of the attenuation length (see section 4.3), and would lead to systematic decreased intensity integrals with increasing measurement time. Assuming measurements, which start at the maximal fill height level and measure the intensity integrals for decreasing levels, the effect of the aging process would decrease the intensities at low fill height levels at most. The resulting biased intensity integrals are too small for small filling levels and the attenuation length would be overestimated. The inverted case is present for measurements starting at their minimal filling level. Here, the steady decrease of the intensity with time affects the higher filling levels most, creating a much steeper slope than expected and change the attenuation length to much smaller values than in reality. To guarantee a precise attenuation length measurement, this time dependent intensity decrease has to be eliminated, either by using a new lamp

or, as it may occur suddenly within a series, by correcting the intensity integrals. A lamp change is done in case the voltage of the current lamp passes a value of 11.6 V at a fixed current of 8.4 A. Is it not possible to finish the measurement series before the aging process starts, a longterm measurement over several hours can be investigated to determine the current slope of the decrease of the incident intensity. A linear function is used to model the decreasing behavior in a first approximation. Taking into account the obtained fit parameters, the intensity integrals can be corrected with respect to their measurement time, eliminating the aging effect. Such a tool is already implemented in the offline analysis. The following measurement results for the attenuation length are obtained without the tool, as new halogen lamps are installed before aging effects have been observed.

5.1.3 Determination of the critical fill height level

Taking into account the systematic uncertainty sources described above, it is clear, that focal and vibration induced beam size broadening is limiting the measurements to a fill height level, where the intensity information can be detected without significant losses. This minimum filling level is referred to as critical fill height level. For its determination, several measurements are investigated to determine beam shape sizes and possible intensity losses. Fig. 5.14 shows an exemplary test measurement for different fill height levels between 0.3 and 1.4 m. It shows raw data pictures for several different liquid levels with increased contrast for better comparison. The pictures have uprising numbers, corresponding to upraising fill height levels measured in channels. The resulting calibrated fill heights are within 0.3 m and 1.4 m. With respect to the beam shapes and sizes of the measurements, it can be seen that for a fill height level of around 0.7 to 0.8 m (corresponding to the picture with the label 51X) the beam size is in the same order as the sensor area.

To approximate the intensity losses, the calibrated, dark noise corrected sensor data are used. The calculation of an integral of a small rectangle at each sensor edge gives the amount of intensity near the borders. Approximating the size of the illuminated beam area cut off at the borders with the two dimensional data histograms, the lost intensity is estimated by scaling the intensity found in the rectangle to the illuminated area. The approximated intensity losses are shown in table 5.1 and can be used as a first estimation.

The determined intensity losses are calculated under the assumption, that the beam is well centered on the sensor and the dominant vibration perturbations are present and unchanging over time. For all other cases, the loss of intensity is much higher than the given results. The values differ for small deviations from the ideal centered position and can not be used as an overall uncertainty, but suit as a first approximation and a lower limit. The corresponding measured intensities are biased by the loss, leading to smaller measured values for decreasing fill heights. This leads to a decreased slope of the Beer-Lambert fit function and to an overestimation of the determined attenuation length. Due to the fact that for much lower filling levels, these losses are much higher, the critical fill height level is determined to be at 0.8 m.
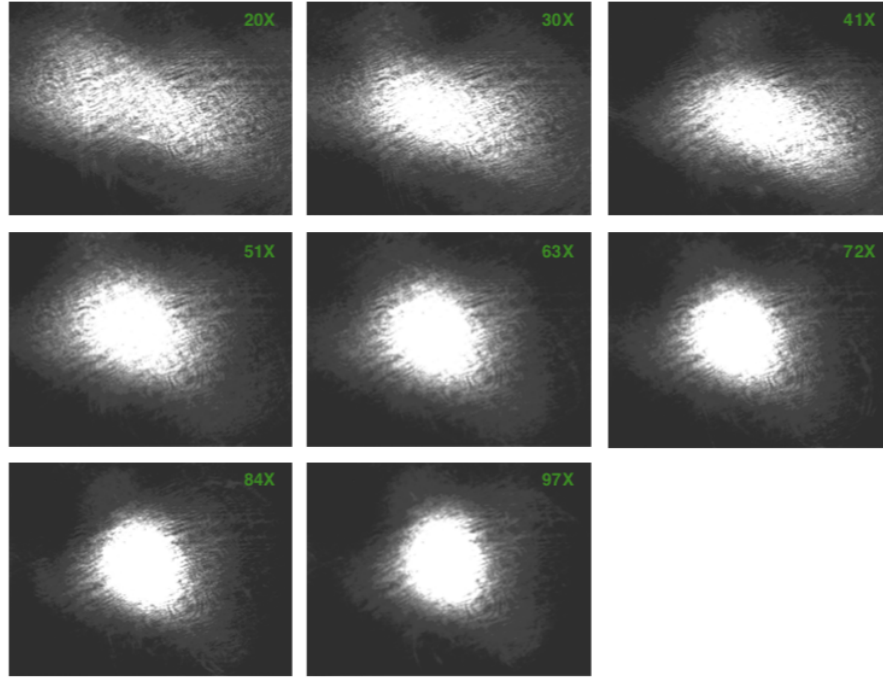
Figure 5.14: Raw data pictures taken for several different low fill height levels of the same measurement series with increased contrast settings. The determined critical fill height will be the minimal filling level, for which the loss of intensity is negligible. Fill height levels below the determined minimum show a decreased intensity due to losses at the sensor edges. It can be seen, that up to a fill height level of 0.76 m (51X) the intensity losses are small, whereas for lower filling levels, this is no longer the case.

Fill height in m	approx. intensity loss in %	offset corrected intensity loss in %
0.61	9.7	8.6
0.76	4.2	3.1
0.87	2.2	1.1
1.03	1.6	0.6
1.37	2.0	0.9
1.72	2.1	1.0
2.09	1.6	0.5
2.48	1.2	0.2
2.68	1.1	0

Table 5.1: Approximated intensity losses due to a limited sensor size and a vibration and focus induced beam size broadening. Given are the estimated losses in percent as function of the fill height. Assuming no losses for the maximal filling level, the corrected intensity losses are also given.

This limit enables to create a maximal light path length through the medium of $\sim$ 2.0 m.

5.1.4 Reconstruction of intensity losses (bsc)

There is a focal and vibration induced broadening of the beam size, limiting the measurable filling levels due to un-negligible losses of the intensity. The critical fill height level limits the measurement range to a level, where losses are approximately 2 % to suppress the systematic influence. The measurement results are biased by this effect and the determined attenuation length is overestimated because of a decreased slope of the corresponding fit. To correct the measured intensity integrals and to possibly further enlarge the light path through the sample medium and enable a more precise determination of the attenuation length, the possibility of an intensity reconstruction (bsc)[6] is developed in the framework of this work. Applying the bsc, the lost intensity is approximated and used to correct the calculated intensity integrals. The 2-dim sensor histogram shows the beam size, shape and its position on the sensor. This can be used to identify areas, where a part of the intensity is cut off. The 1-dim x- and y-intensity profiles, showing possible changes in the beam shape or position, are used to reconstruct the intensity losses. Assuming a perfect centered and undistorted beam spot, the intensity distribution in both intensity profiles looks like a centered peak with steep slopes towards the edges of the sensor, falling rapidly to zero. For a fill height level of 2.66 m, the resulting intensity distribution is almost ideal and can be seen in fig. 5.15. The profile shows a sharp peak with small width in the intensity distribution, indicating that the beam shape is small and focused. Its tails and corresponding slopes are decreasing to zero within the sensor's spatial range, showing no distortions. Therefore, the assumption of an ideal beam is in good agreement to the experimental results.

For decreasing filling levels, the beam size is becoming bigger. At some point, the decrease of the tails to zero in the intensity distribution can not be seen any more, because of a cut on the sensor edges. This is also true for mechanical changes like external shocks, which force the centered beam out of its adjustment, shifting it towards the edges.

As the beam is shifted out of the center of the sensor due to a perturbation, the intensity distribution is shifted, too, and parts of it are cut. Because of the contribution of the cut areas to the intensity integrals, a reconstruction of the lost intensity is possible by modeling the behavior of the tails. Assuming that the beam has a finite spatial distribution, the intensity profiles are plotted from the calibrated, dark noise corrected data pictures and their tails are fitted with exponential functions. Exemplary intensity distributions with fitted exponential functions can be seen in fig. 5.16. Shown are both calibrated, dark noise corrected intensity profiles for the same data picture. By fitting exponential functions to the tails of the peak, information about the slopes are gained, which can be used to predict the behavior of

---

[6]Shortcut for the intensity reconstruction, originating from the term beam shift correction.
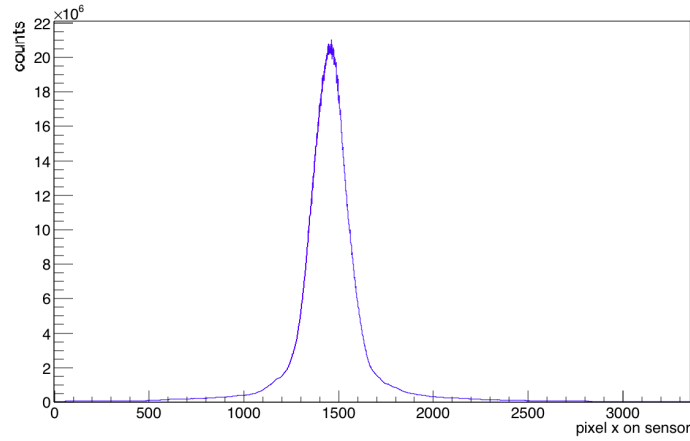
Figure 5.15: Calibrated x-intensity profile of a sensor picture taken at a wavelength of 430 nm and a fill height level of 2.66 m. The beam profile shows a sharp and small intensity distribution and looks approximately like a perfect, ideal beam. This fact can be used for the intensity reconstruction method.

(a)

(b)
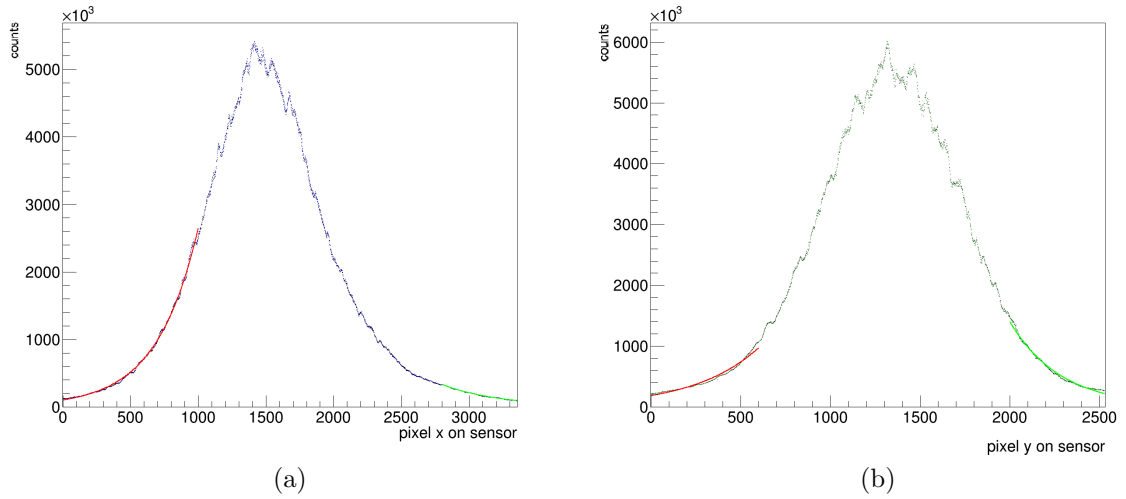
Figure 5.16: Intensity profiles for a measurement taken at 430 nm and a fill height of around 0.8 m. In (a) the x-intensity profile is shown with both fitted exponential functions to model the intensity distribution beyond the sensor borders. Although it is well centered, it can be seen that the tails are not falling to zero within the sensor size. In (b) the corresponding y-intensity profile is plotted. Fitting both slopes with exponential functions, the intensity integrals from the end points of the sensor to infinity are calculated and are also added as a correction to the measured intensity integral.

Figure 5.17: Scheme of all areas, which have to be taken into account for the intensity reconstruction method. Due to the fact that a part of the intensity is cut at all sensor edges the reconstruction uses the integral to infinity for all dimensions. Shown is the area of the sensor picture in the middle, which intensity integral can be calculated and eight different other areas, which have to be considered.
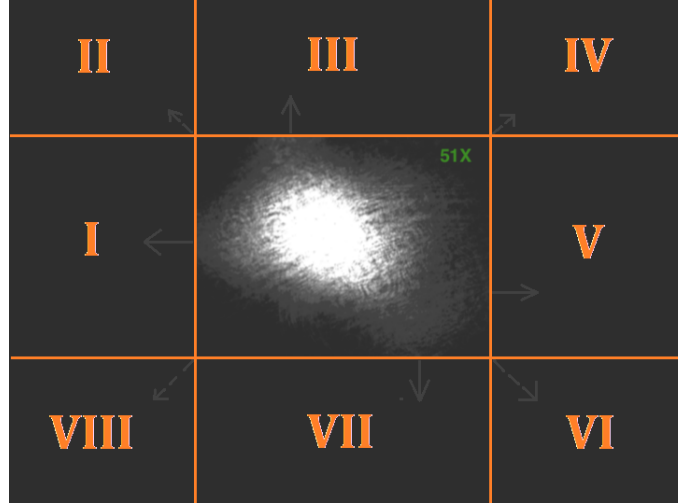
the intensity distribution beyond the sensor borders. Integrating the exponential fitting functions from the edges of the sensor to infinity correspond to the intensity losses. These integrals are added as a correction to the measured intensity integrals, shifting them to higher values.

The determination of the intensity integrals from exponential fits is performed for every single data picture. This means, that also beams of ideal shape are modeled, and their corrected intensity integrals are determined. Considering the assumption, that the beam at this height is ideal, the determined intensity integral for a maximal fill height is handled as an offset. Reason for the behavior, that the distribution for high filling levels is not decreasing to zero within the sensor dimensions may be parasitic ambient light, which could not be found in the case of PALM. Another possibility can be vibrational induced stray light, as the beam is growing much bigger than the sensor size at some occasions. Also dis-adjustments between the entrance window and deflection mirror may be possible.

The offset is determined to be less than $1.5\,\%$ in total for filling levels around $2.7\,\mathrm{m}$, assuming a centered beam spot and the common present dominant vibrations. The determined exact values from the bsc at the maximal fill height are subtracted from all other correction integrals. For an accurate correction, several areas of possible intensity losses have to be taken into account and are shown in fig. 5.17. Shown are a raw sensor picture in the middle and several different areas of possible intensity losses. The measured intensity integral I_{meas} is limited to the sensor size. Possible intensity losses are distributed in the areas numbered from I to VIII and

contribute to the total intensity integral I_{total}. Therefore, these areas are considered for the reconstruction method. Generally, the total intensity is the integral of all contributions of all dimensions. With reference to the naming in fig 5.17, the total intensity integral I_{total} can be determined:

$$I_{\text{total}} = I_{\text{meas}} + \sum_{i=\text{I}}^{\text{VIII}} I_{i\,\text{bsc}}, \tag{5.5}$$

with the calculated reconstructed intensities I_{bsc} from each area and I_{meas} the intensity integral over all sensor pixels:

$$I_{\text{meas}} = \sum_{x=0}^{3354} \sum_{y=0}^{2529} I(x,y). \tag{5.6}$$

Hereby, $I(x,y)$ are the counted intensity entries per pixel. To obtain the intensity contributions of the areas I to VIII, the x and y-intensity profiles of the sensor picture are used. Modeling the tails with exponential functions, the integral from the sensor edges to infinity is calculated and determined to be the integral corrections. Assuming a well centered beam with almost circular shape, but distorted by the dominant, unchanging vibrations, the areas II, IV, VI and VIII have small contributions, compared to the others. The sum of their contributions is determined to be in the order of 10^{-6} compared to the intensity integral of the sensor at a fill height level of $0.8\,\text{m}$ and can be neglected. This simplifies the reconstruction to

$$I_{\text{total}} \sim I_{\text{meas}} + \int_{-\infty}^{0} i_l(x)dx + \int_{3354}^{\infty} i_r(x)dx + \int_{-\infty}^{0} i_d(y)dy + \int_{2529}^{\infty} i_u(y)dy. \tag{5.7}$$

Hereby, $i_l(x)$, $i_r(x)$ are the modeled exponential functions for each (left and right) tail of the x-intensity profile and $i_u(y)$, $i_d(y)$ the corresponding functions for the y-intensity profile. This leads to a total intensity of

$$I_{\text{total}} = I_{\text{meas}} + I_{\text{corr}}, \tag{5.8}$$

with I_{corr} the sum of all intensity corrections. The assumption of negligible contributions from areas II, IV, VI and VIII may has to be reconsidered if one of the stated conditions is not fulfilled. Assuming an almost ideal light beam, the determined intensity correction I_{corr}^0 at the maximal fill height is subtracted from all other intensity corrections I_{corr} as an offset:

$$I_{\text{total}} = I_{\text{meas}} + I_{\text{corr}} - I_{\text{corr}}^0. \tag{5.9}$$

To test the stated intensity reconstruction, several sample pictures at fill heights of more than $2.3\,\text{m}$ are chosen, which show a characteristic beam shift over time. The intensity integral of a picture without a beam shift is used as reference and it is assumed, that for this integral at the given height the intensity loss is negligible. For several sensor pictures with increasing beam shifts, the intensity losses are reconstructed and the corrected intensity integrals are compared to the reference.

It is found, that the reconstructed intensity losses are in good agreement to the approximated intensity losses shown in table 5.1. Furthermore, the reconstructed integrals show a mean deviation of less than 0.5 %. This is also found for reconstructed intensity integrals of fill heights below 2.3 m, where a random sample of pictures is taken. The mean deviation is determined to be ~ 0.45 % and is used as the systematic uncertainty of the method. This holds for intensity reconstructions of pictures with beam shifts of less than 5 mm and fill heights above the critical fill height level. For other cases, the reconstruction is not tested yet.

5.2 Measurement scheme

The following measurements are performed with a cooled CCD sensor at -15 ° C for background suppression. For measurement preparation, the lamp is started and operated at 8.4 A (100 W) to optimize the stability behavior and lifetime of the halogen lamp. A thermalization time of at least 5.5 hours is guaranteed for optimal measurement conditions. Furthermore, the exposure time is selected in a way, that the measured intensity per pixel is not beyond the saturation limit and on the same time in a good signal to background ratio. To eliminate possible effects caused by the halogen lamp, longterm measurements are performed between single measurement series and filling levels to monitor the intensity for several hours. Halogen lamps are exchanged, if the voltage limit of 11.6 V for a fixed current of 8.4 A is reached, eliminating the occurrence of lamp aging effects. After a liquid level is chosen, the beam spot is adjusted at the center of the sensor. For mechanical or vibrational mode changes, the light beam is re-adjusted after each single picture. Taking several pictures for statistics, each is screened and selected manually, neglecting those with beam shifts of several mm, reflections and possible diffraction effects. Neither a change of the wavelength nor of the monochromator parameters is done within a measurement series. A series contains at least 8 to 13 different fill height level measurements. After performing a measurement series, the raw data are checked for temperature fluctuations and for exposure time fluctuations, which are corrected by the offline analysis. Neglecting broken pixels and applying a pixel-by-pixel gain calibration and a dark noise correction, the intensity integral of each single picture is calculated and used to determine the total mean intensity integral of a fill height level. The attenuation length is determined by fitting the Beer-Lambert-law to the intensity integrals for different fill height levels.

5.3 Measurement results

Several LAB samples are investigated as candidates for the JUNO scintillator solvent to check, if they match the stated goal of an attenuation length of more than 20 m, at 430 nm as is proposed by the JUNO collaboration [JUN15], [Cao18]. All systematic uncertainty sources described in 5.1.2 are taken into account for the results given in
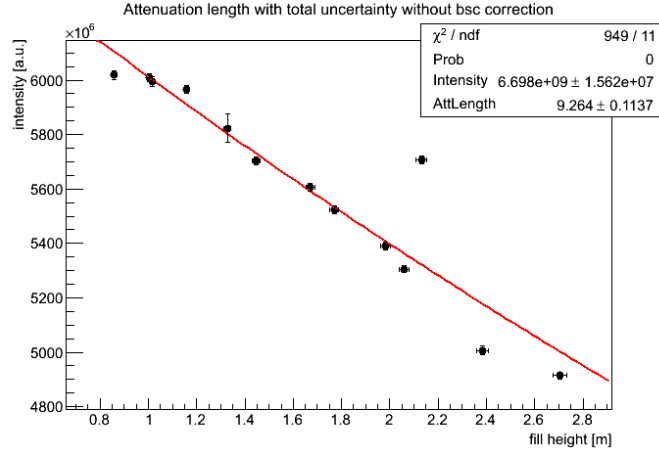
Figure 5.18: First measurement series to determine the attenuation length of raw LAB at 430 nm. Plotted are the measured intensity integrals in arbitrary units against the calibrated filling level in m. The incident intensity, which is a free parameter, and the attenuation length are determined by the Beer-Lambert-fit. The systematic uncertainty source of intensity losses at the sensor borders is neglected and the result represents an upper limit for the real attenuation length.

this chapter. In a first step, the measurements without considering possible intensity losses at the sensor borders are shown and as a consequence, the attenuation length results are an upper limit for the real value of the sample liquid. To eliminate the influence of vibrations, mechanical instabilities and the corresponding intensity losses, the new intensity reconstruction, developed in the framework of this work, is applied to the same data to obtain more accurate results for the attenuation lengths. These are given as final results in a second step.

5.3.1 Commercial untreated LAB

For testing the reproducibility of the results obtained with the PALM experiment and to enable a comparison to former results obtained by [Hel15a], commercial, untreated LAB is used. The sample originates from the petroleum source of Egypt and was produced in 2013. Since its production, the sample was exposed to oxygen, light and heat. Please note, that the following measurements are done with a sample from the same batch used to perform the measurement results shown in [Hel15a]. To investigate the attenuation length of the liquid several measurements at a wavelength of 430 nm are performed. Furthermore, attenuation lengths at 410, 450 and 633 nm are determined for a more complete picture.

Reproducibility measurements at 430 nm

A first measurement result for untreated LAB at 430 nm is shown in fig. 5.18. The
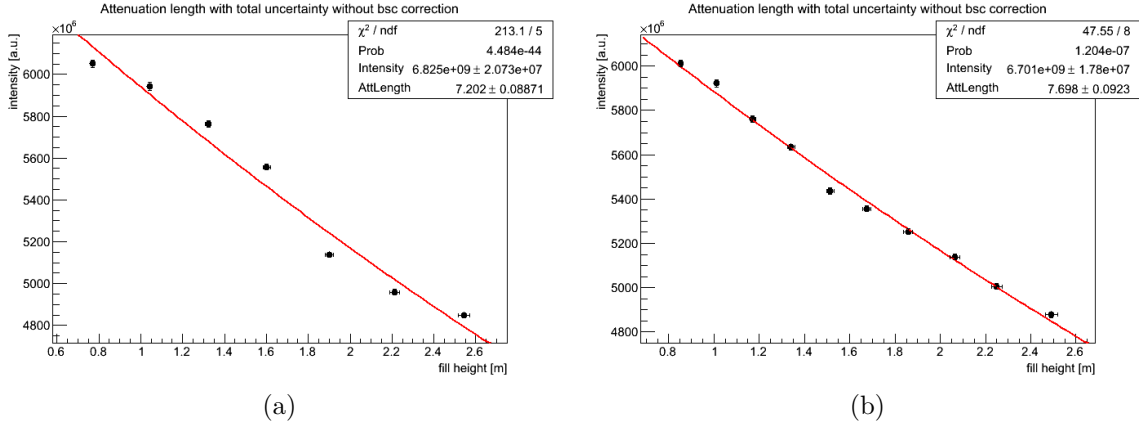
Figure 5.19: Reproduction measurement series of the same raw LAB at 430 nm from the critical to the maximal filling level. Both measurement series are taken with the same lamp without switching it off in between. The systematic uncertainty source of intensity losses at the sensor edges is not considered and the given attenuation length values are upper limits.

calculated, calibrated intensity integrals are plotted against the filling level in m. A Beer-Lambert-fit with the corresponding fit parameters attenuation length (in m) and the incident intensity (in arbitrary units), which is a free parameter, are given. Please note, that all systematic uncertainty sources mentioned in 5.1.2 are taken into account, except for the intensity losses at the sensor edges. This effect is increasing with decreasing filling levels and affects the smallest fill height level at most, which leads to the fact that the measured intensity integrals are smaller than in reality and the corresponding slope of the Beer-Lambert-fit is too small. As a consequence, the attenuation length values are overestimated. This effect is induced by beam size broadening of focus and vibrations as well as beam shifts, vibration mode changes and external shocks, which all dis-locate the centered beam towards the sensor borders. Because of these effects, the experimental data are biased and the obtained attenuation lengths are upper limits for the true parameter value.

Reproduction measurements of the same sample performed under same conditions can be found in fig. 5.19 for comparison. Due to the systematic uncertainty source of intensity losses, the given uncertainty is underestimated, making it difficult to compare the measurement results. The best obtained value is used as upper limit for the attenuation length of raw LAB at 430 nm ± 9 nm:

$$\Lambda_{\mathrm{raw}}^{430} < 7.29\,\mathrm{m}. \tag{5.10}$$

This does not satisfy the goal to determine the attenuation length accurately. As the intensity losses are not only influenced by focus and vibration induced beam size broadening for decreasing filling levels, but also for dis-adjustments of the beam referred to the centered sensor position and possible losses due to beam shifts, which are present in most cases due to the ongoing constructional work, the influence of
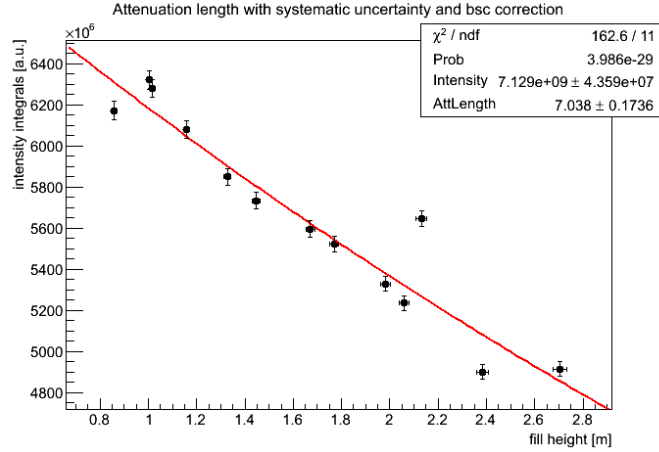
Figure 5.20: Measurement series for raw LAB at 430 nm, which was shown in fig. 5.18, after applying the intensity reconstruction. Plotted are the corrected intensity integrals in arbitrary units in dependence on the calibrated filling level in m, with the incident intensity being a free fit parameter.

the systematic uncertainty source differs a lot, making a simple uncertainty estimation not appropriate. To determine the attenuation length more precisely and to consider the intensity losses, the intensity reconstruction method described in section 5.1.4 is applied. It calculates the approximated intensity loss of each single measurement picture and corrects the determined intensity integral means. This leads to a shift of the corrected intensity integrals to higher values, especially for decreasing filling levels, increasing the slope of the Beer-Lambert-fit and the corresponding attenuation length is corrected to smaller values. These corrected results can be found in fig. 5.20 and 5.21.   The results for all measurements are in good agreement within the given uncertainty, except for the attenuation length obtained from fig. 5.21 (a), where a lamp aging process may have started. It can be seen, that the PALM experiment is able to reproduce reliable measurement results and the investigations performed to suppress and deal with the present vibrations in the framework of this work are successful. Furthermore, the applied reconstruction method performs properly and the determined total uncertainties are reliable. The best value of the attenuation length results is chosen to be the final result at a wavelength of $(430 \pm 9)\,\text{nm}$:

$$\Lambda_{\text{raw}}^{430} = (7.04 \pm 0.17)\,\text{m}, \tag{5.11}$$

for a sample of raw LAB, originating from Egypt. The result found by [Hel15a] for the same LAB sample is not in good agreement to the results found by the PALM experiment. This can be explained by the fact, that the sample liquid was exposed to oxygen, heat and light for several years before being re-measured in the PALM setup for comparison. Investigations show, that these influences change the
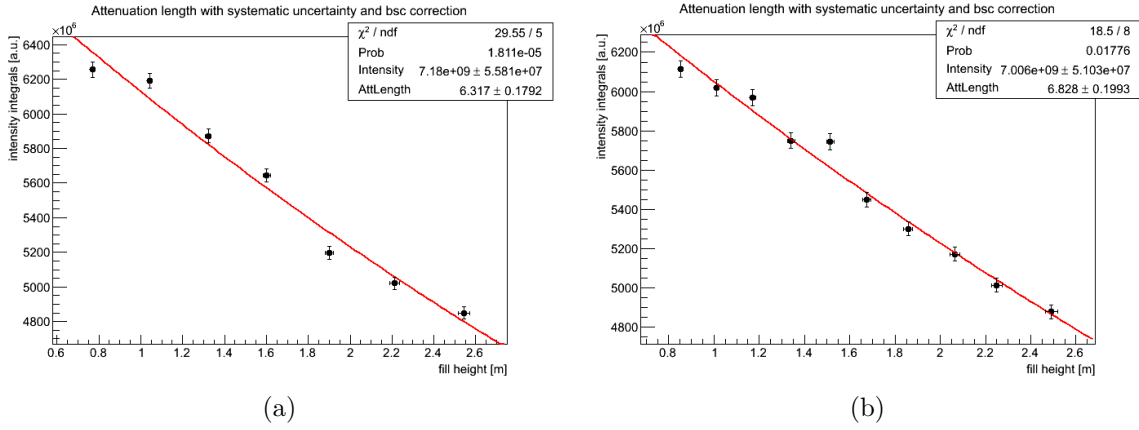
Figure 5.21: Measurement series of raw LAB at $430\,\mathrm{nm}$ from the critical to maximal filling level after applying the bsc method. The uncertainty given is total. Please note that the measurements have the same ordering as in fig. 5.19.

optical parameters significantly [Pru15]. Furthermore, it is not known, if the results obtained by [Hel15a] include the systematic effects of aging processes of the halogen lamp or possible intensity losses.

Results obtained in the region of interest

For a more complete picture the attenuation length of other adjacent wavelengths is determined, too. Fig. 5.22 shows the results obtained at a wavelength of $(410 \pm 5)\,\mathrm{nm}$. In (a) the measurement result before and in (b) after applying the intensity reconstruction is shown. The upper limit for the true attenuation length is determined to be:

$$\Lambda_{\mathrm{raw}}^{410} < 4.06\,\mathrm{m}. \tag{5.12}$$

After applying the reconstruction (b), the final result for the raw LAB sample at $(410 \pm 5)\,\mathrm{nm}$ is determined to be

$$\Lambda_{\mathrm{raw}}^{410} = 3.91 \pm 0.07\,\mathrm{m}. \tag{5.13}$$

Both results are in good agreement to each other. As the attenuation length is rather small, the intensity losses and the reconstruction have a small influence on the final result. This changes with rising attenuation lengths. A similar measurement series is performed at $450\,\mathrm{nm}$ and can be found in fig. 5.23. Shown are the measured intensity integrals against the liquid level. In (a) the result without the intensity reconstruction is plotted and an upper limit can be given for the attenuation length:

$$\Lambda_{\mathrm{raw}}^{450} < 15.00\,\mathrm{m}. \tag{5.14}$$

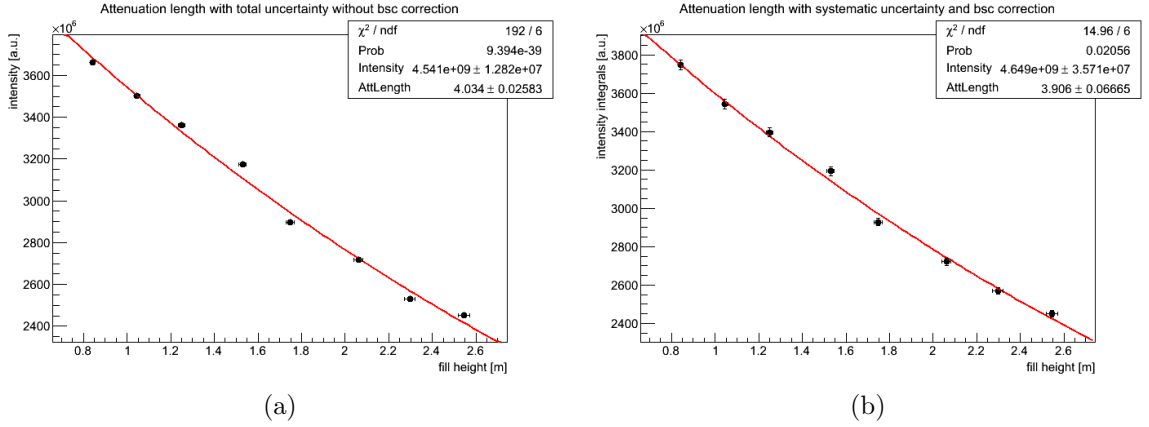(a)   (b)

Figure 5.22: Measurement series of raw LAB at a wavelength of 410 nm. Plotted
            are the calculated intensity integrals in arbitrary units as a function
            of the sample fill height in m. The Beer-Lambert-fit is shown as well
            as the attenuation length given in m. In (a) the measurement series
            without considering the intensity losses is shown, whereas in (b) the
            corrected intensity integrals are plotted after applying the intensity
            reconstruction.

(a)   (b)
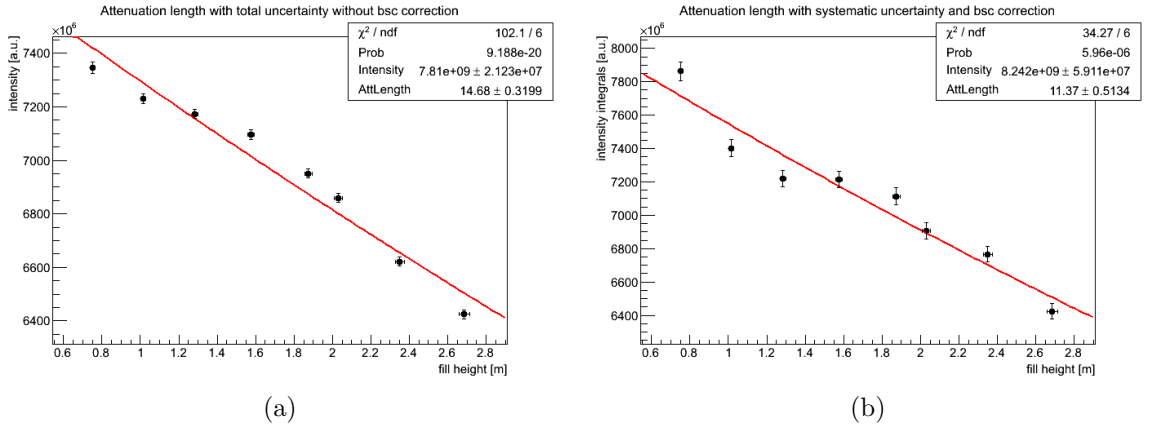
Figure 5.23: Measurement results with (see (a)) and without, shown in (b), intensity
            reconstruction for a raw LAB sample at 450 nm. Plotted are the calcu-
            lated intensity integrals in arbitrary units over the sample fill height in
            m. The Beer-Lambert-fit is used to determine the attenuation length.
            Due to the neglect of intensity losses, the results from (a) are used
            as upper limits for the attenuation length of the liquid. The result
            obtained with bsc is used as final result.

Figure 5.24: Measurement series at 633 nm for raw LAB without (a) and with (b) the intensity reconstruction. Plotted are the intensity integrals as a function of the fill height as well as the corresponding Beer-Lambert-fit.

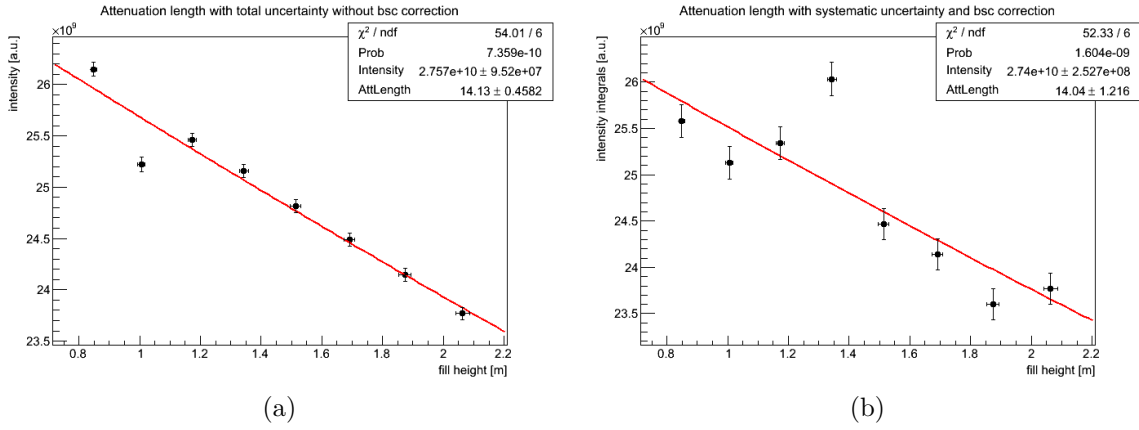The final result for the attenuation length at (450 ± 10) nm can be found in (b) and is determined to be

$$\Lambda^{450}_{\text{raw}} = 11.37 \pm 0.51 \, \text{m}. \tag{5.15}$$

Result at a wavelength of 633 nm

To measure attenuation lengths at wavelengths with higher incident intensities, another measurement series is performed at a wavelength, where the halogen lamp has a much higher output. Furthermore, it is considered to reproduce the results with a laser optic for comparison. Due to the usage of a helium-neon laser with a wavelength of 632.8 nm, measurements at this wavelength are performed. The measurement series can be found in fig. 5.24. An upper limit of the attenuation length is determined to be

$$\Lambda^{633}_{\text{raw}} < 14.59 \, \text{m} \tag{5.16}$$

at (633 ± 24) nm. Taking into account the intensity integrals before and after reconstruction, it can be seen, that instead of an increase of the integrals at lower filling levels, a decrease can be found. Considering the used method, it is clear, that this originates from the determined offset. The reconstructed intensity at the highest fill height is distorted by a beam shift. Because of the mean calculation of the intensity integrals, such outliers of single pictures have an un-negligible impact on the result and the reconstructed value is much higher than the reconstructed intensities for lower filling levels, which corrects them to smaller intensity integrals. Furthermore, an outlier at ~ 1.3 m can be identified in the reconstructed data set, which can not be seen in the original data (a). The overestimated reconstruction is caused by inaccurate limits for the exponential fits. The measurement series with and without the bsc reconstruction can be compared to identify possible overestimated intensity

corrections. A first result for the attenuation length at $(633 \pm 24)\,\mathrm{nm}$ is determined to be:

$$\Lambda_{\mathrm{raw}}^{633} = (14.04 \pm 1.22)\,\mathrm{m}. \tag{5.17}$$

5.3.2 LAB purified with aluminum oxides

Due to the necessity of an attenuation length of more than $20\,\mathrm{m}$ at $430\,\mathrm{nm}$ for the JUNO detector, several purification techniques are investigated to further improve optical and radioactive purity of the liquid scintillator. Former studies investigated the effect of an aluminum oxide column purification on the attenuation length of LAB [Pru15]. Testing the effectivity of different aluminum oxides, too, it is found that a two step aluminum oxide purification process with $100\,\mathrm{g}$ alkaline aluminum oxide and a pore size of $150\,\text{Å}$ in combination with a purification with $50\,\mathrm{g}$ of acid aluminum oxide and a pore size of $90\,\text{Å}$ afterwards increases the attenuation length over a wide range of wavelengths, except the absolute values are not known due to measurements obtained with the UV/Vis spectrometer and the resulting huge uncertainties [Pru15]. To determine the absolute attenuation length values before and after the two step purification, a sample volume of six liters of LAB, purified with both aluminum oxides, was produced in 2015 and is measured in PALM.

Results in the region of interest

The attenuation length of the prepared sample is investigated at the wavelength 420, 430 and $440\,\mathrm{nm}$ to reproduce the trend seen in the UV/Vis results [Pru15]. It is expected, that the absolute attenuation length values are increasing for increasing wavelengths in $(420\text{ - }440)\,\mathrm{nm}$. The LAB sample, purified with both aluminum oxides, is referred to as MC-LAB in the following. Fig. 5.25 shows two measurements of the MC-LAB at a wavelength of $(420 \pm 5)\,\mathrm{nm}$. Shown are the calibrated, calculated intensity integral means plotted as a function of the sample fill height level. The corresponding parameters of the Beer-Lambert-fit are given for (a) and a reproduction measurement is plotted in (b). All systematic uncertainty sources discussed in section 5.1.2 are considered, except intensity losses. It can be seen, that both measurements give a similar value for the attenuation length, although they are not in good agreement within the stated uncertainty. This can be explained by the systematic influence of intensity losses, which are not considered. The best obtained lower limit is used as an upper boundary for the true attenuation length of the two step purified LAB sample at $(420 \pm 5)\,\mathrm{nm}$:

$$\Lambda_{\mathrm{MC}}^{420} < 15.47\,\mathrm{m}. \tag{5.18}$$

For the measurements taken at $420\,\mathrm{nm}$, the corrected intensity integrals after applying the reconstruction method are plotted as a function of the filling level and can be found in fig. 5.26. After applying the intensity reconstruction and correcting the integral means for the intensity losses at the sensor borders, both measurements
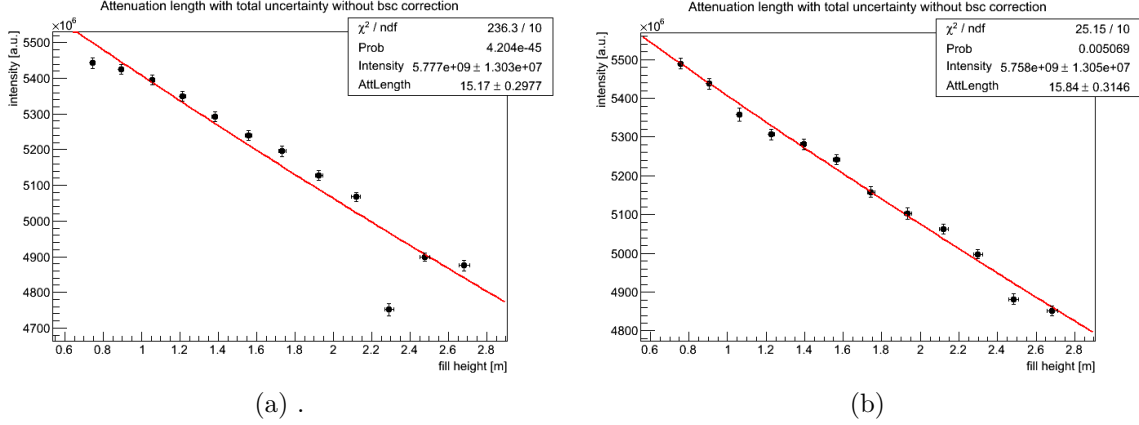
(a) .   (b)

Figure 5.25: Measurement series for MC-LAB, which is purified in a two step process with different aluminum oxides at 420 nm (a) and a reproduction measurement (b). Shown are the calibrated mean intensity integrals against the corresponding fill height levels. The intensity losses on the sensor edges are not included and the results are upper limits for the true attenuation length parameter.
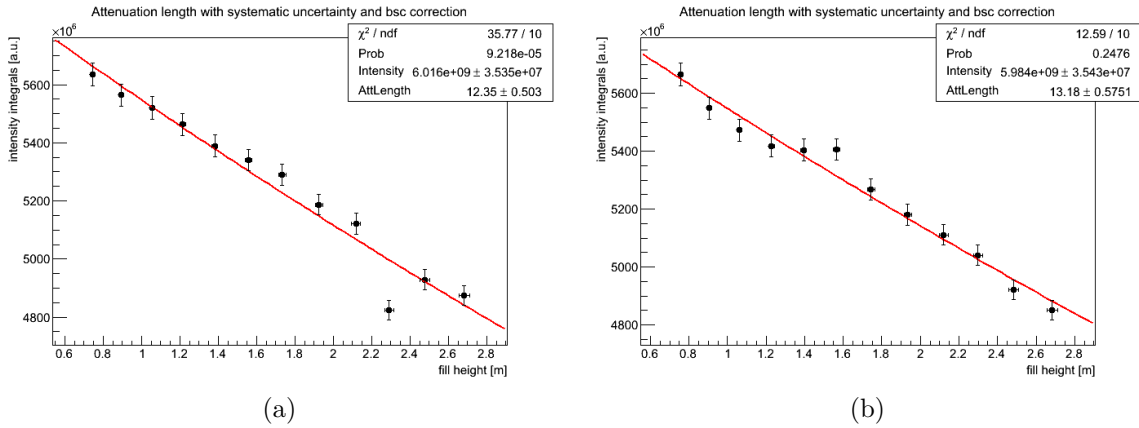

(a)   (b)

Figure 5.26: Same measurement series (also in same order) shown in fig. 5.25, but with applied intensity reconstruction at a wavelength of 420 nm for the MC-LAB sample. Measurement (b) is a reproduction measurement and is in good agreement to the found result in (a).
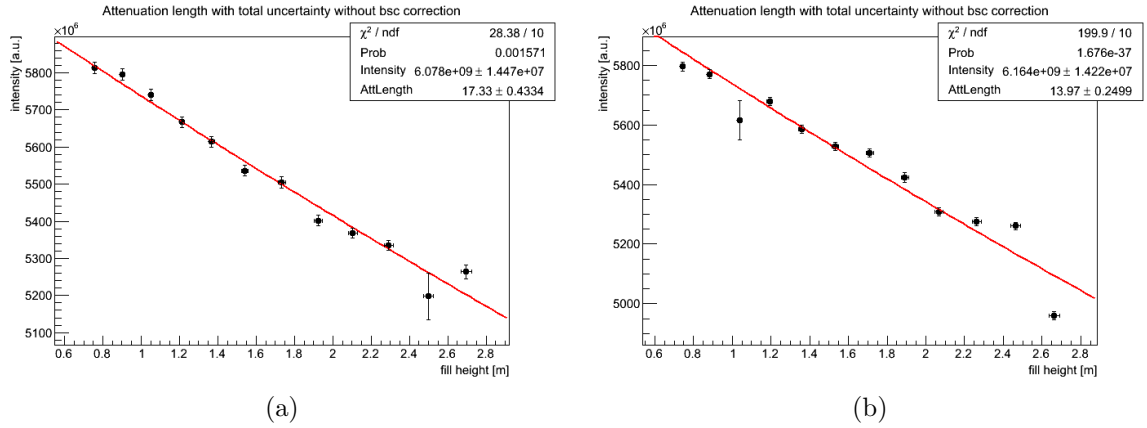
Figure 5.27: Measurement series of MC-LAB at 430 nm without taking intensity losses at sensor edges into account in (a) and a reproduction measurement is shown in (b). Plotted are the processed intensity integral means against the fill height level. The Beer-Lambert-fit is used to determine the attenuation length. The measurement in (b) is biased by mechanical instabilities, which occur during measurement time because of constructional work.

are in good agreement within the stated uncertainty. The attenuation length at $420\,\mathrm{nm} \pm 5\,\mathrm{nm}$ is determined to be

$$\Lambda^{420}_{\mathrm{MC-LAB}} = 13.18 \pm 0.58\,\mathrm{m}, \tag{5.19}$$

taking the best measurement value as final result. Further measurement series are performed at 430 nm and can be found in fig. 5.27. A measurement series (a) and its reproduction (see (b)) at 430 nm and their corresponding attenuation length values are shown, without taking the systematic uncertainty source of intensity losses into account. The upper limit of the attenuation length at $(430 \pm 9)\,\mathrm{nm}$ is determined to be

$$\Lambda^{430}_{\mathrm{MC-LAB}} < 17.76\,\mathrm{m}, \tag{5.20}$$

taking into account the observation of instabilities during the measurement shown in (b). Because of the fact, that the crucial systematic uncertainty source of intensity losses is not considered in both measurements, it is difficult to compare the results. It is found, that during the measurement plotted in (b), mechanical instabilities occurred, changing the adjustment between sample tube and deflection mirror. These instabilities originate from constructional work and make it difficult to adjust the beam permanently at the same centered position. This has an impact on the intensity loss and make it also necessary to re-adjust the beam after each single picture. Applying the intensity reconstruction for the results obtained at 430 nm, the corrected intensity integrals of both measurements can be found in fig. 5.28, in the same order as plotted in 5.27. Shown are both measurement series with
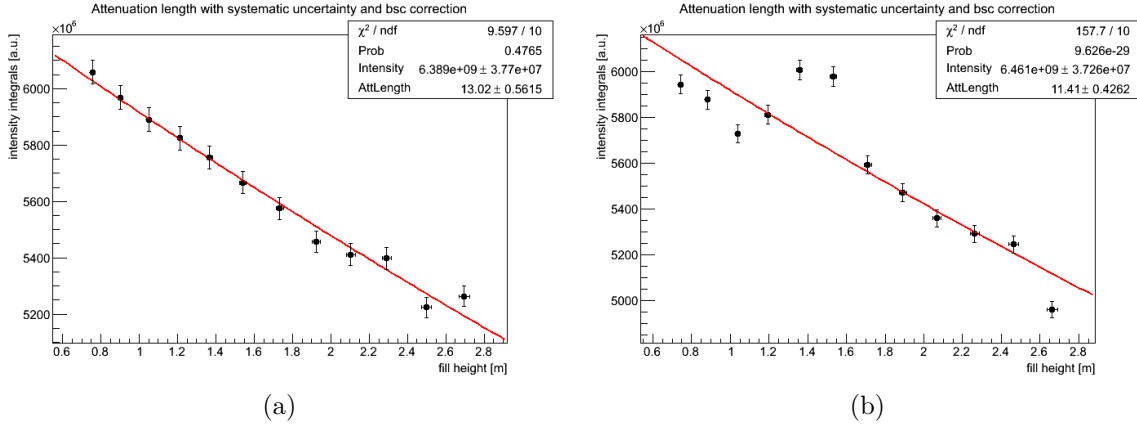
Figure 5.28: Corrected intensity integrals of the same measurement series shown in 5.27 for 430 nm of the MC-LAB sample after applying the intensity reconstruction. In (b) overestimated corrected intensity integrals can be identified.

corrected intensity integrals against the filling level. The given uncertainties are total and include possible intensity losses at the sensor borders. Both measurement results differ in the given confidence interval. This is because of the instabilities in the system, detected during the reproduction measurement. The present beam shifts distort the intensity reconstruction, which tends to overestimate the intensity correction. This is either due to inaccurate fitting limits or too big intensity losses, which increase the uncertainty of the predicted intensity losses of the fit model. This can be seen for the filling levels $\sim 1.3\,\mathrm{m}$ and $\sim 1.5\,\mathrm{m}$. Due to this instabilities, the final result at $430\,\mathrm{nm} \pm 9\,\mathrm{nm}$ is determined to be

$$\Lambda^{430}_{\mathrm{MC-LAB}} = 13.02 \pm 0.56\,\mathrm{m}. \tag{5.21}$$

For a more complete picture and the possibility to reproduce the trend of the attenuation length values seen for the UV/Vis measurements, also a measurement series at $440\,\mathrm{nm}$ is investigated. Two measurement series and their corresponding attenuation lengths can be found in fig. 5.29. Shown are the calculated intensity integrals over their filling level without considering possible intensity losses at the sensor borders, making a direct comparison between both measurements difficult. As upper limit for the attenuation length of LAB, purified with a two step aluminum oxide method at $(440 \pm 9)\,\mathrm{nm}$, the best limit is chosen:

$$\Lambda^{440}_{\mathrm{MC-LAB}} < 27.12\,\mathrm{m}. \tag{5.22}$$

The same measurement series are corrected with the intensity reconstruction method to consider the influence of intensity losses at the sensor borders. The corrected measurement results can be found in fig. 5.30. Possible intensity losses at the sensor borders, originating from vibration or focus induced beam broadening and small
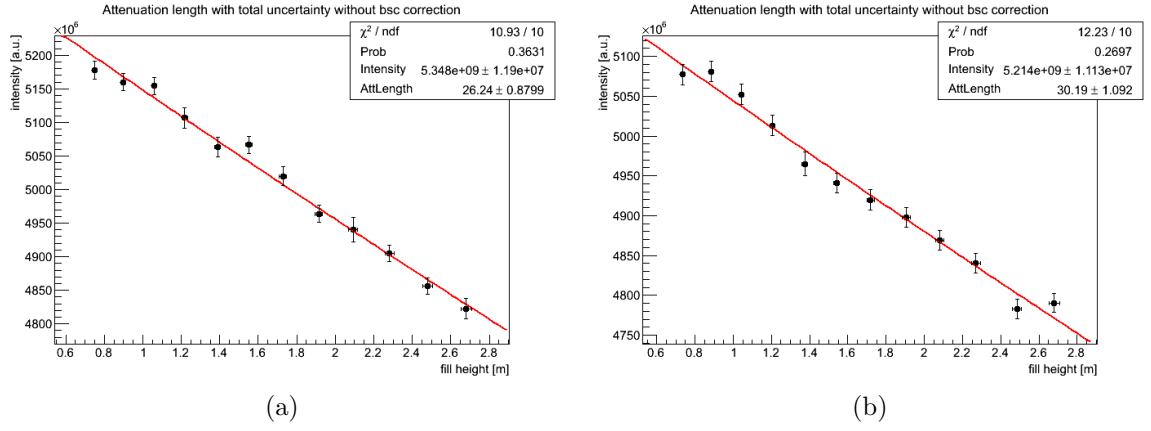
Figure 5.29: Measurement series for MC-LAB at a wavelength of 440 nm. Plotted
are the calibrated intensity integrals against the fill height levels with
total uncertainties, except the systematic uncertainty source of intensity
losses at the sensor edges. The measurements can be used to determine
an upper limit for the attenuation length.

Figure 5.30: Measurement series at 440 nm for the two step aluminum oxide purified
LAB sample after applying bsc on the data plotted in 5.29. Shown are
the corrected intensity integrals over the fill height. The red line is the
corresponding Beer-Lambert-fit to determine the attenuation length.

(a)   (b)

Figure 5.31: Measurement result (a) and a reproduction measurement (b) for the determination of the attenuation length of MC-LAB at a wavelength of 633 nm. The systematic influence of possible intensity losses are not considered here.
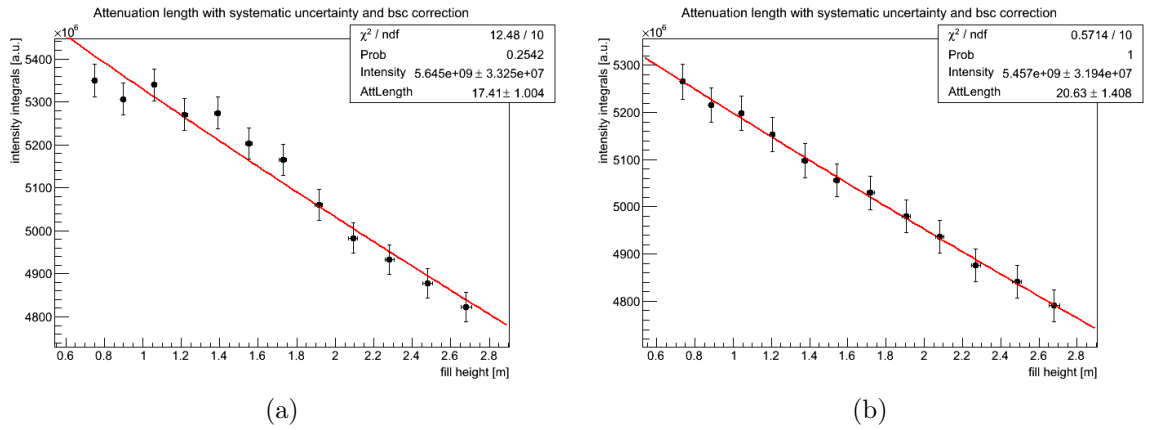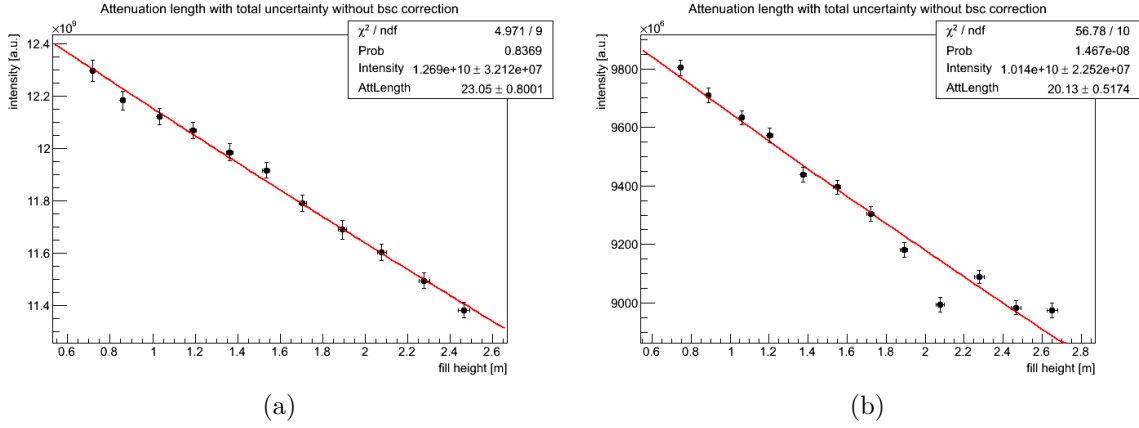
beam shifts are taken into account. The discrepancy between both measurement results is not understood completely. Both plots show a rather good agreement to the Beer-Lambert-fit and possible outliers, indicating overestimated integrals from beam shifts, are not present. Furthermore, both measurements are performed within a time window of less than 24 hours, excluding a possible degeneration of the sample liquid. Also a possible contamination during the first measurement series can be excluded, as the reproduction measurement shows a higher attenuation length. Taking into account measurement time and circumstances, it may be possible that a small change of the incident intensity took place, which would be in good agreement with an observed change of the voltage on the power supply unit from 11.45 V to 11.46 V. Because of a longterm measurement of a time period of one night within the measurement series, a possible influence on the measurement can not be excluded and would explain the decreased slope of the Beer-Lambert-fit. As a final result for the purified LAB sample with aluminum oxides at (440 ± 9) nm, the attenuation length from measurement 5.30 (a) is taken:

$$\Lambda_{\mathrm{MC-LAB}}^{440} = 17.41 \pm 1.00 \, \mathrm{m}. \tag{5.23}$$

Results at a wavelength of 633 nm

For a cross-check with another optical system and a better comparison to other samples, the attenuation length is also determined at a wavelength of 633 nm. The results can be found in fig. 5.31 without applying the intensity reconstruction. Both measurements show the calculated intensity integrals as a function of the filling level as well as the corresponding fit function and its parameters. Due to instabilities during the measurements, the attenuation length at a wavelength of (633 ± 24) nm
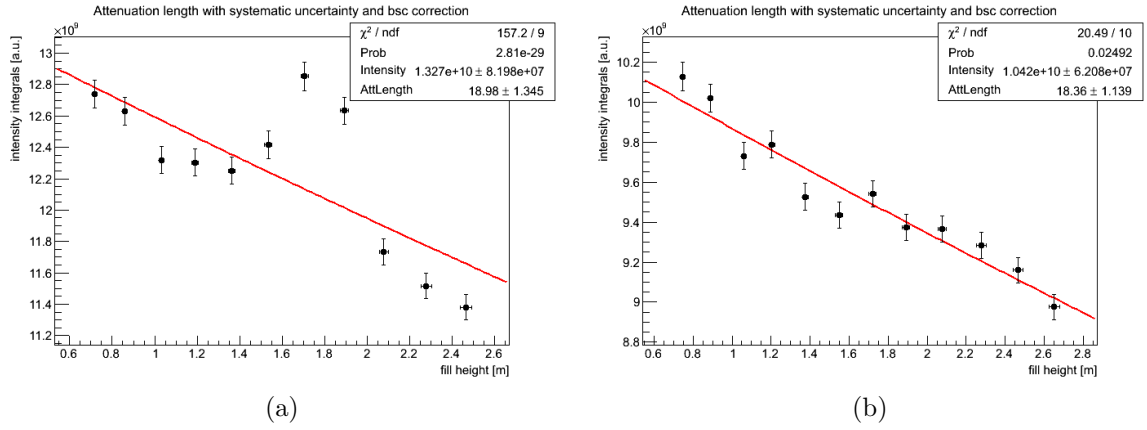
Figure 5.32: Measurement series in the same order as shown in fig. 5.31, but after taking into account the systematic influence of intensity losses, for the MC-LAB sample at a wavelength of 633 nm.

is determined to be limited to

$$\Lambda_{\text{MC}-\text{LAB}}^{633} < 20.65 \, \text{m}. \tag{5.24}$$

Applying the intensity reconstruction, the corresponding measurements and attenuation lengths are shown in fig. 5.32. Both measurement results are in good agreement to each other within the stated uncertainty. Outliers are visible at $\sim 1.7 \, \text{m}$ and $1.9 \, \text{m}$ in fig. 5.32 (a), which originate from a beam shift and corresponding inaccurate limits for the model fit functions. Due to the fact that the mean intensity integral is calculated, it is affected by such overestimated outliers. To identify such overestimated intensity integrals, the comparison between measurement series with and without the intensity reconstruction can be used. The final result of MC-LAB at a wavelength of $(633 \pm 24) \, \text{nm}$ is

$$\Lambda_{\text{MC}-\text{LAB}}^{633} = 18.36 \pm 1.14 \, \text{m}, \tag{5.25}$$

due to the identified outliers in the reproduction measurement.

5.3.3 Untreated special Nanjing LAB

As the JUNO detector is built in Jiangmen, it is considered to choose a LAB supplier next to the site to minimize the risk to pollute the liquid scintillator during transport. Furthermore, the selected manufacturer in Nanjing, China, uses a different method to synthesize LAB, called the HF acid method [JUN15]. This, pared with the usage of raw material from another petroleum source, may has an crucial impact on the optical and radioactive purity. In cooperation with the collaboration, a batch of special manufactured, high purity LAB is produced under optimized conditions to test its suitability for JUNO. First tests at the Institute of High Energy Physics
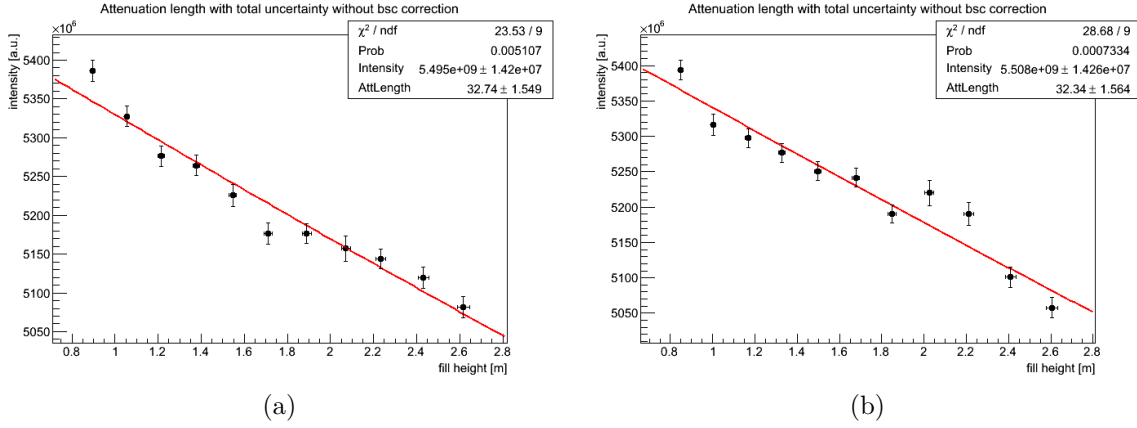
(a)

(b)

Figure 5.33: Measurement series of untreated, special manufactured Nanjing LAB for a selected wavelength of 420 nm. Plotted are the calibrated mean intensity integrals against the measured fill height. The data are fitted with the Beer-Lambert law for determining the attenuation length. Note that the given uncertainty is underestimated because of the fact that not all systematic uncertainty sources are taken into account. Both measurements limit the attenuation length and are in good agreement to each other.

in Beijing show an attenuation length of roughly 20 m at 430 nm [JUN15] [Cao18]. Further measurements are in good agreement [Gao13] [Yu15]. A batch of special manufactured Nanjing LAB from 2015 (NJ #7) is measured at 420, 430, 440 and 633 nm in the PALM experiment. In the following, the sample is referred to as special Nanjing LAB.

Results in the region of interest

The measurement results for special manufactured Nanjing at a wavelength of 420 nm can be found in fig. 5.33. Shown are two measurement series with their corresponding Beer-Lambert-fits and determined parameters. The uncertainty given for the intensities include all described systematic uncertainty sources, except the correction of the intensity loss at the sensor edges. This leads to the fact, that the corresponding attenuation length is higher than in reality. Nevertheless, both measurements are in good agreement to each other. As the systematic uncertainty of an intensity loss at the sensor edges is not included, an upper limit for the attenuation length of the liquid is obtained. As a first result, the attenuation length of the special treated Nanjing LAB at (420 ± 5) nm is limited by the best obtained limit to be

$$\Lambda^{420}_{\text{Nanjing}} < 33.90 \, \text{m}. \tag{5.26}$$

To further improve the results obtained by the PALM experiment, an intensity reconstruction, as described in section 5.1.4, is applied to the data. In the case of

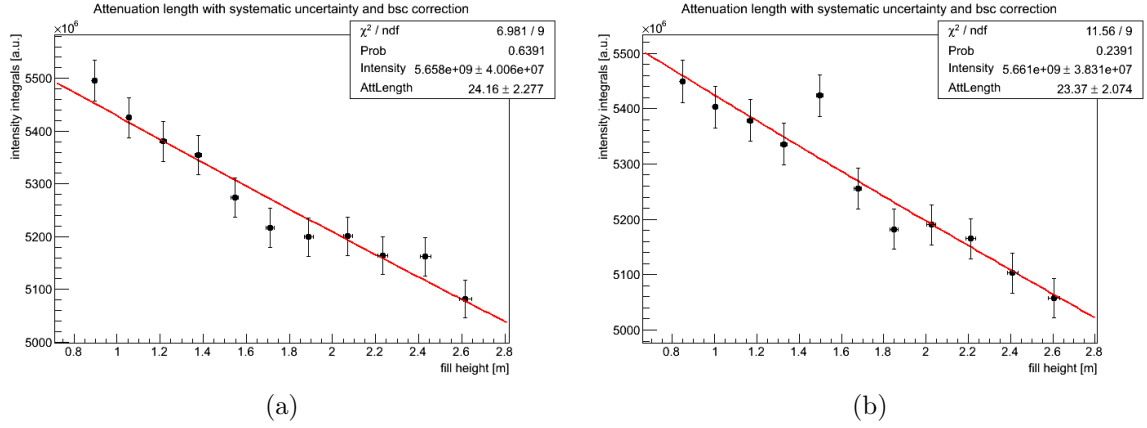(a)   (b)

Figure 5.34: Measurement series shown in fig. 5.33 after applying the intensity reconstruction for special Nanjing LAB at a wavelength of 420 nm. Shown are both measurements in their same order again.

the Nanjing LAB, the results obtained for 420 nm can be found in fig. 5.34. Shown are the measurement series in the same order as in fig. 5.33, but with applied intensity reconstruction. The resulting attenuation lengths can also be seen and are in good agreement to each other. Therefore the fit value of the best measurement series is given as the result for the attenuation length at (420 ± 5) nm for special Nanjing LAB to be

$$\Lambda^{420}_{\text{Nanjing}} = 24.16 \pm 2.28\,\text{m}. \tag{5.27}$$

A second investigation is performed at the wavelength of 430 nm and the resulting fits without an intensity reconstruction can be found in fig. 5.35. The calibrated intensity integral means are plotted against the filling levels. Because of the fact that no intensity reconstruction is applied, it is difficult to compare the results. But due to observed fluctuations within the incident light during the measurement series shown in (a) the attenuation length at a wavelength of (430 ± 9) nm is limited to be less than:

$$\Lambda^{430}_{\text{Nanjing}} < 24.36\,\text{m}. \tag{5.28}$$

An intensity reconstruction is applied for both measurements and their results are shown in fig. 5.36. After applying the intensity reconstruction, the measurement results from 5.35 are corrected and shifted to higher values for decreasing filling levels. The corresponding attenuation lengths are in no good agreement. This can be explained by the observed instability of the incident light for the measurement shown in (a) and may be caused by the halogen lamp[7] but there is a hint, that there are instabilities in the electrical main supply of the laboratory, which may have caused the fluctuation, too. The final attenuation length result for (430 ± 9) nm is

---

[7]A brand new halogen lamp is used for the special Nanjing sample measurements and a typical aging process is less probable.
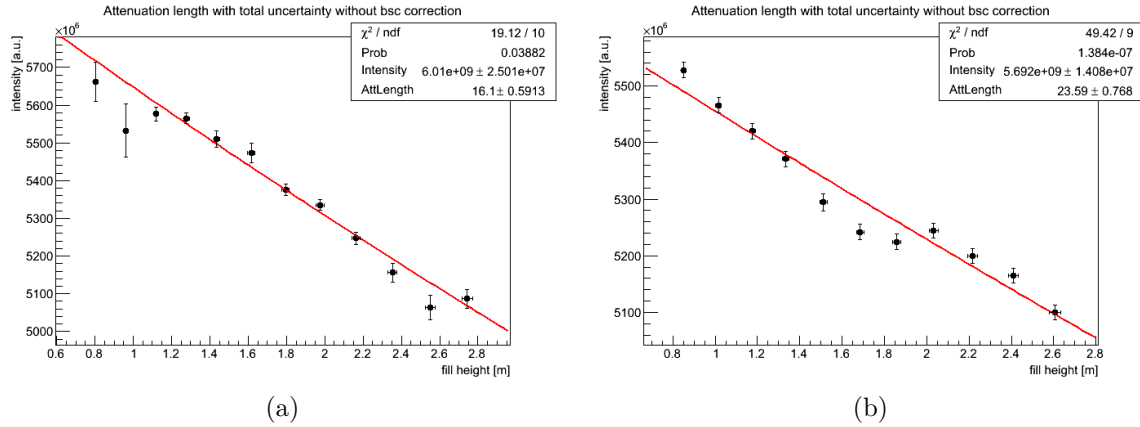
Figure 5.35: Measurement results for special Nanjing LAB at a wavelength of 430 nm. Plotted are the calibrated intensity integrals as a function of the fill height levels. The corresponding Beer-Lambert fit is shown, determining the attenuation length. Note that possible intensity losses at sensor borders are not included, which leads to an overestimation of the attenuation length.
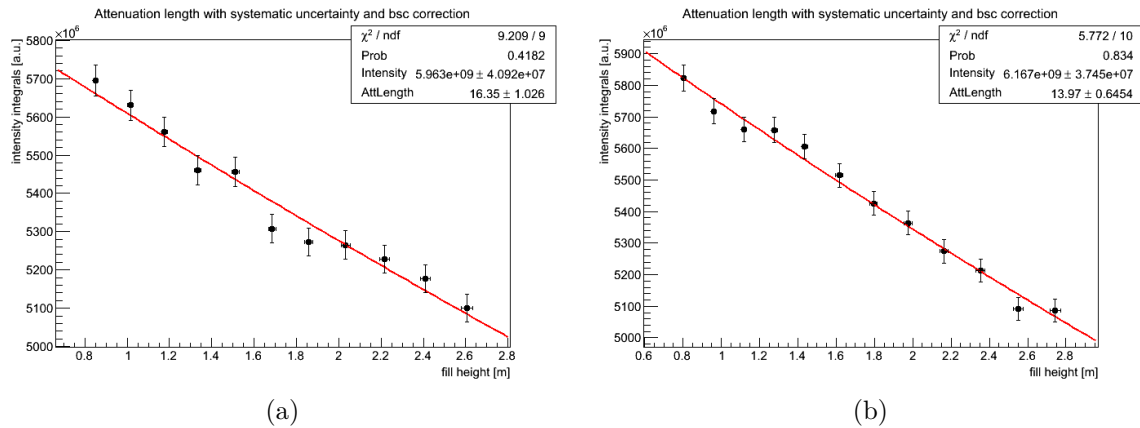
Figure 5.36: Measurements, plotted in the same order as in fig. 5.35, corrected by the intensity reconstruction method for special Nanjing LAB. Shown are both measurements and their resulting Beer-Lambert-fits at a wavelength of 430 nm.

(a)   (b)

Figure 5.37: Corresponding attenuation lengths of measurement series performed for special produced Nanjing LAB at a wavelength of 440 nm. Shown are both measurement and reproduction measurement for comparison. As explained before, the intensity losses are not corrected in this plots.

determined to be

$$\Lambda_{\text{Nanjing}}^{430} = 13.97 \pm 0.65 \, \text{m}. \tag{5.29}$$

This is in good agreement to the results obtained by [Gao13] with similar special Nanjing LAB samples and is also the case for measurement probes performed by [Cao18] 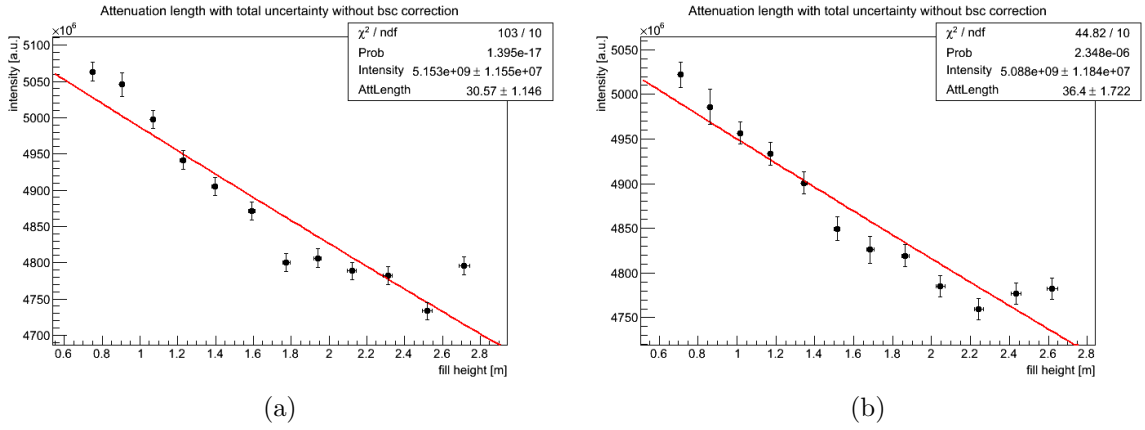and [Yu15]. For a more complete picture, similar measurements at (440 ± 9) nm are also performed and the corresponding results are shown in fig. 5.37. It shows two measurement series and their resulting fit and fit parameters without considering a possible intensity loss. The corresponding upper limit for the attenuation length at (440 ± 9) nm is determined to be

$$\Lambda_{\text{Nanjing}}^{440} < 31.72 \, \text{m}. \tag{5.30}$$

The results with applied intensity reconstruction at 440 nm are shown in fig. 5.38. After applying the reconstruction method, the results for the corrected attenuation lengths are comparable and in good agreement to each other. The final result of special Nanjing LAB at (440 ± 9) nm is

$$\Lambda_{\text{Nanjing}}^{440} = 23.54 \pm 1.88 \, \text{m}. \tag{5.31}$$

Determination of the attenuation length at 633 nm

To also determine the attenuation length at a wavelength with much higher incident intensity and also to compare the results with an independent optical system, a measurement series at 633 nm is performed and shown in fig. 5.39. The intensity integrals are plotted against the liquid level in m. During both measurements, several significant beam shifts occurred and re-adjustments of the beam had to be
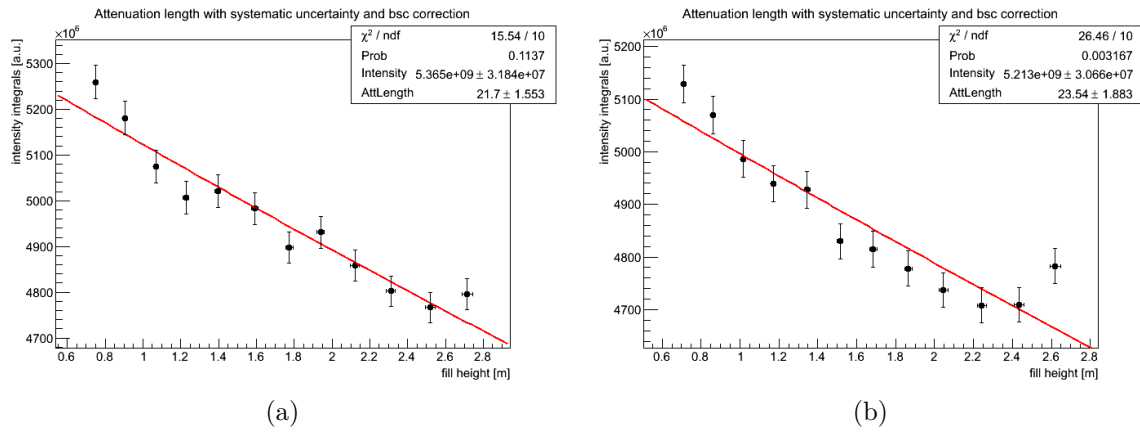
Figure 5.38: Measurement results in the same order as shown in fig. 5.37 after applying the intensity reconstruction and in so doing, taking the intensity loss at the sensor edges into account. The measurements shown are taken at 440 nm for special Nanjing LAB.
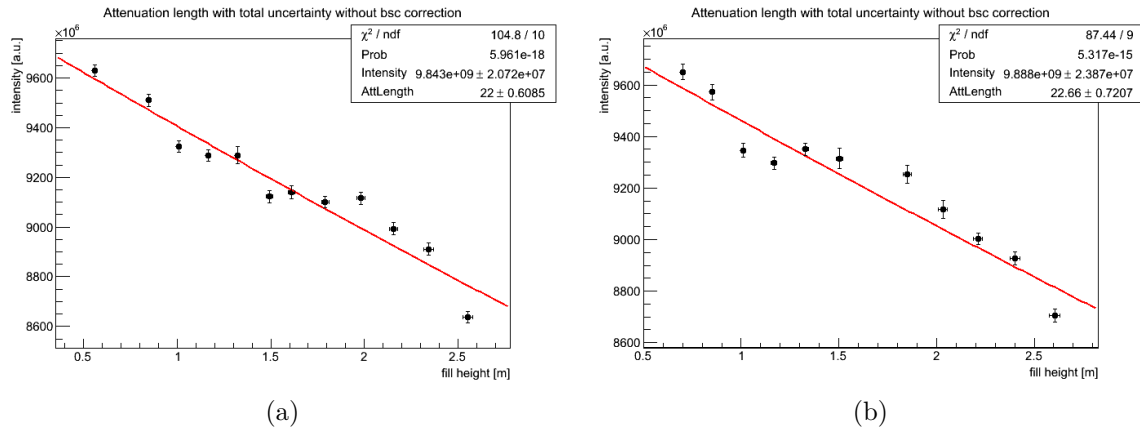
Figure 5.39: Measurement series for the determination of the attenuation length at 633 nm to compare the results with another optical system. Shown are two measurement series performed under same conditions with the Beer-Lambert-fit and its corresponding parameters. Note that the systematic influence of intensity losses is not considered here.

(a)   (b)
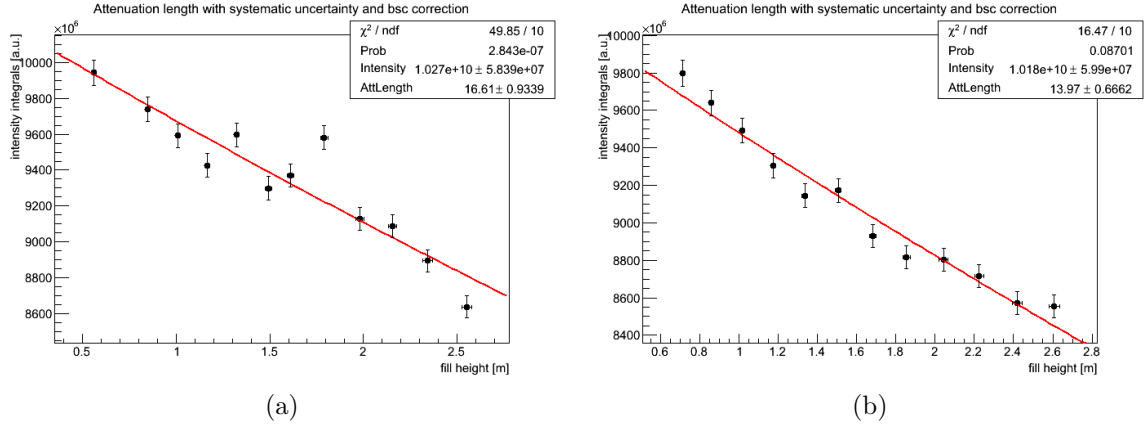
Figure 5.40: Corrected intensity integrals of both measurement series shown in fig.
5.39 in the same order after applying the intensity reconstruction at
633 nm. Also the the corresponding Beer-Lambert-fits and parameter
results are plotted.

done after each single picture. For the attenuation length of special Nanjing LAB
at (633 ± 24) nm, the best limit is used to limit the attenuation length to less than

$$\Lambda_{\text{Nanjing}}^{633} < 22.61 \, \text{m}. \tag{5.32}$$

Applying the bsc method, the corresponding results are given in fig. 5.40 in the same
order as shown in fig. 5.39 for better comparison. The corrected intensity integrals
are plotted over the fill height level and the total uncertainties for the intensity inte-
grals are given. The result of the Beer-Lambert-fit is also shown and the attenuation
length of the measurement (a) and its reproduction measurement (b) are in no good
agreement within the stated uncertainty. This can be explained by the instabilities
during both measurements. The beam shifts change the detected intensity integrals
significantly. Because a reconstruction is performed for each single data picture,
the corrected intensity integrals differ a lot and due to a mean calculation of the
corrected integrals the reconstructed integral is affected by outliers. The final result
for the attenuation length is the best obtained value

$$\Lambda_{\text{Nanjing}}^{633} = 16.61 \pm 0.93 \, \text{m}. \tag{5.33}$$

at (633 ± 24) nm.

5.3.4 Raw LAB from Daya Bay site

For achieving the goal of an attenuation length of more than 20 m, several pu-
rification techniques, as is mentioned in chapter 2, are investigated by the JUNO
collaboration and currently tested at the Daya Bay underground laboratory. Sample
probes from the Daya Bay purification plant prototypes are shipped to TUM for an
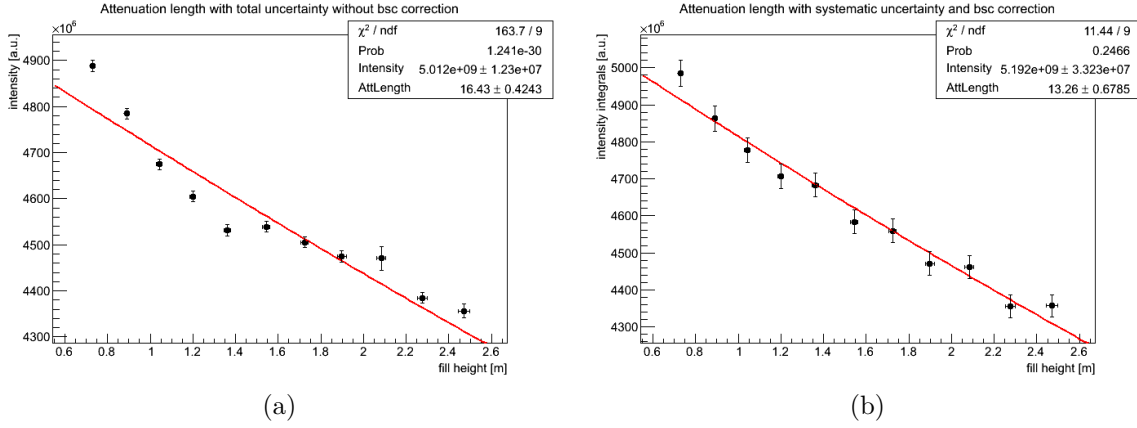
Figure 5.41: Measurement series for raw Nanjing LAB at 420 nm, which is used as raw material for the purification plant prototypes. Plotted are the intensity integrals in arbitrary units as a function of the fill height in m. A Beer-Lambert-fit is used to determine the attenuation length. In (a) the measurement series without the intensity reconstruction is shown, which means that the systematic uncertainty source of intensity losses at the sensor edges are not considered yet. In (b) the same measurement with the developed intensity reconstruction is shown.

investigation in the PALM experiment to determine the absolute attenuation length values after the purification process for the first time. To compare and evaluate the purification process, the raw material is also investigated. The raw LAB favored for the JUNO scintillator is produced in the common production process in Nanjing, which is the difference to the optimized synthesis of special Nanjing LAB. In this section, the raw LAB chosen as raw material for the purification procedures is measured for several wavelengths. In the following, it is referred to as raw Nanjing LAB.

Results in the region of interest

The attenuation length at a wavelength of 430 nm is crucial for JUNO. Therefore, measurements are performed at 430 nm but also at 420 and 440 nm for a better understanding. The results obtained for 420 nm are shown in fig. 5.41. Plotted are the intensity integrals against the fill height levels in m. The Beer-Lambert-law is used as a fit model to obtain the attenuation length from the data. In (a) an upper limit for the attenuation length at 420 nm is plotted, where the systematic effect of possible intensity losses at the sensor edges is not considered. The upper limit for the attenuation length is determined to be

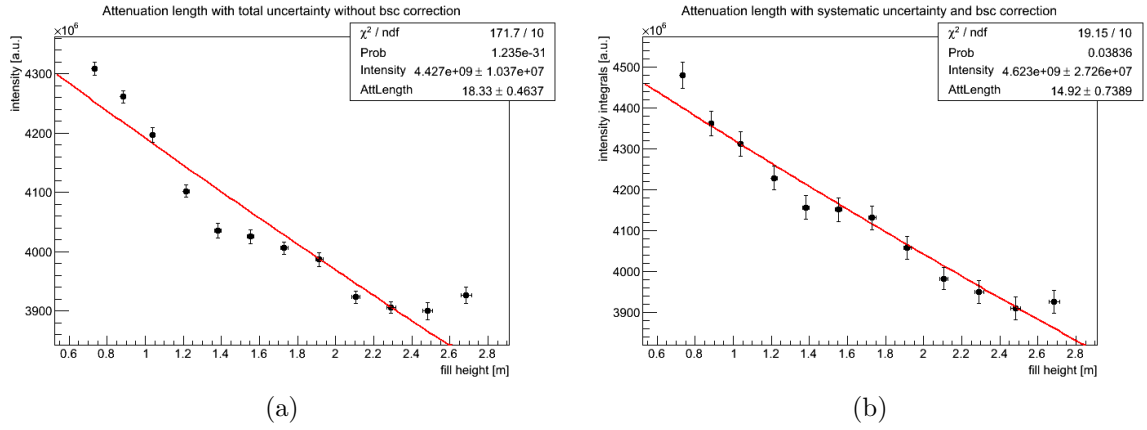$$\Lambda_{\text{Nj}-\text{raw}}^{420} < 16.85 \,\text{m}. \tag{5.34}$$

Figure 5.42: Measurement series performed for raw Nanjing LAB at a wavelength of 430 nm. Plotted are the intensity integrals against the liquid fill height. The Beer-Lambert-fit is used to determine the attenuation length. The measurement series without accounting the systematic loss of intensity at the limited sensor borders are shown in a), whereas in (b) the same measurement with applied intensity reconstruction is plotted. Note that the result obtained without the bsc is giving an upper limit for the attenuation length.

As already explained in section 5.1.4, these losses tend to overestimated the true attenuation length of the liquid. In the framework of this work, an intensity reconstruction method is developed, which corrects the intensity integrals by their losses and eliminates the systematic uncertainty source. The corrected intensity integrals and corresponding fit and parameters can be found in (b).

The increase of the beam size for decreasing filling levels is induced by the focus and the presence of vibrations, which distort the detected intensity integral. The intensity reconstruction is used to approximate the intensity losses and corrects the integrals and a final result for the attenuation length at 420 nm for the raw Nanjing LAB can be given to be

$$\Lambda_{\text{Nj-raw}}^{420} = 13.26 \pm 0.68 \, \text{m}. \tag{5.35}$$

The same approach is used for the results measured at 430 nm, which can be found in fig. 5.42 without (a) and with (b) the intensity reconstruction. In (a) the measured intensity integrals as a function of the fill height levels are shown without considering possible intensity losses. The result obtained is overestimated, giving a limit for the attenuation length values to be

$$\Lambda_{\text{Nj-raw}}^{430} < 18.79 \, \text{m}. \tag{5.36}$$

at (430 ± 9) nm. Considering possible intensity losses, the final result for the attenuation length at the same wavelength but after using the developed reconstruction
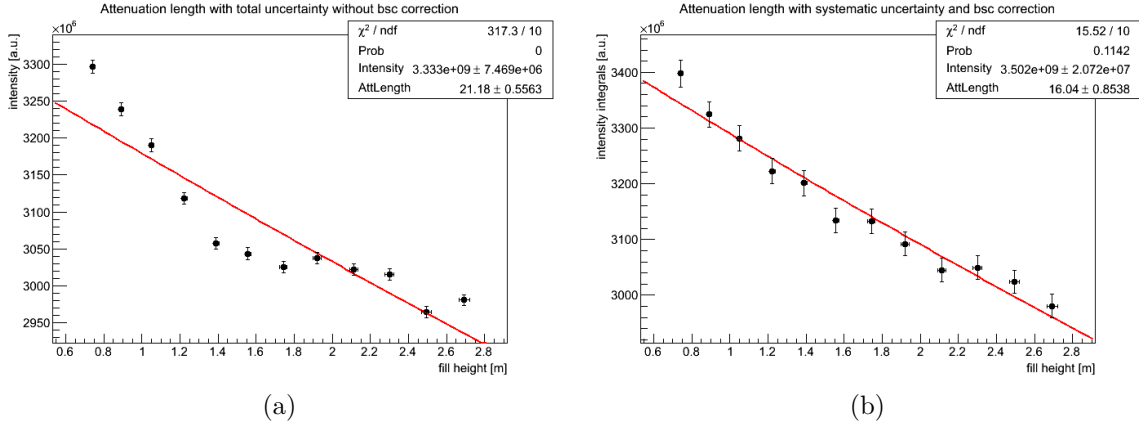
Figure 5.43: Measurement series for raw Nanjing LAB at a wavelength of 440 nm, used as raw material for the purification plant prototypes. Plotted are the intensity integrals against the liquid fill heights and a Beer-Lambert-fit is used to determine the attenuation length. In figure (a) the measurement series without an intensity reconstruction is shown, limiting the values of the true attenuation length. In (b) the systematic uncertainty source of intensity losses is taken into account and a final result is shown.

method for the raw Nanjing LAB is

$$\Lambda_{\text{Nj}-\text{raw}}^{430} = 14.92 \pm 0.74 \, \text{m}. \tag{5.37}$$

For a complete picture, also the attenuation length at a wavelength of 440 nm is investigated and the results can be found in fig.5.43. Similar to the approach of the other two measurement series, the figure shows the determined overestimated result for the attenuation length at (440 ± 9) nm in (a), which is

$$\Lambda_{\text{Nj}-\text{raw}}^{440} < 21.74 \, \text{m}, \tag{5.38}$$

and a final result is obtained and shown in (b):

$$\Lambda_{\text{Nj}-\text{raw}}^{440} = 16.04 \pm 0.85 \, \text{m}. \tag{5.39}$$

Investigation at a wavelength of 633 nm

The results at this wavelength are used on the one hand to investigate another wavelength region for the performance of the purification technique, but also to cross-check the results with another optical system and at higher incident intensities, too. The measurement series are performed at 633 nm and can be found in fig. 5.44. Shown are the results obtained without (a), and with the applied intensity reconstruction (b). After reconstruction, it can be noticed, that the absolute values

(a)   (b)
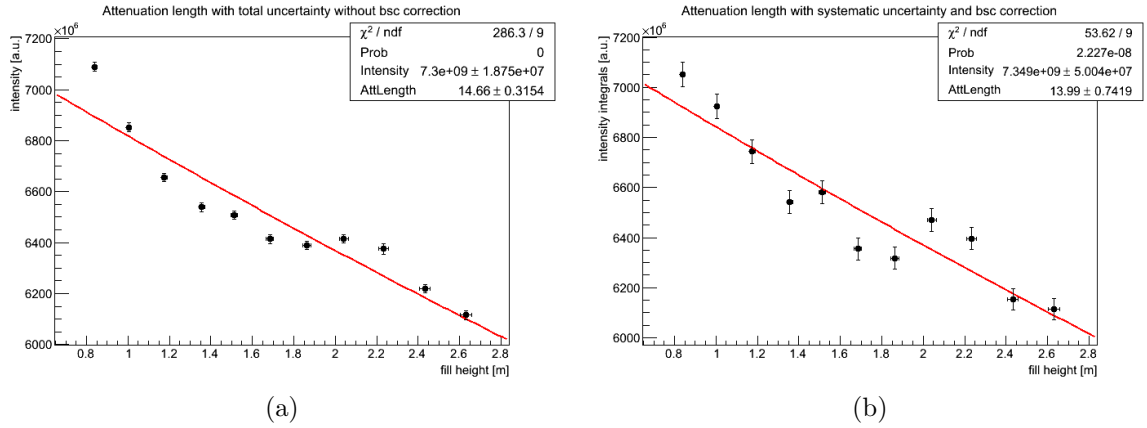
Figure 5.44: Measurement series for raw Nanjing LAB and investigated at a wave-
length of 633 nm, which is used as raw material for the purification
plant prototypes.The intensity integrals are plotted against the liquid
fill height and a Beer-Lambert-fit is used to determine the attenuation
length from the data. In (a) the measurement series without corrected
intensity losses is shown and in (b) the result with the applied intensity
reconstruction is given.

of the intensity integrals decrease for most of the data points. This is due to the
fact, that the intensity integral at maximal filling level is used as an offset. The
presence of a beam shift at the maximal fill height leads to an intensity correction,
which is much higher as for other measurement points. Nevertheless, the correlation
between the data points is not affected. Taking into account the result from (a), the
upper limit of the attenuation length is determined to be:

$$\Lambda_{\text{Nj-raw}}^{633} < 14.98\,\text{m}. \tag{5.40}$$

The final result for the attenuation length of raw Nanjing LAB before a purification
is determined to be

$$\Lambda_{\text{Nj-raw}}^{633} = 13.99 \pm 0.74\,\text{m} \tag{5.41}$$

at $(633 \pm 24)\,\text{nm}$.

5.3.5 LAB, purified in Daya Bay purification plants

The raw Nanjing LAB shown before is used as raw material for the purification
prototypes, which are located at the Daya Bay underground laboratory. The raw
material is purified using steam stripping, water extraction, aluminum oxide column
and distillation purification techniques. The attenuation length of the purified LAB
is investigated for the first time in a long tube experiment and therefore, a sample
is shipped to TUM to be measured in the PALM experiment. In the following, the
sample is referred to as purified Nanjing LAB.

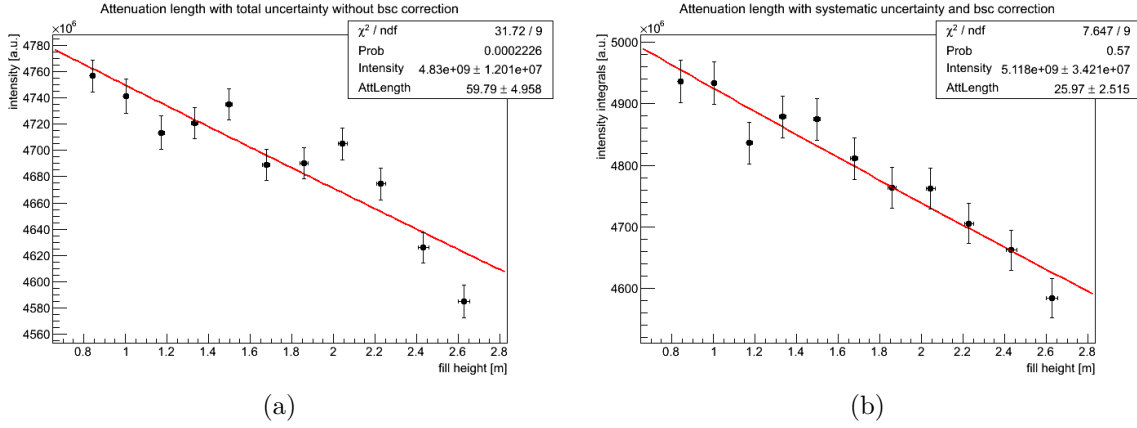Figure 5.45: Attenuation length results measured at 420 nm for the purified Nanjing LAB sample, which is purified in the purification prototypes in Daya Bay. In (a) the measurement results without the intensity reconstruction is shown and gives an upper limit for the true attenuation length, as possible intensity losses on the sensor are not considered. In (b) the same measurement series with corrected intensity integrals is plotted after applying the reconstruction method.

Results for wavelengths in the region of interest

The attenuation length of the purified Nanjing LAB is investigated at 420, 430 and 440 nm to test the influence of the purification techniques. Fig. 5.45 shows the measurement series without (in (a)) and with (see (b)) the applied intensity reconstruction. Plotted are the mean intensity integrals against the fill height levels. From the results obtained in (a) an upper limit for the attenuation length is determined to be

$$\Lambda_{\text{Nj−pur}}^{420} < 64.75 \, \text{m}. \tag{5.42}$$

Due to possible intensity losses and the fact of vibration and focus induced beam broadening, the systematic uncertainty source of the intensity losses at the sensor borders is increasing with decreasing filling levels. Therefore the intensity reconstruction is developed in the framework of this work and is explained in section 5.1.4. Correcting the intensity integrals by their possible losses, the final attenuation length at $(420 \pm 5) \, \text{nm}$ is determined to be:

$$\Lambda_{\text{Nj−pur}}^{420} = 25.97 \pm 2.52 \, \text{m}. \tag{5.43}$$

The crucial attenuation length for the JUNO collaboration is the value at a wavelength of 430 nm and the corresponding results are plotted in fig. 5.46. Similar to the case at 420 nm, the measurement series shown in (a) does not include the systematic uncertainty of possible intensity losses at the limited sensor. It can be seen, that the measurement is dominated by mechanical instabilities, which result

(a)   (b)
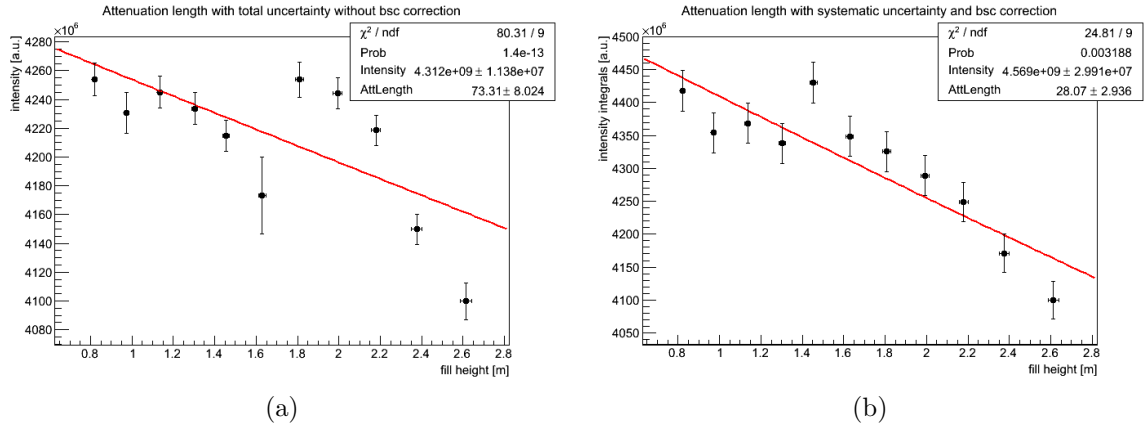
Figure 5.46: Measurement results of the attenuation length at 430 nm for the pu-
rified Nanjing LAB. The measurement in (a) is without the intensity
reconstruction. Please note that the systematic uncertainty source of
possible intensity losses is not corrected here. In (b) the same measure-
ment with corrected intensity integrals is plotted.

in beam position shifts. The corresponding upper limit for the attenuation length
is given by the Beer-Lambert-fit:

$$\Lambda_{\text{Nj}-\text{pur}}^{430} < 81.33 \, \text{m}. \tag{5.44}$$

In (b) the same measurement is shown, but after applying the intensity reconstruc-
tion and correcting the integrals by their possible intensity losses. The final result
for the purified Nanjing LAB at (430 ± 9) nm is determined to be

$$\Lambda_{\text{Nj}-\text{pur}}^{430} = 28.07 \pm 2.94 \, \text{m}. \tag{5.45}$$

Furthermore, the measurement results for a similar investigation at 440 nm can be
found in fig. 5.47, showing also the uncorrected measurement series in (a), and the
corrected intensity integrals and their corresponding attenuation length in (b). Due
to a possible overestimation of the attenuation length, the result of (a) is an upper
limit for the attenuation length:

$$\Lambda_{\text{Nj}-\text{pur}}^{440} < 90.14 \, \text{m}. \tag{5.46}$$

Taking into account the reconstructed intensity from the developed reconstruction
method, the final result for the attenuation length at (440 ± 9) nm is obtained to be

$$\Lambda_{\text{Nj}-\text{pur}}^{440} = 34.62 \pm 4.53 \, \text{m}. \tag{5.47}$$

Attenuation length results at 633 nm

For a comparison to results obtained for other samples and to cross-check them
with another optical system, a measurement series is also investigated at 633 nm
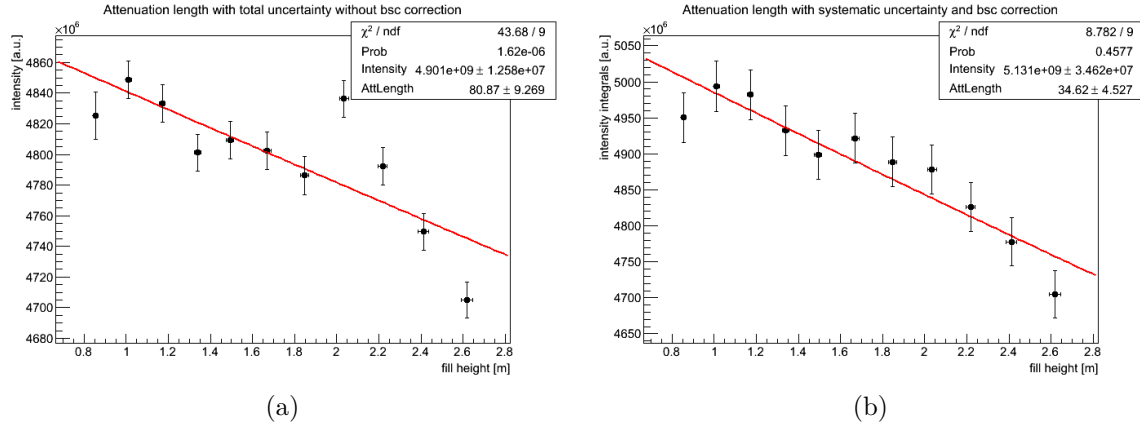
Figure 5.47: Intensity integrals plotted against the fill height level at a wavelength of 440 nm without (a) and with (b) the intensity reconstruction for the Nanjing LAB, purified in the Daya Bay purification plants.
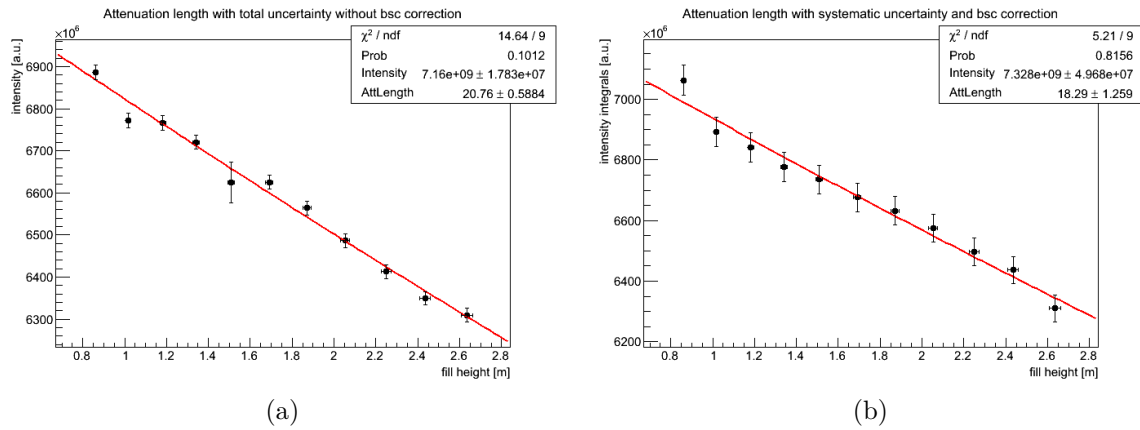

Figure 5.48: Intensity integral means without (a) and with (b) the applied intensity reconstruction for the purified Nanjing LAB at 633 nm. The results from (a) are used to give an upper limit for the attenuation length.

and can be found in fig. 5.48. Plotted are the results without (a) and with (b) the intensity reconstruction. The result from (a) can be used to give an upper limit for the attenuation length:

$$\Lambda_{\text{Nj-pur}}^{633} < 21.35\,\text{m} \tag{5.48}$$

at $(633 \pm 24)\,\text{nm}$. The final result for the attenuation length is determined to be

$$\Lambda_{\text{Nj-pur}}^{633} = 18.29 \pm 1.26\,\text{m}. \tag{5.49}$$

5.3.6 Discussion and outlook

For a better overview, the results for all measured LAB samples and wavelengths are summarized in table 5.2. Taking into account the trend for the attenuation

wavelength	Λ_{raw} [m]	$\Lambda_{\text{MC-LAB}}$[m]	Λ_{Nanjing}[m]	$\Lambda_{\text{Nj-raw}}$[m]	$\Lambda_{\text{Nj-pur}}$[m]
410 nm	3.91 ± 0.07	-	-	-	-
420 nm	-	13.18 ± 0.58	24.16 ± 2.28	13.26 ± 0.68	25.97 ± 2.52
430 nm	7.04 ± 0.17	13.02 ± 0.56	13.97 ± 0.65	14.92 ± 0.74	28.07 ± 2.94
440 nm	-	17.41 ± 1.00	23.54 ± 1.88	16.04 ± 0.85	34.62 ± 4.53
450 nm	11.37 ± 0.51	-	-	-	-
633 nm	14.04 ± 1.22	18.36 ± 1.14	16.61 ± 0.93	13.99 ± 0.74	18.29 ± 1.26

Table 5.2: Final results for the attenuation length of several LAB samples at different wavelengths for better comparison.

length found by measurements with an UV/Vis spectrometer for raw LAB, a steady increase of the attenuation length by increasing wavelengths is expected in the range of $(410\text{-}450)\,\text{nm}$ [Pru15]. The results found with PALM for raw LAB, originating from Egypt, are in good agreement to this expectation and for the first time, absolute values can be given. Furthermore, a similar trend is also expected for the MC-LAB sample and the results found with PALM are in no contradiction to this. The MC-LAB sample originates from the same batch, which was also measured in the UV/Vis spectrometer in 2015 and has been exposed to oxygen, heat and light since. This implies, that the purification effect of aluminum oxides on the raw LAB may increase the attenuation length to even higher values.

Similar measurements with an UV/Vis spectrometer are performed for LAB samples from Nanjing [JUN15] and are in good agreement to the increasing trend found by the PALM experiment, except for the sample of special Nanjing LAB. It is less probable that the attenuation length at 430 nm is so low compared to the adjacent wavelengths. Several reproduction measurements showed similar values for the attenuation length at 430 nm. The experiment used no nitrogen atmosphere during the measurements and a degeneration of the optical parameter by oxygen is possible, although the time period is less than three days. Further investigations have to be done to identify, if this result is characteristic for the sample or caused by a

contamination. Assuming the increasing trend found as true, this would mean, that the real attenuation length of the special Nanjing LAB at 430 nm may be slightly increased compared to the result of 420 nm in the given uncertainty range (or the value at 420 nm may be slightly lower) and in the order of more than 20 m.

Comparing the sample results for raw LAB and MC-LAB, originating from the same manufacturer and batch, it can be seen, that the attenuation length at 430 nm is increased significantly by the purification with alkaline and acid aluminum oxide both. This is in good agreement to the trend found in [Pru15], but for the first time, an absolute attenuation length value can be given. Also an increase at 633 nm is found, which is also expected. Taking into account the steady increasing trend within (410 - 450) nm, the attenuation length for the aluminum oxide purified LAB at 420 and 440 nm is also increased compared to raw LAB. Optimizing the storage of the sample by using nitrogen layers to eliminate the exposure to oxygen as well as to store it in the dark and cool, the attenuation length may be increased further and its quality may be conserved for longer time periods. This results make the aluminum oxide purification technique a useful tool to improve the optical transparency of the scintillator solvent used for the JUNO detector.

The comparison of both raw LAB samples, originating from Egypt and Nanjing, shows that the attenuation length at (410 - 450) nm is much higher for the sample originating from Nanjing. Such a difference can be explained by different manufacturers and production processes. Furthermore, the LAB originating from Nanjing is synthesized differently, using another chemical production process. It can be seen clearly, that the LAB from Nanjing is favored as solvent for the JUNO scintillator due to its higher attenuation length and the availability next to the experimental site of the underground observatory in Jiangmen. Former results from [Hel15a] for the same batch of raw LAB show higher attenuation lengths than found in PALM, which can be explained by the insufficient storage and a time window of more than two years between both measurements. Nevertheless, also the former results can not compete with the values obtained for the raw Nanjing LAB. This is also true for the MC-LAB, as the raw Nanjing LAB shows similar values for the optical parameter without purification.

The attenuation lengths of raw and special Nanjing LAB differ significantly, except for 430 nm. Specially manufactured Nanjing LAB shows increased values in (420 - 440) and at 633 nm compared to the raw Nanjing LAB. The measurements shown for both Nanjing LAB samples seem to have a similar attenuation length at 430 nm, but due to the trend for the attenuation length of LAB found for UV/Vis results, it is likely, that the real attenuation length of the specially manufactured LAB is higher. This leads to attenuation lengths in the order of 20 m, which could be achieved without any purification, and makes the specially processed LAB a promising candidate as raw material of the liquid scintillator used in JUNO. The special Nanjing LAB sample is manufactured under optimized conditions and no purification technique has been used so far. It has to be checked, if the application of further purification techniques can increase the attenuation length even more. Furthermore, the optimized conditions have to be installed in the common

manufacturing process to guarantee a sample liquid of 20,000 tons with the same quality, which makes it expensive. Another possibility, which is under consideration, is the usage of raw Nanjing LAB as raw material for the scintillator and applying purification techniques, as described in section 3.2.

Several efforts are made to investigate the influence of different purification techniques on the optical and radioactive purity of LAB to maximize the attenuation length. Comparing the results of raw Nanjing LAB with purified Nanjing LAB, which is purified in the Daya Bay purification plant prototypes, it can be seen that the values of the attenuation length of all measured wavelengths can be improved significantly. The combination of steam stripping, distillation, water extraction and aluminum oxide column purification can improve the relevant attenuation length at 430 nm from $14.92\,\mathrm{m} \pm 0.74\,\mathrm{m}$ to $28.07\,\mathrm{m} \pm 2.94\,\mathrm{m}$. This results show, that an attenuation length of more than 20 m at 430 nm can be achieved and that the proposed energy resolution of at least 3 % at 1 MeV can be realized. Further optimizations in the purification pilot plants would enable the JUNO detector to determine the neutrino mass hierarchy with an unprecedented energy resolution of more than the stated one. Also the more expensive special Nanjing LAB can not compete with the purified Nanjing LAB, favoring raw Nanjing LAB and the application of the purification techniques for the JUNO scintillator.

The developed intensity reconstruction shows a good performance for measurement pictures with similar characteristics. This can be seen for most of the shown measurements, although some mean intensity integrals seem to be distorted by outliers. This can be explained by differences between the single measurement pictures like un-negligible beam position differences, which have much more influence on the intensity losses than the broadening effect. Such differences can occur for instabilities during the measurements and due to inaccurate limits for the fit model functions used to reconstruct the intensity losses. A possible solution is the usage of the median or a weighted mean instead of a mean calculation, as they are less affected by outliers. Also a restriction of deviations of the beam position from the center of the sensor would suppress the occurrence of outliers of single pictures.

Due to their importance, the results obtained with the halogen lamp optic are considered to be cross-checked by another optical system. To testify the results, an alternative optic with a laser is installed.

5.4 Measurements with a laser optic

Cross-checking the results found by the PALM experiment, another optical system is considered. Instead of a halogen lamp in combination with a monochromator for monochromatic light production, a laser is chosen as an alternative light source. As lasers commonly have much higher intensities than the light produced by the halogen lamp, neutral density filters have to be used to attenuate the incident light to a level, where the CCD sensor is able to detect the incoming intensity without saturating single pixels. To conserve the halogen lamp optic and its adjustments,
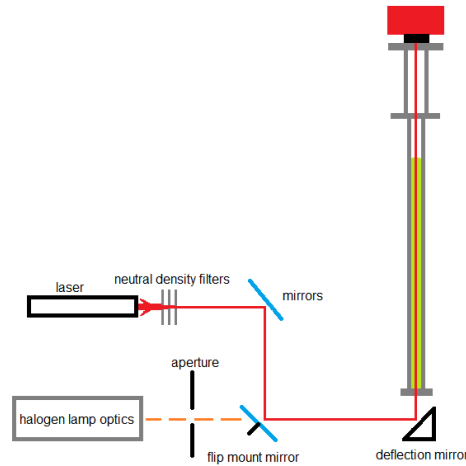
Figure 5.49: Alternative optical system to check the results found in the PALM experiment with a halogen lamp and a monochromator. A helium neon laser is used as an alternative light source. Neutral density filters are installed to attenuate the laser light beam. Several mirrors reflect the laser beam to the deflection mirror. Using a flip mount mirror, the light beam from the alternative optic can be coupled into the sample tube without changing any optical component from the former optic. By a 90° flip, the laser optic is disabled.

the laser beam is coupled into the system by a second mirror optic. A scheme of the installation can be found in fig. 5.49. Several mirrors reflect the laser beam to the deflection mirror, where the light is coupled into the sample tube without changing the former optical components of the halogen lamp. One of the mirrors is mounted in a flipper mount, which enables to flip the mirror by 90°. Flipping the flip mirror upright, the laser light beam is reflected to the deflection mirror and reaches the CCD sensor. A re-flip disables the new light path from the deflection mirror and make measurements with the former halogen lamp optic possible without changes, except the adjustments done with the deflection mirror. To eliminate potential parasitic light, both light sources are not used at the same time. A picture of the optical system can be found in fig. 5.50. The laser is a helium neon laser, emitting linear polarized light at 632.8 nm with a beam diameter of approximately 0.5 mm and a minimum power output of 0.8 mW. The coherence length is 30 cm [Tho15]. Due to the usage of the CCD camera device, the detected intensity of the laser is far too high and saturates most of the pixels. Therefore, the exposure time is set to its minimum value of 0.02 s and a combination of several neutral density filters is used to attenuate the laser efficiently for a first test setup.
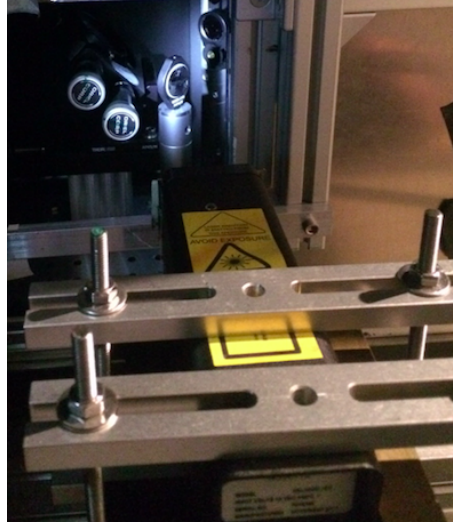
Figure 5.50: Picture of the laser system. The helium neon laser is mounted to a translation stage for better adjustment. Two fixed and one movable mirror are used to reflect the produced light beam to the deflection mirror and into the sample tube. After fine tuning of the position, the laser beam is centered on the CCD sensor without changing any other parameters.

Light source stability test

To check the performance of the laser test setup and to characterize the time stability, the sample tube is emptied to eliminate possible effects related to the liquid and longterm measurements are performed. These are further used to identify systematic influences of the beam position of the laser, intensity fluctuations as well as effects from optical components. Fig. 5.51 shows the result of a longterm intensity study performed with the new laser optic. The intensity integrals are plotted against the measurement time. After a warm up time of half an hours and adjusting the laser beam on the sensor, the measurement is started. The figure shows, that instead of a steady intensity plateau, significant changes of the incident intensity are observed. Several intensity peaks can be identified and their maxima decrease with time. This is also true for the FWHM of the intensity peaks and is a strong hint for the occurrence of interference in the setup. There are two possibilities, which have to be considered: first, the usage of two quartz glass windows on top and on the bottom of the sample tube and second, the neutral density filters installed directly after the laser. Exchanging the neutral density filters (NDF) to one NDF with a higher optical density would eliminate one source of possible interference. Due to the fact that the sample tube can be set under nitrogen atmosphere and also pressure, the second quartz glass window is used to seal the sample tube. This makes it difficult to eliminate the second source of possible interference.

Taking into account the FWHM and the usual time period for a measurement series,
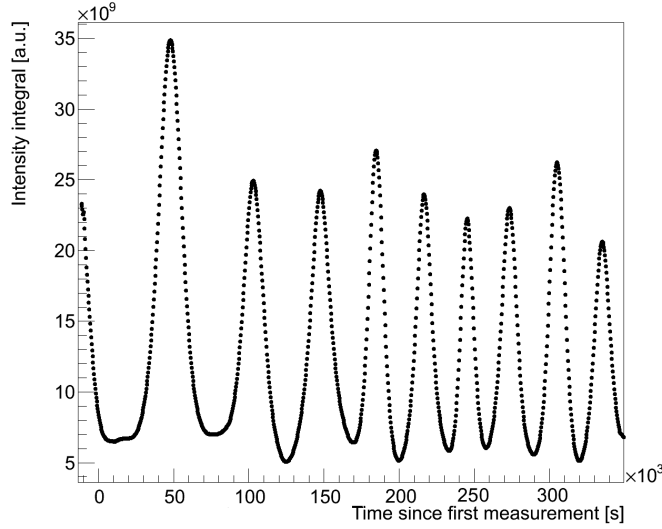
Figure 5.51: Longterm stability measurement over a time period of 80 hours with a laser at 632.8 nm, performed with an emptied sample tube. Shown are the calculated intensity integrals over the measurement time. The occurrence of several minima and maxima is a strong hint for interference effects within the experiment.

it is clear that the incident intensity has to be monitored for the current test setup, too, to eliminate its effects on the result. Due to the construction of the current setup and its mechanical components, the installation of a monitoring system is not possible without reconstructing the dark boxes, changing the whole optical translation stage table to a bigger one and re-building the optical systems, which would lead to new adjustments between optical table, sample tube, CCD sensor and deflection mirror. A monitor of the laser intensity before and after the measurement series can be performed more easily and is used for the current test setup. The longterm measurements can be used to interpolate the fluctuating intensity of the laser during the time of a measurement series. To do this, it has to be guaranteed, that the effect of the intensity can be distinguished from possible effects of the sample liquid. Therefore, longterm measurements with a filled sample tube are performed as well. Such a measurement can be found in fig. 5.52 at a fill height level of 2.66 m with the purified Nanjing LAB sample from Daya Bay. The measurement shows the same characteristic intensity peaks, which could also be seen for the empty tube measurements. This implies that the effect of the intensity fluctuation is dominant compared to all others. Influences of beam shifts and distortions can be identified as distortions at the peak shapes. Also the decreasing FWHM values can be identified clearly. An explanation are mechanical changes of the position of the mounted sample tube, which would change the interference pattern with time.
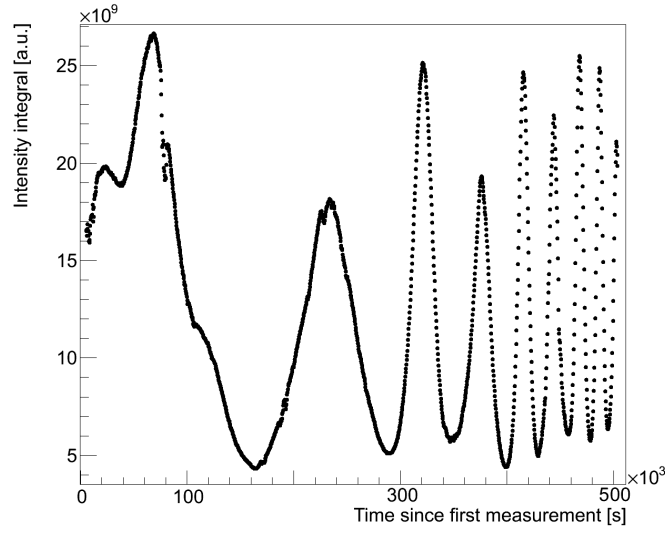
Figure 5.52: Longterm measurement of the intensity integrals over time with a laser at a wavelength of 632.8 nm, performed at a fill height level of approximately 2.6 m for comparison to the emptied tube measurements in fig. 5.51.

Modified measurement principle

Longterm measurements before and after the measurement series can be used to approximate the behavior of the incident intensity during the measurement series in a first approach. Fit functions are used to predict the incident intensity for a given time. Optimizing the measurement principle declared in section 4.3, the intensity integrals of the sensor pictures can be normalized, dividing them by the incident intensity I_0, which is no longer a free fit parameter:

$$\frac{I(x,t)}{I_0(t)} = e^{-\frac{x}{\Lambda}}. \tag{5.50}$$

Hereby, $I(x,t)$ is the attenuated intensity after the light traveled a path of x meters through a medium, measured at time t and Λ is the attenuation length of the liquid. Plotting the modified Beer-Lambert-Law to the data, the attenuation length is determined.

Critical fill height

Fig. 5.53 shows an exemplary laser beam on the CCD sensor for an emptied sample tube. The colorized laser beam shape is almost circular and can be centered on the sensor (a). Nevertheless, it is bigger than the beam spot produced by the halogen lamp (see. fig. 4.7 for comparison), which can be identified more easily in (b) for a logarithmic intensity scale. Furthermore, much higher intensities per pixels are

<div align="center">(a)   (b)</div>

Figure 5.53: Colorized picture of the laser beam for an empty sample tube with normal (a) and logarithmic scale (b) for better comparison. The colors correspond to the intensity.
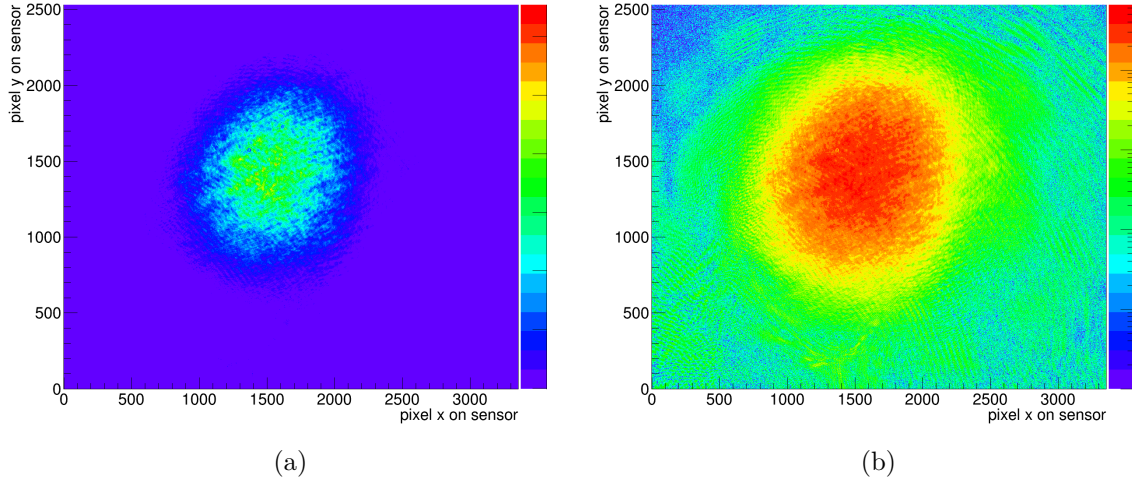
detected by the CCD sensor. Studying the differences of both optical systems, also the beam spot for a filled sample tube is shown in fig. 5.54 at a filling level of 2.66 m. The beam size of the laser is not increasing significantly in comparison to the laser beam taken with an emptied setup, because it is not focused and should not broaden for decreasing fill heights, except for possible vibrations. This is the case for the light beam produced by the halogen optic. To determine possible intensity losses at the limited sensor borders, several fill height levels are investigated and are shown in fig. 5.55. Similar to the approach of determining a critical fill height for the halogen lamp in section 5.1.3, several fill height levels are used to approximate possible intensity losses for the laser beam, too. After applying offline analysis tools, the beam at 2.66 m (marked as 188X) shows a cut area due to a dis-adjustment between deflected beam and the entrance window. It can be seen by eye, that the critical fill height of the halogen lamp can not be used for the laser optic (see fig. 5.14). The laser beam is much bigger than the beam produced by the halogen lamp for higher fill heights. Although there is no focus present, vibration induced beam broadening can be identified clearly. Because of the occurrence of perturbing vibrations, the laser beam spot is distorted and broadens with decreasing filling levels. A consequence are intensity losses at the small CCD sensor. Such a behavior is also found for the beam of the halogen lamp optic. Assuming a light beam centered in the middle of the sensor, the intensity losses for different fill height levels can be approximated and are shown in table 5.3. The same method also used for the halogen lamp optic is applied to approximate the intensity losses and for a direct comparison, see table 5.1 in section 5.1.3. A direct comparison between the results found for the beam of the halogen lamp and the laser show, that the approximated intensity losses are much
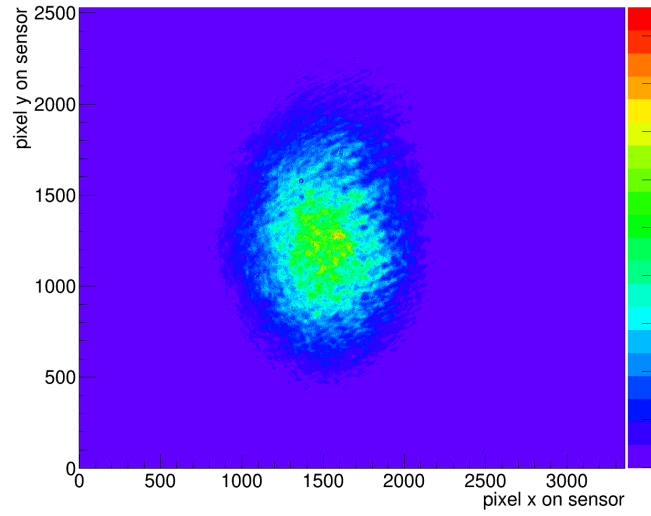
Figure 5.54: Exemplary laser beam after passing a sample liquid of 2.66 m in height. The colors correspond to the detected intensity. The beam size is not changing significantly, compared to the beam of the emptied tube, see fig. 4.7.
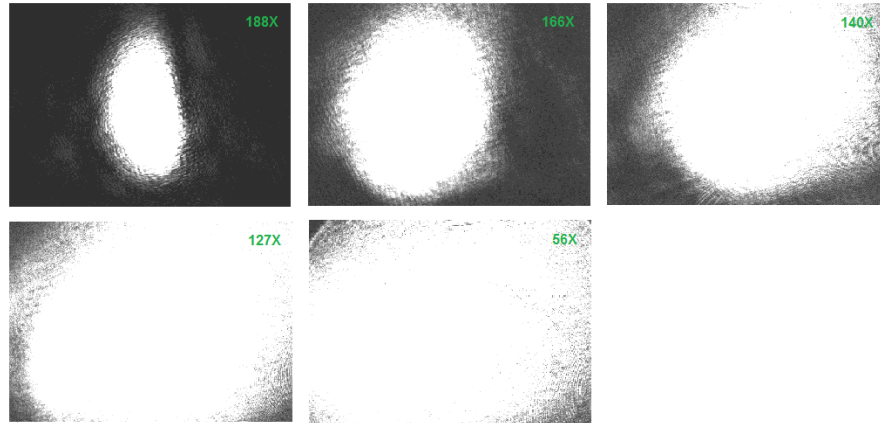
Figure 5.55: Raw data pictures of the laser beam for several different fill height levels with increased contrast settings for better comparison. The determined critical fill height is the minimal filling level, for which the losses of intensity are still negligible. Please note, that the beam at 2.66 m, marked as 188X, shows a cut area on the right.

Fill height [m]	approx. intensity loss [%]	offset corrected intensity loss [%]
0.83	31.8	30.5
0.99	32.7	31.4
1.15	29.2	27.9
1.32	21.5	20.2
1.49	21.5	20.2
1.66	14.6	13.3
1.85	12.5	11.1
2.03	12.9	11.6
2.23	7.6	6.2
2.40	4.7	3.4
2.59	3.2	1.9
2.72	1.3	0

Table 5.3: Approximated intensity losses induced by beam size broadening for adjusted laser beams. Given are the estimated losses in percent against the measured fill height level. Assuming no losses for the maximal filling level, the corrected intensity losses are also given.

higher for the laser optic and the critical fill height level determined for the halogen lamp can not be applied to the laser optic. Determining the critical liquid level under same conditions, it is found that the critical fill height level for the laser is $\sim$ 2.5 m to 2.6 m. This leads to an effective light path of 0.1 m to 0.2 m, which means, that the effect of the attenuation is comparable to the one expected for the UV/Vis spectrometers, see section 4.4. Due to vibrations, intensity losses, interferences and changes in the incident intensity, the laser optic can neither compete with common UV/Vis spectrometers nor with the halogen lamp optic.

An energy reconstruction could be used to improve the effective light path without changing the current setup. But due to the fact that the total amount of intensity on the sensor is also much higher than for the beam produced by the halogen lamp, it has to be checked, if the stated intensity reconstruction (see section 5.1.4) can be applied in its current form, due to the stated assumptions.

Test measurement at 632.8 nm

Taking into account longterm measurements to interpolate the intensity fluctuation during a measurement series, the change of the incident intensity is determined to be $\sim$ 26 % within the time period of the measurement. The incident intensity can be modeled and interpolated. For this, longterm measurements are fitted with a model function. Due to the fact that the measurement start is located at a decreasing tail of one of the incident intensity peaks, the decrease is modeled with a linear function in a first approximation.

Determining the time dependent incident intensity from fit models, a first test mea-
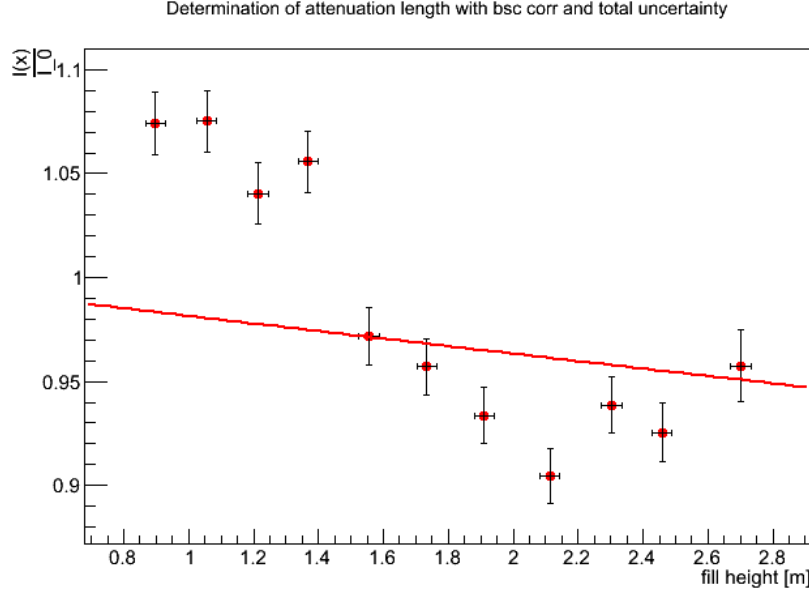
Figure 5.56: Exemplary intensity measurements with the laser beam for a comparison to the halogen lamp optic. Therefore, the critical fill height and the intensity reconstruction of the halogen lamp is used. Note that the uncertainties are underestimated.

surement with the laser optic is performed. For a direct comparison to the results from the halogen lamp optic, the critical fill height level and intensity reconstruction of the halogen lamp are used and the corresponding result is shown in fig. 5.56. Shown are the intensity integrals, divided by the approximated incident intensity. The stated uncertainties include the statistical uncertainty as well as an approximated systematic uncertainty of 1 % for the model function of the incident intensity and 0.45 % for the applied intensity reconstruction are used in a first approximation. A detailed systematic error source study has to be performed in the future. The modified Beer-Lambert-law is fitted to the data and the corresponding attenuation length to test the performance of the intensity reconstruction method. A first test result of $\sim 54\,\mathrm{m} \pm 7\,\mathrm{m}$ is obtained, but due to unknown and neglected crucial uncertainties, it represents no final result and is dismissed. Comparing the result to the one from the halogen lamp optic, see fig. 5.48, the result from the laser is excluded by the upper limit of the other optical system. The measurement result is a strong hint for an inappropriate intensity reconstruction, too.

Discussion

First test measurements are performed with the purified Nanjing LAB from the Daya Bay pilot plants for the laser optic at a wavelength of 632.8 nm. Comparing the results from laser and halogen lamp optic, it is clear that the halogen lamp optic shows a much better performance in the current setup, as no interference pattern

can occur. Eliminating the effect of possible interference, the neutral density filters should be changed to one with higher optical density. The fact that two quartz glass windows seal the sample tube makes it difficult to eliminate this possible origin of interference patterns. An idea is the change of the sealing PTFE ring in the lower entrance window flange. Instead of using a plane ring, the new PTFE seal can be manufactured with an increasing thickness to one end to guarantee, that both glass windows are not parallel to each other. This makes the adjustment of the beam spot on the CCD sensor even more challenging. Because of the un-negligible intensity fluctuations caused by interference, precise measurements are only possible, if the incident intensity of the laser source is well known. This can be done by monitoring the intensity, using a beam splitter and a photodiode. Before the laser beam is reflected to the deflection mirror, the beam can be split, one part is coupled into the sample tube, whereas the other is measured by the light detector. Because of the construction of the current experiment, the setup has to be changed significantly to install a beam splitter and a photodiode. Optical translation stage table as well as dark boxes have to be redesigned and reconstructed and both optical systems have to be moved and re-built. Furthermore, the sample tube and CCD sensor have to be re-adjusted in reference to the changed system. The beam splitter has to be mounted movable, too, as the halogen lamp optic should not be disabled, but should be used at the same time as the laser optic. Furthermore, a neutral density filter with a higher optical density is needed to attenuate the laser light to a level, where the CCD sensor pixels are not saturated. This would make it possible to increase the exposure time from $0.02\,\text{s}$ to higher values and it can be guaranteed that influences of the shutter mechanism can be excluded. Another problem arising is the increased beam size of the laser, which makes it impossible to reproduce measurement results under the same conditions as for the halogen lamp optic, as the critical filling level is much smaller. Because of the fact that the laser beam is not focused, but shows a much bigger beam size, it can not compete with the halogen lamp optic. Furthermore, it is found that the laser beam is increased by present vibrations, too. A special lens can be used to focus the laser light to the CCD sensor, decreasing the beam size. This would decrease the critical fill height level also. A second option is the usage of another CCD device with a bigger sensor. Note, that the change to a bigger sensor does improve the critical filling level, eventually, but reflections at the sample walls due to increased beam sizes are still present[8]. As a consequence, the experiment has to be optimized in a way, that all sources of perturbations are eliminated. It may have to be moved to another experimental site to eliminate influences of neighbored experiments or constructional work. Ideas for further improvements of the whole experiment are proposed in section 4.6.9.

---

[8]Please note that the diameter of the sample tube is less than $25\,\text{mm}$.

Chapter 6

Positronium Lifetime Determination Measurement (PoLiDe) Setup

As described in chapter 2, the dominant detection channel for $\bar{\nu}_e$ in JUNO is the inverse beta decay, where a positron and a neutron are produced after the interaction of an $\bar{\nu}_e$ with the scintillator target material:

$$p + \bar{\nu}_e \rightarrow n + e^+. \tag{6.1}$$

The positron annihilates with an electron, which creates a prompt signal, whereas a characteristic γ is emitted after the neutron is captured on hydrogen:

$$n + p \rightarrow d + \gamma. \tag{6.2}$$

The created signal is called a delayed signal, as it appears approximately 200 μs after the prompt signal [Gra16]. This gives a clear signature for the $\bar{\nu}_e$ interaction which can be used for background rejection [Fra11]. But there is a possibility that positrons are not annihilating with the electron at the instant, but form a temporary bound state with the electron called positronium (Ps). Positronium is a bound state similar to the hydrogen atom with the proton replaced by the positron. There are two different states depending on the spin coupling of both particles. For 25 % of the created positronium, the spin singlet state is populated with total spin equal zero which is called para-positronium (p-Ps). 75 % of positronium are populating the spin triplet state with total spin equal one, called ortho-positronium (o-Ps) [Fra11]. Unlike the direct annihilation of positron and electron, the positronium states have mean lifetimes of 125 ps (p-Ps) up to 142 ns (o-Ps) in vacuum [AlR94] [Nic90]. p-Ps typically annihilates via a two body decay, emitting 511 keV γ-rays, whereas the dominant decay channel of o-Ps is the emission of three γ-rays in vacuum. In matter,

o-Ps has a strongly reduced effective lifetime due to chemical reactions, spin-flips[1] or pick-off annihilations[2], shortening the effective lifetimes of o-Ps to a few ns in organic liquids and favoring a two body decay. The three body decay is suppressed to a negligible fraction[3] [Fra11] [Tao72]. Due to the effective lifetime of a few ns of o-Ps, the time difference between the energy deposition of the interacting positron and the annihilation signal is exceeding to a level, where calorimetric scintillation detectors may be unable to separate them. This leads to a distortion in the time distribution of the detected photoelectrons (the so called pulse shape) in reference to a direct positron annihilation [Fra11]. Such distortions in the positron pulse shape affect not only the detection of the antineutrinos via IBD, but also reconstructed events like β^+ decays, which may represent dominant background sources for neutrino detectors [Fra11]. The fact of a distorted time distribution can be used to discriminate between positron and electron events in a liquid scintillator neutrino detector, though. As the $\beta - n$ decay of cosmogenic ^{8}He and ^{9}Li isotopes can mimic IBD signals, these are expected to be a dominant background source in JUNO (see fig. 2.4 in chapter 2). Applying an positron-electron discrimination, this background can be suppressed efficiently [JUN15] [Sch17b] [Che16].

6.1 Former experiments and results

Positron annihilation lifetime spectra have been measured with standard PALS (Positron Annihilation Lifetime Spectroscopy) systems for common used organic liquid scintillators before [Fra11] [Abe14] [Che16]. In principle, a radioactive β^+ emitter is used to produce positrons, which interact in a scintillator liquid sample and form positronium with a certain probability. The bound state decays and two characteristic annihilation gammas are produced. Experiments measure the time difference between the positron production and annihilation γ. Therefore two scintillator detectors are used in coincidence, monitoring a sample liquid. This means, that only events are taken into account for the data acquisition, where both detectors detect a signal within a set time window. The scintillator detectors are a coupled plastic scintillator and a photomultiplier tube each. In most cases ^{22}Na with a Q-value of 2.842 MeV, is chosen, because each positron is emitted together with a characteristic ~ 1.275 MeV γ, which is created by the ^{22}Na decay due to the de-excitation of the produced daughter nucleus and is used as start signal for the time measurements. The source is usually encapsulated in Kapton foils. The radioactive source is placed in the sample container, right into the sample liquid. The sample container, with sample liquid and radioactive source, is positioned between both plastic scintillator detectors and is in direct contact to them. Within a time gate of several tens of ns, the detection of one of the annihilation γ is expected, as the produced positron is annihilating with an electron in the sample. This annihilation

---

[1]A spin-flip converts o-Ps in p-Ps [Tao72].

[2]The positron from an o-Ps annihilates with an electron from the surrounding medium [Tao72].

[3]The effective lifetime is shortened to 100 ns in gases and 100 ps in metals [Deu51] [Bel53].

γ are detected by the scintillator detectors and used as stop signals. The time differences between start and stop signals are measured to obtain positron annihilation lifetime spectra [Fra11].

Measurements for the pure liquid scintillator LAB are already introduced in [Fra11] and [Che16]. The result for the mean lifetime τ_2 of o-Ps[4] in LAB is determined to be 3.08 ± 0.03 ns [Fra11], which is in good agreement to the value 3.10 ± 0.07 ns obtained by [Che16]. In both experiments also the probability I_2 for the formation of o-Ps is determined for pure LAB. The formation probability of $54\% \pm 0.5\%$ [Fra11] is in contradiction to $(43.7 \pm 1.2)\%$ [Che16].

6.2 Measurement principle

Despite the results obtained for pure LAB, the three component liquid scintillator used for JUNO has to be investigated to determine the positron annihilation lifetime very precisely. To perform a positron lifetime spectroscopy using the JUNO scintillator, the Positronium Lifetime Determination (PoLiDe) experiment is developed, using a similar experimental approach as the common PALS setups. The measurement principle is the same: positrons are produced by a radioactive source and the time difference between their creation and annihilation is measured. But instead of using two detectors in coincidence for the detection of start and stop signals, three detectors are used. Two 3 inch plastic scintillator detectors detect both diametrically emitted e^+-e^- annihilation γ with an energy of 511 keV each within a certain time window. Are both photons detected in coincidence, a valid stop signal for the time measurements is obtained. A third 1 inch photomultiplier tube is used to detect the scintillation light produced in the sample liquid is used as valid start signal for time measurements. The positron emitted from the radioactive source is traversing the scintillator medium, where it deposits its kinetic energy via interactions with sample molecules, exciting or ionizing them. Excited scintillator molecules are de-exciting via photon emission, creating scintillation light[5].

Together, all three signals produce a triple coincidence signature, which makes a sufficient background reduction of contributions correlated to single faked stop signals and annihilation events outside the sample liquid possible [Sch17b].

6.3 Setup of the experiment

The experiment contains two scintillator detectors and a photomultiplier tube as well as a sample compartment with the sample liquid and a radioactive source as positron emitter. A scheme of the setup can be found in fig. 6.1. The scintillator detectors are photomultiplier tubes with diameters of 3 inches, which are coupled to plastic scintillators. Within a cylindrical aluminum dark box, the PMT is slit into a guided

---

[4]In the literature the index 2 refers to o-Ps, whereas index 1 is used for p-Ps.

[5]See chapter 3 for more detail.
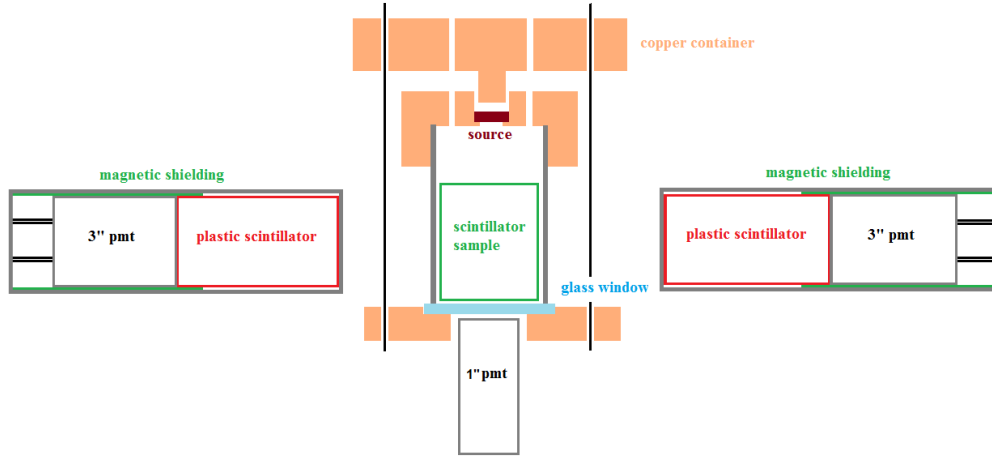
Figure 6.1: Scheme of the PoLiDe setup. Two 3 inch plastic scintillator detectors
and a photomultiplier tube are monitoring the liquid scintillator sample
within the sample container. The plastic scintillator detectors are PMTs
coupled mechanically to plastic scintillator cylinders. Both components
are embedded in an aluminum dark box and a magnetic shielding. The
coupling is done via pressure. Within the sample container, the radioac-
tive source is placed on top of the liquid but separated by gas. At the
bottom of the container, a glass window is mounted, where a third 1 inch
PMT is installed, also coupled mechanically to the window glass. The
third PMT is monitoring scintillation light created in the sample after
positron interactions, and both plastic scintillator detectors are used to
detect the positron annihilation γ.

Figure 6.2: Picture of a PMT, mounted to a customized spring holder with screws. The four springs are pressing the PMT to the sample compartment with a steady pressure, ensuring a firm mechanical coupling. This PMT is mounted vertically, in direct contact to the bottom of the sample compartment for scintillation light detection.

hold and stored in the dark. This should help to re-position the PMT module, if the system has to be opened or parts have to be changed. The scintillator material is added from the other side of the aluminum box and is positioned tight by a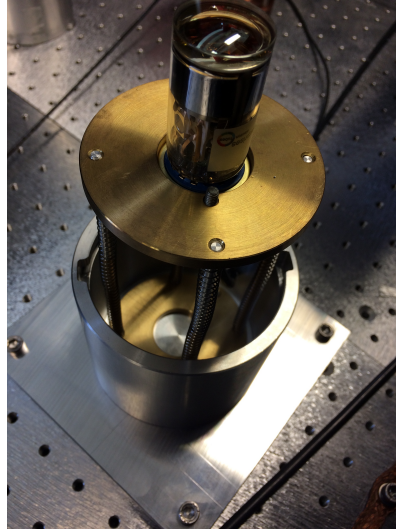dding the cap of the box. The coupling is done mechanically only by a steady pressure of the PMT against the scintillation material with a customized spring holder construction. Therefore, four springs are placed around a guide ring, used for the positioning of the 3 inch PMT, which is pressed against the scintillation material by closing the second aluminum cap and positions the detector at a central, parallel position in the aluminum box. Both aluminum boxes also contain a layer of μ-shielding to suppress magnetic fields.

The same coupling method is used for the 1 inch PMT, which is not equipped with a plastic scintillator, but is pressed directly against the glass on the bottom of the sample compartment to detect scintillation light. A picture of the third PMT, mounted to the spring holder for a steady pressure to the sample compartment, can be seen in fig. 6.2. The PMT has a mountable flange, constructed by the manufacturer. With two screws it can be mounted to a customized holder disk. The disk itself is mounted to four springs, which use a guidance tube due to their lengths, and are mounted to a third aluminum dark box at an optical table. The dark box has different inner diameters and contains the photomultiplier tube, but also the sample container, which is guided and hold by the box. The sample compartment is built modularly and is designed to contain the scintillator liquid and the radioactive source. The source can be placed on top of the liquid in a customized compartment and is not in contact with the sample liquid. This is a major difference to common

Figure 6.3: Picture of the manufactured sample container with its upper copper cap
removed. The sample liquid can be filled into the container on top of
the compartment. After filling, the radioactive source is placed in its
compartment, customized to the source plate. To guarantee that the
radioactive source is placed flat in the compartment and is not wiggling
around, the upper copper cap is placed on top of the compartment,
pressing slightly to the source plate for a flat and straight positioning.
Please note that the shown original copper tube has been changed to an
aluminum tube.

PALS setups. The sample container parts are manufactured from copper and the
complete compartment can be seen with removed copper cap in fig. 6.3. The sample
liquid is filled into the container, which is sealed gas tight by PTFE encapsulated
rings due to their chemical compatibility to the scintillator material. On top, there
is a compartment for the placement of the radioactive source above the sample
liquid, having no direct contact. After the radioactive source is placed, a copper
cap is placed on top of the sample compartment to seal it. At the same time,
the cap is positioning the radioactive source flat and straight. Two gas valves are
mounted on top of the cap for the possibility to create a nitrogen atmosphere. On
the bottom, a customized disk is mounted, which holds an acrylic glass window,
where the 1 inch PMT is placed for measurements. Due to a higher reflectivity,
an aluminum tube is manufactured and is used to contain the sample liquid. This
increases the scintillation light detected by the PMT.

The sample container can be filled with removed upper copper cap and radioactive
source plate. Without additional electronics the injected sample volume is measured

Figure 6.4: Picture of the manufactured sample container, fully mounted. The source is placed in the compartment above the scintillator sample, filled in the cooper tube. On the bottom of the tube, another cap is mounted, which contains a centered glass window and a guide mount for a 1 inch PMT. All parts are sealed with PTFE encapsulated rings. An entrance and an exit gas valve are installed to enable the creation of a nitrogen atmosphere. Please note that the copper tube was changed to an aluminum tube.

precisely to fill the tube to a certain filling level with sample liquid. After filling, the radioactive source plate can be placed in its compartment again, and the copper cap can be placed on top. With four threaded bars, the parts are pressed together firmly, sealing the sample compartment. The sample container fully mounted can be seen in fig. 6.4.

Both plastic scintillator detectors are mounted in a line and the sample container is placed between both of them. The full setup is built on an optical table and stored in the dark in a Faraday cage. The distance between both mounted plastic scintillator detectors can be varied due to their mounting on a table.

6.4 Electronics

After the annihilation of a positron with an electron in the sample liquid, two characteristic $511\,\mathrm{keV}$ γ are produced and can be detected by the plastic scintillator detectors. The electronics used for further signal processing is shown in fig. 6.5.
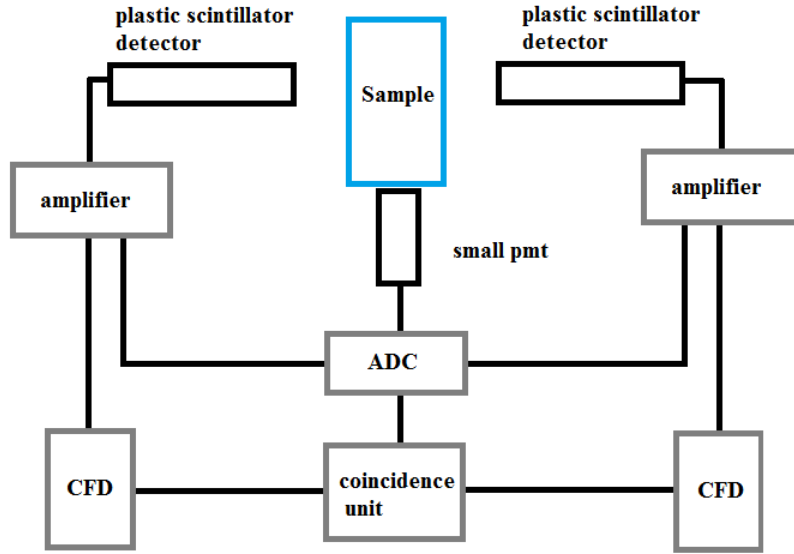
Figure 6.5: Scheme of the read out electronics used for PoLiDe. Two plastic scintillator detectors are detecting 511 keV annihilation γs after a possible positronium annihilation. Both detector signals are amplified and split. One part is used as input of the FADC, whereas the second is passed to a constant fraction discriminator. If the incoming signal has a pulse height exceeding a set threshold, a rectangle signal is produced by the CFDs and fed into a coincidence unit. Are there signals from both CFDs in a certain time gate, the coincidence unit triggers the FADC to start the data taking. Recorded are both plastic scintillation detector signals as well as the signal originating from the 1 inch PMT.

The signals of both scintillation detectors are amplified, before being split. One part is used as input voltage for a flash analog to digital converter (FADC) for data taking, whereas the other is fed into a constant fraction discriminator (CFD) unit. CFDs generate rectangle signals with a certain time gate, if the height of the incoming voltage pulses passes a set threshold.

Both CFD output channels are connected to a coincidence unit. In the case of an incoming signal from both CFDs within a set time gate, the coincidence unit will trigger the data taking and will record the signals of both scintillation detectors as well as the signal from the small 1 inch PMT, which is directly connected to the FADC.

6.5 First result and outlook

Compared to common PALS setups, the PoLiDe experiment uses a triple coincidence to determine valid start and stop signals. The usage of both 511 keV annihilation γ in coincidence as a valid stop signal instead of a single hit in one of the detectors suppresses background contributions, where single events can fake start signals. Furthermore, the radioactive source is not placed in the sample liquid as is the case for common PALS experiments, but on top. Due to the fact, that positronium can also be produced in the Kapton foils of the radioactive source encapsulation, the measured lifetime spectra can be distorted. In the case of the PoLiDe experiment, such events are rather suppressed, as the probability for the detection of the annihilation γ in both diametrically positioned detectors is small. For start signals, scintillation light is used and as a consequence, only positron events are taken into account, where the positron hit the liquid scintillator [Sch17b] [Sch17a]. Please note that the energy and time reconstruction as well as the full analysis of the recorded signal waveforms is performed offline. In the framework of a master thesis, the experimental setup is tested and optimized, based on several Monte Carlo simulations. For detailed information, refer to [Sch17a]. PMTs and electrical components are tested, their transit times and time jitters are determined and optimized, too [Sch17a]. A precise background study is investigated with Monte Carlo simulations, revealing several correlated background contributions, which can be classified [Sch17b]:

- So called outside annihilation events. Positrons deposit their energy in the sample liquid, but due to reflection or emission of thermalized positrons or positronium, an annihilation event outside the material takes place. It is found that this is the dominant background component for the 1 inch PMT in the low energy region.

- 1275 keV γ, generated by the decay of a daughter nucleus, which itself originate from a ^{22}Na decay, is detected together with another (fake) hit. This events contribute to the background distribution in the high energy region for all PMTs, which dominates the spectra in the high energy region.

- At least one of the 511 keV annihilation γ can also deposit a small portion of energy in the sample volume. In case they also produce a valid stop signal, they mimic a triple coincidence event. Such events are less dominant compared to the contribution of annihilations outside the sample material.

- Also backscattering of a single 511 keV γ, creating a hit in both plastic scintillator detectors has a minor contribution to the correlated background.

A first result for the lifetime of o-Ps in the full JUNO scintillator is obtained in the framework of a master thesis [Sch17a]. As a preliminary result, the lifetime of o-Ps is determined to be 2.97 ± 0.04 ns[6]. Be aware, that the given uncertainty is only

---

[6]For detailed information, please refer to [Sch17a].

statistical and therefore a comparison to the results found by [Fra11] and [Che16] may be difficult. Furthermore, a first result for the formation probability of o-Ps in the JUNO scintillator is found to be $I_2 = 44\% \pm 3\%$, which is in good agreement with [Che16], determined for pure LAB [Sch17b].

As a next step, systematic uncertainty sources of the PoLiDe experiment have to be investigated. Systematic influences like PMT calibration uncertainty, total time resolution of the setup, time stability of electronics and system as well as possible effects of the dark noise of the PMTs and the efficiency of applied cuts have to be investigated to determine the effects of possible fluctuations on the final results [7]. Furthermore, sample measurements should be repeated, not only to check the influence of the position of the radioactive source and varying sample container positions, but to determine the reproducibility of the measurements, too. Due to the fact that the three component scintillator sample is based on LAB from the petroleum source of Egypt, but the LAB used for the JUNO scintillator is most probable manufactured in China due to short transport and better performance[8], another measurement should be done to crosscheck, if both three component scintillators show the same behavior. Both LAB samples not only originate from different petroleum sources and may have different compositions and impurities, but they are also synthesized differently [JUN15]. This may have an impact on the positronium lifetime and formation probability and should be investigated further. Future measurements will also include different liquid scintillator samples. The PoLiDe experiment is modular built, making it easy to change materials and/ or electronic components. Plastic scintillators and PMTs can be changed easily to optimize detection efficiency and time resolution. Liquid scintillators not even based on petroleum can be measured by changing the modules and materials to guarantee chemical compatibility. For example, the new proposed THEIA [Gan15] detector will use a water based liquid scintillator. It would be possible to measure this scintillator in PoLiDe as well.

---

[7]Please note that this list is not exhaustive.

[8]See chapter 5 for comparison for further detail in respect to the differences in the attenuation length.

Chapter 7

Conclusions

The primary goal of the Jiangmen Underground Neutrino Observatory (JUNO) is the determination of the neutrino mass hierarchy. Therefore, the JUNO experiment contains a neutrino detector with a fiducial volume of 20,000 tons of liquid scintillator and is currently under construction in Jiangmen, China. For the determination of the neutrino mass hierarchy, the intermediate baseline experiment needs an energy resolution of at least 3 % at 1 MeV, which can be achieved mainly by the improvement of radioactive and optical purity of the liquid scintillator.

The attenuation length of the sample liquid has to be at least 20 m at 430 nm to guarantee the stated energy resolution. Commercially available LAB, the solvent for the JUNO scintillator, typically has attenuation lengths around 9 m to 12 m and purification methods are considered and currently under investigation. Because of the fact that the attenuation length has been determined from measurements with commercial UV/Vis spectrometers, the resulting values for the attenuation lengths have huge uncertainties, making a precise determination impossible. Therefore, the Precision Attenuation Length Measurement (PALM) experiment is set up.

The PALM experiment is a customized UV/Vis spectrometer with light paths of more than 2.0 m through a medium and a current wavelength range from 370 nm to 1,200 nm. Its purpose is the precise determination of the attenuation length of different LAB samples, which are favored for the JUNO scintillator, to evaluate, if the stated goal of an attenuation length of 20 m at 430 nm can be achieved. For the first time, absolute attenuation length values are determined for purified LAB samples, treated with different purification techniques. During tests with the setup, vibrations from the surroundings are identified as the main systematic uncertainty source. A dedicated search for vibrational sources has been performed and the climate system of the underground laboratory is identified as omnipresent source of dominant vibrations. Special dampers are installed and customized clamps and mounts are constructed to suppress vibrations of different sources. The installation of an optimized CCD camera holder shows a sufficient vibration suppression in the frequency range from 40 Hz to 50 Hz. An express decoupling device is installed to

separate sample tube and storage tank systems to eliminate possible points of excitation but mechanical impacts destroy the beam adjustments and no reduction of the perturbed beam shape has been found. Taking into account the possibility to change the resonance frequency of the system, a special damping device is constructed with a mass two times higher than the sample tube system. Due to the start of the constructional work outside the laboratory at the same time, the positive effects of the device could not be tested reliably. There is a hint that former vibrational sources like pumps and doors are negligible after the installation. Further investigations have to be performed to test the influence of the device. Furthermore, the aperture before the deflection mirror is changed to a smaller diameter, restricting the beam size and enabling sample measurements. Background originating from reflections is suppressed due to the size limitations and former unpredictable effects are eliminated. Stability measurements with a filled sample tube show similar fluctuations as are found for the emptied sample tube. An exhaustive systematic error search is investigated and influences of several systematic uncertainty sources are testified, e. g. the limited lifetime of the light source, mechanical changes or perturbation induced beam size broadening, which leads to intensity losses on the sensor edges. A critical fill height level is determined, where the beam can be adjusted almost completely on the sensor. This limits the total light path to 2.0 m through a medium. To consider the systematic uncertainty of intensity losses at the sensor edges, an intensity reconstruction method is introduced and shows a good performance. This new method makes it possible to determine the attenuation length accurately, although vibrations are still present.

For the first time, absolute attenuation lengths are obtained for favored LAB samples, which were purified with different techniques. Several samples have been investigated and due to its importance, the result for a LAB sample purified in the Daya Bay purification pilot plants is stated here. The measurements of LAB before and after the purification steps in the pilot plants show an increase of the attenuation length from 14.92 ± 0.74 m to 28.07 ± 2.94 m at a wavelength of 430 nm, which is a promising result with respect to the goal of at least 20 m to obtain the stated energy resolution. Furthermore, the positive effect of the aluminum oxide column purification with absolute attenuation length values is obtained for the first time. The results are cross-checked by measurements at adjacent wavelengths and reproduction measurements.

An alternative optical system with a laser as light source has been installed to check the results obtained with the halogen lamp. First test measurements with an empty and filled sample tube on the one hand give a strong hint, that interference, possibly created because of the usage of the glass windows to seal the sample tube and several neutral density filters, distorts the stability of the incident intensity. On the other hand, it is found that the beam spot is much bigger than the beam of the halogen lamp optic, which leads to sufficient intensity losses at the sensor borders and restricts the critical fill height level, which is defined as the minimal filling level, where such losses are negligible. At this point, the laser optic can not compete with the halogen lamp optic without changing the current setup.

Using the inverse β-decay as dominant detection channel in JUNO, a background suppression is performed by using the time coincidence of positron annihilation and neutron capture signals for event identification. Since positrons may not annihilate directly, but built a bound state with the electron called positronium, the time distribution between energy deposition and the annihilation signal is distorted, which has an impact on event reconstruction algorithms, pulse shape discrimination and background suppression. To determine the positronium lifetime spectra, a new experimental setup has been developed, which differs to the common Positron Annihilation Lifetime Spectra (PALS) setups. Using a triple coincidence of both γ from the positron annihilation and scintillation light of a liquid scintillator, a sufficient background suppression can be achieved. A first result for the lifetime of ortho-positronium (o-Ps) in the three component JUNO liquid scintillator is determined to be 2.97 ± 0.04 ns and a first formation probability of o-Ps is found to be $44\,\% \pm 3\,\%$.

Bibliography

[Abe08]   C. ABERLE: *Optimierung der Fluoreszenzcharakteristik von Flüssigszintillatoren des Double Chooz Reaktorneutrinoexperiments,* diploma thesis, Ruprecht-Karl-Universität Heidelberg (2008).

[Abe14]   Y. ABE ET AL.: *Ortho-positronium observation in the Double Chooz Experiment,* JHEP 2014: 32, arXiv:physics.ins-det/1407.6913v2, (2014).

[Ale06]   ALEPH, DELPHI, L3, OPAL, SLD COLLABORATIONS, LEP, SLD: *Precision Electroweak Measurements on the Z Resonance,* Phys. Rept. **427** 257, arXiv:hep-ex/0509008v3, (2006).

[Alo14]   J. R. ALONSO ET AL.: *Advanced Scintillator Detector Concept (ASDC): A Concept Paper on the Physics Potential of Water-Based Liquid Scintillator,* arXiv: physics.ins-det/1409.5864v2 (2014).

[AlR94]   A. H. AL-RAMADHAN, D. W. GIDLEY: *ANew precision measurement of the decay rate of singlet positronium,* Phys. Rev. Lett. **72**, 1632-1635 (1994).

[Akh00]   E. KH. AKHMEDOV: *Neutrino physics,* arXiv:hep-ph/0001264v2 (2000).

[An12]   F. P. AN ET AL. [DAYA BAY COLLABORATION]: *Observation of Electron-Antineutrino Disappearance at Daya Bay,* Phys. Rev. Lett. **108**, 171803 (2012).

[An13]   F. P. AN ET AL. [DAYA BAY COLLABORATION]: *Improved measurement of electron antineutrino disappearance at Daya Bay,* Chin. Phys. C **37**, 011001 (2013).

[An14]   F. P. AN ET AL. [DAYA BAY COLLABORATION]: *Spectral Measurement of Electron Antineutrino Oscillation Amplitude and Frequency at Daya Bay,* Phys. Rev. Lett. **112**, 061801 (2014).

[An15a]   F. P. AN ET AL. [DAYA BAY COLLABORATION]: *New Measurement of Antineutrino Oscillation with the Full Detector Configuration at Daya Bay,* Phys. Rev. Lett. **115** 111802, arXiv:hep-ex/1505.03456v2 (2015).

[An15b]   F. P. AN ET AL.: *Neutrino Physics with JUNO,* arXiv:physics.ins-det/1507.05613v2 (2015).

[Ask15]   M. Askins et. al.: *The Physics and Nuclear Nonproliferation Goals of WATCHMAN: A WAter CHerenkov Monitor for ANtineutrinos,* arXiv:physics.ins-det/1502.01132v1 (2015).

[Bel53]   R. E. Bell, R. L. Graham: *Time distribution of positron annihilation in liquids and solids,* Phys. Rev. **90**, 644 - 654 (1953).

[Bil03]   S. M. Bilenky: *Neutrino Oscillations in the framework of the tree-neutrino mixing,* arXiv:hep-ph/0307186v2 (2003).

[Bil12a] S. M. Bilenky: *On the phenomenology of neutrino oscillations in vacuum,* arXiv:hep-ph/1208.2497v1 (2012).

[Bil12b] S. M. Bilenky: *Neutrino. History of a unique particle,* arXiv:hep-ph/1210.3065v1 (2012).

[Bir64]   J. B. Birks: *The Theory and Practice of Scintillation Counting,* International Series of Monographs on Electronics and Instrumentation, vol. 27, Pergamon Press (1964).

[Bir70]   J. B. Birks: *Photophysics of Aromatic Molecules,* Wiley-Interscience, Wiley and Sons Ltd (1970).

[Boh83]   C. F. Bohren, D. R. Huffman: *Absorption and Scattering of Light by Small Particles,* John Wiley & Sons (1983).

[Cao18]   D.-W. Cao et al.: *Light Absorption Properties of the High Quality Linear Alkylbenzene for the JUNO Experiment,* arXiv:physics.ins-det/1801.08363v1 (2018).

[Che16]   Ya-Ping Cheng et al. : e^+/e^- *Discrimination in Liquid Scintillator and Its Usage to Suppress $^8He/\,^9Li$ Backgrounds,* Chin. Phys. C **41** (1) (2017) 016101, arXiv:physics.ins-det/1605.00941v2 (2016).

[Che18]   TU Chemnitz: *Die Fourier - Transformation,* Technical University of Chemnitz, https://www.tu-chemnitz.de/informatik/ThIS/downloads/courses/ws02/datkom/Fouriertransformation.pdf, author and date unknown, (2018).

[Dan62]   B. Danby et al: *Observation of High-Energy Neutrino Reactions and the Existence of Two Kinds of Neutrinos,* Phys. Rev. Lett. **9**, 36 - 44 (1962).

[Dem04]   W. Demtröder: *Experimentalphysik 1 - Mechanik und Wärme,* Springer Verlag, 3th edition (2004).

[Deu51]   M. Deutsch: *Evidence for the formation of positronium in gases,* Phys. Rev. **82**, 455-456 (1951).

[Don01]   DONUT COLLABORATION (K. KODAMA ET AL.): *Observation of tau neutrino interactions,* Phys. Lett. **B504** 218-224, arXiv:hep-ex/0012035 (2000).

[Eas10]   EASTMAN KODAK COMPANY: *DEVICE PERFORMANCE SPECIFICATION, Revision 5.4 MTD/PS-0996, KODAK KAF-8300 IMAGE Sensor,* www.kodak.com (2010).

[Enz16]   H. ENZMANN: *An On-line Attenuation length Monitor for JUNO,* presentation at the spring meeting of the German Physics Society (2017).

[Fra11]   D. FRANCO, G. CONSOLATI, D. TREZZI: *Positronium signature in organic liquid scintillators for neutrino experiments,* Phys. Rev. C **83** 015504, arXiv:hep-ph/1011.5736v3 (2011).

[For15]   R. J. FORD FOR THE SNO+ COLLABORATION: *A Scintillator Purification Plant and Fluid Handling System for SNO+,* arXiv:physics.int-det/1506.08746 (2015).

[Fuk08]   M. FUKUGITA, T. YANAGIDA: *Physics of Neutrinos and Applications to Astrophysics,* Springer Verlag (2008).

[Gan15]   THEIA INTEREST GROUP (G. D. O. GANN ET AL.): *Physics Potential of an Advanced Scintillation Detector, Introducing THEIA,* arXiv:physics.ins-det/1504.08284v1 (2015).

[Gao13]   L. GAO ET AL.: *Attenuation length measurements of liquid scintillator with LabVIEW and reliability evaluation of the device,* arXiv:physics.ins-det/1305.1471v1 (2013).

[Ge13]   S.-F. GE, K. HAGIWARA: *Physics Reach of Atmospheric Neutrino Measurements at PINGU,* JHEP 2014:24, arxiv:hep-ph/1312.0457 (2014).

[Gno05]   GNO COLLABORATION (M. ALTMANN ET AL.): *Complete results for five years of GNO solar neutrino observations,* Phys. Lett. **B616**174-190, arXiv: hep-ex/0504037 (2005).

[Gra16]   M. GRASSI [JUNO COLLABORATION]: *The Jiangmen Underground Neutrino Observatory,* Proc. of Science, vol. 274 arXiv:physics.ins-det/1609.01638v2 (2016).

[Gri87]   R. J. GRITTER, J. M. BOBBITT, A. E. SCHWARTING: *Einführung in die Chromatographie,* Springer Verlag (1987).

[Hag07]   K. HAGIWARA, N. OKAMURA, K. SENDA: *Physics potential of T2KK: An extension of the T2K neutrino oscillation experiment with a far detector in Korea,* arXiv:hep-ph/0607255 (2007).

[Hei18]   T. Heinz: *Cavity enhanced long light path attenuation length measurement,* presentation at the spring meeting of the German Physics Society (2018).

[Hel15a]   D. A. Hellgartner: *Advanced Event Reconstruction in LENA and Precision Attenuation-Length Measurements in Liquid Scintillators,* PhD thesis, Technical University Munich (2015).

[Hel15b]   D. A. Hellgartner: *Private communication,* (2015).

[Hol07]   A. F. Holleman, N. Wiberg: *Lehrbuch der Anorganischen Chemie,* Walter de Gruyter (2007).

[INO15]   INOX Color: www.inox-color.de (2015).

[Inv13]   InvenSense Inc.: *MPU-6000 and MPU-6050 Product Specification Revision 3.4,* https://store.invensense.com/datasheets/invensense/MPU-6050_DataSheet_V3%204.pdf (2017).

[JUN15]   The JUNO collaboration: *JUNO Conceptual Design Report,* arxiv:physics.ins-det/1508.07166v2 (2015).

[Key17]   KEYENCE Deutschland,: *Datenblatt AP-44,* www.keyence.de, author unknown (2018).

[Kim15]   S.-B. Kim: *Status and Prospects of Reactor Neutrino Experiments,* arxiv: hep-ph/1504.08268 (2015).

[Kra96]   L. Kraus, A. Koch, S. Hoffstetter-Kuhn: *Dünnschichtchromatographie,* Springer Labor Manual, Springer Verlag (1996).

[Li16]   Y.-F. Li: *Jiangmen Underground Neutrino Observatory: Status and Prospectives,* Particle Physics at the Year of the Light, pp. 27-33, 17th Lomonosov Conference on Elementary Particle Physics, arxiv:physics.ins-det/1606.04743v1 (2017).

[May85]   T. Mayer-Kuckuk: *Atomphysik,* Teubner Studienbücher Physik (1985).

[Mak62]   Z. Maki et al.: *Remarks on the Unified Model of Elementary Particles,* Prog. Theor. Phys. Vol. **28** No. 5, 870-880 (1962).

[Men05]   O. Mena, S. Palomares-Ruiz, S. Pascoli: *Determining the Neutrino Mass Hierarchy and CP-Violation in NOvA with a Second Off-Axis Detector,* Phys. Rev. **D73** 073007, arXiv:hep-ph/0510182 (2006).

[Men06]   O. Mena, H. Nunokawa, S. Parke: *NOνA and T2K: The race for the neutrino mass hierarchy,* Phys. Rev. **D75** 033002, arXiv:hep-ph/0609011v1 (2007).

[Nic90]   J. S. NICO ET AL.: *Precision measurement of the orthopositronium decay rate using the vacuum technique,* Phys. Rev. Lett. **65**, 1344 (1990).

[Nob15]   ROYAL SWEDISH ACADEMY OF SCIENCE: *Scientific Background on the Nobel Price in Physics 2015,* https://www.nobelprize.org/nobel_prizes/physics/laureates/2015/advanced-physicsprize2015.pdf (2017).

[Oli14]   K. A. OLIVE ET AL. (PARTICLE DATA GROUP): *LEPTONS,* Chin. Phys. C **38**, 090001 (2014) and 2015 update, http://pdg.lbl.gov/2015/tables/rpp2015-sum-leptons.pdf (2016).

[Oli15]   K. A. OLIVE ET AL. (PARTICLE DATA GROUP): *Review of Particle Physics,* Chin. Phys. C **38**, 090001 (2014).

[Ott93]   G. OTTER, R. HONECKER: *Atome-Moleküle-Kerne,* Band I Atomphysik, B. G. Teubner Stuttgart (1993).

[Paul30]   W. E. PAULI: *Offener Brief an die Gruppe der Radioaktiven bei der Gauvereins-Tagung zu Tübingen,* CERN archive transcription, http://cds.cern.ch/record/83282/files/meitner_0393.pdf (1996).

[Pru15]   S. M. PRUMMER: *Precision Measurements of Optical Attenuation Lengths of LAB for the JUNO Neutrino Experiment,* master's thesis, Technical University of Munich (2015).

[Ran17]   G. RANUCCI [JUNO COLLABORATION]: *Status and prospects of the JUNO experiment,* European Physical Journal Conferences **136**, 04001 (2017).

[Ras18]   RASPBERRY PI FOUNDATION: https://www.raspberrypi.org (2018).

[Rei56]   F. REINES, C. COWAN: *Detection of the free neutrino,* Phys. Rev. **90**, 830 - 831 (1956).

[Sal18]   G. SALAMANNA [JUNO COLLABORATION]: *STATUS AND PHYSICS POTENTIAL OF THE JUNO EXPERIMENT,* arXiv:hep-ex/1801.05580v1 (2018).

[Sag02]   SAGE COLLABORATION (J. N. ABDURASHITOV ET AL.: *Measurement of the Solar Neutrino Capture Rate by the Russion-American Gallium Solar Neutrino Experiment During One Half of the 22-Year Cycle of Solar Activity* J. Exp. Theor. Phys. **95**, arXiv:astro-ph/0204245 (2002).

[Sch97]   N. SCHMITZ: *Neutrinophysik,* Teubner Studienbücher Physik (1997).

[Sch88]   P. J. SCHULTZ, K. G. LYNN: *Interaction of positron beams with surfaces, thin films, and interfaces,* Rev. Mod. Phys. **60**, 701 - 779 (1988).

[Sch17a]   M. SCHWARZ: *First Measurements of Lifetime and Formation Probabil-
            ity of Orthopositronium in the JUNO Liquid Scintillator,* master's thesis,
            Technical University of Munich (2017).

[Sch17b]   M. SCHWARZ ET. AL: *Measurements of the Lifetime of Orthopositron-
            ium in the LAB-Based Liquid Scintillator of JUNO,* preprint paper, in
            preparation (2018).

[Sch20]   M. SCHWARZ: *Characterization and development of the liquid argon
            veto for GERDA and the future LEGEND experiment, and analysis of
            GERDA Phase II data,* PhD thesis, Technical University of Munich, in
            preparation ($\sim$ 2020).

[Sno02]   SNO COLLABORATION (Q. R. AHMAD ET AL.): *Direct Evidence for
            Neutrino Flavor Transformation from Neutral-Current Interactions in
            the Sudbury Neutrino Observatory,* Phys. Rev. Lett. **89**, arXiv:nucl-
            ex/0204008 (2002).

[Str11]   D. STROHSCHEIN: *Experimentelle Modalanalyse und aktive
            Schwingungsdämpfung eines biegeelastischen Rotors,* Kassel univer-
            sity press (2011).

[SuK98]   SUPER-KAMIOKANDE COLLABORATION (Y. FUKUDA ET AL.): *Ev-
            idence for oscillation of atmospheric neutrinos,* Phys. Rev. Lett. **81**
            arXiv:hep-ex/9807003 (1998).

[Tai18]   TAICA CORPORATION: http://www.taica.co.jp/gel-english/ (2018).

[Tao72]   S. J. TAO: *Positronium annihilation in molecular substances,* J. Chem.
            Phys. **56** (11) 5499-5510 (1972).

[Tho15]   THORLABS: *THORLABS HNLS008R, HNLS008L Self Contained,
            Red HeNe Laser System User Guide,* Rev. C, March, 23 (2015).

[Tip04]   P. A. TIPLER, G. MOSCA: *Physik Für Wissenschaftler und Ingenieure,*
            second edition, Spektrum AKADEMISCHER VERLAG (2004).

[Vog95]   H. VOGEL: *Gerthsen Physik,* Springer-Verlag, 18th edition (1995).

[Wan]   X. WANG: *A new attenuation length measurement system and light yield
            measurement,* JUNO Collaboration Meeting Beijing, July (2015).

[Wik13]   WIKA DATENBLATT PE 81.61: *Hochwertiger Druckmessumformer für
            allgemeine industrielle Anwendungen Typ S-20,* WIKA, author unknown
            (2013).

[Yan15]   G. YANG ET. AL. : *Neutrino mass hierarchy determination at reactor
            antineutrino experiments,* arXiv:physics.ins-det/1509.08747v3 (2015).

[Yu15] G.-Y. Yu et al. : *Some new progress on the light absorption properties of linear alkyl benzene solvent,* Chin. Phys. C **40** 1, arXiv:physics.ins-det/1504.05444v2 (2015).

[ZeiXX] Zeiss AG.: *Bedienungsanleitung MQ3,* author and date unknown.

[Zha08a] L. Zhan, Y. Wang, J. Cao, L. Wen: *Determination of the Neutrino Mass Hierarchy at an Intermediate Baseline,* Phys. Rev. D **78** 111103, arXiv:hep-ex/0807.3203v2 (2008).

[Zha08b] L. Zhan: *JUNO: A Next Generation Reactor Antineutrino Experiment,* Nuclear and Particle Physics Proceedings 273-276, 1825 - 1829, Elsevier (2016).

[Zho15] X. Zhou et al: *Rayleigh scattering of linear alkylbenzene in large liquid scintillator detectors,* Rev. Sci. Instrum. **86** 073310, arxiv:physics.ins-det/1504.00987v2 (2015).